

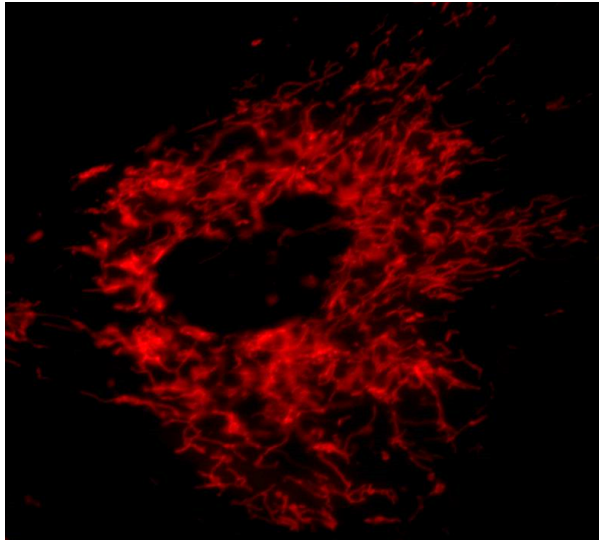
**Porphyrinic-nanoplatfoms: controlled
intracellular generation of reactive
oxygen species in human mesenchymal
stem cells**

Andrea Sofia Caetano das Neves Lavado MSc

**Thesis submitted to the University of
Nottingham for the degree of Doctor of
Philosophy**

July, 2014

Dedication



*I dedicate this thesis to my beloved parents
Frederico and Alzira
With all my heart*

Abstract

Reactive Oxygen Species (ROS) are known as important intracellular signaling molecules. These are also well known for their role in oxidative stress and cellular damage, leading to their involvement in several pathologies. Despite the widespread postulation of ROS mechanisms, little is actually known about the immediate response in living cells to the generation of these highly reactive compounds. The development of nanoplatforms incorporating photosensitizers would permit the generation of ROS at specific sub-cellular locations and determine the *in situ* cellular response.

The work presented in this thesis describes the development of porphyrinic nanoplatforms for the controlled generation of ROS and investigates their impact on the surface marker expression of human Mesenchymal Stem Cells (hMSCs).

Surface tailoring of polyacrylamide nanoparticles with alkyne and amine functionalities were exploited to achieve stable reactive chemical groups for further conjugation. Nanoplatforms surface was also modulated with trimethylammonium functionalities for the development of nanosystems for sub-cellular targeting and facilitated uptake. Physicochemical characterisation of alkyne and alkyne/trimethylammonium functionalised constructs showed sizes in the range of 40 nm with a positive surface charge. Alkyne/trimethylammonium nanosystems

were found to be stable over long periods of time, whilst amino functionalised nanosystems were found to be prone to aggregation.

Mechanisms of conjugation were exploited to create covalent linkage of porphyrinic photosensitizers to mono and dually functionalised constructs. Conjugation through "click chemistry" allowed stable coupling with alkyne and alkyne/trimethylammonium nanosystems. To overcome aggregation associated with amino functionalised nanoplateforms, porphyrin conjugated monomers were synthesised which resulted in stable polyacrylamide nanoparticles. The developed conjugated nanosystems showed final sizes in the range 40-100 nm, while conjugates with surface charges greater than $+20\text{ mV}$ have led to sizes higher than 100 nm.

The effect of surface charge on cellular delivery was investigated and nanosystems with a surface charge in the range $+13\text{ mV}$ to $+18\text{ mV}$ proved optimal in terms of cell delivery and viability. It was found that highly charged nanosystems (above $+20\text{ mV}$) remained attached to the cellular membrane and had a negative effect on cell viability. In addition, intracellular co-localisation studies showed preferential mitochondrial targeting of the delivered nanosystems.

Production of ROS in nanoparticle treated hMSCs was achieved by exposure to light at wavelength of 575 nm. For porphyrin conjugated nanosystems a single light dosage resulted in a "blast zone" in the irradiated area where significant production of hydrogen peroxide was also observed. Titration of the amount of porphyrin conjugated at the surface of nanoparticles resulted in systems with dif-

ferent levels of ROS production. Control of ROS generation allowed development of a nanoplatform that was used to expose cells to repeated exposure of ROS over a time period of 100 minutes.

The surface marker expression of hMSCs treated with porphyrin conjugated nanosystems was investigated. In the absence of light the surface marker expression of hMSCs was maintained, positive for CD29 and CD105 and negative for CD34 and CD45. Increased generation ROS in hMSCs did not produce alterations in the surface marker expression of cells, and over two generations of treated cells (light and nanoparticles) no changes were detected in surface marker expression.

The developed nanoplatforms have the potential to be applied as a tool to investigate the cellular mechanisms and metabolism associated with different levels of oxidative stress. In addition, these nanosystems could also represent an innovative platform for theranostic applications (drug delivery/diagnostic).

Acknowledgements

I would like to thank both of my supervisors Dr Jonathan Aylott and Dr Weng Chan for their guidance and support throughout this thesis.

I would like to acknowledge the financial support from the EPSRC.

I would like to express my gratitude to Dr Rhodri Jones for his patience, held and guidance. I would like to thank to my collaboration, Dr Francesca Giuntini, Dr Ross W Boyle, Dr Andrew Beeby and Miss Gery Rosser.

I would like to thanks to Amer Alhaj Zen for his friendship and collaboration in this work. Also thank you to Peter Magennis for his help.

Thanks also to my friends and colleagues in D38 - Veeren Chauhan, Erin Wik-antyasning, Arran Basra, Arpan Desai, Robby Pineda, Leo Marques, Leigh-Anne Carroll, Rosie Adsley, for all their help and suggestions, and also for making our lab a truly great place in which to work. Thanks for the golden hours and the golden moments!

Thanks to all my friends and colleagues from CBS, Glen Kirkham, Fabio Rui, Adam Taylor, Gavin Morris, Stephanie Strohucker, Sivaneswary Genapathy, Robert Hampson for all their help.

Thank you, to Paul Cooling and Christine Grainger-Boulton for the incredible help and patience throughout these four years. Also thank you to Emma King and Ian

Ward for all their help with the microscopy. Also thank you to all my colleagues and friends from Boots Science Building.

A very special thank you to my friends Ivan Lafayette, Daniela Alves and Andrea Goncalves, for their friendship, patience and encouragement. To my dear friend Susana Moleirinho thanks for all the encouragement and friendship.

A very special thank you to my dearest parents and best friends in the whole world, Frederico e Alzira for the incredible support, love and guidance you have always given me. I could not have asked for more supportive parents, and would never have reached this point without your unwavering confidence in me.

Contents

List of figures	xi
List of Figures	xi
List of tables	xx
List of Tables	xx
List of Abbreviations	1
1 General Introduction	1
1.1 Reactive Oxygen Species	1
1.2 Photosensitizers	3
1.2.1 Photosensitizers Characteristics	3
1.2.2 Photosensitized Reactions	5
1.2.2.1 Photosensitization Type I Reactions	6
1.2.2.2 Photosensitization Type II Reactions	8
1.3 Photosensitizers Applications	10
1.3.1 Photodynamic therapy	11
1.4 Porphyrins as photosensitizers	13
1.4.1 Generations of porphyrinic based photosensitizers	16
1.4.2 Effects of photosensitizers.	18

1.5	Nanotechnology.	19
1.5.1	Polyacrylamide nanoparticles	20
1.5.2	Polyacrylamide nanoparticles	20
1.5.2.1	Polyacrylamide nanoparticles and photosensitizers	21
1.6	Aims	23
1.7	Thesis Structure	25
2	Instrumentation materials and methods	31
2.1	Instrumentation	31
2.1.1	Size Characterization of nanoparticles.	31
2.1.1.1	Dynamic Light Scattering (DLS).	31
2.1.1.2	Disc Centrifuge (CPS)	32
2.1.2	Surface characterization of nanoparticles: Zeta Potential.	34
2.1.3	Fluorescence Characterization	36
2.1.4	Fluorescence Microscopy	37
2.1.5	Flow cytometry (FCM).	37
2.2	Materials and Methods	40
2.2.1	Reagents	40
2.2.2	Exploiting the surface chemistry of polyacrylamide nanoparticles	41
2.2.2.1	Synthesis of <i>N</i> -propargyl acrylamide (III)	41
2.2.2.2	Synthesis of polyacrylamide nanoparticles (PANPs)	42
2.2.2.3	Amino Functionalised Polyacrylamide Nanoparticles (AmNPs)	43

2.2.2.4	Polyacrylamide tetramethyl Ammonium Function- alised Nanoparticles (TNPs)	44
2.2.2.5	Synthesis of polyacrylamide alkyne functionalised nanoparticles (ANPs)	46
2.2.2.6	Synthesis of alkyne-trimethyl ammonium polyac- rylamide nanoplatfoms (ATNPs).	47
2.2.3	Development of porphyrin polyacrylamide nanosystems . . .	50
2.2.3.1	Development of porphyrin polyacrylamide nanosystems <i>via</i> amino-isothiocyanate conjugation.	50
2.2.3.1.1	Optimization of conjugation reaction con- ditions: amino functionalised nanoparticles.	50
2.2.3.1.2	Conjugation of 5-(4- isothiocyanatophenyl)-10,15,20-tris- [(4-N-methylpyridinium)yl] porphyrinato zinc(II)trichloride (ZnPNCS) to amino functionalised polyacrylamide nano- particles: PAmNPC	50
2.2.3.1.3	Capping of porphyrin amino nano- particles (ZnPCNPC)	51
2.2.3.1.4	Synthesis of Porphyrin nanoparticles . . .	53
2.2.3.1.5	Synthesis of porphyrin polyacrylamide nanoparticles (ZnPNPs)	54

2.2.3.1.6	Synthesis of porphyrin trimethyl ammonium polyacrylamide nanoparticles (ZnPTNPs)	56
2.2.4	Development of porphyrin polyacrylamide systems <i>via</i> click chemistry methodologies.	58
2.2.4.1	Optimization of conjugation reaction conditions: alkyne functionalised nanoparticles.	58
2.2.4.2	Conjugation of 5-4-[2-(azidoethoxy)ethyl]phenyl-10,15,20-tris-[(4-methylpyridinium)yl] porphyrinato zinc(II)trichloride (ZnPN ₃) <i>via</i> alkyne functionalised polyacrylamide nanoparticles (ZnPANPC)	58
2.2.4.3	Synthesis of porphyrin trimethyl ammonium nanoparticle conjugates. (ZnPATNPC)	60
2.2.5	Characterisation of nanoparticles	63
2.2.5.1	Dynamic Light Scattering (DLS): Size analysis of functionalised nanoparticles	63
2.2.5.2	Zeta Potential: Surface analysis of functionalised nanoparticles	63
2.2.6	Human fetal Liver mesenchymal stem cell culture	65
2.2.6.1	Thawing of stored fetal liver cells	65
2.2.6.2	<i>In vitro</i> cell culture of hMSCs	66
2.2.6.3	Harvesting of hMSCs	66
2.2.6.4	Cryopreservation of hMSCs	67

2.2.7	Cellular delivery of nanoparticles	68
2.2.8	Nanoparticle uptake analysis	68
2.3	Cellular viability analysis	69
2.3.1	Cellular effects of PATNPC activation	70
2.3.2	Controlled generation of ROS in hMSCs	71
2.3.3	Titration of porphyrin with alkyne-trimethyl ammonium polyacrylamide nanoplateforms (PATNP).	72
2.3.4	Immunophenotypic characterisation of treated hMSCs	74
2.3.4.1	Immunophenotypic characterisation of hMSCs treated with CuPATNPC or ZnPATNPC	74
2.3.4.2	Portable LED light system	75
2.3.4.3	Immunophenotypic characterisation of irradiated hMSCs treated with CuPATNPC or ZnPATNPC	76
2.3.5	Data analysis	78
3	Exploiting the surface chemistry of polyacrylamide nanoparticles	79
3.1	From Reverse Microemulsions to Polyacrylamide Nano- particles	79
3.1.1	Reverse Microemulsions	79
3.1.2	Polymerisation of acrylamide in reverse micelles.	82
3.2	Results and Discussion	86
3.2.1	Acrylamide monomers containing functional groups.	86
3.2.2	Characterization of size distribution of functionalised nano- particles.	89
3.2.2.1	Polyacrylamide nanoparticles	90

3.2.2.2	Amino functionalised nanoparticles	91
3.2.2.3	Alkyne functionalised nanoparticles	93
3.2.2.4	Alkyne/trimethyl ammonium functionalised nano- particles	94
3.2.3	Surface charge characterization of functionalised nano- particles: Zeta Potential.	96
3.2.3.1	Comparison of nanoparticle sizes	98
3.2.3.2	Size distribution of nanoparticles: Dynamic light scattering (DLS) vs. differential centrifugation (CPS).	101
3.2.3.3	Nanoparticles stability over time: DLS character- isation.	102
3.3	Conclusions	105
4	Development of Porphyrin Polyacrylamide Nanoparticle Sys- tems.	108
4.1	Introduction	108
4.1.1	“Click chemistry”	111
4.1.1.1	The mechanism of Alkyne-Azide CuAAC.	111
4.1.1.2	Sources of Cu(I).	113
4.2	Results and Discussion	115
4.2.1	Spectroscopic characterisation of porphyrins	115
4.2.2	Development of porphyrin polyacrylamide systems <i>via</i> amino-isothiocyanate conjugation.	119
4.2.2.1	Optimisation of conjugation reaction conditions. . .	119

4.2.2.2	Spectroscopic characterisation of NP-porphyrin conjugates.	121
4.2.2.2.1	Capped porphyrin-nanoparticle conjugates (XVI - ZnPCNPC).	121
4.2.2.2.2	Porphyrin nanoparticles (XVII -ZnPNPs)	123
4.2.2.2.3	Porphyrin trimetylammonium nanoparticles (XVIII - ZnPTNPs)	125
4.2.2.3	Size characterisation of porphyrin-NP conjugates. .	126
4.2.2.4	Surface characterisation of NP-conjugates.	129
4.2.3	Development of porphyrin polyacrylamide systems <i>via</i> click chemistry methodologies.	132
4.2.3.1	Optimisation of conjugation click reaction conditions.	132
4.2.3.1.1	Click reaction of NPs with azidocoumarin.	133
4.2.3.1.2	Effect of copper (I) bromide in the absorption of metallated porphyrins.	136
4.2.3.2	Spectroscopic characterisation of NP-porphyrin conjugates.	139
4.2.3.3	Size characterisation of NP-porphyrin conjugates. .	140
4.2.3.4	Surface characterisation of NP-conjugates.	142
4.3	Conclusions	144
5	Delivery of nanoparticles to human Mesenchymal Stem Cells	146
5.1	Introduction	146
5.1.1	Endocytic mechanisms for cellular uptake of nanoparticles and size effect	147

5.1.1.1	Phagocytosis	148
5.1.1.2	Pinocytosis	148
5.1.1.3	Surface charge and cellular uptake	151
5.1.2	Nanoparticle engineering and sub-cellular fate	152
5.1.2.1	Cationic nanosystems and associated cytotoxicity. . .	154
5.2	Results and Discussion	156
5.2.1	Cellular uptake of positively charged polyacrylamide nanosystems	157
5.2.1.1	Internalisation of positively charged nanoplateforms. .	157
5.2.1.2	Sub-cellular co-localisation of internalised positively charged nanosystems.	161
5.2.1.3	Impact of positively charged nanoparticles on hM- SCs: Viability versus particle uptake.	167
5.2.2	Cellular uptake of porphyrin nanosystems	176
5.2.2.1	Effects and internalisation of free porphyrin.	177
5.2.2.2	Effects and internalisation of porphyrin- nanoparticle conjugates (ZnPATNPCs).	184
5.2.2.3	Effects and internalisation of porphyrin nanosys- tems. (ZnPTNPs	192
5.3	Conclusions	200

6	Porphyrinic nanoplateforms for the controlled generation of ROS in stimulated human Mesenchymal Stem Cells	202
6.1	Introduction	202
6.1.1	Porphyrins: production of reactive oxygen species	203

6.1.2	Zinc and copper porphyrins as photosensitizers	204
6.2	Results and Discussion	206
6.2.1	Porphyrin-NPs:ROS generation in hMSCs	207
6.2.1.1	Detection of ROS	207
6.2.1.2	Imaging hMSCs: Multichannel fluorescence stitching	208
6.2.1.3	Effect of porphyrin-NPs on cells when irradiated with light	211
6.2.2	ZnPATNPC for the controlled generation of ROS in hMSCs.	214
6.2.2.1	ZnPATNPC: Modulation of conjugated porphyrin .	215
6.2.2.1.1	Size and surface charge characterisation of ZnPATNPC.	216
6.2.2.1.2	Fluorescence characterisation of ZnPAT- NPC	218
6.2.2.2	Cellular effects of porphyrin modulated nanosystems.	219
6.2.2.3	Effect of 5 % ZnPATNPC on cells when irradiated by light: Controlled generation of ROS.	221
6.3	Conclusions	225
7	Impact of ROS in the differentiation state of Mesenchymal Stem Cells	228
7.1	Mesenchymal Stem Cells	228
7.1.1	Immunophenotypic Characterisation of hMSCs	230
7.1.1.1	Cell Surface Molecules	230
7.1.1.2	Cell surface molecules characteristic of MSCs . . .	231
7.1.1.3	Role of ROS on the undifferentiated state of hMSCs	233

7.2	Results and Discussion	235
7.2.1	Morphology of hMSCs	235
7.2.2	Characterisation of hMSCs:	236
7.2.3	Effect of nanoparticle delivery on the surface marker expres- sion in hMSCs:	240
7.2.4	Impact of ROS on surface marker expression in hMSCs: . . .	242
7.2.4.1	Light system for the irradiation of hMSCs	243
7.2.4.2	Surface profile of hMSCs upon light treatment . . .	246
7.3	Conclusions	255
8	Conclusions and Future Perspectives.	257
	Bibliography	264
	Appendix A Analytical data Monomers	301
	Appendix B Analytical data Porphyrins	302
	Appendix C Analytical data probe for ROS detection	305

List of Figures

1.1	Main sources, formation and cellular responses to reactive oxygen species.	2
1.2	Schematic illustration of photosensitizer activation by a modified Jablonski diagram.	6
1.3	Diagrammatic representation of the molecular orbitals of oxygen [1,2].	9
1.4	Schematic diagram of photodynamic therapy.	12
1.5	Ball and stick representation of the X-Ray crystal basic structure of a porphine	14
1.6	Typical absorption of porphyrins.	15
1.7	Selected examples of photosensitizers.	17
1.8	Schematic diagram of nanoparticle design and applications.	19
2.1	Schematic diagram of Disc centrifuge.	33
2.2	Zeta potential measurement.	34
2.3	Jablonski Energy Diagram	36
2.4	Schematic diagram of flow cytometry analysis.	38
2.5	Chemical structure of (3-aminopropyl)methacrylamide)	43

2.6	Chemical structure of 3-acrylamidopropyl trimethyl ammonium hydrochloride.	44
2.7	Chemical structure of <i>N</i> -propargyl acrylamide.	46
2.8	Chemical structure of 3-acrylamidopropyl trimethyl ammonium hydrochloride and <i>N</i> - propargyl acrylamide.	47
2.9	Synthetic scheme to afford porphyrin-amino nanoparticle conjugates.	51
2.10	Capping reaction of porphyrin-amino nanoparticles with acetic anhydride.	52
2.11	Synthetic scheme to afford ZnPMA.	53
2.12	Synthetic scheme to afford porphyrin polyacrylamide nanoparticles(ZnPNP)	55
2.13	Synthetic scheme to afford porphyrin trimethyl ammonium polyacrylamide nanoparticles(ZnPTNP)	56
2.14	Synthetic scheme to afford Porphyrin-Alkyne nanoparticle conjugates	59
2.15	Synthetic scheme to afford porphyrin-alkyne/trimethyl ammonium nanoparticle conjugates (PATNPC)	61
2.16	Synthetic scheme to afford titrated conjugation of porphyrins with ATNPs.	73
2.17	Portable light system.	76
3.1	Schematic representation of water-in-oil microemulsions	80
3.2	Vinyl addition polymerization of acrylamide.	83
3.3	Nanoparticles functionalised monomers	87
3.4	Synthetic scheme to afford <i>N</i> - propargylacrylamide	87

3.5	Mechanism of acrylation of amine-alkyne derivatives to afford <i>N</i> -propargylacrylamide.	88
3.6	¹ H-NMR spectra of <i>N</i> -propargylacrylamide in CDCl ₃	89
3.7	Size distribution of polyacrylamide nanoparticles	91
3.8	Size characterisation of amino functionalised nanoparticles	92
3.9	Size characterisation of alkyne functionalised nanoparticles	93
3.10	Size characterisation of alkyne/trimethyl ammonium functionalised nanoparticles	95
3.11	Surface charge of functionalised polyacrylamide nanoparticles.	98
3.12	Comparison of size variation in polyacrylamide functionalised nanoparticles	99
3.13	Size characterisation of functionalised and non-functionalised polyacrylamide nanoparticles	101
3.14	Time-dependent size characterisation of polyacrylamide functionalised nanoparticles	103
4.1	Common coupling mechanisms used for conjugation.	110
4.2	Click chemistry	112
4.3	Absorption spectra of porphyrins in dH ₂ O	117
4.4	Emission spectra of porphyrins	118
4.5	Mechanism of reaction fluorescamine with amino functionalised nanoparticles	119
4.6	Emission spectrum of amino and non-functionalised nanoparticles upon reaction with fluorescamine	120
4.7	Reaction of porphyrin-amino nanoparticles with acetic anhydride.	122

4.8	Emission spectra of porphyrin-amino nanoparticles upon reaction with fluorescamine.	123
4.9	Synthetic scheme to afford ZnPMA	124
4.10	Absorption and emission spectra of ZnPNP (XVII).	125
4.11	Absorption and emission spectrums of ZnPTNPs (XVIII).	126
4.12	Hydrodynamic diameter of porphyrin nanosystems.	127
4.13	Hydrodynamic diameter of porphyrin nanosystems after 10 months of storage at -18° C.	128
4.14	Porphyrin nanosystems surface charge characterisation, zeta potential.	130
4.15	Reaction that occurs from incubation of fluorescamine with alkyne functionalised nanoparticles.	134
4.16	Emission spectra of alkyne and non-functionalised nanoparticles upon reaction with 3-azidocoumarin mediated by copper(I)	135
4.17	Absorption spectra of ZnPN ₃ in presence of CuBr after 20 hours of incubation.	137
4.18	Fluorescence characterisation of alkyne modified nanoparticles and its non-functionalised counterparts after CuAAC reaction with ZnPN ₃	138
4.19	Representative absorption and emission spectrum of porphyrin- al- kyne/(2.5 %), trimethylammonium nanoparticle conjugates (2.5 % ZnPTNPC)	139
4.20	Hydrodynamic diameter of porphyrin nanosystems measured by dy- namic light scattering.	140

4.21	Hydrodynamic diameter of porphyrin nanosystems measured by dynamic light scattering after 10 months storage.	142
4.22	Zeta potential characterisation of porphyrin plkyne/trimethyl ammonium NP's.	143
5.1	Intracellular mechanisms of nanoparticle uptake	151
5.2	Representative <i>live-cell</i> imaging of hMSCs treated with 5 mg/ml of 2.5 % TNPs.	158
5.3	Representative <i>live-cell</i> imaging of hMSCs treated with 5 mg/ml of 5 % TNPs.	159
5.4	Representative <i>live-cell</i> imaging of hMSCs treated with 5 mg/ml of 10 % TNPs functionalised nanoparticles.	160
5.5	Representative analysis of intracellular co- localisation of 2.5 % TNPs	162
5.6	Representative analysis of intracellular co- localisation of 5% TNPs	164
5.7	Representative analysis of intracellular co- localisation of 10 % TNPs.	166
5.8	Representative bi-variate plot of cell survival/apoptosis analysis by flow cytometry.	167
5.9	Analysis of cellular uptake of positively charged nanoparticles by flow cytometry.	169
5.10	Analysis of cellular viability in hMSCs treated with 2.5 %, 5 % and 10 % TNPs by flow cytometry.	172
5.11	Analysis of necrotic/late apoptotic events in hMSCs treated with cationic nanosystems by flow cytometry.	174

5.12	Representative image of hMSCs viability assessment by flow cytometric analysis of positive selection for mitotracker green.	177
5.13	Representative time-lapse <i>live cell</i> imaging of hMSCs treated with 5 μ g/ml of porphyrin.	178
5.14	Representative analysis of intracellular co-localisation of porphyrin dye.	179
5.15	Analysis of cellular viability in hMSCs treated with porphyrins by flow cytometry.	182
5.16	Analysis of cellular uptake of porphyrin in hMSCs treated by flow cytometry.	183
5.17	Representative time-lapse <i>live cell</i> imaging of hMSCs treated of ZnPATNPCs.	185
5.18	Representative analysis of intracellular co-localisation of ZnPATNPCs.	186
5.19	Analysis of cellular viability in hMSCs treated with ZnPATNPCs by flow cytometry.	189
5.20	Analysis of cellular uptake of ZnPATNPCs in hMSCs by flow cytometry.	191
5.21	Representative time-lapse <i>live cell</i> imaging of hMSCs treated with ZnPTNPs.	192
5.22	Representative analysis of intracellular co-localisation of ZnPTNPs.	194
5.23	Analysis of cellular viability in hMSCs treated with porphyrin entrapped trimethyl ammonium nanoparticles by flow cytometry. . . .	196
5.24	Analysis of cellular uptake of porphyrin entrapped trimethyl ammonium nanoparticles in hMSCs by flow cytometry.	198

6.1	Schematic representation of the porphyrinic nanoplateforms in study.	206
6.2	Detection of H_2O_2 .	208
6.3	Schematic representation of live cell experimental design for studying photosensitizer activation.	210
6.4	Multichannel 2D mosaic imaging.	213
6.5	Characterisation of functionalised nanoplateforms in comparison with their porphyrin conjugated counterparts.	218
6.6	Fluorescence emission spectra of titrated porphyrins at the surface of polyacrylamide nanoparticles.	219
6.7	Effects of titrated porphyrin nanoplateforms in hMSCs upon single light dosage exposure.	221
6.8	Live cell imaging of endogenous H_2O_2 production upon irradiation of treated hMSCs.	224
7.1	Representative multilineage differentiation potential of MSCs.	230
7.2	Schematic diagram of monoclonal antibody interaction with the surface receptors in Mesenchymal Stem Cells (MSCs).	232
7.3	Representative phase contrast image of adherent cells isolated from foetal liver microenvironment, resembling spindle-shaped fibroblastic-like MSCs.	236
7.4	Characterisation of adherent cells isolated from foetal liver microenvironment.	237
7.5	Representative immunophenotypic profile of hMSCs isolated from foetal liver microenvironment, P^3 to P^{10} .	239

7.6	Effect of nanoparticle internalisation on the immunophenotypic profile of hMSCs, representative from P ³ to P ¹⁰	241
7.7	Portable light system for photosensitizer activation.	243
7.8	Live cell imaging of endogenous H ₂ O ₂ production upon irradiation of treated hMSCs.	245
7.9	Immunophenotypic characterisation of hMSCs upon different light dosages.	248
7.10	Flow cytometric analysis of the incidence of apoptosis in hMSCs stimulated to produce ROS upon light exposure.	250
7.11	Flow cytometric analysis of the incidence of necrosis in hMSCs stimulated to produce ROS upon light exposure.	251
7.12	Immunophenotypic characterisation of hMSCs upon exposure to 20 light dosages followed by subculture.	253

List of Tables

2.1	Chemical composition of the monomer solution of trimethyl ammonium functionalised nanoparticles.	46
2.2	Chemical composition of the monomer solution of alkyne/trimethyl ammonium functionalised nanoparticles.	48

2D	Two dimensional
3D	Three dimensional
a.u.	Arbitrary units
AmNPs	Amino functionalised nanoparticles
ANPs	Alkyne functionalised nanoparticles
AOT	Dioctyl sulfosuccinate sodium Salt
APMA	N-(3-aminopropyl)methacrylamide
APS	Ammonium persulphate
ATNPs	Alkyne-trimethylammonium polyacrylamide nanoparticles
BPTFMC	4-methyl-7-{{4-(phenylboronic pinacol ester)methoxy}coumarin
Brij30	Polyethylene glycol dodecyl ether
CD	Cluster of differentiation
CPPs	Cell penetrating peptides
CPS	Disc centrifuge
CuAAC	Cu-catalysed azide-alkyne cycloaddition
CuPATNPC	Copper porphyrin alkyne-trimethylammonium polyacrylamide nanoparticles conjugates
CuPN ₃	5-(4-isothiocyanatophenyl)-10,15,20-tris-[(4-N-methylpyridinium)yl]porphyrinato copper(II)trichloride
DCM	Dichloromethane
dH ₂ O	Deionised water
DIPEA	Diisopropylethylamine
DLS	Dynamic light scattering
DMSO	Dimethyl sulfoxide
ECD	Phycoerythrin-texasred-X
EGF	Epidermal growth factor
FBS	Fetal Bovine Serum
FCM	Flow Cytometry
FITC	Fluorescein isothiocyanate
FL	Fluorescent light
FSC	Forward Scatter
HBSS	Hank's Balanced Salt Solution
hMSCs	human mesenchymal stem cells
HpD	Hematoporphyrin IX
HPLC	High-performance liquid chromatography

HTFMC	4-methyl-7-{{[4-(phenylboronic pinacol ester)]methoxy}coumarin
I	Intensity
IC	Internal Conversion
ISC	Intersystem crossing
LDL	Low-density Lipoprotein
LDV	Laser Doppler Velocimetry
LED	Light Emission Diode
MMP	Mitochondrial membrane potential
MRC	Medical Research Council
MTG	Mitotracker green
MTR	Mitotracker red
NMR	Nuclear Magnetic Resonance
NPs	Nanoparticles
P/S	Penicillin/ streptomycin
PAA	Polyacrylamide
PANPs	Polyacrylamide nanoparticles
PC5	Phycoerythrin cyanine 5
PCS	Photon correlation spectroscopy
PDMA	Polydecylmethacrylamide
PEBBLEs	Probes encapsulated by biologically localized embedding
PI	Propidium Iodide
pKa	Dissociation constant
PLS	Portable light system
PNCS	5-(4-isothiocyanatophenyl)-10,15,20-tris-[(4-N-methylpyridinium)yl]porphyrinato trichloride
PNP	Porphyrin polyacrylamide nanoparticles
PS	Photosensitizer
PS ₀	Photosensitizer singlet ground state
QELS	Quasielastic light scattering
R	Region
ROS	Reactive oxygen species
RPMI	Roswell Park Memorial Institute
S ₀	Ground state
S ₁	First excited singlet state

S ₂	Second excited single
SEC	Size Exclusion Chromatography
SOD	Superoxide dismutase
SSC	Side Scatter
T ₁	Excited triplet state
TEA	Triethylamine
TEMED	N,N,N',N'-tetramethylethylenediamine
TMA	Trimethylammonium
UV-vis	Ultraviolet-visible
w/v	Weight per volume
ZnPAmNPC	Zinc porphyrin-amine nanoparticle conjugates
ZnPATNPC	Zinc porphyrin alkyne-trimethylammonium polyacrylamide nanoparticles conjugates
ZnPATNPC	Zinc porphyrin alkyne-trimethylammonium polyacrylamide nanoparticles conjugates
ZnPCNPC	Zinc porphyrin capped nanoparticle conjugates
ZnPMA	5-[4-[(3-(3-methylthioureido) propyl methacrylamide) phenyl]-10,15,20-tris-[(4-methylpyridinium)yl]] porphyrinato zinc(II) trichloride
ZnPN ₃	5-(4-isothiocyanatophenyl)-10,15,20-tris-[(4-N-methylpyridinium)yl]porphyrinato zinc(II)trichloride
ZnPNCS	5-(4-isothiocyanatophenyl)-10,15,20-tris-[(4-N-methylpyridinium)yl]porphyrinato zinc(II)trichloride
ZnPTNP	Zinc porphyrin trimethylammonium polyacrylamide nanoparticles
ZP	Zeta potential
λ _{em}	Wavelength emission
λ _{exc}	Wavelength excitation

Chapter 1

General Introduction

1.1 Reactive Oxygen Species

Molecular oxygen is a basic and essential component of all living systems. A portion of the oxygen taken into living cells can be converted into reactive oxygen species [3–6].

Reactive oxygen species (ROS) is a term used to refer to the collective amount of molecules or ions which are mainly formed by the incomplete one-electron reduction of oxygen (e.g. superoxide) but also include non-radical derivatives of molecular oxygen (e.g. hydrogen peroxide). The most relevant ROS in cellular systems are superoxide ($\text{O}_2^{\bullet-}$), hydrogen peroxide (H_2O_2) hypochlorous acid (HOCl), singlet oxygen ($^1\text{O}_2$), lipid peroxides (ROOH) and hydroxyl radical (OH^\bullet).

Reactive oxygen species are seen as the angels and demons of cellular metabolism. ROS are essential for cell survival by being intermediates of essential signalling processes and defence against infections. On the other hand, excessive amounts

of ROS contributes to cellular damage and modifications of molecules and DNA.

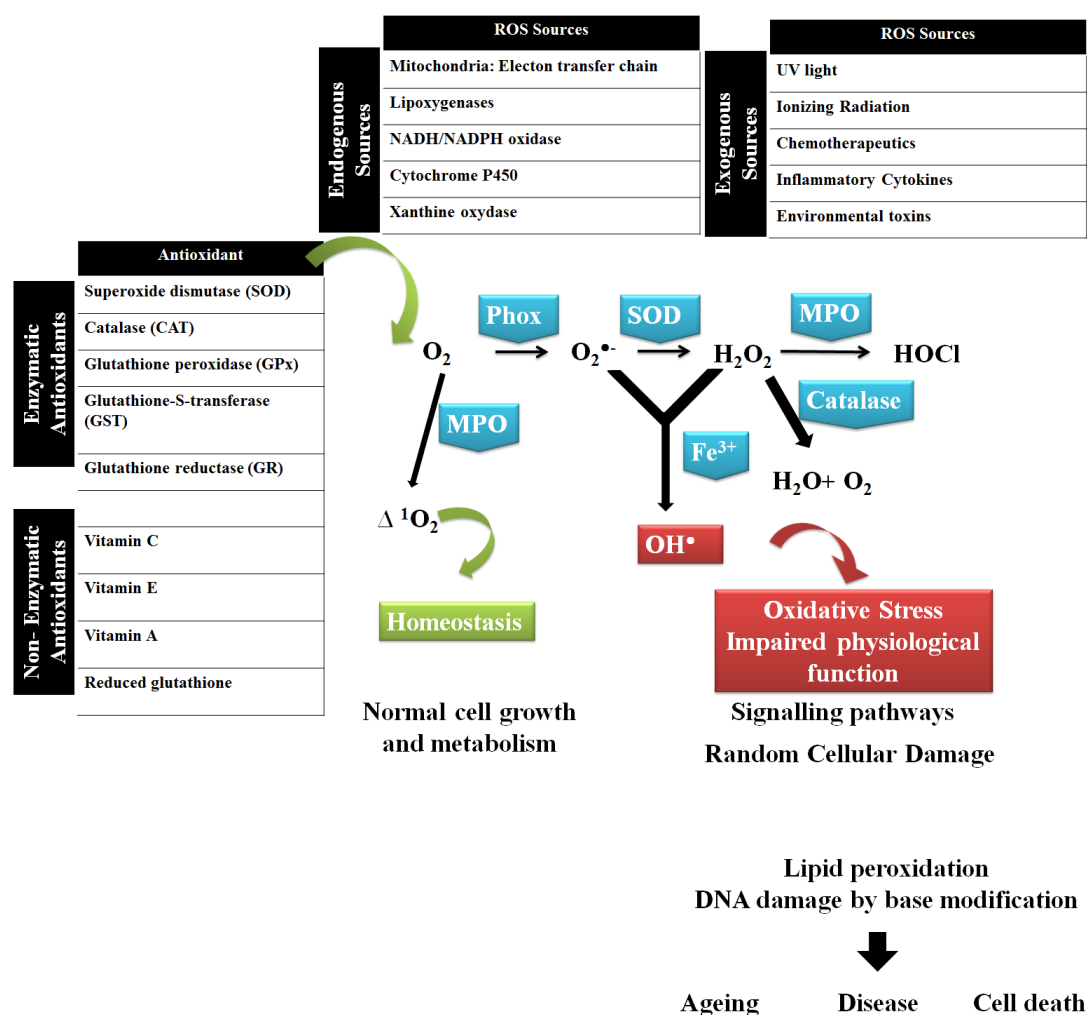


Figure 1.1: Main sources, formation and cellular responses to reactive oxygen species. Under physiological conditions, reactive oxygen species are constantly produced, mainly in mitochondria, endoplasmatic reticulum and cellular membranes. In addition, in normal conditions, the ROS produced are highly regulated and metabolised by sophisticated enzymatic and non-enzymatic antioxidant defences, maintaining physiological homeostasis. Increased ROS production may arise from exogenous sources, metabolic disorders or mitochondrial diseases. When ROS production exceeds the antioxidant capacity of the cellular system, oxidative stress, lead to an impaired physiological function affecting important signalling pathways and causing random cellular damage such as lipid peroxidation and DNA damage. Oxidative stress is responsible for the development of several diseases (e.g cancer, ageing and cell death). [6–9]

In general, superoxide is the primary ROS generated intracellularly and it is believed that mitochondria are the main organelle of ROS generation. Figure 1.1 summarises the main processes of ROS reaction as well as the main antioxidant

systems involved in ROS clearance. Increased ROS production with failure in its clearance leads to an augmented oxidative environment, also known as oxidative stress. Oxidative stress arises from the incapacity of antioxidant systems to remove ROS. Accumulation of ROS leads to toxicity due to their high reactivity towards DNA, proteins and lipids [9, 10].

Oxidative stress has been correlated with several conditions, such as inflammation, cancer, Parkinsons and Alzheimers [9–12].

1.2 Photosensitizers

The word, photosensitizer has its origin in two main roots; the first, “photo”, is derived from the Greek for “light”, while the second is a Latin-derived word, “sensus” which represents the concept of something affected by external factors [13].

A photosensitizer (PS), is defined as a molecule that mediates the transference of light energy into a chemical reaction (transfer of electrons) and/or to molecular oxygen. Photosensitization reactions are simple and controllable, aiming for the production of singlet oxygen ($^1\text{O}_2$). Photosensitization reactions require three components: presence of oxygen, light of an appropriate wavelength and PS capable of using energy absorbed from the light to excite oxygen to its singlet state [13, 14].

1.2.1 Photosensitizers Characteristics

Generally, photosensitizers share a common delocalised aromatic structure with large conjugated systems of double bonds.

In the absence of photoactivation, the PS molecules do not present unpaired electron spins [15]. Once activated by light energy (equation 1.1), the PS

(absorption of photons), an electron is promoted to a higher-energy molecular orbital leading to an excited, short-lived ($\approx 1\text{-}100$ ns) singlet state ($^1\text{PS}^*$), without any changes in its electron spin [2, 15, 16]. The lifetime of the singlet excited state is too short to allow significant interactions with the surrounding molecules.



Subsequently, the excited state can either decay to the ground state by emitting a fluorescent photon (reaction 1.2) or proceed *via* intersystem crossing

(reaction 1.4)(ISC) to afford the excited triplet states ($^3\text{PS}^*$). The excited triplet state *via* ISC is a spin-forbidden process, facilitated by a spin-orbit coupling; thus at this stage, the spin of the electron is no longer conserved. From the triplet excited state, the PS can either undergo a second spin-forbidden inversion, returning to the ground state by emitting a phosphorescent photon (reaction 1.5), or it can lose energy through radiation-less transitions upon collisions with other molecules (reaction 1.6) [2, 15–18].

1.2.2 Photosensitized Reactions

The longer lifetimes (≥ 500 ns) of the excited triplet state of the PS allow significant interactions with surrounding molecules, which is essential for efficient photosensitized reactions. Figure 1.2 is an illustrated schematic of a modified Jablonski diagram of photosensitizer activation. From the excited triplet state interactions with surrounding molecules two types of photosensitized reactions arise, both involve interaction with molecular oxygen.

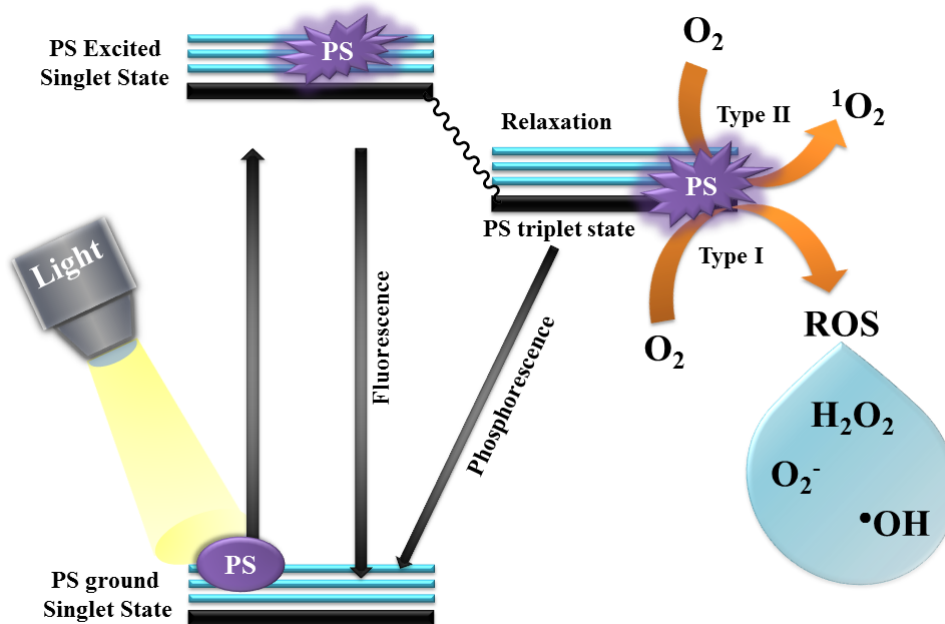
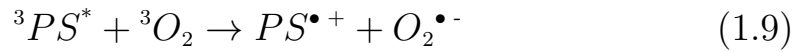
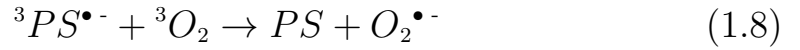
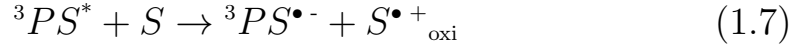


Figure 1.2: Schematic illustration of photosensitizer activation by a modified Jablonski diagram. The PS is primarily excited by the absorption of energy, which results in its first excited singlet state. Subsequently, the PS can relax into a longer and more stable triplet state through intersystem crossing (ISC). The interaction of PS triplet state with molecular oxygen leads to two type of reactions, Type I and Type II, with the production of reactive oxygen species and singlet oxygen, respectively.

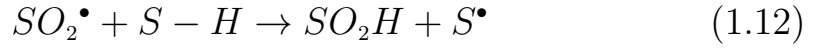
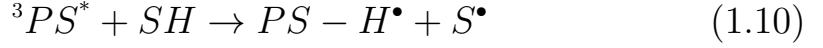
1.2.2.1 Photosensitization Type I Reactions

Type I photosensitized reactions involve a radical or redox reaction of $^3\text{PS}^*$ with surrounding substrate molecules (S), leading to two possible pathways. The first (Reaction 1.7) involves the interaction of $^3\text{PS}^*$ (excited triplet state PS) with the surrounding molecules by exchange of an electron (oxidation). Thus, a photosensitizer radical ion is formed, $^3\text{PS}^{\bullet-}$, as well as an acceptor radical cation ($\text{S}^{\bullet+}_{\text{oxi}}$). The substrate radical cation ($\text{S}^{\bullet+}_{\text{oxi}}$) immediately reacts with molecular oxygen $^3\text{O}_2$ producing superoxide radical anion ($\text{O}_2^{\bullet-}$). The production of superoxide is not particularly reactive with biological systems, thus does not, by itself cause much oxidative damage. However, the reaction of superoxide with itself

(dismutation) mediated by the enzyme superoxide dismutase (SOD), leads to the production of hydrogen peroxide. Superoxide also plays an important role in the production of the hydroxyl radical. Superoxide is able to donate an electron to metal ions, which further acts as catalysts to convert hydrogen peroxide into a hydroxyl radical. Most of the radicals produced through these reactions interact with molecular oxygen producing reactive oxygen species (ROS) such as (OH^\bullet), (HO_2^\bullet), ($\text{O}_2^{\bullet-}$) and (H_2O_2). The production of the hydroxyl radical (OH^\bullet), an extremely reactive radical which oxidises a high number of biomolecules, activates cytotoxic effects causing damage of fatty acids and lipids [2, 18–20].

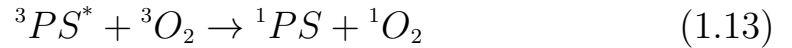


A second Type I process involves the abstraction of a hydrogen from a substrate molecule to the ${}^3P^*$ (reduction), reaction 1.10. This type of mechanism leads to the production of free radicals which react immediately with molecular oxygen, resulting in the formation of oxygen intermediates, reactions 1.11; 1.12. This second mechanism also leads to the production of reactive oxygen intermediates which produce cytotoxic events.



1.2.2.2 Photosensitization Type II Reactions

Type II reactions are dependent on the presence of ground state molecular oxygen and are energy transfer dependent. The excited photosensitizer reacts with ground state oxygen by energy transfer, yielding singlet oxygen (Reaction 1.13) [2, 15, 16, 18, 21, 22].



Collisions between the excited triplet state photosensitizer and ground state molecular oxygen lead to the production of two low-lying singlet excited states; $^1\Delta_g$ (95 kJ/mol) and $^1\Sigma_g^+$ (158 kJ/mol). The main difference between these two states relates to the electronic configuration of the π -antibonding orbitals, as schematically represented in Figure 1.3 [1, 2, 15].

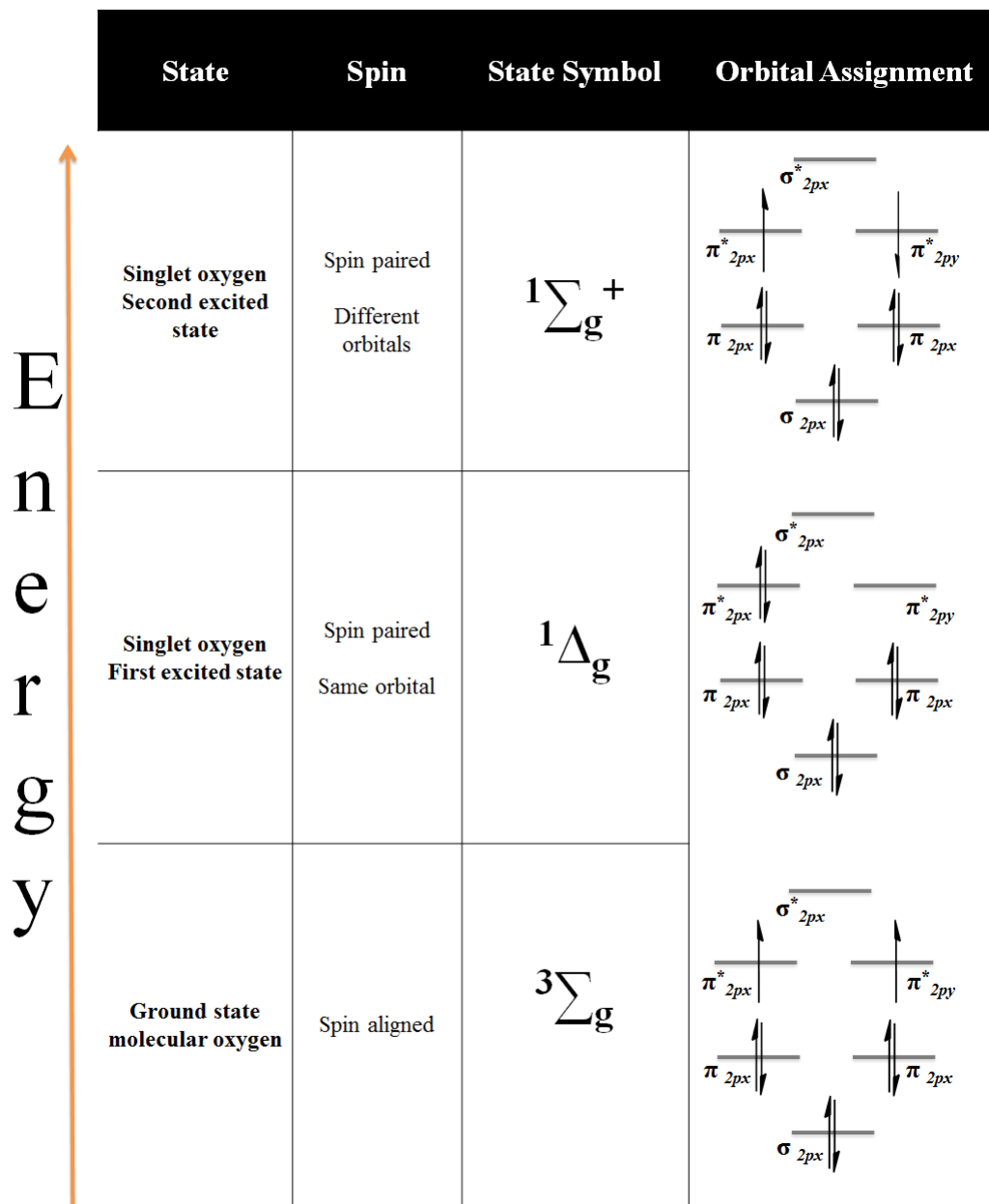


Figure 1.3: Diagrammatic representation of the molecular orbitals of oxygen [1, 2].

The second excited state of oxygen is similar to the one of ground state, except the last two electrons have antiparallel spins. The longer life of the first excited state of oxygen, $^1\Delta_g\text{O}_2$, is due to spin-forbidden transitions from this state to the ground state one ($^3\Sigma_g\text{O}_2$). The opposite happens to the second excited state, due to spin-allowed transitions from the second to the first excited state ($^1\Delta_g\text{O}_2$) its species are short lived [1, 2].

Similar Type I reactions, ROS produced *via* Type II mechanisms also results in intermediates which can react with biological molecules. Proteins are primary targets of oxidative degradation. That is due to the high reactivity of some amino acids (e.g. cysteine, methionine, tyrosine) [23–25]. Similarly, DNA can also be extensively affected by oxidative damage [19, 20, 25].

1.3 Photosensitizers Applications

The use of light alone or in combination with chemical compounds (photosensitizers) was long known as a therapeutic methodology. Light as a treatment vehicle can be traced back to ancient China, Egypt and India. At that time, light was used to treat various diseases such as psoriasis, rickets vitiligo and skin cancer [2, 25–28]. In 1903, Finsen was awarded with a Nobel Prize in Physiology and Medicine resulting from his studies showing that light could be used for the treatment of subcutaneous tuberculosis, known as *Lupus vulgaris* [18, 28, 29].

Many others further contributed to the use of light and photosensitizers as a therapeutic methodology, introducing the concept of photodynamic therapy. In 1903, Oscar Raab showed that combination of acridines and light could be lethal to protozoan paramecium. Subsequently, von Tappeiner and Jesionek reported on the use of eosin and light (topically administered) for the treatment of skin cancer, this being the first evidence of photodynamic therapy [18, 29].

Several years passed until a significant breakthrough appeared. In 1975,

Dougherty, *et al.* reported on the administration of HpD (Hematoporphyrin IX) and light for the complete eradication of mammary tumour growth, which was subsequently also observed for bladder carcinoma. In Canada, in 1993, an HpD derivative, photofrin[®]-(purer form) received approval for the treatment of bladder cancer. Later, in 1995, photofrin[®] use was approved in the United States for the treatment of esophageal cancer [18].

1.3.1 Photodynamic therapy

The principle of photodynamic therapy is schematically represented in Figure 1.4. The photosensitizer is administrated intravenously or topically and concentrated at the tumour site. The affected region is then irradiated with light of an appropriate wavelength (dependent on the absorption wavelength of the phototsensitizer). The short lifetime of ROS limits their cytotoxic action to the surrounding area of their generation, thus the diseased cells are selectively eradicated [2, 28, 30].

One of the main aspects of photodynamic therapy is the penetration of light into the diseased tissue. Light absorption through the tissue is known to be optimal in the range of 650-850 nm, designated as a phototherapeutic window. For wavelengths below 650 nm, skin photosensitivity and endogenous chromophores (e.g. reduced form of collagen, deoxyhemoglobin and melanin) are the main disadvantages. On the other hand, absorption band wavelengths longer than 850 nm are not of sufficient energy for singlet oxygen production. Furthermore, the absorption of water at 1300 nm interferes with photodynamic efficiency [2, 28, 30].

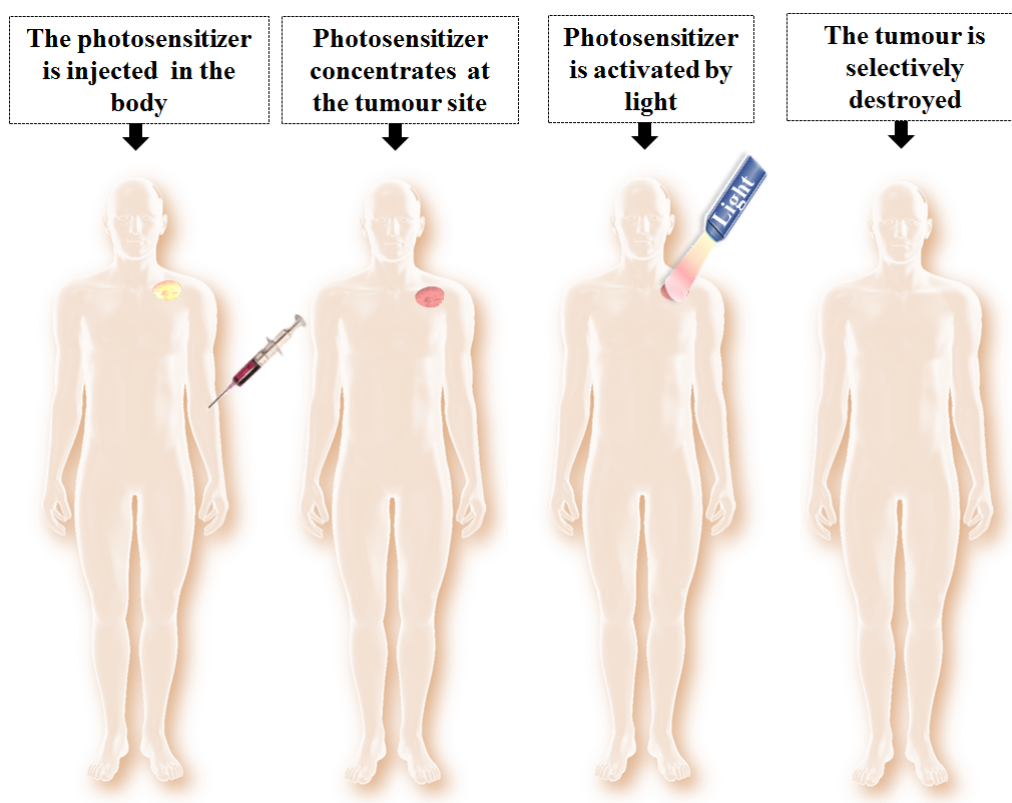


Figure 1.4: Schematic diagram of photodynamic therapy. [28]modified

With increased interest in photodynamic activity as a therapeutic agent, some disadvantages were found with the photosensitizers being used at that time. Poor solubility, sub-optimal tumour selectivity and; poor light penetration (due to the small extinction coefficient at 630 nm wavelengths) were the main major limitations associated with the first generation of photosensitizers. In order to overcome these disadvantages, several new photosensitizers were developed and their essential characteristics for optimal photodynamic activity were defined as follows:

- The photosensitizer needs to be chemically pure, of known composition and of high stability [25, 27, 28, 30];

- Low levels of dark toxicity for both animals and humans [25, 27, 28, 30];
- Accumulation preferential at the target tissue [25, 27, 28, 30];
- It should have strong absorption and high extinction coefficient ($>20.000\text{-}30.000\text{ M}^{-1}\text{ cm}^{-1}$) in the red region of the electromagnetic spectrum to allow deeper tissue penetration. Optimum tissue penetration depth between 650-850 nm [2, 28];
- Rapid clearance from the body [2, 28];
- Appropriate photophysical characteristics: high quantum yield of triplet formation ($\Phi_T \geq 0.5$); high singlet oxygen quantum yield ($\Phi_\Delta \geq 0.5$); long triplet state lifetime [2, 28];
- Ideally, it should be water soluble or soluble in harmless aqueous solvent mixture [25, 27, 28, 30];
- No aggregation in biological environments, as this decreases its photochemical activity [25, 27, 28, 30];
- Facile synthesis and scale up.

1.4 Porphyrins as photosensitizers

Porphyrins, an expression derived from the ancient Greek word *porphura*, used to describe the colour purple, refer to a class of highly coloured naturally occurring compounds [29]. Porphyrins are characterised by a hetrocycle macrocycle structure of twenty carbons and four nitrogen atoms, of which porphine is the simplest of all; Figure 1.5; (A). Porphine basic structure consists of tetrapyrrolic units (Figure

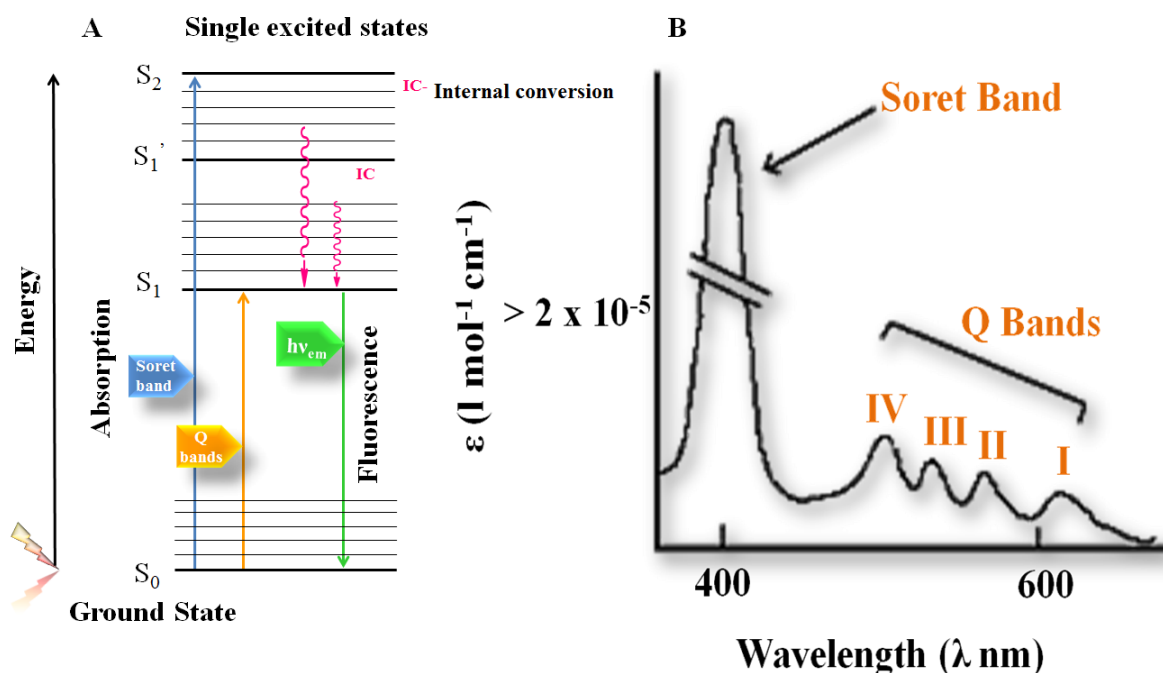


Figure 1.6: Typical absorption of porphyrins. (A)- Modified Jablonski energy diagram; (B)- Representation of a typical porphyrin absorption spectra. Modified from [2].

The Soret band is a consequence of porphyrin's strong electronic transitions from the ground state to the singlet excited state. On the other hand, Q-bands result from weak transitions to the first excited singlet state [29].

Due to the nitrogen atoms present on the porphyrinic ring, the binding of metal atoms is facilitated, leading to the formation of metalloporphyrins. It is widely recognised that metalloporphyrins play an important role in essential biological processes, such as photosynthesis, oxygen transport and storage. The coordination of porphyrins with metal ligands has been extensively explored and several metals have been assembled with porphyrins. Such complexes have been applied as a model for a biological electron transporter, oxygen transport and metalloenzymes [2, 28, 29].

1.4.1 Generations of porphyrinic based photosensitizers

From the various photosensitizers developed until 1980, porphyrins and porphyrins-related compounds were the most relevant approaches from a clinical point of view [18,27]. Therefore, three generations of photosensitizers were defined.

The first generation, referred to above, relates to the HpD derivative, photofrin. These compounds presented many drawbacks, such as the weaker absorptions at long wavelengths (e.g. 630 nm). It was also found that the ‘purified’ photofrin presented several porphyrin-containing products (≈ 60), making their manufacture difficult [27,28,31].

The second generation of photosensitizers emerged around 1980, aiming to develop porphyrin analogues that absorb in the far-red spectral region (to increase tissue penetration). The photosensitizers of this generation were designed and developed incorporating optimal photodynamic activity (described above). Foscan and phthalocyanines are examples of porphyrin analogues with good photodynamic activity. Figure 1.7 shows the structure of Foscan and Phthalocyanine as examples of photosensitizers with good photodynamic activity. Many more second generation porphyrin analogues were developed and are reviewed elsewhere [27,28,31].

The third generation aimed to introduce porphyrin carriers. The photosensitizers were used by porphyrin analogues developed from the second generation, but it were used by coupling with carriers to achieve selective targeting and

accumulation. Figure 1.7 shows a protoporphyrin IX- cyclic RGD conjugate, a system developed for the specific targeting of tumour endothelial cells. The cyclic RGD (arginin-glycine-aspartic acid motif) presents high affinity with receptor $\alpha_v \beta_3$ - integrin which is overexpressed in endothelial cells (in and around the tumour). Thus, this system aims to potentiate the vascular effect of PDT by specifically targeting the tumour vessels [27, 31].

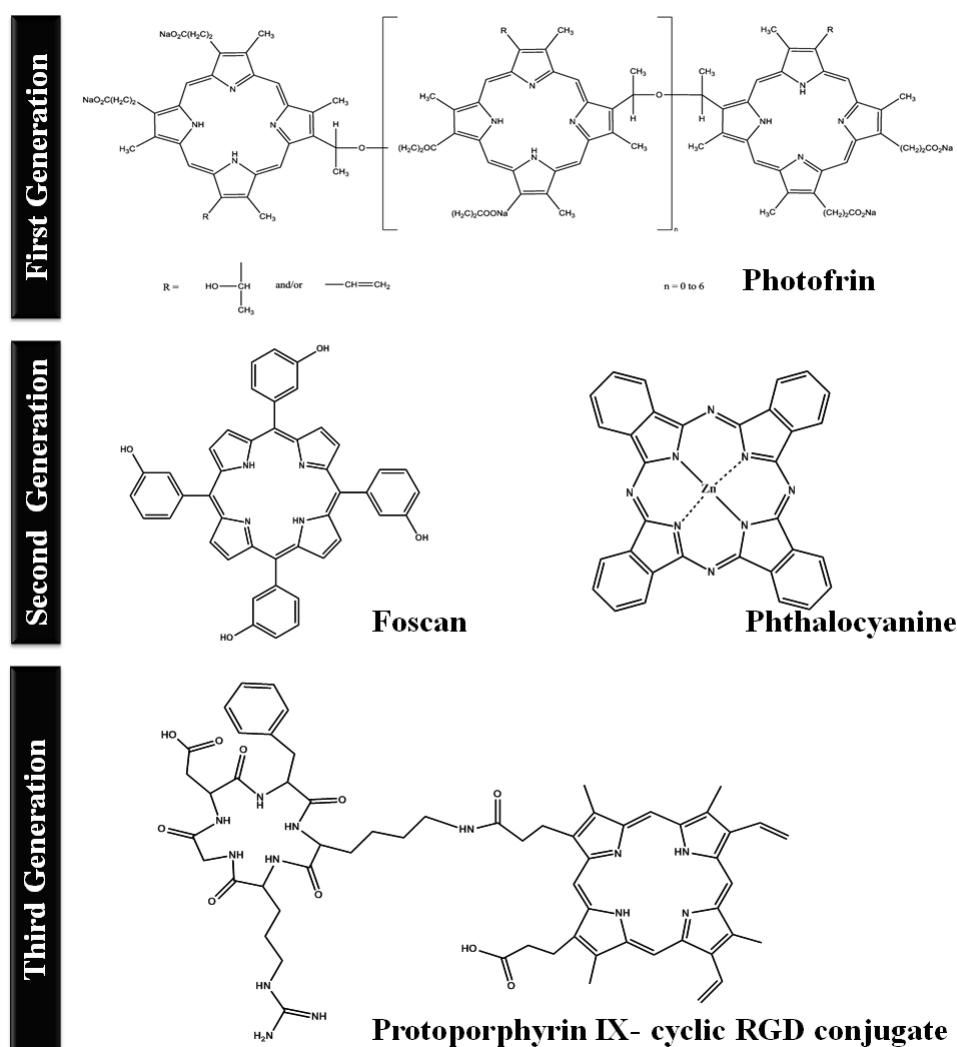


Figure 1.7: Selected examples of photosensitizers.

1.4.2 Effects of photosensitizers.

The distribution of photosensitizers in the cell dictates their efficiency to produce ROS. ROS are characterised by short-lifetimes, thus, their action will occur close to the site of its location. Therefore, once the PS is activated, the type of photodamage depends on the exact subcellular localisation of the photosensitizers [25,27].

The sub-cellular localisation of photosensitizers is mainly dependent on their physicochemical characteristics (e.g. net charge, hydrophobicity, degree of symmetry of the PS) [2, 15, 25].

The intracellular activity of photosensitizers is envisaged specifically to destroy diseased cells. In this perspective, porphyrin photosensitizers are known to eliminate diseased cells through two types of cell death, necrosis or apoptosis. Necrosis, is a mechanism accompanied of violent and quick cell degeneration which results from extensive cellular damage. Necrosis is characterised by the disruption of organelles and subsequent disruption of the plasma membrane, which later results in the release of cellular contents to the extracellular environment. On the other hand, apoptosis is characterised as a genetically programmed cell death and, occurs normally in physiological (programmed cell death) and pathological conditions. This mechanism is accompanied of several biochemical and morphological changes (e.g. chromatin condensation, formation of apoptotic bodies, etc) [27].

1.5 Nanotechnology.

Nanotechnology was first introduced by Norio Taniguchi in 1974 to refer to materials in nanometers ($1\text{ nm} = 1 \times 10^{-9}\text{ m}$) [32, 33]. It is an area focused on the development of synthetic and analytical tools in the submicrometer dimensions, specifically dimensions up to 100 nm. In this size range, materials present improved properties compared with the same material at greater sizes [32]. In addition, nanomaterials differ from other materials as a consequence of their increased surface area and quantum effects, leading to enhanced reactivity, strength, shape, electrical properties and *in vivo* behaviour [32, 34].

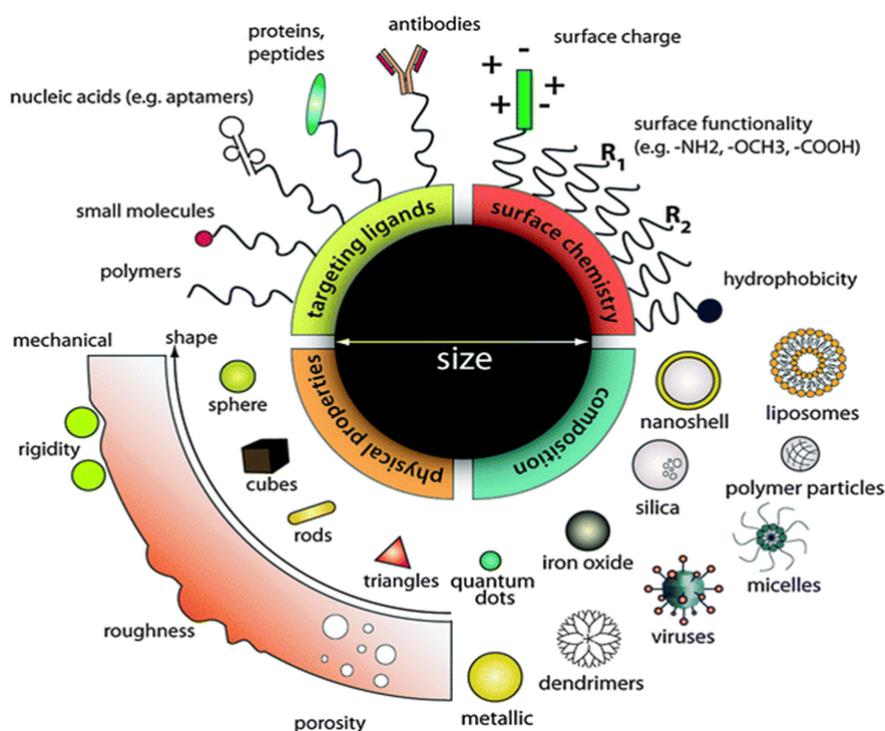


Figure 1.8: Schematic diagram of nanoparticle design and applications. Nanoplatfroms can be assembled from a variety of materials which confer different shapes and diverse chemical and physical properties. The surface can be manipulated to accommodate several ligands, e.g. for biological targeting. Such characteristics provide an applicability of these systems in several areas. Adapted from reference [35].

Over recent years, several types of nanomaterials have been developed with diverse chemical and physical characteristics (Figure 1.8); however, their advant-

ages share common principles. Their small size and high surface-to-volume ratios makes them highly tailorable, therefore surface charge, hydrophobicity, solubility and stability can be easily manipulated (Figure 1.8). In addition, the small size also confers facilitated interaction with biological systems. This flexibility of nanomaterials confers a high range of applicability, such as drug delivery, medical imaging, sensing, diagnostics, etc [35,36].

1.5.1 Polyacrylamide nanoparticles

In 1996 Kopelman, *et al.* introduced the concept of PEBBLEs (Probes Encapsulated By Biologically Localised Embedding), which is a generic term used to describe nanometre-sized spherical optical sensing devices manufactured by techniques which exploit the use of biologically inert polymers. PEBBLEs technology was developed for a non-invasive and real time monitoring of ions and small molecules in biological systems [37–41]. Several types of matrix were developed, polyacrylamide (PAA) [42], polydecylmethacrylate (PDMA), sol gel and organic modified silicates (ormosils). Hydrophilic moieties are better suited to PAA matrices, hydrophobic moieties in PMDA matrices, and amphiphilic dyes in sol-gel or ormosils [38,43,44].

1.5.2 Polyacrylamide nanoparticles

Polyacrylamide nanoparticles have been recognised as being of high interest as they offer unique physical, chemical and biological properties [34,35,45–47], the main advantages being biocompatibility (hydrophilicity), low size (20-100nm) and

inert and non-toxic matrix [2, 37]. Furthermore, due to their porosity, high surface area and adaptable architecture, these nanoplateforms potentially have several types of combinations with targeting moieties [34, 45, 48, 49]. On the one hand, the porous matrix allows the entrapment of molecules, which otherwise may cause cellular toxicity and/or diminished activity by interaction with cellular components [39, 42, 43], while on the other, the adaptable large surface area allows the introduction of multiple chemically reactive groups for covalent linkage of molecules (i.e. targeting agents), conferring lower toxicity and adverse side reactions and improving solubility, delivery and sub-cellular localisation. Such characteristics allow a great diversity of applications, such as drug and gene delivery, biosensing, tissue engineering, diagnostic and many others [34, 50–52]. Polyacrylamide nanoparticles have been mainly developed in a biosensing context, for intracellular real time monitoring of analytes such as Cu^{2+} [53, 54], Ca^{2+} [43, 44], Mg^{2+} , Zn^{2+} [55], glucose [56] and pH [57–59], O_2 [60, 61] among many others. Furthermore, they have also been considered of high interest in the delivery of DNA, proteins, enzymes, imaging and therapeutic agents [62, 63].

1.5.2.1 Polyacrylamide nanoparticles and photosensitizers

Exploiting toxicity induced by ROS, photodynamic therapy has been given considerable importance in the treatment of diseases such as cancer (several types) and macular degeneration, among others. This approach uses photosensitizers, light and molecular oxygen as the main therapeutic agents.

In a therapeutic context, photosensitizers present appealing features. However some limitations arise, such as the low solubility of most photosensitizers (decreasing its photodynamic efficiency), low loading, low targeting of specific tissues

and cytotoxicity. Several groups reported that the combination of nanoplatfoms with photosensitizers has been associated with enhanced photodynamic efficiency as a consequence of: (1) the increased amount of photosensitizer delivered; (2) improved solubility of the photosensitizer (3) engineerable nanoplatform surface allowing combination with multiple targeting moieties in order to improve charge, delivery, and sub-cellular localisation.

An increased number of publications refer to the application of nanoparticles in the context of targeted drug delivery, polyacrylamide nanoparticles were previously applied as carriers for photosensitizers, for the increased delivery of photosensitizers (e.g. methylene blue, porphyrins) to tumour cells. These nanoplatforms contain photosensitizers aimed at facilitating external administration and production of high levels of singlet oxygen, inducing the destruction of tumour cells [63–67]. In addition, the encapsulation of photosensitizers in the polyacrylamide porous matrix has also been directed to circumvent the cytotoxicity of some photosensitizers [63, 68, 69]. Gupta, *et al.*, also showed the development of polyacrylamide nanoparticles containing dual functionality by incorporating a fluorescent imaging agent for non-invasive detection of tumours and delineation of tumour margins, as well as the presence of a photosensitizer for selective photodynamic action under diseased cells [63, 67].

From a diagnosis/monitoring point of view, Josefsen, *et al.* have described the development of a porphyrinic nanotool capable of reporting calcium mobility as a consequence of photosensitizer activation and ROS generation [2, 70]. The nanotool

developed, incorporated surface conjugated photosensitizer (*via* amino functionalisation). Furthermore, a calcium sensitive dye entrapped in the polymeric matrix (protected from intracellular environment), was used to monitor calcium variations as a consequence of increase in intracellular oxidative stress. The main limitation of the reported work was the *in situ* production of identifiable levels of ROS [2,70] upon photosensitizer activation with light of appropriate wavelength.

1.6 Aims

Although the use of nanoparticles as carriers of photosensitizers has been exploited in several areas, the effectiveness of these therapeutics is still limited to the control and knowledge of biological signalling pathways involved in disease.

Based on the work previously developed by Josefsen, the present project aims for the development of porphyrinic nanoplatforms to stimulate hMSCs for the intracellular production of ROS in a controlled manner. This technology introduces a nanotool to study the real time effects of ROS in cells [2]. In addition, as a proof of principle, these porphyrinic nanoplatforms are aimed at the specific investigation of ROS impact on the differentiation state of primary foetal liver hMSCs. Because of the high potential of hMSCs, the development of such a system can present great knowledge and advance the area of cell therapy.

For the development of a nanotool for *in situ* ROS generation the main aims were as given below.

The development of stable multifunctionalised nanoplatforms containing a

chemical reactivity for further conjugation with porphyrinic moieties and a cationic functionality to facilitate the interaction between nanoparticles and cellular membrane for uptake and intracellular trafficking. The stability of these systems is greatly important to preserve the photodynamic activity of photosensitizers as well as the efficiency of conjugation.

The establishment of a protocol of conjugation between porphyrinic moieties and multifunctionalised nanoplatforms. The importance of this step depends on the preservation of the photosensitizer's chemical structure and purity, which are required for their optimal activity upon light exposure.

The determination of the efficient cellular uptake, cytotoxicity and intracellular trafficking, with mitochondrial co-localisation. The accumulation of porphyrinic nanoplatforms at the mitochondria relates to its importance, sensitivity and relation with ROS signalling pathways. In addition, it is also aimed to investigate the possible cytotoxic effects of the cellular uptake of these nanoplatforms. Excluding the cytotoxicity of these nanosystems, aims to isolate further toxic effects exclusively to an increase in oxidative stress. The investigation of the real time effects of ROS generation in hMSCs, providing evidence of identifiable and increasing levels of ROS generation in hMSCs loaded with porphyrinic nanoplatforms and exposed to light of appropriated wavelengths (for photosensitizer activation). It is also aimed to isolate cytotoxic effects and ROS, increasing the photodynamic activity of photosensitizer.

The developed porphyrinic nanotool is intended to assist in the study of ROS impact on the undifferentiated state of primary hMSCs.

1.7 Thesis Structure

The present interdisciplinary PhD project details the development of a nanotool for the *in situ* generation of reactive oxygen species and evaluates the impact of these species in the hMSCs undifferentiated state. The chapters are organised as below:

Chapter two gives a brief overview of the techniques used for nanoparticle characterisation, cellular imaging and immunofluorescence as well as detailed methodologies used in the present thesis.

Chapter three details the development and characterisation of mono and multifunctionalized polyacrylamide nanoparticles.

Chapter four entails the development and characterisation of linkage between polyacrylamide nanoparticles and porphyrins.

Chapter five investigates the uptake in hMSCs of the nanoplateforms developed in chapters three and four, and also characterises their sub-cellular localisation and cytotoxic effects.


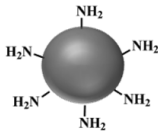
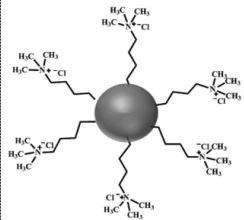
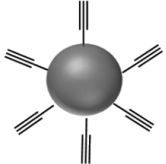
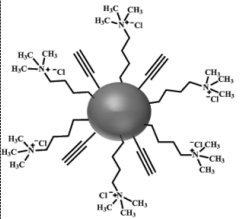
Chapter six uses the porphyrinic nanotools developed in chapter four to generate reactive oxygen species endogenously in hMSCs.

Chapter seven combines all the knowledge developed in the thesis to investigate the impact of reactive oxygen species on the surface characterisation of hMSCs.

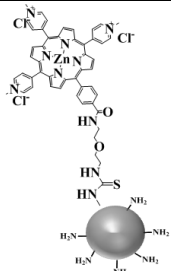
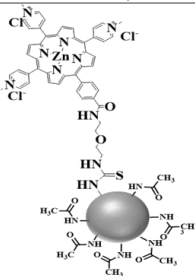
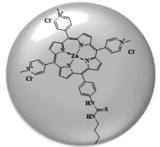
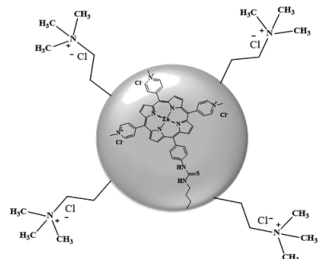
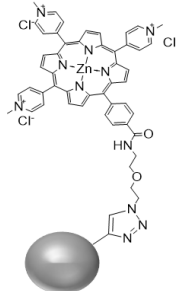
Chapter eight provides an overall conclusion of the project and addresses future perspectives

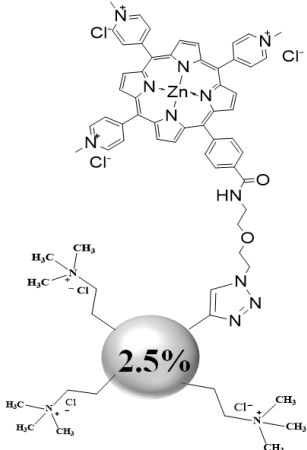
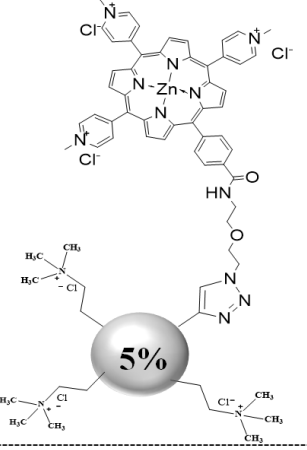
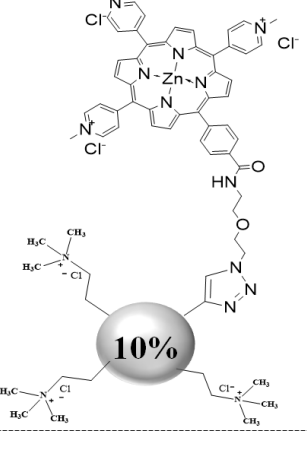
The tables presented below aim to give an overall description and rationale of the design of the nanoplateforms developed along this thesis, as well as porphyrins and functionalised monomers.

	Entry	Nanoparticle functionalization	Functionalization Monomer
Mono Functionalized NPs	I	Amino	
	II	Trimethyl ammonium	
	III	Alkyne	
Dually Functionalized NPs	IV	Trimethyl ammonium/ Alkyne	

Polyacrylamide Nanoparticles Functionalities				
Entry	Schematic Diagram	Name	Abbreviation	Design Rationale
V		Polyacrylamide nanoparticles	PANPs	<ul style="list-style-type: none"> • Polyacrylamide nanoparticles without functionalizations • Reactions control.
VI		Amino functionalized polyacrylamide nanoparticles	AmNPs	<ul style="list-style-type: none"> • Investigate if aggregation of amino functionalized nanoparticles could be prevented by capping of amino reactivity's. • Time course studies indicate that nanoparticle aggregation was not prevented by capping.
VII		Trimethylammonium functionalized polyacrylamide nanoparticles	TNPs	<ul style="list-style-type: none"> • Provide positive surface charge to polyacrylamide nanoplateforms. • Aiming facilitated uptake, sub cellular targeting and stability.
VIII		Alkyne functionalized polyacrylamide nanoparticles	ANPs	<ul style="list-style-type: none"> • Provide chemically reactive groups for conjugation. • Alternative to amino reactivity.
IX		Trimethylammonium/Alkyne functionalized polyacrylamide nanoparticles	ATNPs	<ul style="list-style-type: none"> • Development of dually functionalized nanosystems with options for conjugation (alkyne functionality) and cellular uptake/targeting (trimethyl ammonium functionality).

Porphyrins Index			
Entry	Chemical Structure	Abbreviation	Work rationale
X		Free base	<ul style="list-style-type: none"> • Photodynamically active molecule; • Isothiocyanate chemically reactive bounds allows covalent linkage with amino functionalized nanoplatfroms;
XI		CuPN ₃	<ul style="list-style-type: none"> • Quenched photodynamic activity due to he presence of copper metal center- control of photodynamic activity ; • Azide chemically reactive bounds allows covalent linkage with alkyne functionalized nanoplatfroms;
XII		ZnPNCS	<ul style="list-style-type: none"> • Photodynamically active molecule; • Isothiocyanate chemically reactive bounds allows covalent linkage with amino functionalized nanoplatfroms;
XIII		ZnPN ₃	<ul style="list-style-type: none"> • Photodynamically active molecule; • Azide chemically reactive bounds allows covalent linkage with alkyne functionalized nanoplatfroms;
XIV		ZnPMA	<ul style="list-style-type: none"> • Photodynamically active molecule; • Acrylamide porphyrin monomer allows direct incorporation at the nanoplatfroms polyacrylamide matrix at the time of synthesis ;

Porphyrin nanoplatforms			
Entry	Chemical Structure	Abbreviation	Work rationale
XV		ZnPAmNPC	<ul style="list-style-type: none"> Development of porphyrin-nanoparticles conjugates <i>via</i> amino-isothiocyanate reaction with formation of an isothiurea bond;
XVI		ZnPCNPC	<ul style="list-style-type: none"> Development of porphyrin-nanoparticles conjugates <i>via</i> amino-isothiocyanate reaction with formation of an isothiurea bond; Inactivation of remaining reactive amino functionalities with acetic anhydride with an amide bond formation;
XVII		ZnPNPs	<ul style="list-style-type: none"> Development of nanoplatforms with photosensitizers protected (entrapped) by the polyacrylamide matrix;
XVIII		ZnPTNPs	<ul style="list-style-type: none"> Development of nanoplatforms with photosensitizers protected (entrapped) by the polyacrylamide matrix; Introduction of trimethyl ammonium functionalities at the surface for facilitated cellular uptake and endosomal escape;
XIX		ZnPANPC	<ul style="list-style-type: none"> Development of porphyrin-nanoparticles conjugates <i>via</i> alkyne-azido reaction with formation of an triazole bond;

Positively charged porphyrin nanoparticle conjugates			
Entry	Chemical Structure	Abbreviation	Work rationale
XX		2.5% ZnPTNPC	<ul style="list-style-type: none"> • Development of porphyrin-nanoparticles conjugates <i>via</i> alkyne-azido reaction with formation of an triazole bond; • Introduction of 2.5 % of trimethyl ammonium functionalities to investigate cellular uptake and endosomal escape and sub-cellular targeting;
XXI		5% ZnPTNPC	<ul style="list-style-type: none"> • Development of porphyrin-nanoparticles conjugates <i>via</i> alkyne-azido reaction with formation of an triazole bond; • Introduction of 5 % of trimethyl ammonium functionalities to investigate cellular uptake and endosomal escape and sub-cellular targeting;
XXII		10% ZnPTNPC	<ul style="list-style-type: none"> • Development of porphyrin-nanoparticles conjugates <i>via</i> alkyne-azido reaction with formation of an triazole bond; • Introduction of 10% of trimethyl ammonium functionalities to investigate cellular uptake and endosomal escape and sub-cellular targeting;

Chapter 2

Instrumentation materials and methods

2.1 Instrumentation

2.1.1 Size Characterization of nanoparticles.

2.1.1.1 Dynamic Light Scattering (DLS).

Size characterisation of nanoparticles is important for applications in nanomedicine. The influence of nanoparticle size in particle uptake, circulation time, tissue distribution and intracellular fate has been widely reported [45, 50, 71–75]. One of the most explored techniques in particle size determination is dynamic light scattering (DLS) also referred as or quasielastic light scattering (QELS).

DLS is a technique that allows the measurement of particle size at the nanometer scale. The principle behind this technique is the measurement of the scattering intensity of a laser light source from particles which are suspended in solution [76]. This scattering is due to the random Brownian motion of

the particles. Brownian motion is defined as the movement of particles as a consequence of random collisions with the molecules of the liquid that surrounds the particle. The theory of Brownian motion for DLS is that small particles move quickly and large particles move more slowly. The relationship between the size of a particle and its speed due to Brownian motion is defined in the Stokes-Einstein equation 2.1.

$$d(H) = \frac{kT}{3\pi\eta D} \quad (2.1)$$

where:

$d(H)$ = Hydrodynamic diameter

D = Translational diffusion coefficient

k =Boltzmann's constant

T = Absolute temperature

η = Viscosity

2.1.1.2 Disc Centrifuge (CPS)

Disc centrifuge is an instrument for particle size determination, based on the principle of differential centrifugation with a resolution in size from 5 nm up to 75 μm . Disc centrifuge is composed of a hollow optically clear disc and a monochromatic light of 405 nm as shown in Figure 2.1.

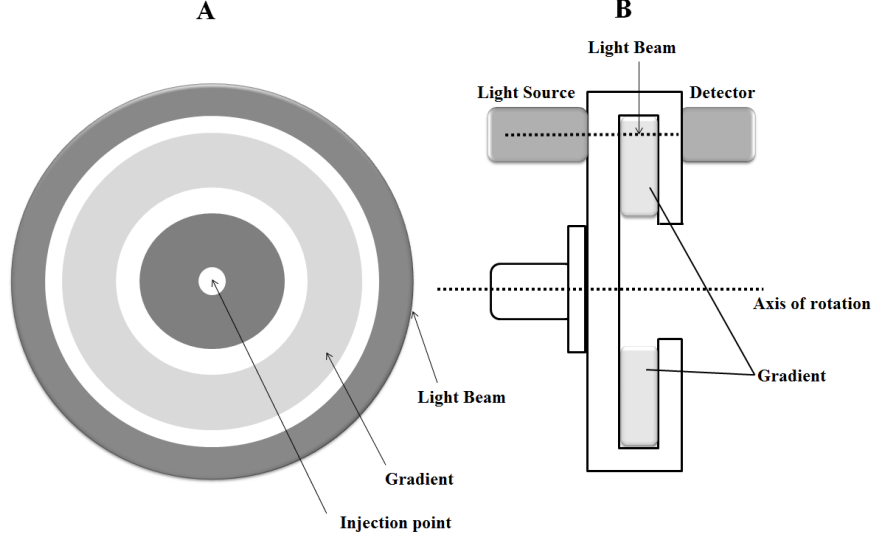


Figure 2.1: Schematic diagram of Disc centrifuge. A- front view, B- cross section.

The principle behind this technique is particle sedimentation under a gravitational field according to Stoke's Law. Upon sample application into the disc, a thin layer is formed which accelerates radially to the surface of the fluid. The sedimentation of the particles is dependent of their size and density and also influenced by the density of the gradient. The differences in size establish the time taken to reach the detector beam.

The particle size is then calculated by the time that particles take to reach the detector using a modified Stoke's Law, corrected for gravitational force with the distance from the center of rotation.

$$D = \sqrt{\frac{18\eta \ln(\frac{R_f}{R_i})}{(\rho_P - \rho_F)\omega^2 t}} \quad (2.2)$$

Where D is particle diameter (cm), η solvent viscosity (poise), ω is the rotational speed (radians/sec), R_i is the starting radii of formation (cm), R_f is the ending radii of formation, ρ_P the density of the particle (g/ml), ρ_F is the density of the fluid (g/ml) and t the arrival time (sec).

2.1.2 Surface characterization of nanoparticles: Zeta Potential.

The surface charge characterization of a particle is achieved by the determination of its zeta potential ξ , also called electrokinetic potential. The principle behind this technique is a consequence of the fact that a charged particle in solution will be surrounded by a liquid layer of opposite charge at its surface, called the double-diffuse layer, Figure 2.2. The double diffused layer is composed of two regions, an inner region (Stern layer) where the ions are strongly bound and a more diffuse outer layer of charges. Within the outer layer exist a notional boundary responsible for the stability between ions and particles, called slipping plane, within this plane particles and ions move as a single entity. Zeta potential is the potential difference between the slipping plane and the bulk solvent.

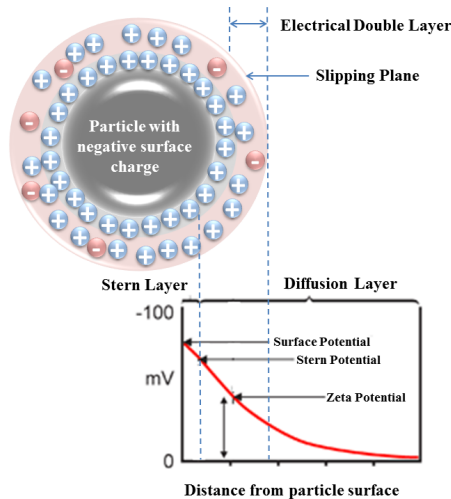


Figure 2.2: Schematic representation of Zeta Potential: The zeta potential is the charge mV measured at the slipping plane.

Zeta potential determination is then achieved by applying an electric field across a sample and determining the velocity of movement of particles towards the electrode. This velocity will be proportional to the zeta potential and is meas-

ured as a frequency shift in the incident light using the laser Doppler velocimetry technique (LDV) Thus, the electrophoretic mobility μ_E is calculated from equation 2.3

$$\mu_E = \frac{V}{E} \quad (2.3)$$

where:

μ_E = electrophoretic mobility

V = velocity

E = applied field

Thus, zeta potential(ξ) is determined by applying the Henry equation 2.4

$$\xi = \frac{3\eta\mu_E}{2\varepsilon f(ka)} \quad (2.4)$$

where:

ξ = zeta potential

η = bulk viscosity

μ_E = electrophoretic mobility

ε = permittivity of the medium

$f(ka)$ = Henry's function

2.1.3 Fluorescence Characterization

The process of fluorescence was first identified by the British scientist Sir George Stokes in 1852 and is described as a process of luminescence. The process of luminescence is divided in two groups, fluorescence and phosphorescence which are distinguished by the nature of the excited state. Fluorescence arises from an excited singlet state, where the electron of the excited orbital is paired with a second electron, of opposite spin, in the ground-state orbital, due to the opposite spin the electron from the excited orbital, returns to the ground state with the emission of a photon represented in Figure 2.3. Phosphorescence is a result of the emission of light from triplet excited states, opposite to fluorescence, in here the electron of the excited orbital and from the ground state present the same spin, which means that transitions to the ground state are not allowed, leading to low emission rates (10^3 - 10^0) [77].

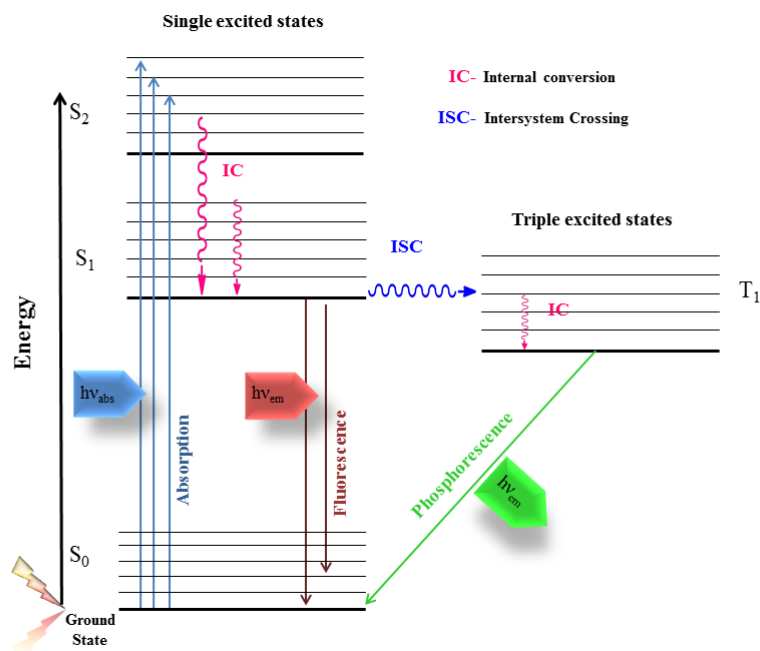


Figure 2.3: Jablonski Energy Diagram

2.1.4 Fluorescence Microscopy

Fluorescence microscopy is an essential tool in biology; it allows identifying cells and sub-cellular components and also single molecules [77].

The principle of fluorescence microscopy is the irradiation of a specimen (excitation light) with adequate wavelengths, and then collects an emitted light, which is separated from the excitation light. Fluorescent microscopes can use laser, mercury-vapour or xenon arc lamps as light sources. Light of a specific wavelength or set of wavelengths is produced by passing light through a wavelength selective exciter filter. The resultant light reflects off a dichromatic mirror along the microscope objective lens to the specimen. For fluorescent specimens the collected emission light passes through a dichromatic mirror. Subsequently, the emitted light is filtered by a barrier filter which block the excitation wavelength and the emitted light irradiates spherically in all directions [77].

2.1.5 Flow cytometry (FCM).

Flow cytometry (FCM) is a laser-based methodology for the analysis of individual biological particles [78–80]. The principle of flow cytometry is based on physics laws (e.g. optics; fluids; electronics) which are applied for the detection of particles and cells that move in a liquid stream through laser [79]. In Figure 2.4, a schematic diagram of flow cytometry analysis is represented. The particles/cells are pressurized directly into a isotonic fluid, under laminar flow, the sample becomes hydro-dynamically focused within the sheath stream which allows single cells to pass through a single file [79,81]. At that point, a beam of monochromatic light (normally a laser) crosses the cells.

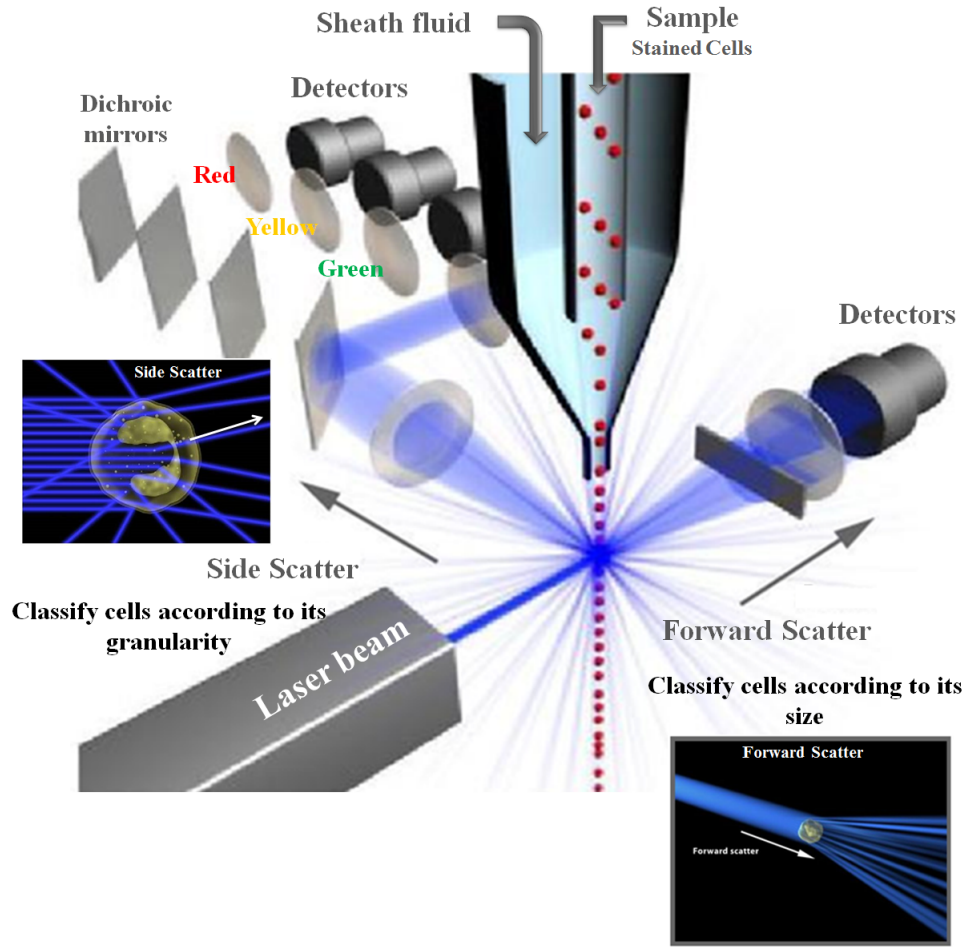


Figure 2.4: Schematic diagram of flow cytometry analysis. The single cell sample laminar flow is hydro-dynamically focused through a nozzle tip. Cells pass individually through an interrogation point. The scattered and fluorescent light are collected by optical and electronic systems which translates light signal into data. Modified from [82]

Scattered and fluorescent light are collected by optical and electronic systems. The scattered light relates to structural and morphological cell aspects. Forward-scattered light (FSC) is collected just off the axis of the incident beam and relates to the cell surface area and size. Side-scattered light (SSC) is collected at 90° of the incident beam and is proportional to cell complexity and granularity [79,81,83,84].

The emitted light is collected at right angle of the incident beam *via* optics that direct the given light thorough a series of dichronic mirrors that isolates the light at specific wavelengths [81,83]. The fluorescence measurements at different

wavelengths provide quantitative and qualitative information about fluorochrome-labelled cells. In flow cytometry, separated channels are used to detect fluorescent light (FL). The number of detectors varies among the machines but are either silicon photodiodes or photomultiplier tubes. The silicon photodiodes are normally used for forward scatter measurements, if the signal is strong. On the other hand, photomultiplier tubes are ideal for fluorescence reading, once are more sensitive to light [79].

2.2 Materials and Methods

2.2.1 Reagents

acrylamide, *N,N'*-methylenebisacrylamide, ammonium persulphate (APS), triethylamine (TEA) *N,N,N',N'*-tetramethylethylenediamine (TEMED), Brij[®]30, dioctyl sulfosuccinate sodium salt (98%) (AOT), acryloyl chloride (97%), *N,N*-diisopropylethylamine (99%), *N*-(3-aminopropyl)methacrylamide (APMA), propargylamine (98%), 3-acrylamidopropyl tetramethyl ammonium chloride were purchased from Sigma-Aldrich[®]. hexane, absolute ethanol, ethyl acetate, chloroform, methanol, acetonitrile were purchased from fischer Scientific[®]. dichloromethane (DCM, 99%) was purchased from Acros-Organics. HPLC grade water obtained from a Maxima USF ELGA system (UK). Gases were purchased from BOC (UK).

Culture media M199 (Cat No. M2154 [A]), media M199 without phenol red (Cat No. M3769[B]), penicillin/streptomycin (Cat No.P4333) L-glutamine (Cat No.G6392) trypsin/EDTA (Cat No. T4299), Hybri-Max[™] DMSO (dimethyl sulfoxide) $\geq 99.7\%$ (Cat NO. D2650), Freezing container Nalgene[®]Mr Frosty (Cat No. C1562) were purchased from Sigma-Aldrich[®].

Fetal Bovine Serum (FBS) was purchased from Biosera (Cat No.FB-1001H). Hank's Balanced Salt Solution (HBSS) Gibco[®](Cat No. 14185-045).

Antibodies Beckman Coulter: CD29 (FITC)- fluorescein isothiocyanate; PN IM0791U ($\lambda_{\text{ex}} = 488 \text{ nm}$; $\lambda_{\text{em}} = 520 \text{ nm}$). CD105 (PE)- phycoerythrin; PN A07414 ($\lambda_{\text{ex}} = 488 \text{ nm}$; $\lambda_{\text{em}} = 565 \text{ nm}$). CD45 (ECD)-PhycoerythrinTexas Red-X; A07784

($\lambda_{\text{ex}}=488\text{ nm}$; $\lambda_{\text{em}}=620\text{ nm}$). CD34 (PC5)-phycoerythrin-cyanine5; PN IM2650U
($\lambda_{\text{ex}}=488\text{ nm}$; $\lambda_{\text{em}}=665\text{ nm}$)

The porphyrins described along the thesis were developed and generously provided by Dr. Francesca Giuntini, University of Hull, Chemistry department. The dye 3-azidocoumarin was kindly provided and synthesized by Dr. Peter Magennis based on the protocol developed by Sivakumar and colleagues [85,86].

2.2.2 Exploiting the surface chemistry of polyacrylamide nanoparticles

2.2.2.1 Synthesis of *N*-propargyl acrylamide (III)

N-propargyl acrylamide was synthesized according to a modified procedure described by Malkoch, *et al.* [87]. Propargylamine (0.60 mL, 9.37 mmol) and *N,N*-diisopropylethylamine (1.96 mL, 11.24 mmol) were added to a 2-neck round bottom flask and dissolved in dry DCM (3 mL). To the mixture was then added dropwise a solution of acryloyl chloride (0.91 mL, 11.20 mmol) in dry DCM (2 mL). The reaction was left to stir overnight under a nitrogen atmosphere, after which the organic phase was removed by rotary evaporation. The crude product was subsequently dissolved in ethyl acetate (50 mL) and washed three times with an aqueous bicarbonate solution, twice with a brine solution and twice with distilled water. After collecting and drying the organic phase over MgSO_4 , ethyl acetate was evaporated in vacuo to dryness. The crude product was further purified by silica column chromatography eluting with a solvent mixture consisting of 60% *n*-hexane and 40% of ethyl acetate, to give a yellow pale oil (yield 480 mg, 47%) ; the purity of the final product was determined by NMR (see Appendix A).

2.2.2.2 Synthesis of polyacrylamide nanoparticles (PANPs)

The methodology for the synthesis of polyacrylamide nanoparticles (**V**) was first described by Clark, *et al.* [43] and is based on the free radical polymerisation of acrylamide in a reverse phase microemulsion. The water-in-oil microemulsion was prepared by dissolving the surfactants, polyethylene glycol dodecyl ether (3.08 g; 0.0026 mol) (Brij[®]30) and dioctyl sulfosuccinate (AOT) (1.59 g; 0.0036 mol) in deoxygenated hexane (42 ml purged with argon for 30 minutes). Separately, a monomer solution was prepared by mixing acrylamide (0.54 g; 0.0076 mol) and *N,N'*-methylenebis(acrylamide) (0.16 g; 0.001 mol) in 1.8 ml of deionized water. For nanoplatfroms incorporating FITC-dextran entrapped, 30 μ l of a 1 mg/ml FITC-dextran (10 000 MW) solution in water was added to the monomer solution. The reaction was then carried in complete absence of light.

The monomer solution was then added to the reverse-microemulsion which was left to form (\sim 10 minutes) in a sealed argon environment. The polymerisation was initiated by the addition an ice cold solution of ammonium persulphate (APS) (10% w\;v; 30 μ l) in water and *N,N,N',N'*-tetramethylethylenediamine (TEMED) (15 μ l), the reaction was allowed to proceed for 2 hours. Hexane was removed by rotary evaporation (Butchi Rotavapor R-200). To the remaining viscous solution was added 50 ml of absolute ethanol which were divided into two centrifuge tubes and then spun at 6000 rpm on a centrifuge (Hermle Z300 centrifuge) for 6 minutes to pellet the nanoparticles. The washing procedure was repeated 6 times in order to remove the excess of surfactant. Finally, the nanoplatfroms were re-suspended in 10 ml of absolute ethanol which was removed by vacuum filtration through a 0.02 μ m filter (Sartorius Stedim Biotech, Anodisc 25). The dried nanoparticles

were subsequently stored at -18°C .

2.2.2.3 Amino Functionalised Polyacrylamide Nanoparticles (AmNPs)

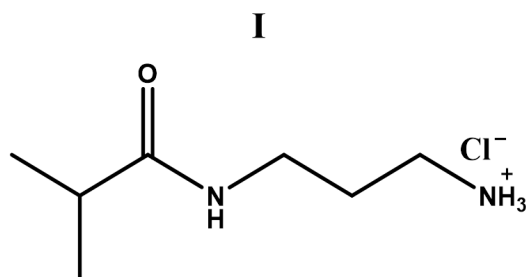


Figure 2.5: Chemical structure of (3-aminopropyl)methacrylamide) (APMA).

Further conjugation possibilities were exploited by tailoring polyacrylamide nanoparticles with several functional groups. The method for surface modification was according to Welser, *et al.* [87]. The generation of an NH_2 functionalization at the surface of polyacrylamide nanoparticles (**VI**) was achieved by the replacement of 2 % (by mol) of acrylamide in the monomer solution by *N*-(3-aminopropyl)methacrylamide hydrochloride (APMA), Figure 2.5. The monomer solution consisted of acrylamide (0.00745 mol; 529.5 mg), *N*-(3-aminopropyl)methacrylamide hydrochloride (1.52×10^{-4} mol, 27.2 mg) and *N,N'*-methylenebis(acrylamide) (0.16 g; 1 mmol) in 1.8 ml of deionized water. The polymerisation was carried out in the same way as for polyacrylamide nanoparticles, see section 2.2.2.2.

2.2.2.4 Polyacrylamide tetramethyl Ammonium Functionalised Nanoparticles (TNPs)

II

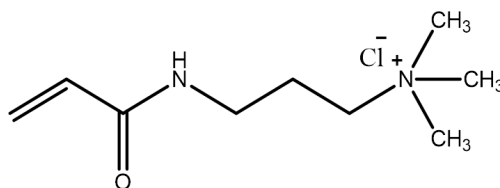


Figure 2.6: Chemical structure of 3-acrylamidopropyl trimethyl ammonium hydrochloride.

In order to modify the surface charge of polyacrylamide nanoparticles, tetramethyl ammonium functionalities were used, Figure 2.6. The method for synthesis of tetramethyl ammonium functionalised nanoparticles (**VII**) was according to a modified procedure described by Sun, *et al.* [59]. Briefly, the water-in-oil microemulsion was prepared by dissolving the surfactants, polyethylene glycol dodecyl ether (3.08 g; 0.0026 mol) (Brij[®]30) and dioctyl sulfosuccinate (AOT) (1.59 g; 0.0036 mol) in deoxygenated hexane (42 ml purged with argon for 30 minutes). The monomer solution was prepared by replacing trimethyl ammonium total weight in acrylamide (75 %) and *N,N'*-methylenebisacrylamide (25 %). The final composition of the monomer solution varied according to values described on Table 2.1. The monomers were diluted in deionized water, in a final volume of 1.8 ml. For nanoplateforms incorporating FITC-dextran entrapped, 30 μ l of a 1 mg/ml FITC-dextran (10 000 MW) solution in water was added to the monomer solution. The

reaction was then carried in complete absence of light.

The monomer solution was then added to the reverse-microemulsion which was left to form (~ 10 minutes) in a sealed argon environment. The polymerisation was initiated by the addition an ice cold solution of ammonium persuphate (APS) (10% w\%v; 30 μ l) in water and *N,N,N',N'*-tetramethylethylenediamine (TEMED) (15 μ l), the reaction was allowed to proceed for 2 hours. Hexane was removed by rotary evaporation (Buchi Rotavapor R-200). To the remaining viscous solution was added 50 ml of absolute ethanol which were divided into two centrifuge tubes and then spun at 6000 rpm on a centrifuge (Hermle Z300 centrifuge) for 6 minutes to pellet the nanosensors. This washing procedure was repeated 6 times in order to remove the excess of surfactant. Finally, the nanoplatfoms were re-suspended in 10 ml of absolute ethanol which was removed by vacuum filtration through a 0.02 μ m filter (Sartorius Stedim Biotech, Anodisc 25). The dried nanosensors were subsequently stored at -18°C .

Trimethyl ammonium functionalization

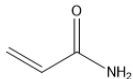
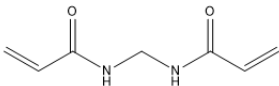
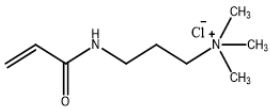
Monomer Solution	2.5%		5.0%		10.0%	
	mmol	mg	mmol	mg	mmol	mg
 Acrylamide	7.35	522.55	7.10	504.98	6.61	470.03
 N,N'-methylene-bis-acrylamide	1.00	154.18	0.96	148.33	0.89	136.68
 3-acrylamidopropyl trimethyl ammonium hydrochloride	0.11	23.3	0.23	46.70	0.45	93.30

Table 2.1: Chemical composition of the monomer solution of trimethyl ammonium functionalised nanoparticles.

2.2.2.5 Synthesis of polyacrylamide alkyne functionalised nanoparticles (ANPs)

III

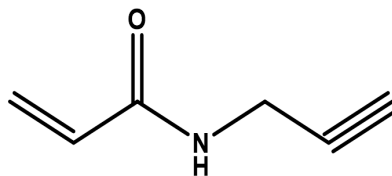


Figure 2.7: Chemical structure of *N*-propargyl acrylamide.

In order to introduce a alkyne functionality to the polyacrylamide nanoparticles (**VIII**) the procedure firstly described by Welser, *et al.* [87], was used where 2 % (by mol) of acrylamide was replaced in the monomer solution by *N*- propargyl acryl-

amide. In Figure 2.7 is showed the chemical structure of *N*- propargyl acrylamide. The procedure followed a similar path as for amino functionalised nanoparticles, the monomer solution was then composed of acrylamide (3.73 mmol; 529.5 mg), *N,N'*-methylenebis(acrylamide) (0.16 g; 1.0 mmol) and *N*-propargylacrylamide (0.11 mmol, 25 mg). The process of polymerization and recovery of nanoparticles was carried out in the same way as for polyacrylamide nanoparticles, see section 2.2.2.2.

2.2.2.6 Synthesis of alkyne-trimethyl ammonium polyacrylamide nanoplatfoms (ATNPs).

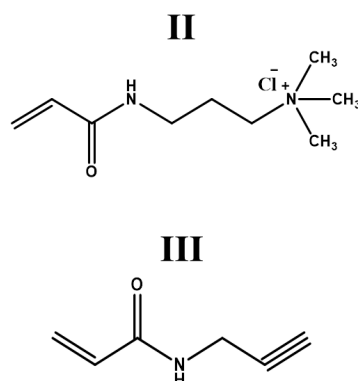


Figure 2.8: Chemical structure of (II) 3-acrylamidopropyl trimethyl ammonium hydrochloride and (III) *N*- propargyl acrylamide.

The synthesis of alkyne/trimethyl ammonium polyacrylamide nanoparticles (IX) was based on the combination of the mono functionalised systems previously reported [43, 59, 87]. The synthesis of ATNPs was based on a free radical polymerisation of acrylamide monomers in a reverse phase microemulsion. The water-in-oil microemulsion was prepared by dissolving the surfactants, polyethylene glycol dodecyl ether (3.08 g; 0.0026 mol) (Brij[®]30) and dioctyl sulfosuccinate (AOT)

(1.59 g; 0.0036 mol) in deoxygenated hexane (42 ml purged with argon for 30 minutes). The monomer solution was prepared by replacing trimethyl ammonium total weight in acrylamide (75 %) and *N,N'*-methylenebisacrylamide (25 %). The final composition of the monomer solution varied according to values described on Table 2.1. The monomers were diluted in deionized water, in a final volume of 1.8 ml. For nanoplateforms incorporating FITC-dextran entrapped, 30 μ l of a 1 mg/ml FITC-dextran (10 000 MW) solution in water was added to the monomer solution. The reaction was then carried in complete absence of light.

The monomer solution was then added to the reverse-microemulsion which was left to form (\sim 10 minutes) in a sealed argon environment.

Alkyne/ trimethyl ammonium functionalization

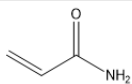
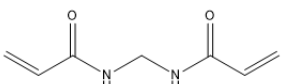
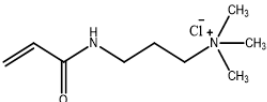
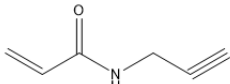
Monomer Solution	2.5%		5.0%		10.0%	
	mmol	mg	mmol	mg	mmol	mg
 Acrylamide	7.09	503.83	6.84	486.23	6.34	451.28
 <i>N,N'</i> -methylene-bis-acrylamide	0.96	147.93	0.92	142.08	0.85	130.43
 3-acrylamidopropyl trimethyl ammonium hydrochloride	0.11	23.30	0.23	46.70	0.45	93.30
 <i>N</i> -propargylacrylamide	0.11	25.00	0.11	25.00	0.11	25.00

Table 2.2: Chemical composition of the monomer solution of alkyne/trimethyl ammonium functionalised nanoparticles.

The polymerisation was initiated by the addition of ammonium persuphate (APS) (10 % w/v; 30 μ l) in water and *N,N,N',N'*-tetramethylethylenediamine (TEMED) (15 μ l), the reaction was allowed to proceed for 2 hours. Hexane was removed by rotary evaporation (Buchi Rotavapor R-200). To the remaining viscous solution was added 50 ml of absolute ethanol which was split into along two centrifuge tubes and then spun at 6000 rpm on a centrifuge (Hermle Z300 centrifuge) for 6 minutes to pellet the nanosensors. This procedure was repeated 6 times in order to remove the excess of surfactant. Finally, the nanosensors were re-suspended in 10 ml of absolute ethanol which was removed by vacuum filtration through a 0.02 μ m filter (Sartorius Stedim Biotech, Anodisc 25). The dried nanosensors were subsequently stored at -18°C (yield 580 mg, 83%).

2.2.3 Development of porphyrin polyacrylamide nanosystems

2.2.3.1 Development of porphyrin polyacrylamide nanosystems *via* amino-isothiocyanate conjugation.

2.2.3.1.1 Optimization of conjugation reaction conditions: amino functionalised nanoparticles.

The incorporation of the amine functionality at the surface of nanoparticles was investigated by the reaction with fluorescamine. In order to confirm the presence of reactive amine groups onto amino functionalised nanoparticles a solution of fluorescamine in DMSO (5 mg/ml) was prepared and subsequently added (300 μ l) to suspensions of polyacrylamide nanoparticles (non functionalised) and APMA nanoparticles (amino functionalised) in deionized water (3 ml; 1 mg/ml), and allowed to react for 30 minutes. The fluorescence of resulting solutions was measured following excitation at 385 nm using a Varian Cary Eclipse fluorescence spectrometer (Varian, UK).

2.2.3.1.2 Conjugation of 5-(4-isothiocyanatophenyl)-10,15,20-tris-[(4-N-methylpyridinium)yl] porphyrinato zinc(II)trichloride (ZnPNCs) to amino functionalised polyacrylamide nanoparticles: PAmNPC

The conjugation of isothiocyanate zinc porphyrin (**XII**) with amino functionalised polyacrylamide nanoparticles (**VI**) was achieved by suspending 50 mg of NPs in water (1 ml) followed by the addition of zinc porphyrin (3.2×10^{-4} mmol). To confer basicity to the reaction mixture, as required for the optimal conjugation of amines with isothiocyanates, pure TEA (15 μ l) was added. The volume of the reaction

mixture was completed with deionised water to a final volume of 2 ml with water, and the reaction was allowed to proceed stirring for 18 hours at room temperature in total absence of light.

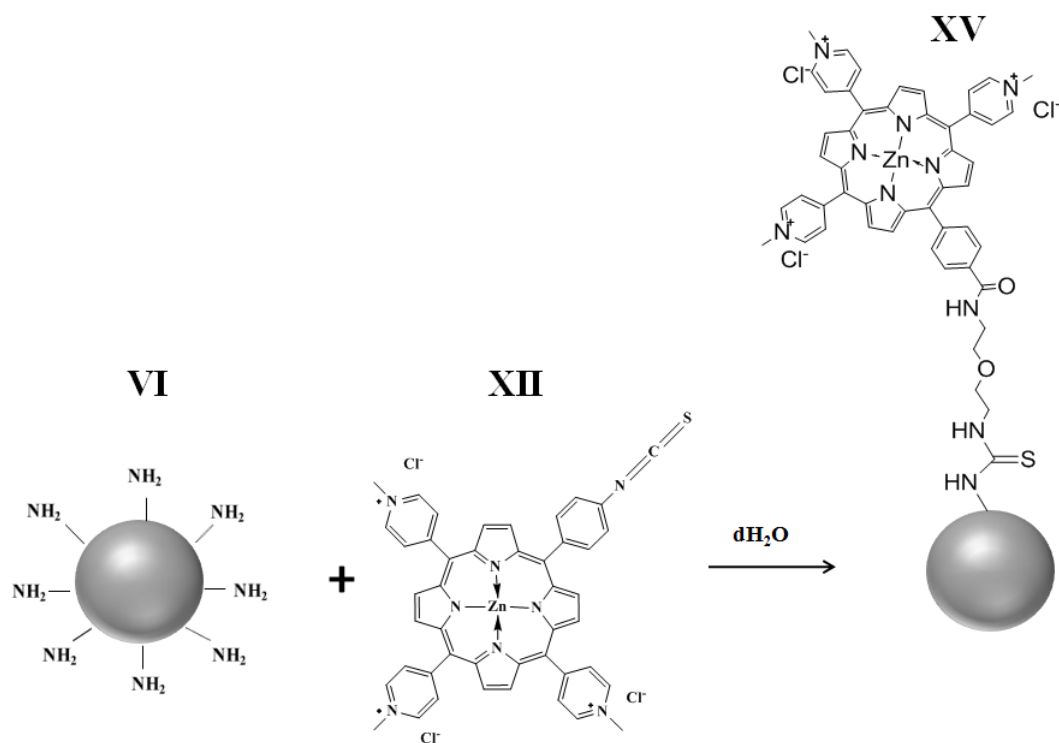


Figure 2.9: Synthetic scheme to afford porphyrin-amino nanoparticle conjugates (PAmNPC): (VI) Amino functionalised polyacrylamide nanoparticles; (XII) 5-(4-isothiocyanatophenyl)-10,15,20-tris-[(4-N-methylpyridinium)yl]porphyrinato zinc(II) trichloride (ZnPNCS); (XV) Porphyrin-amino nanoparticle conjugates.

Once the reaction time was completed, porphyrin nanoparticle conjugates were purified using desalting columns. The reaction mixture was loaded into a PD10 (sephadex-25) column and eluted with 3 ml of deionized water. The resultant nanoparticles were washed with ethanol (5 ml, 2 times) by centrifugation. The resultant dark green porphyrin conjugated nanoparticles (XV) were subsequently dried *in vacuo* (yield 45 mg, 90%).

2.2.3.1.3 Capping of porphyrin amino nanoparticles (ZnPCNPC) In order to avoid aggregation, non-reacted amines in PAmNPC (XV) were blocked,

Figure 4.7, by the use of acetic anhydride (**1**). To achieve this, PAmNPCs (100 mg) were precipitated in absolute ethanol (5 ml) and incubated with acetic anhydride (5 ml; 0.053 mol) stirring for 2 hours in the absence of light. The resultant nanoparticles were washed with ethanol (5 ml, 5 times) by centrifugation. Finally, the nanosensors were re-suspended in 10 ml of absolute ethanol which was removed by vacuum filtration through a 0.02 μm filter (Sartorius Stedim Biotech, Anodisc 25). The dried nanoparticles (**XVI**) were subsequently stored at -18°C (yield 75 mg, 75 %).

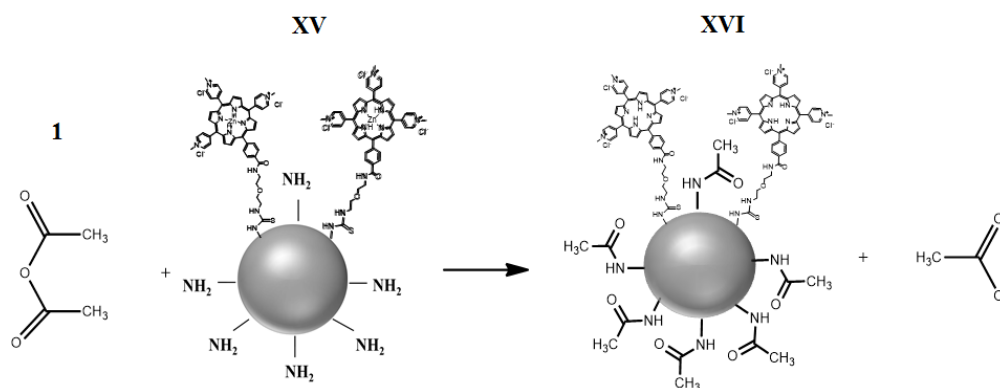


Figure 2.10: Capping reaction of porphyrin-amino nanoparticles with acetic anhydride. (**1**)- acetic anhydride. (**XV**)- PAmNPC. (**XVI**)- ZnPCNPC.

In order to confirm the presence of any remaining amine groups following the capping of amino functionalised nanoparticles a solution of fluorescamine in DMSO (5 mg/ml) was prepared and subsequently added (300 μl) to suspensions of polyacrylamide nanoparticles (non functionalised) and APMA nanoparticles (amino functionalised) in deionized water (3 ml; 1 mg/ml), and allowed to react for 30 minutes. The fluorescence of resulting solutions was measured following excitation at 385 nm using a Varian Cary Eclipse fluorescence spectrometer (Varian, UK).

2.2.3.1.4 Synthesis of Porphyrin nanoparticles Synthesis of 5-[4-[(3-(3-methylthioureido)propyl methacrylamide)phenyl]-10,15,20-tris-[(4-methylpyridinium)yl]] porphyrinato zinc(II) trichloride.

To avoid aggregation of PAmNPCs and aiming for the covalent attachment of porphyrins to the polyacrylamide matrix, a porphyrin incorporating an acrylamide functionalisation was synthesized, as represented in Figure 2.11 (**XIV**). The synthesis of (**XIV**) was achieved by reacting (7 mg; 7×10^{-3} mmol) 5-(4-isothiocyanatophenyl)-10,15,20-tris-[(4-N-methylpyridinium)yl] porphyrinato zinc(II) trichloride (**XII**) with (1.27 mg; 7.11×10^{-3} mmol) of the monomer *N*-(3-aminopropyl)methacrylamide hydrochloride (**I**) in deionized water (final volume 2 ml) in the presence of 5 μ l of triethylamine, to increase the pH of the reaction mixture.

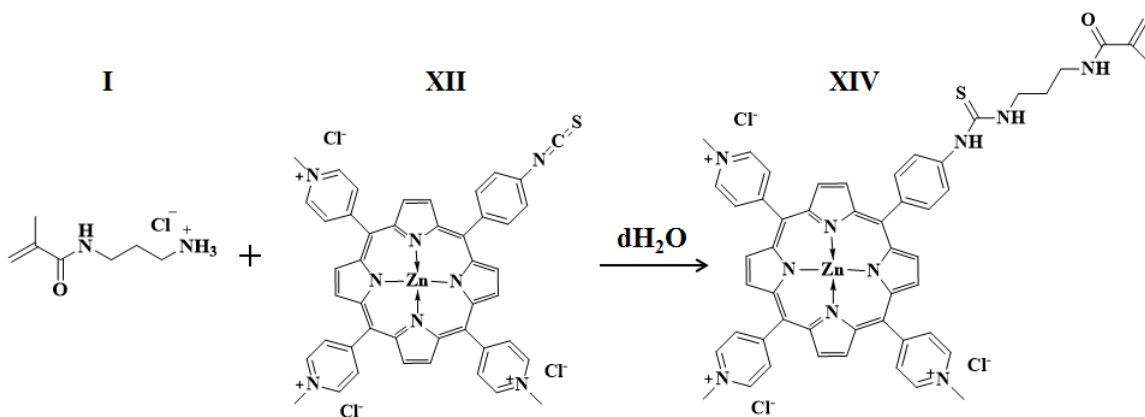


Figure 2.11: Synthetic scheme to afford 5-[4-[(3-(3-methylthioureido) propyl methacrylamide) phenyl]-10,15,20-tris-[(4-methylpyridinium)yl]]porphyrinato zinc(II) trichloride (ZnPNCs) (**XIV**). (**I**)- *N*-(3-aminopropyl)methacrylamide hydrochloride; (**XII**)- 5-(4-isothiocyanatophenyl)-10,15,20-tris-[(4-N-methylpyridinium)yl]porphyrinato zinc(II) trichloride.

The reaction was left stirring overnight at room temperature, protected from

light. Once completed, the reaction mixture was freeze dried and a porphyrin powder (dark brown) was achieved (see Appendix B).

2.2.3.1.5 Synthesis of porphyrin polyacrylamide nanoparticles (Zn-PNPs) The synthesis of porphyrin polyacrylamide nanoparticles was achieved by incorporating in the reaction mixture an acrylamide porphyrin monomer (**XIV**), Figure 2.12. The acrylamide porphyrin monomer was further added and polymerised in reverse micelles as previously referred in Section 2.2.2.2. The final concentration of porphyrin monomer added to the monomer mixture was based on the amount of porphyrin conjugated with amino functionalised NPs, Section 2.2.3.1.2. Briefly, a water-in-oil microemulsion was formed by combining the surfactants Brij[®]30 (3.08 g; 0.0026 mol) and AOT (1.59 g; 0.0036 mol) in deoxygenated hexane (42 ml). Subsequently, a monomer solution (in deionized water) containing the monomers (**i**); (**ii**) and (**XV**) in the proportions described in Figure 2.12 were added to the reverse microemulsion. The monomers polymerisation in reverse micelles was initiated by the addition of APS (10 % w/v; 30 μ l) and TEMED (15 μ l) (yield 550 mg, 71%).

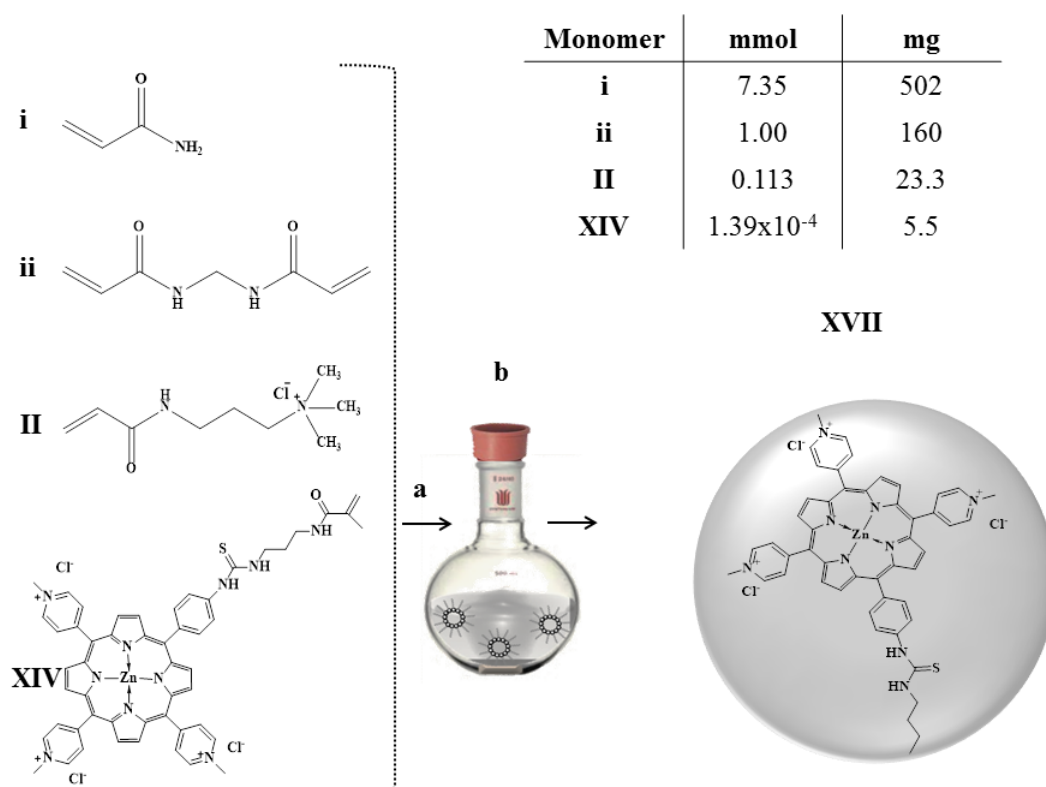


Figure 2.12: Synthetic scheme to afford porphyrin polyacrylamide nanoparticles (ZnPNP): (**i**)- acrylamide; (**ii**)-*N,N'*-methylenebis(acrylamide); (**XIV**)-5-[4-[(3-(3-methylthioureido)propylmethacrylamide)phenyl]]-10,15,20-tris-[(4-methylpyridinium)yl] porphyrinato zinc(II) trichloride. Monomers **i**, **ii** and **XIV** were mixture (**a**) and subsequently added and reacted in reverse micelles (**b**) to form nanoparticles containing porphyrins (**XVII**).

The reaction was allowed to proceed by 2 hours at room temperature under argon environment, once completed the hexane was removed by rotary evaporation (Buchi Rotavapor R-200). Therefore, the microemulsion was destabilized by the precipitation of porphyrin entrapped polyacrylamide nanoparticles in ethanol (50 ml). The removal of unreacted monomers and surfactants was achieved by centrifugal washes with ethanol. Finally, the nanosensors were re-suspended in 10 ml of absolute ethanol which was removed by vacuum filtration through a 0.02 μm filter (Sartorius Stedim Biotech, Anodisc 25). The dried nanosensors were subsequently stored at -18°C (yield 620 mg, 89%).

2.2.3.1.6 Synthesis of porphyrin trimethyl ammonium polyacrylamide nanoparticles (ZnPTNPs) As demonstrated in Chapter 3, specific applications of nanoparticles can be attained by modulation of its surface characteristics. A Variation on the surface charge of porphyrin nanoparticles was performed by incorporating the monomer 3-acrylamidopropyl tetramethyl ammonium chloride at the time of synthesis. As described above for porphyrin nanoparticles, porphyrin entrapped trimethyl ammonium nanoparticles were obtained following a similar procedure.

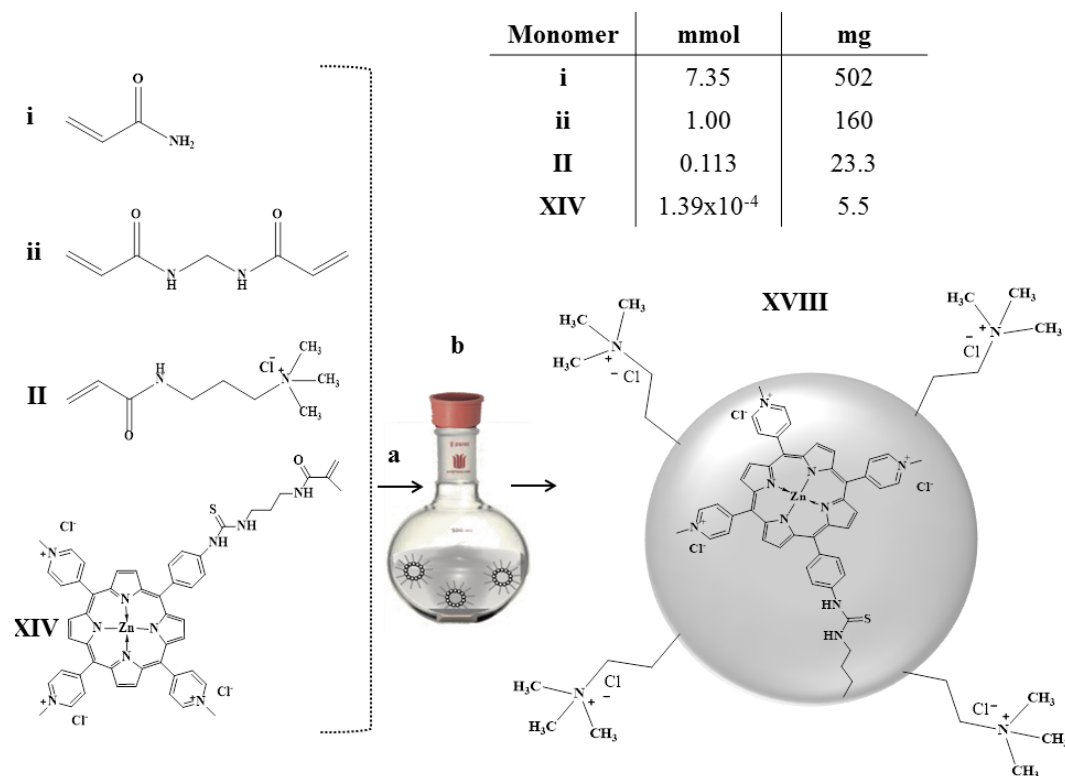


Figure 2.13: Synthetic scheme to afford porphyrin trimethyl ammonium polyacrylamide nanoparticles (ZnPTNPs): (**i**)- acrylamide; (**ii**)-*N,N'*-methylenebis(acrylamide); (**II**)- 3-acrylamidopropyl trimethyl ammonium hydrochloride; (**XIV**)- 5-4-[(3-(3-methylthioureido)propylmethacrylamide)phenyl]-10,15,20-tris-[(4-methylpyridinium)yl] porphyrinato zinc(II)trichloride. Monomers **i**; **ii**; **II** and **XIV** were mixture (**a**) and subsequently added and reacted in reverse micelles (**b**) to form trimethyl ammonium nanoparticles containing porphyrins (**XVIII**).

Briefly, the monomer solution was prepared by combining the monomers (**i**), (**ii**), (**II**) and (**XIV**) represented in Figure 2.13. The monomer solution was

subsequently added to a reverse microemulsion created by the combination of AOT (1.59 g; 0.0036 mol), Brij[®]30 (3.08 g; 0.0026 mol) and deoxygenated *n*-hexane (42 ml). The polymerisation and purification of the resultant nanoparticles were according to the procedure described above, Section 2.2.3.1.5 (yield 580 mg, 83%).

2.2.4 Development of porphyrin polyacrylamide systems *via* click chemistry methodologies.

2.2.4.1 Optimization of conjugation reaction conditions: alkyne functionalised nanoparticles.

The incorporation of the alkyne functionality at the surface of nanoparticles was investigated by reaction with 3-azidocoumarin [86]. In order to confirm the presence of reactive alkyne groups a solution of 3-azidocoumarin in DMSO (5 mg/ml) was prepared and subsequently added (200 μ l) to suspensions (50 mg/ml) of polyacrylamide nanoparticles (non-functionalised) and alkyne functionalised. The catalyst CuBr (0.05 mmol) was dissolved in DMSO (200 μ l) and added to the reaction mixture above. The final volume of the reaction mixture was completed with deionised water to 2 ml with water, and the reaction was allowed to proceed stirring for 1 hour at room temperature in total absence of light. The fluorescence of resulting solutions was measured following excitation at 390 nm (λ_{em} = 478 nm) using a Varian Cary Eclipse fluorescence spectrometer (Varian, UK).

2.2.4.2 Conjugation of 5-4-[2-(azidoethoxy)ethyl]phenyl-10,15,20-tris-[(4-methylpyridinium)yl] porphyrinato zinc(II)trichloride (ZnPN₃) *via* alkyne functionalised polyacrylamide nanoparticles (ZnPANPC)

The conjugation of azido zinc porphyrin (**XIII**) with alkyne polyacrylamide nanoparticles (**VIII**) was achieved by the application Cu-catalysed azide-alkyne

cycloaddition (CuAAC) method, also designated by “click reaction”.

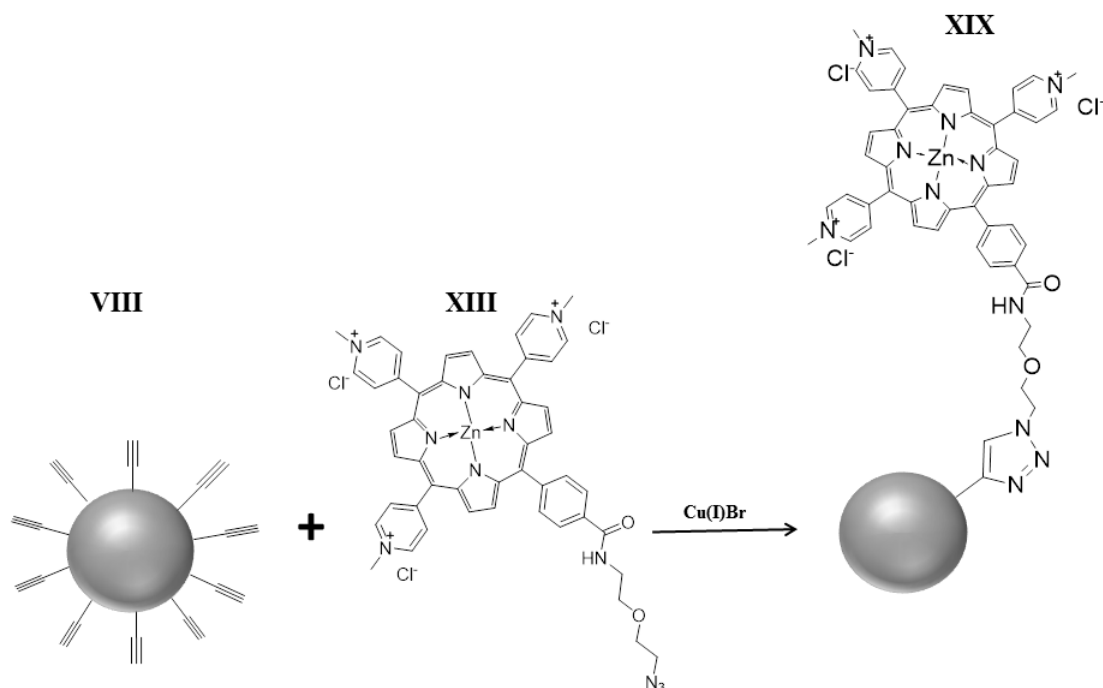


Figure 2.14: Synthetic scheme to afford Porphyrin-Alkyne nanoparticle conjugates: (VIII) Alkyne functionalised polyacrylamide nanoparticles; (XIII) 5-4-[2-(azidoethoxy)ethyl]phenyl-10,15,20-tris-[(4-methylpyridinium)yl]porphyrinato zinc(II)trichloride (ZnPN₃); (XIX) Porphyrin alkyne nanoparticles conjugates (ZnPANPC).

The reaction between alkyne-azide functionalities was performed by suspending 50 mg of alkyne functionalised nanoparticles (VIII) in water (1 ml) followed by the addition of azido zinc porphyrin (XIII) (3.2×10^{-4} mmol). The catalyst CuBr (0.05 mmol) was dissolved in DMSO (200 μ l) and added to the reaction mixture above. The volume of the reaction mixture was completed with deionised water to a final volume of 2 ml with water, and the reaction was allowed to proceed stirring for 18 hour at room temperature in total absence of light. Subsequently, porphyrin nanoparticle conjugates were purified using desalting columns, the reaction mixture was loaded into a PD10 (sephadex-25) column and eluted with 3

ml of deionized water. The resultant nanoparticles were washed with ethanol (5 ml, 2 times) by centrifugation. The resultant dark green porphyrin conjugated nanoparticles (**XIX**) were subsequently dried *in vacuo* (yield 43 mg, 86%).

2.2.4.3 Synthesis of porphyrin trimethyl ammonium nanoparticle conjugates. (ZnPATNPC)

Conjugation of 5-4-[2-(azidoethoxy)ethyl]phenyl-10,15,20-tris-[(4-methylpyridinium)yl] porphyrinato zinc(II)trichloride (ZnPN₃) via alkyne/trimethyl ammonium functionalised polyacrylamide nanoparticles: (ZnPATNPC)

The conjugation of porphyrin with alkyne- trimethyl ammonium polyacrylamide nanoparticles (ATNPs) was achieved by the application Cu-catalysed azide-alkyne cycloaddition (CuAAC) method, also designated as “click Reaction”.

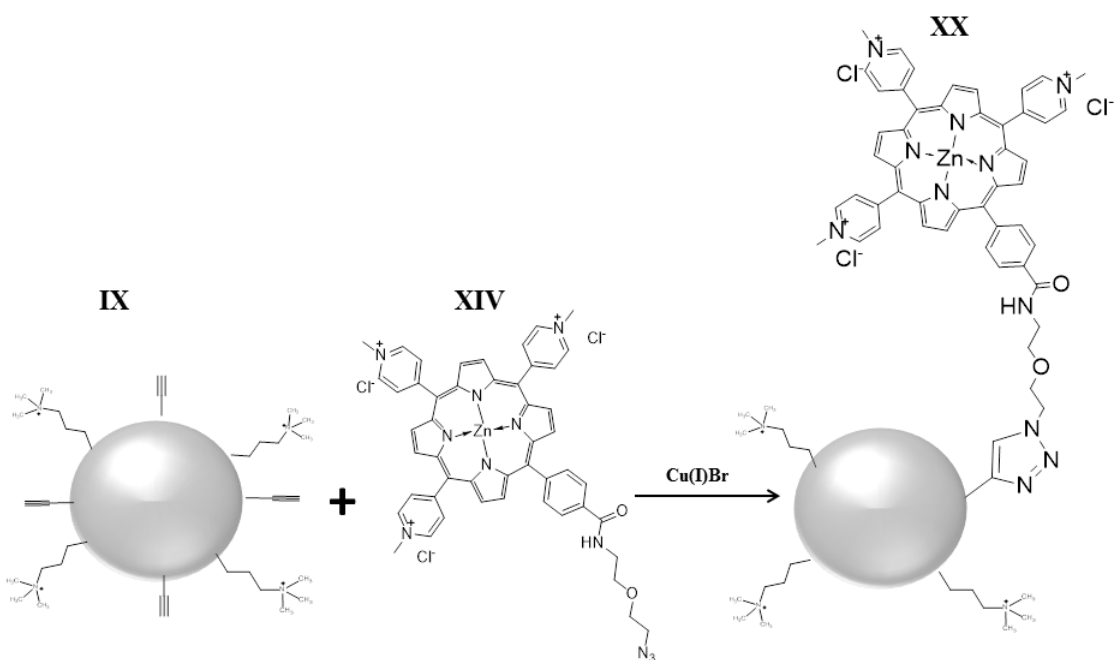


Figure 2.15: Synthetic scheme to afford porphyrin-alkyne/trimethyl ammonium nanoparticle conjugates (PATNPC): **(IX)** alkyne/trimethyl ammonium functionalised polyacrylamide nanoparticles; **(XIII)** 5-4-[2-(azidoethoxy)ethyl]phenyl-10,15,20-tris-[(4-methylpyridinium)yl]porphyrinato zinc(II)trichloride (ZnPN_3); **(XX)** Porphyrin-alkyne/trimethyl ammonium nanoparticle conjugates.

The reaction between alkyne-azide functionalities were performed by suspending 50 mg of ATNPs in water (1 ml) followed by the addition of Zn porphyrin (0.152 μmol Zn porphyrin) according to the scheme represented in Figure 2.15. The catalyst CuBr (0.05 mmol) was dissolved in DMSO (200 μl) and added to the reaction mixture above. The volume of the reaction mixture was completed with deionised water to a final volume of 2 ml with water, and the reaction was allowed to proceed stirring for 18h at room temperature in total absence of light. Subsequently, porphyrin nanoparticle conjugates were purified using desalting columns, the reaction mixture was loaded into a PD10 (sephadex-25) column and eluted with 3

ml of deionized water. The resultant nanoparticles were washed with ethanol (50 ml, 2 times) by centrifugation. The resultant dark green porphyrin conjugated nanoparticles (**XX**) were subsequently dried *in vacuo* (yield 580 mg, 80%).

2.2.5 Characterisation of nanoparticles

2.2.5.1 Dynamic Light Scattering (DLS): Size analysis of functionalised nanoparticles

The size characterization of non functionalised and surface modified nanoparticles was performed by DLS using a Zeta sizer nano series instrument (Nano-ZS; Malvern Instruments, Malvern UK), model ZEN 3600 equipped with an He-Ne internal laser (633 nm; Max 5mW). Samples of nanoparticles were suspended in deionized water (1 % w/v)), which had previously been filtered using a 0.02 μm filter (Sartorius Stedim Biotech, Anodisc 25), and aliquoted into a low volume glass cuvette (ZEN2112; 12 μl). Measurements were taken with an angle of 173° backscatter (NIBS) at 25°C, each analysis was made up of eleven correlation analysis lasting ten seconds each. To estimate the repeatability of the measurements, three aliquots of each sample was measured three times under the same conditions. Furthermore, the reproducibility of the synthesis of nanoparticles was also evaluated, for which three batches of nanoparticles were synthesized and size analysis was performed as described above. The results were extracted from nano software and the hydrodynamic radius was represented as a function of intensity distribution and undersize curve.

2.2.5.2 Zeta Potential: Surface analysis of functionalised nanoparticles

Surface characterization of nanoparticles was performed by the measurement of zeta potential using a Zeta sizer nano series instrument (Nano-ZS; Malvern Instruments, Malvern UK). Suspensions of nanoparticles were prepared in phosphate buffer pH 7.2 (0.1 % w/v) with an ionic strength of 5 mM and further injected

into a clear disposable zeta cell (DTS1060C), each analysis was made up of 100 runs, three measurements with a delay of 10 seconds each. The determination of zeta potential was achieved by Henry equation, described in Section 2.1.2. Furthermore, Henry's function ($f(Ka)$) was set for 1.5, known as Smoluchowski approximation for aqueous conditions. The results were expressed as the mean of three measurements.

2.2.6 Human fetal Liver mesenchymal stem cell culture

Human fetal liver was collected into RPMI medium containing penicillin/streptomycin by the MRC-Wellcome Trust Human Developmental Biology Resource, Newcastle-upon-Tyne, UK with appropriate maternal consents following ethical approval by the Newcastle and North Tyneside Research Ethics Committee in accordance with Human Tissue Authority regulatory guidelines. Samples from a gestational age between 8 & 9 weeks, determined using published Carnegie staging (Bullen and Wilson, 1997) were used in this study. Samples were received within 24 hours of collection. Upon receipt of the tissue, a single cell suspension was prepared by physical disruption of the fetal liver, as previously described (Jones, 1999). Thereafter, the cell suspensions were transferred to RPMI containing 1 0% dimethyl sulphoxide (Sigma Aldrich, Dorset, UK) and 20 % heat inactivated fetal bovine serum (FBS - Sigma), in cryovials, then stored in liquid nitrogen (vapor phase) at -186°C .

2.2.6.1 Thawing of stored fetal liver cells

The isolation of hMSCs from the foetal liver microenvironment was achieved based on the characteristic adherence of these cells to tissue culture plastic as described by Friednestein [88]. Therefore, and immediately before use, a frozen cell suspension was thawed by agitation in a 37°C water bath. The cell suspension was immediately transferred to a sterile universal container and 20 ml HBSS added dropwise with constant agitation. The resultant suspension was centrifuged at 500 xg for 10 minutes, the supernatant discarded and the cells resuspended in medium, as detailed below. After 48 hours, any non-adherent cells along with culture

liquid were discarded, the adherent cells washed twice with HBSS and the medium had been replaced.

2.2.6.2 *In vitro* cell culture of hMSCs

The cell culture of hMSCs was based on a protocol developed by Coupland, *et al.* to which were introduced some modifications [89]. Approximately 5×10^6 cells were grown in T25 culture flasks in 5 ml of complete medium. The chosen medium was M199 as a source of vitamins, inorganic salts and amino acids [90]. The medium was further supplemented with 20 % heat inactivated FBS, as source of a large number of growth factors and extracellular matrix molecules which confer an enhanced cell attachment to plastic surfaces as well as proliferation. [91]. Subsequently, 1 % (v/v) of L-glutamine (10 μ l/ml) was added as an essential amino acid, intermediate in many metabolic pathways and alternative substrate to glucose for energy. The medium preparation was completed by the addition of antibiotics, 1 % (v/v) P/S (10 μ l/ml) in order to confer bacterial protection. All the supplements were previously sterilized through a 0.2 μ m syringe filter before being added to the medium. Special care was taken in the addition of the supplements to the medium, all supplements were freshly added in order to avoid degradation. The cells were maintained at 37°C, 5 % CO₂, 90% humidity and medium was replaced every two days.

2.2.6.3 Harvesting of hMSCs

Cells were harvested at 70-90% confluence by enzymatic digestion. Confluent T25 flasks were subcultured at a ratio of 1:3. Prior to trypsinization, cells were washed twice with HBSS, followed by the addition trypsin/EDTA (0.0025%/0.5%) in PBS

and incubation for 3 min at 37°C, 5% CO₂, 90% humidity. Subsequently, the action of trypsin was deactivated by FBS, follow by addition of complete medium (as described above). The cell suspension was centrifuged for 10 min at 500 xg, the supernatant was discarded and cells were resuspended in complete medium as required.

2.2.6.4 Cryopreservation of hMSCs

For cryopreservation, hMSCs at 70-80% confluence were harvested by enzymatic digestion, as described above. The resultant cells were resuspendend in medium M199 supplemented with 10% of Hybri-MaxTM DMSO and 20% of heat inactivated FBS. The cell suspension was aliquoted to 1- 1.5 ml cryovials which were placed on a freezing container containing isopropyl alcohol (Mr Frosty) at −80°C to achieve 1°C/hour cooling rate required for successful cryopreservation of cells. Subsequently the cells were transferred to liquid nitrogen (vapour phase) at −186°C.

2.2.7 Cellular delivery of nanoparticles

For uptake studies, hMSCs were cultured in 8 well plates (LabTek Chamber Slide w / Cover Glass Slide) and allowed to adhere for 24 hours. Subsequently cells were incubated with 5 mg/ml of nanoparticles (sterilized using a 0.02 μ m syringe filter) for a period of 10 hours at 37°C, 5 % CO₂, 90 % humidity. The excess of nanoparticles was removed by washing the cells twice with phenol red and serum free medium. Mitochondrial staining was achieved by adding 5 μ l (0.188 nM) of mitotracker red to hMSCs, incubated with cells for a period of 20 minutes at 37° C, 5 % CO₂, 90 % humidity. Excess of mitotracker red removal was achieved by washing the cells twice with phenol red free medium. The cells were then examined by fluorescence microscopy. Mitochondria was detected by using the following conditions: λ_{exc} = 575 nm; λ_{em} = 632 nm. Nanoparticles were visualized by green emission of FITC (λ_{exc} = 475 nm and λ_{em} = 530 nm). The images reported in the Figures are representative of at least three independent experiments.

2.2.8 Nanoparticle uptake analysis

Nanoparticle internalization was evaluated by fluorescence intensity of FITC dextran entrapped on the matrix of nanoparticles. hMSCs were cultured in 6 well plates and allowed to adhere for 24 hours. Subsequently, cells were incubated with 2.5; 5; 10; 20; 30; 40; 50 mg/ml of nanoparticles (sterilized using a 0.02 μ m syringe filter) for a period of 10 hours at 37°C, 5 % CO₂, 90 % humidity. The excess of nanoparticles/porphyrin was removed by washing the cells twice with

phenol red and serum free medium. Cells were immediately analysed by FCM. The same procedure was applied to control cells.

2.3 Cellular viability analysis

To conduct cellular viability studies, hMSCs were cultured in 6 well plates and allowed to adhere for 24 hours. Subsequently cells were incubated with 2.5; 5; 10; 20; 30; 40; 50 mg/ml of nanoparticles or 5; 10; 20; 30; 40; 50 $\mu\text{g/ml}$ of ZnPN_3 , (sterilized using a 0.02 μm syringe filter) for a period of 10 hours at 37°C, 5 % CO_2 , 90 % humidity. The excess of nanoparticles/porphyrin was removed by washing the cells twice with phenol red and serum free medium. Mitochondrial staining was achieved by adding 5 μl (0.188 nM) of mitotracker red to hMSCs, incubated with cells for a period of 20 minutes at 37° C, 5 % CO_2 , 90 % humidity. Excess of mitotracker red was removed achieved by washing the cells twice with phenol red free medium. Cells were immediately analysed by FCM. The same procedure was applied to control cells.

2.3.1 Cellular effects of PATNPC activation

To determine the effects of irradiation hMSCs containing nanoparticles cultured in 8 well plates (LabTek Chamber Slide w / Cover Glass Slide) and allowed to adhere for 24 hours. Subsequently, the cells were incubated with 5 mg/ml of 5% ZnPATNPC or 10 % ZnPATNPC or 20 % ZnPATNPC (sterilized using a 0.02 μ m syringe filter) for a period of 10 hours at 37° C, 5 % CO₂, 90 % humidity. The excess of nanoparticles was removed by washing the cells with phenol red free medium twice. Mitochondrial staining was achieved by adding 5 μ l (0.188 nM) of mitotracker red to hMSCs, incubated with cells for a period of 20 minutes at 37° C, 5 % CO₂, 90 % humidity. Removal of mitotracker red excess was achieved by washing the cells with phenol red free medium.

To evaluate the formation of ROS, specifically hydrogen peroxide, cells were incubated with BPTFMC and the dye was allowed to be internalized by the cells for a period of 1 hour at 37°C, 5 % CO₂, 90 % humidity. Removal of BPTFMC excess was achieved by washing the cells twice with phenol red free medium. The cells were then examined by fluorescence microscopy. Mitochondria were detected by using the following conditions: λ_{exc} = 575 nm; λ_{em} = 632 nm. Nanoparticles ZnPTNPC were visualized by green emission of FITC (λ_{exc} = 475 nm and λ_{em} = 530 nm). The detection of hydrogen peroxide was evaluated by the conversion of BPTFMC (non-fluorescent) to HTFMC (fluorescent upon increasing quantities of H₂O₂) λ_{exc} = 390 nm and λ_{em} = 435 nm.

Control experiments were based in the analysis of cells submitted to the exact same treatments as described above (mitotracker red, BPTFMC), except the treatment and incubation with nanoparticles. All control and sample images were acquired

simultaneously under the same imaging conditions. The images reported in the figures are representative of at least three independent experiments.

2.3.2 Controlled generation of ROS in hMSCs

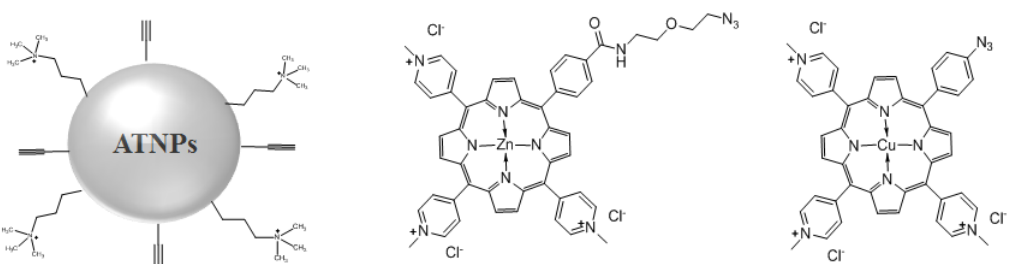
To induce hMSCs to generate ROS on a controlled manner upon light irradiation cells were treated 5 % ZnPATNPC or 5 % CuPATNPC (control). The hMSCs were cultured in 8 well plates (LabTek Chamber Slide w / Cover Glass Slide) and allowed to adhere for 24 hours. Subsequently, the cells were incubated with 5 mg/ml (sterilized using a 0.02 μ m syringe filter) for a period of 10 hours at 37° C, 5 % CO₂, 90 % humidity. Further, the excess of nanoparticles was removed by washing the cells with phenol red medium twice. Mitochondrial staining was achieved by adding 5 μ l (0.188 nM) of mitotracker red to hMSCs, incubated with cells for a period of 20 minutes at 37° C, 5 % CO₂, 90 % humidity. Removal of mitotracker red excess was achieved by washing the cells with phenol red free medium. To evaluate the formation of ROS, specifically hydrogen peroxide, cells were incubated with BPTFMC and the dye was allowed to be internalized by cells for a period of 1 hour at 37° C, 5 % CO₂, 90 % humidity. Removal of BPTFMC excess was achieved by washing the cells with phenol red free medium. The cells were then examined by fluorescence microscopy (Olympus 60x/NA 1.42, Plan Apo N UIS2, 1U2B933). Mitochondria were visualized by red emission using the following conditions: λ_{exc} = 575 nm; λ_{em} = 632 nm. Nanoparticles ZnPTNPC were visualized by green emission of FITC (λ_{exc} = 475 nm and λ_{em} = 530 nm). The detection of hydrogen peroxide was evaluated by the conversion of BPTFMC (non-fluorescent) to HTFMC (increase in fluorescence upon increasing H₂O₂) λ_{exc} =

390 nm and $\lambda_{\text{em}} = 435$ nm. Time-lapse images were collected at each 5 min for a total period of 100 minutes. At each time point the following channels were used: (1) blue channel to identify increase in intracellular quantity of hydrogen peroxide ($\lambda_{\text{exc}} = 390$ nm $\lambda_{\text{em}} = 435$ nm); (2) Green channel to detect internalized nanoparticles ($\lambda_{\text{exc}} = 475$ nm $\lambda_{\text{em}} = 530$ nm); (3) mitotracker red to evaluate and visualize cellular viability ($\lambda_{\text{exc}} = 575$ nm; $\lambda_{\text{em}} = 632$ nm) and (4) bright field DIC to detect morphological alterations in hMSCs. The irradiation of cells was achieved at the same time that mitochondria were imaged with 575 nm wavelength with LED (light emission diode). The power of irradiation was determined by the use of a power meter, 512 μW were registered for an exposed area of 8 mm² with a exposure time of 2 seconds. Control experiments were based in the analysis of cells submitted to the exact same treatments as described above (mitotracker red, BPTFMC), except that were treated with 5 % CuPATNPC. All control and sample images were acquired simultaneously under the same imaging conditions. The images reported in the figures are representative of at least three independent experiments.

2.3.3 Titration of porphyrin with alkyne-trimethyl ammonium polyacrylamide nanoplateforms (PATNP).

The conjugation of porphyrins (Zn porphyrin or Cu porphyrin) with alkyne- trimethyl ammonium polyacrylamide nanoparticles (ATNPs) was achieved by the application Cu-catalysed azide-alkyne cycloaddition (CuAAC) method, also designated by “click Reaction”. The reaction between alkyne-azide functionalities was performed by suspending 50 mg of ATNPs in water (1 ml) followed by the addition

of porphyrin (Zn porphyrin or Cu porphyrin) according to the scheme represented in Figure 2.16. The catalyst CuBr (0.05 mmol) was dissolved in DMSO (200 μ l) and added to the reaction mixture above. The volume of the reaction mixture was completed with deionised water to a final volume of 2 ml with water, and the reaction was allowed to proceed stirring for 18 h at room temperature in total absence of light. Subsequently, porphyrin nanoparticle conjugates were purified using desalting columns, the reaction mixture was loaded into a PD10 (sephadex-25) column and eluted with 3 ml of deionized water. The resultant nanoparticles were washed with ethanol (50 ml, 2 times) by centrifugation. The resultant dark green porphyrin conjugated nanoparticles were subsequently dried *in vacuo*.



Titrated porphyrin (%)	ZnPorphyrin (μmol)	CuPorphyrin (μmol)
75	0.076	0.086
50	0.051	0.058
25	0.025	0.029
10	0.010	0.012
5	5.06×10^{-3}	5.75×10^{-3}

Figure 2.16: Synthetic scheme to afford titrated conjugation of porphyrins with alkyne-trimethyl ammonium polyacrylamide nanoplatforms.

2.3.4 Immunophenotypic characterisation of treated hMSCs

The evaluation of the phenotypic characteristics of hMSCs isolated from fetal liver microenvironment was achieved by FCM. Suspensions of hMSCs were diluted to $\geq 5 \times 10^4$ cells/ml with complete medium 20 % (vol/vol) FBS (as described above) and subsequently centrifuged for 10 minutes at 500 xg. The supernatant was discarded and 5 μ l of the antibody was added. The same procedure was followed multiple colour staining, 5 μ l of each fluorescent tagged antibody was added to the cell suspension. Following the addition of the antibodies, samples were incubated for 30 minutes, at room temperature and kept in the dark. Subsequently, cells were washed with 1 ml of complete medium 20 % (vol/vol) FBS centrifuged at 300 xg for 5 minutes. The supernatant was discarded and cells were further resuspended in 1 ml of medium M199. Cells were immediately analysed by FCM.

2.3.4.1 Immunophenotypic characterisation of hMSCs treated with CuPATNPC or ZnPATNPC

The evaluation of the phenotypic characteristics of hMSCs treated with CuPATNPC or ZnPATNPC was also carried out by FCM. Cells were initially treated with 2.5 mg/ml of CuPATNPC or ZnPATNPC, (prepared as described in Section 2.2.4.2 without FITC-dextran entrapped) filtered through a 0.2 μ m syringe filter and further incubated for a period of 10 hours maintained at 37°C, 5 % CO₂, 90 % humidity. Prior to trypsinisation, cells were washed twice with HBSS, to remove any excess of nanoparticles. Further steps of trypsinization followed the same procedure described in Section 2.2.6.3. Further, suspensions of hMSCs were diluted

to 5×10^5 cells/ml with complete medium 20 % (vol/vol) FBS and subsequently centrifuged for 10 minutes at 500 xg. The supernatant was discarded and 5 μ l of each antibody was added. Following the addition of the antibodies, samples were kept in the dark for 30 minutes at room temperature, after which time cells were washed, with 1 ml of complete medium 20 % (vol/vol) FBS and centrifuged at 300 xg for 5 minutes. The supernatant was discarded and cells were further re-suspended in 1 ml of medium M199. Cells were immediately analysed by FCM. The same procedure was applied to control cells (without addition of NPs).

2.3.4.2 Portable LED light system

For the development of a portable light system, an LED light source (Flood light 130 LED) was coated with two neutral density filters (0.3 ND) to control the optical power of transmitted light. Subsequently, it was adapted (in the top of the density filters) to fit an orange fluorescent acrylic layer, an absorptive filter to selectively transmit light at a wavelength of approximately 575 nm, as represented in **a)** Figure 7.7 . Furthermore, to confine the beam of light to the area of irradiation it was adapted an opaque structure with black interior as shown in **b)** Figure 7.7. Additionally, the optical power output was determined, by the use of a hand-held power meter with integrated sensor and aperture of 8 mm (Laser check RoHS, Coherent), being achieved an output power of approximately $500 \pm 5 \text{ } \mu\text{W}$. The LED output spectra was recorded with a UBS2000 fiber optic spectrometer (Ocean Optics), the resultant wavelength versus intensity was graphically represented.

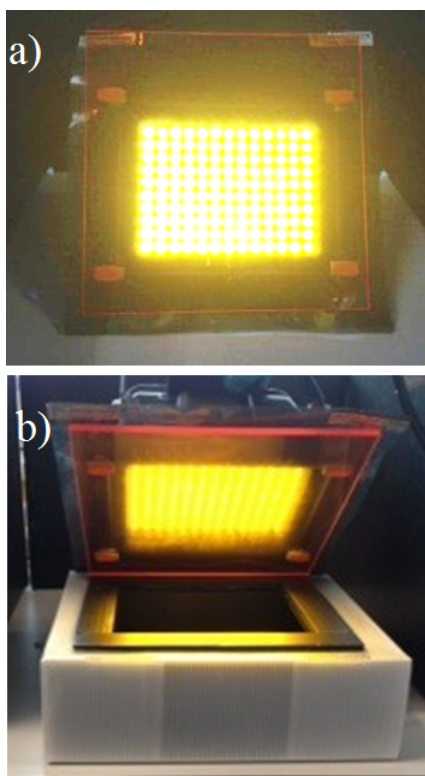


Figure 2.17: Portable light system.

2.3.4.3 Immunophenotypic characterisation of irradiated hMSCs treated with CuPATNPC or ZnPATNPC

To determine the effects of light irradiation on the surface marker profile of hMSCs containing ZnPATNPC 1.5×10^4 hMSCs were cultured in 6 well plates and allowed to adhere for 24 hours at 37°C, 5 % CO₂, 90 % humidity. Subsequently, the cells were incubated with 2.5 mg/ml of ZnPATNPC or CuPATNPC (sterilized using a 0.02 μ m syringe filter) for a period of 10 hours at 37°C, 5 % CO₂, 90 % humidity. Excess nanoparticles were removed by washing twice with HBSS. Four of 6 well plates, were used to assess the effects on increasing doses of light. The first was irradiated 5 times, the second was irradiated 10 times, the third for 15 times and the last irradiated 20 times with PLS. Irradiations were performed for 2 sec at each 5 min , during the recovery cells were kept at 37°C, 5 % CO₂, 90 % humidity. At the

end of 5, 10, 15 and 20 irradiations cells were washed with HBSS trypsinised and subsequently centrifuged for 10 minutes at 500 xg. The supernatant was discarded and 5 μ l of each antibody was added. Following the addition of the antibodies, samples were incubated for 30 minutes in the dark at room temperature, after which the cells were washed, with 1 ml of complete medium 20 % (vol/vol) FBS (as described above), by centrifugation 300 xg for 5 minutes. The supernatant was discarded and cells were further resuspended in 1 ml of medium M199. The same procedure was applied to control cells (without addition of NPs). Cells were immediately analysed by FCM.

2.3.5 Data analysis

Flow cytometry analysis and plot generation was performed by Walter & Elisa analysis software; Eclectic and Lucid (WEASEL). Results are expressed as mean plus or minus standard deviation (SD). For statistical analysis one-way analysis of variance was performed, using Sigma-plot 11.0. P value <0.05 was considered statistically significant.

Chapter 3

Exploiting the surface chemistry of polyacrylamide nanoparticles

3.1 From Reverse Microemulsions to Polyacrylamide Nanoparticles

The synthesis of polyacrylamide nanoparticles is a well documented process which involves the formation of a reverse microemulsion (also called reverse micelles or water-in-oil microemulsion) [43, 92–95]. The water droplets in the reverse microemulsion function as nanoreactors (templates), where, upon the addition of the acrylamide-based water soluble monomers and initiators, the nanosized particles are formed after polymerisation [43, 93–96].

3.1.1 Reverse Microemulsions

Reverse microemulsions were first reported by Schulman & Hoar in 1943, defined as optically transparent and thermodynamically stable systems, comprising aqueous

droplets stabilized in a continuous polar fluid by an interfacial layer of surfactants [97].

The surfactant acts as the driving force in the formation of reverse microemulsions. Surfactants or amphiphiles are molecules characterised by two regions with distinct properties, where a hydrophilic moiety (affinity for water), also called *head*, is covalently linked to a hydrophobic moiety (affinity for oil), also called *tail*. The surfactant head groups enclose an aqueous core which separates the water from the non-polar solvent continuous phase. Consequently, the characteristic structure of these molecules limits their total solubilization in both water and oil phases, thus they tend to accumulate at the water-oil interface [98].

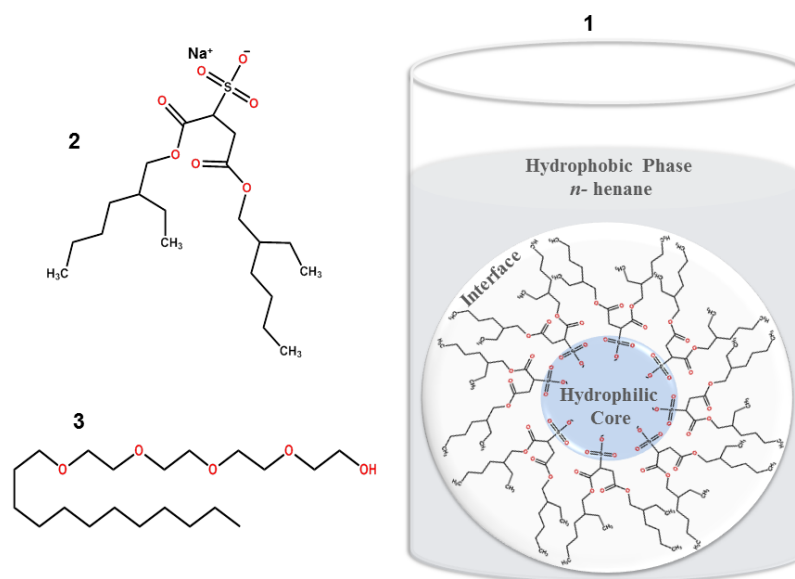


Figure 3.1: Schematic representation of water-in-oil microemulsions: Reverse Micelles (1) consisting of a hydrophilic core compartmentalised by the hydrophilic head of AOT (2) and with the alkyl tails directed to the hydrophobic continuous phase. A co-surfactant (3) is added to introduce more fluidity and decrease the curvature of the droplets.

In water/oil/surfactant systems, increasing concentrations of surfactant adsorption at the interface becomes favourable due to the strong hydrophilic interactions

of the polar head with water. Therefore, as a result of the free energy of solvation of the surfactant at the interface, exclusion of direct water-oil contact is observed. Subsequently, these interactions, at a certain concentration (the CMC) (critical micelle concentration), become saturated and the self-assembly of surfactant occurs, with the formation of aggregates, also called micelles. This concentration is known as critical micelle concentration, CMC. The complete adsorption of surfactant (micelle formation) at the interface leads to a substantial decrease of the free energy of the system, in contrast to what happens when surfactant molecules are dispersed in a continuous medium [98–101]. It is important to note that most of the surfactants are not capable by themselves of lowering the interfacial tension sufficiently to confer stability to reverse micelles. Consequently, the addition of a co-surfactant is often necessary. The co-surfactant is generally a nonionic compound, which contributes for the further lowering of the interfacial tension, introducing more fluidity and decreasing the curvature of the droplets. The decrease of the curvature of the droplets will lead to the reduction of their size. The droplet size in reverse micelles is directly related to the molar ratio of water-to-surfactant (**W**).

$$W = \frac{[H_2O]}{[Surfactant]} \quad (3.1)$$

.

Changing (**W**) in reverse microemulsions can alter the water pool in inverse micelles and, consequently, the size of the resultant micelles. At constant concentrations of surfactant, **W** increases with the increase of [H₂O]. Therefore, the water pool size is an adjustable parameter [98, 101].

3.1.2 Polymerisation of acrylamide in reverse micelles.

It should be emphasized that reverse microemulsions are dynamic systems. Thus, micelles collide via Brownian motion resulting in formation of short-lived clusters. These clusters allow the transference of material between droplets [92, 102, 103]. The aqueous core will accommodate the water soluble acrylamide monomers such as acrylamide and methylene bis-acrylamide. The effects of the water-soluble monomers on the reverse micelles formation and size were previously investigated, and it was found that they exert a co-surfactant effect [104]. The interaction of monomers with the polar head of the surfactant leads to a further reduction on the interfacial tension of the micelles. Consequently, the size of the reverse micelles decreases [92, 98, 105].

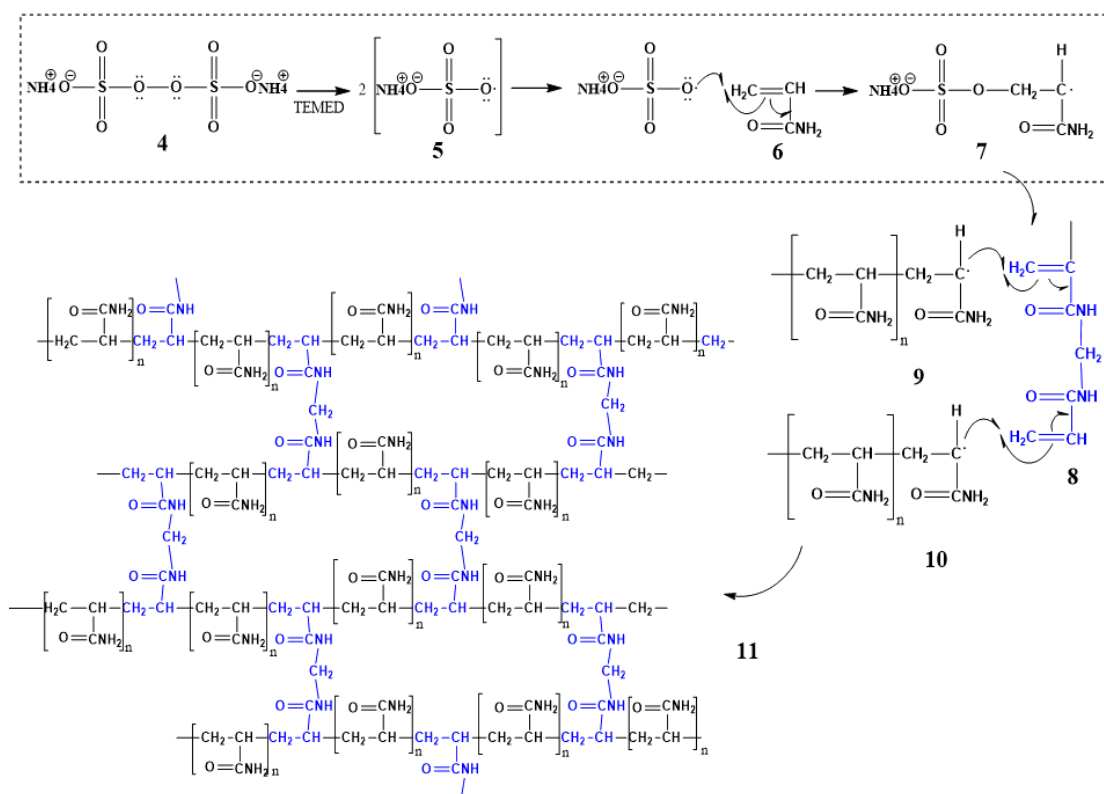


Figure 3.2: Vinyl addition polymerisation of acrylamide. Ammonium persulfate (4) in the presence of TEMED generates sulphate free radicals (5), which in turn react at the carbon-carbon double bond of acrylamide (6) resulting in activated acrylamide monomer free radicals (7). Acrylamide radicals react with acrylamide monomers to form linear polymer chains (8,9), bis-acrylamide containing two carbon-carbon double bonds (10) reacts with 2 acrylamide radical monomers, allowing the formation of bridges between the molecules of acrylamide (11).

The synthesis of the polyacrylamide matrix within in the aqueous droplets from acrylamide monomers proceeds *via* a radical vinyl polymerization which consists of stepwise reactions, as shown in Figure 3.2. In the first step, initiation, a redox pair (reduction-oxidation), APS and TEMED, yields a pair of primary radicals (4,5) [106, 107]. TEMED accelerates the rate of formation of free radicals from persulfate and these in turn catalyze polymerization. Subsequently, the addition of the primary radicals to acrylamide monomers will be part of the second step propagation, where the reaction of activated monomers with inactivated monomers occurs, promoting the propagation of a linear polymer chain (8). Furthermore,

the presence of a cross linker *N,N'*-methylenebis (acrylamide) (**10**) capable of reacting with two acrylamide monomers will induce the combination of linear chains of polymer and the consequent formation of a porous network (**10**). The final step is termination; at this stage the propagation of polymer chain ceases, leading to the formation of polymer dead ends (**11**) and a porous matrix of polyacrylamide is formed in the aqueous droplets of the microemulsion [94, 106, 108]. As in all reactions which involve free radicals as catalysts, the presence of any free radical scavenger will lead to inhibition of the polymerisation reaction. Oxygen is a key free radical scavenger. Thus, the successful synthesis of polyacrylamide nanoparticles in reverse microemulsions is dependent on the appropriate elimination of all dissolved oxygen. Once synthesized, the recovery of the nanoscale polyacrylamide particles from the inverse microemulsion is by rotary evaporation, to remove the organic phase. Subsequently, addition of a polar solvent results in the precipitation of the nanoparticles. The precipitation step allows collection of the final nanospheres by removing the excess of surfactant [2, 89, 109].

Aims

The physiochemical properties of the nanoparticle core are known to be the major factor for determining its specific application, likewise surface properties are imperative. The assignment of specific functionalities at the surface of nanoparticles, combined with their intrinsic characteristics (e.g. pore size, shape, elasticity, swelling), confers control and specificity over the interactions with biomolecules and cells. Therefore, surface functionalisation plays a crucial role in the development of effective tools for diagnostic and therapeutic applications.

The present chapter aims to design and characterize functionalised polyacrylam-

ide nanoparticles. The introduction of different functionalities aimed to provide reactive and stable chemical moieties for further conjugation, but also to assist cellular uptake and specific sub-cellular localisation. To establish the reliability of the synthetic procedure and the presence of the anticipated functionalities, the resultant nanosystems were assessed by several techniques.

3.2 Results and Discussion

The biological applications of nanoparticles rely on their physicochemical properties, such as size, shape, surface chemistry and surface charge, being understood and controlled. For the present work, it was important to determine the characteristics of the nanosystems developed. Zeta potential measurements were used to characterize the production of several positively charged nanosystems. Particle size and size distributions were investigated by dynamic light scattering (DLS) and differential centrifugation (CPS). The analysis of nanoparticle size is difficult, despite the existence of several techniques, as all of them present technical/instrumental limitations due to the small nature of these systems (diameter ≤ 200 nm) [110–112]. Therefore, it was important to investigate nanoparticle size by using complementary techniques.

3.2.1 Acrylamide monomers containing functional groups.

Acrylamide based monomers containing a chemical reactive moiety were used to incorporate specific functionalities to polyacrylamide nanoparticles. The chemical structure of the monomers used to introduce an amine, trimethyl ammonium or alkyne functionalities are represented in Figure 3.3. The referred monomers were incorporated and polymerized within the monomers mixture (acrylamide, methylene bis-acrylamide) at the time of synthesis. The monomers used for the introduction of an amino (Figure 3.3; **(I)**) and trimethyl ammonium functionalities (Figure 3.3; **(II)**) were available commercially.

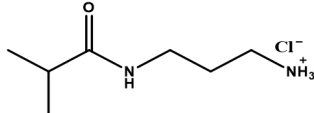
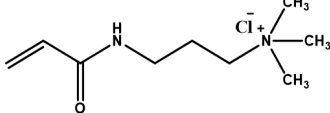
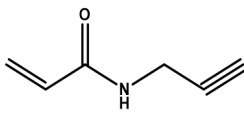
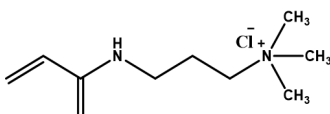
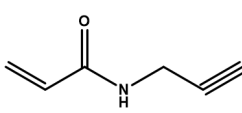
	Entry	Nanoparticle functionalization	Functionalization Monomer
Mono Functionalized NPs	I	Amino	
	II	Trimethyl ammonium	
	III	Alkyne	
Dually Functionalized NPs	IV	Trimethyl ammonium/ Alkyne	
			

Figure 3.3: Nanoparticles functionalised monomers. Mono functionalised nanoparticles: **(I)**- *N*-(3-aminopropyl) methacrylamide hydrochloride. **(II)**- 3-acrylamidopropyl trimethyl ammonium hydrochloride. **(III)**- *N*-propargyl acrylamide. Dually-functionalised nanoparticles: **(IV)**- 3-acrylamidopropyl trimethyl ammonium hydrochloride; *N*-propargyl acrylamide.

With respect to the alkyne modification (Figure 3.3; **(III)**), the monomer propargyl acrylamide was synthesized in our laboratory following the procedure primarily described by Malkoch, *et al.* [113], later modified by Welser, *et al.* [87,114] as represented in Figure 3.4.

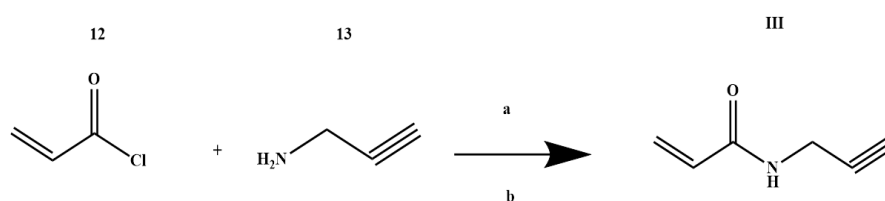


Figure 3.4: Synthetic scheme to afford *N*- propargylacrylamide. **(12)**- acryloyl chloride; **(13)**- propargylamine; **(III)**- *N*-propargylacrylamide; **(a)**- diisopropylethylamine (DIPEA); **(b)**- DCM.

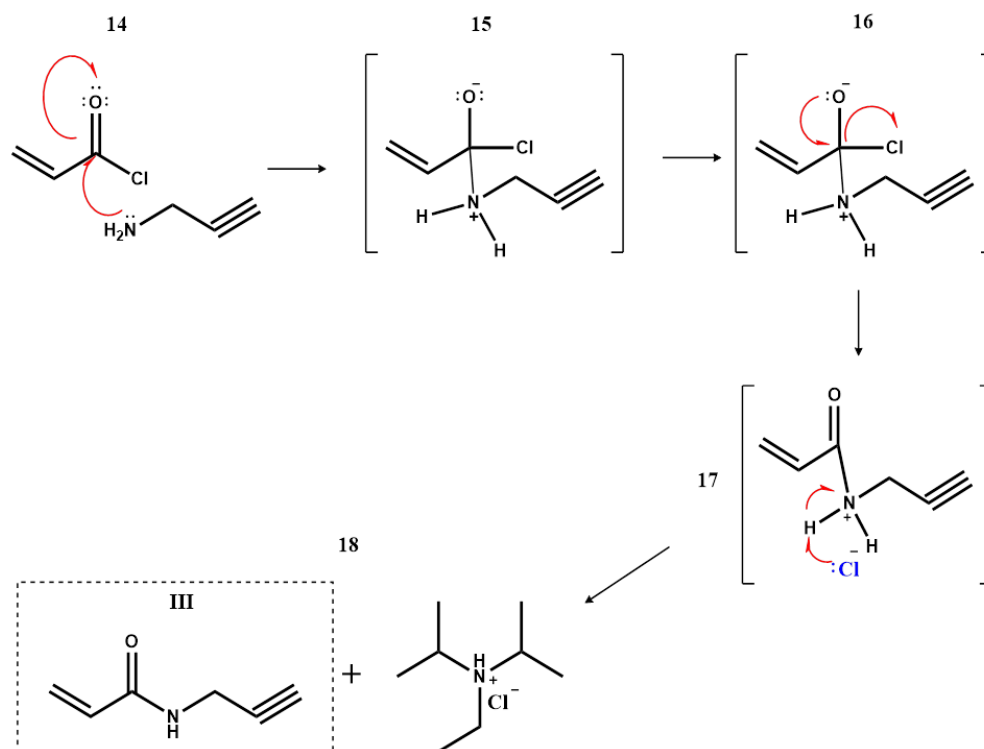


Figure 3.5: Mechanism of acrylation of amine-alkyne derivatives to afford *N*-propargylacrylamide.

Briefly, as depicted in Figure 3.5, the mechanism involves the nucleophilic attack of the carbon atom of acryloyl chloride by the lone pair on the nitrogen atom of propargylamine, (**14**) forming the intermediate (**15**). Subsequently, an elimination step leads to the reformation of the carbon-oxygen double bond with exit of chloride ion (**16**). The hydrogen ion (**17**) was then eliminated by reaction with chloride, to afford propargylacrylamide (**18**). The identity of the product was confirmed by proton NMR, as shown in Figure 3.6. Analytical data was in agreement with earlier publications (see Appendix A) [87]. Therefore, the successful synthesis of the acrylamide based monomer necessary to confer an alkyne functionality to polyacrylamide nanoparticles was possible.

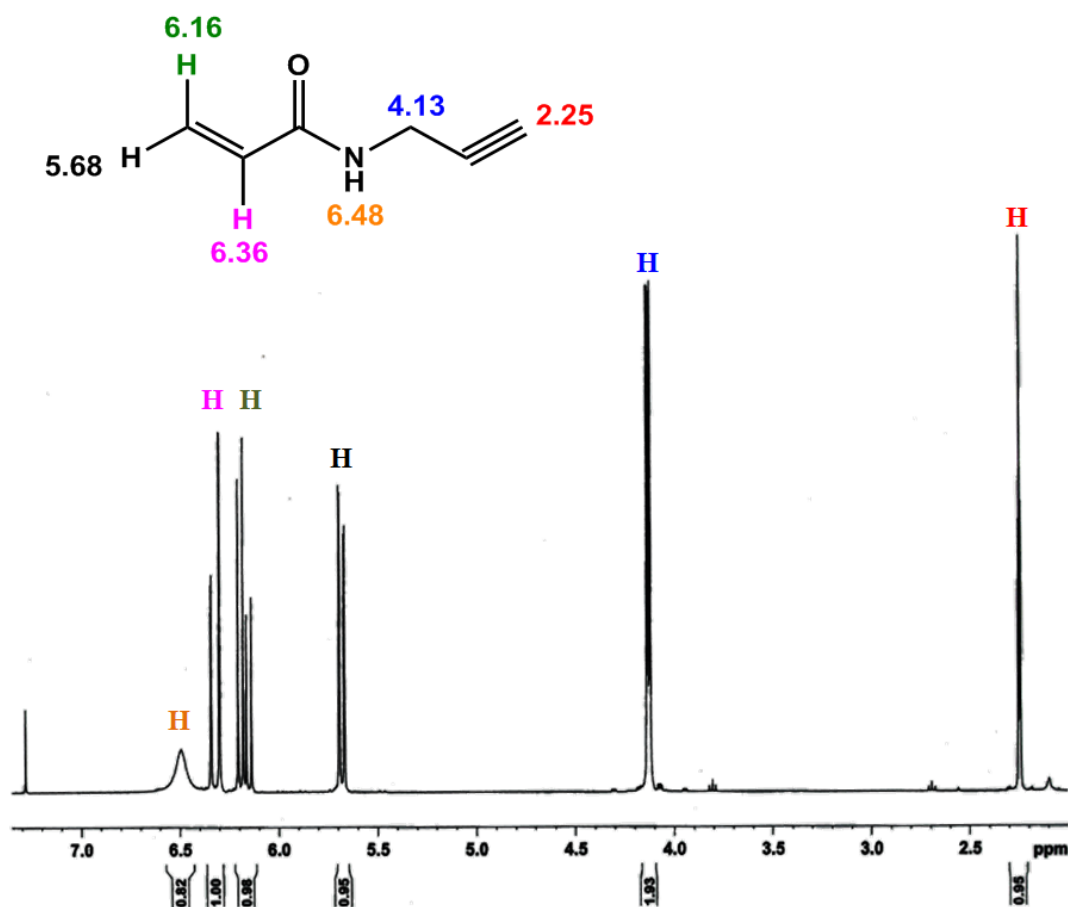


Figure 3.6: ^1H -NMR spectra of *N*-propargylacrylamide in CDCl_3 .

3.2.2 Characterization of size distribution of functionalised nanoparticles.

The present work required the development of nanoparticles with several functionalities for multiple proposes (e.g. conjugation, facilitated uptake, nanoparticle stability). Therefore, nanoparticles were produced containing amino, alkyne or alkyne/trimethyl ammonium functionalisations.

The size characterisation of surface modified polyacrylamide nanoparticles was performed by dynamic light scattering (DLS). The results of dynamic light scattering analysis were presented as function of the intensity distribution and un-

dersize intensity. These graphical representations aimed to show the particle size distribution on the sample analysed. However, the intensity distribution is known to introduce small errors as a consequence of multiple scattering of fewer larger particles. In order to report the most accurate hydrodynamic diameter, the Z-average was used. This parameter is known to be the most stable value recorded by dynamic light scattering for monodisperse and monomodal distributions. Z-average results from the cumulants fit and is defined as the harmonic intensity averaged particle diameter [110–112,115]. A suspension of nanoparticles in water was analysed straight after synthesis and monomodal distributions were observed for both functionalised and non-functionalised nanosystems.

3.2.2.1 Polyacrylamide nanoparticles

Polyacrylamide nanoparticles have been used by several groups for different applications (e.g. ion sensing, vehicles for photosensitizer delivery) [37, 53, 55, 68, 116–119]. In general, it has been described that the cross linked polymerisation of acrylamide carried out in reverse microemulsion leads to production of highly monodispersed particles. Furthermore, the characterisation of these systems indicated a dependence of water/AOT and monomer/crosslinker ratio producing nanoparticulate systems with hydrodynamic diameter between 10 and 50 nm [102, 105, 120]. Similarly with the work previous developed, polyacrylamide nanoparticles were synthesized *via* reverse microemulsion and characterised.

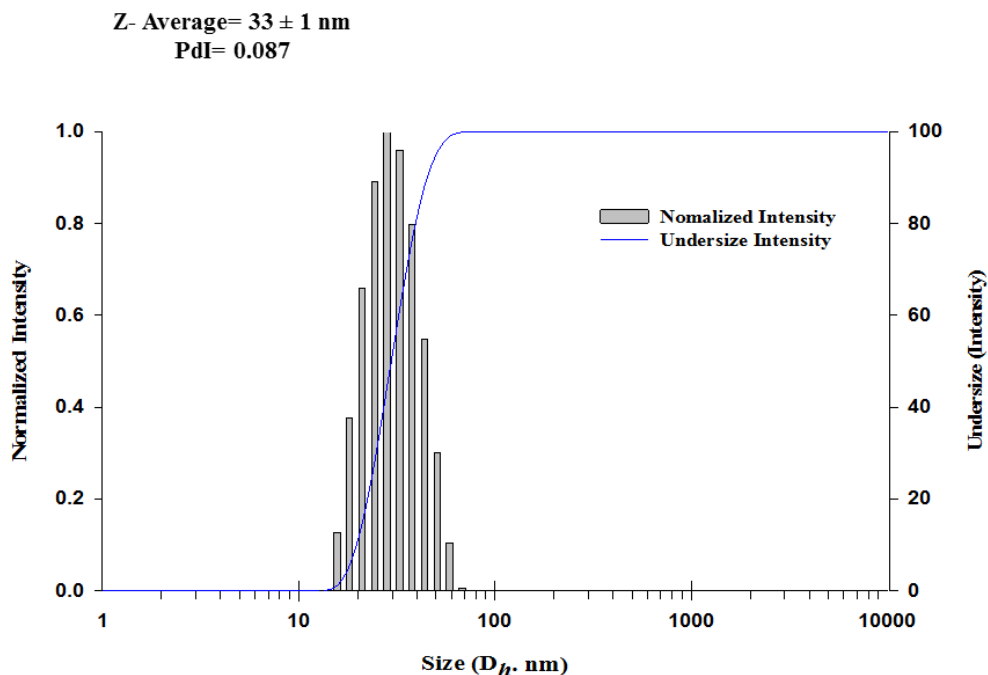


Figure 3.7: Representative size distribution of polyacrylamide nanoparticles characterised by Dynamic Light Scattering- DLS (t=0 day). The results were mean \pm SD of three independent measurements.

In Figure 3.7, the size distribution of polyacrylamide nanoparticles by DLS is represented. A monomodal distribution with a size range 15-60 nm and a median hydrodynamic radius of 33 nm was observed. These results indicated that it was possible to reproduce the synthesis of polyacrylamide nanoparticles with physical size and uniformity, consistent with literature [37, 43, 93, 121].

3.2.2.2 Amino functionalised nanoparticles

Size characterisation of polyacrylamide nanoparticles containing an amino functionality originated a monomodal distribution (Figure 3.8).

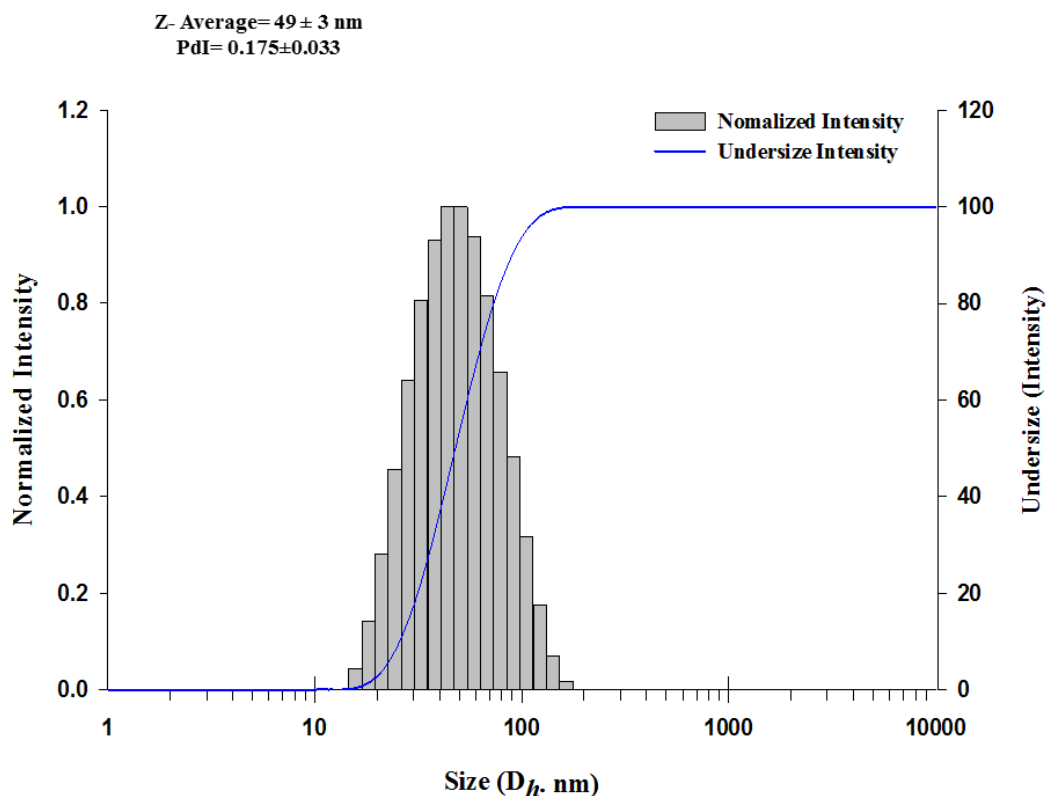


Figure 3.8: Size characterisation of amino functionalised nanoparticles by DLS ($t=0$ day). The results were mean \pm SD of three independent measurements.

The introduction of an amino functionalisation resulted in nanosystems with increased median average of 49 nm compared to their non-functionalised counterparts of 33 nm (Figure 3.7). Furthermore, a wider size distribution was observed, with a size range between 15 and 110 nm. The increased hydrodynamic diameter in amino tailored nanoparticles was previously reported by several groups and attributed to an inherent aggregation pattern of amino functionalised polyacrylamide nanosystems [2, 70, 87, 109, 122, 123]. Moore, *et al.* associated the aggregation phenomenon to a slow aza-Michaelis addition between the *N*-(3-aminopropyl) methacrylamide and the *N,N'*-methylenebis (acrylamide) at the surface of adjacent particles [109]. Although nanoparticles were characterised immediately after synthesis, it is possible that the presence of small aggregates resulted in larger size

distribution of the samples. The agreement of the above results with previous reported values suggests that it is possible to produce polyacrylamide nanoparticles containing an amine functionality.

3.2.2.3 Alkyne functionalised nanoparticles

The impact of tailoring polyacrylamide nanoparticles with alkyne functionalities in particle size was evaluated and is shown in Figure 3.9. Similarly to their non-functionalised counterparts, alkyne modified nanoparticles have shown a monomodal distribution.

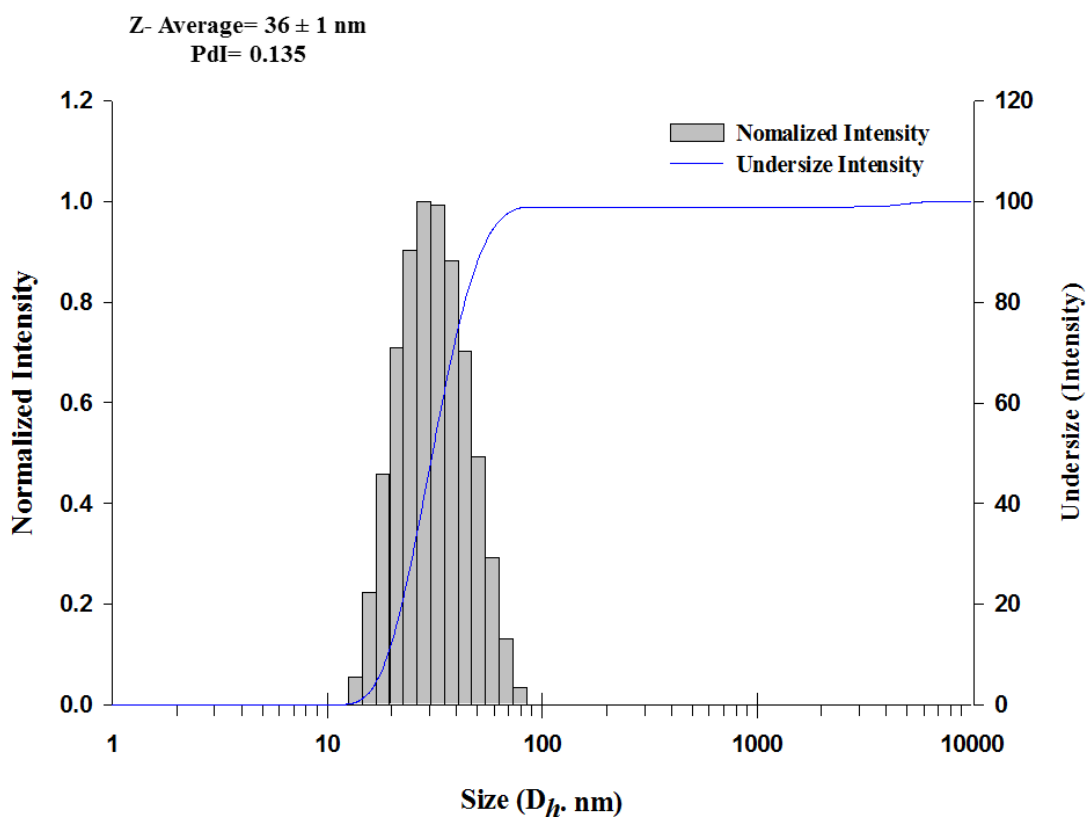


Figure 3.9: Size characterisation of alkyne functionalised nanoparticles by DLS ($t=0$ day). The results were mean \pm SD of three independent measurements.

Small variations in distribution range (12-80 nm) and median hydrodynamic size of 36 nm were verified for alkyne functionalised nanoplatforms. The results

were similar to the ones reported previously by Welser, *et al.* [87], polyacrylamide nanoparticles containing an alkyne functionality resulted in unimodal distributions with 25 nm in hydrodynamic diameter. Small variations in particle size might be a consequence of small alterations on the nanoparticle synthetic procedures.

3.2.2.4 Alkyne/trimethyl ammonium functionalised nanoparticles

Development of alkyne/trimethyl ammonium nanoparticles aimed for design of a construct with a reactive functionalisation for further conjugation (alkyne) and to confer a net positive charge (for facilitated cellular deliver and sub cellular localisation) to the system (trimethyl ammonium). Size characterisation for trimethyl ammonium functionalised polyacrylamide nanoparticles was also evaluated. Trimethyl ammonium functionalisation was achieved by including different percentages of the cationic monomer with acrylamide and *N,N'*-methylenebis(acrylamide) in the polymerisation reaction, which generated three systems containing increasing percentages of the cationic monomer, 2.5 %; 5 % and 10 %, respectively. In this section, the variation in size distribution as a consequence of increasing trimethyl ammonium functionalisation was evaluated.

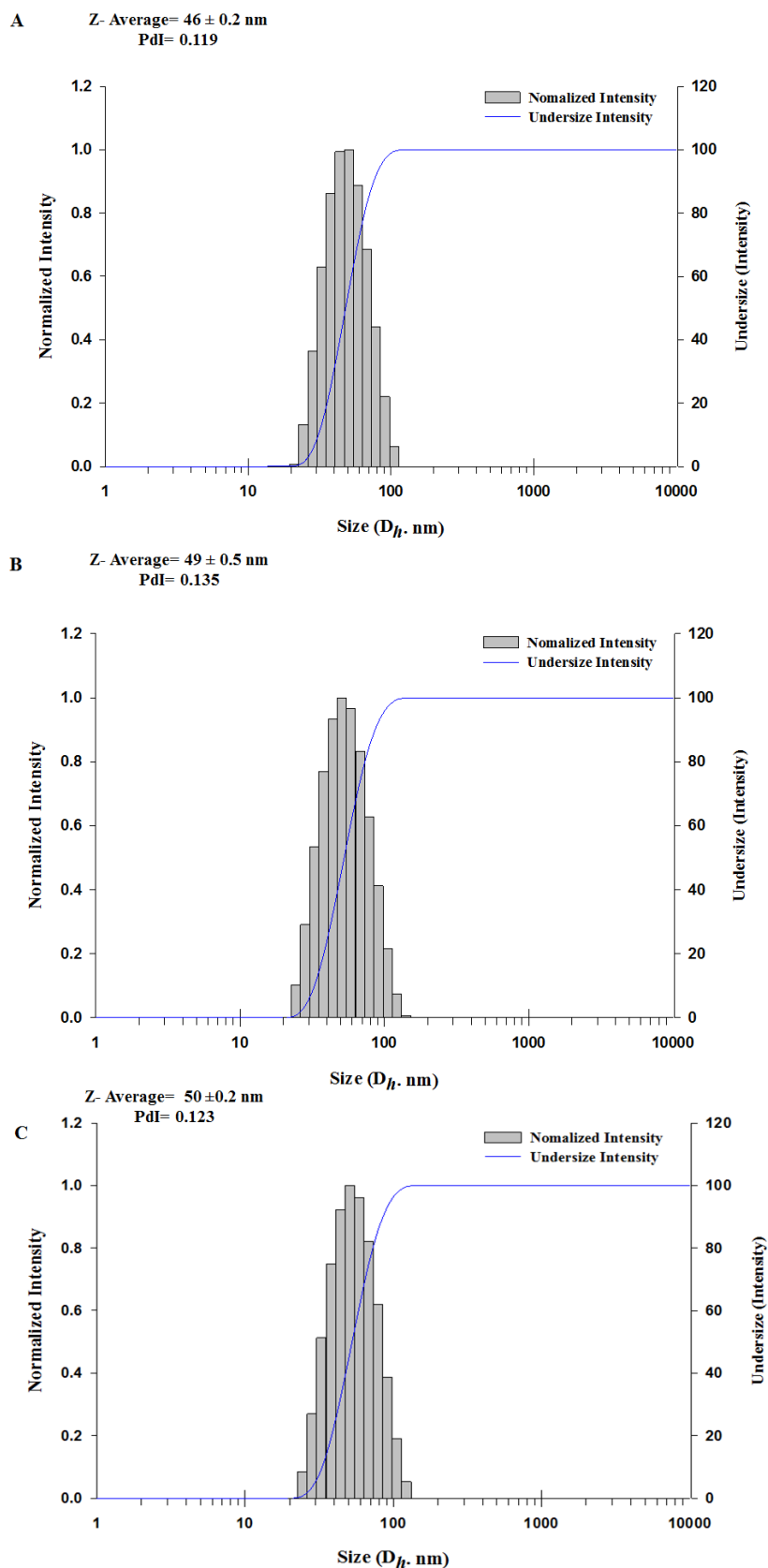


Figure 3.10: Size characterisation of alkyne/trimethyl ammonium functionalised nanoparticles by DLS (t=0 day). (A)- 2.5 % TNPs; (B)- 5 % and (C)- 10 %. The results were mean \pm SD of three independent measurements.

For particles containing 2.5 % of trimethyl ammonium monomer, a monomodal distribution with a Z-average of 46 nm was obtained. Increasing the percentage of trimethyl ammonium monomer (5 %) led to a slight increase in nanoparticle diameter of 3 nm (49 nm). Further increase in trimethyl ammonium addition, to 10 %, led to higher Z-average of 50 nm. Despite the slight variations in Z-average as consequence of increased trimethyl ammonium functionality, the size distributions range was similar for the three systems, 25-120 nm. Sun, *et al.*, reported on the size of polyacrylamide nanoparticles containing trimethyl ammonium functionalities; they observed a size increase with further addition of trimethyl ammonium [59]. The increase in size was associated with the positive charge at the surface of polyacrylamide nanoparticles and an increased osmotic pressure as a consequence of the dissociated counterions [124]. It was also postulated that the introduction of a positively charged monomer lead to a change in water-oil microemulsion during polymerization.

3.2.3 Surface charge characterization of functionalised nanoparticles: Zeta Potential.

Characterisation of surface charge in functionalised polyacrylamide nanoparticles was achieved by determination of electrophoretic mobility. Zeta potential was further calculated by applying Henry equation (Chapter 2, Section 2.1.2). Zeta potential measurements were performed at 25°C, with Hepes buffer (1 mM) at pH 7.0. Particle surface charge was found to be neutral for non-functionalised as well as for alkyne tailored nanoparticles with zeta potential values of -3 mV, as shown in Figure 3.11. The introduction of an amino group in the polymeric

matrix of the nanoparticles generated an increase in zeta potential to $+18\text{ mV}$. This was expected and was in agreement with previous reports [109,125]. The results indicated the successful insertion of an amino chemical modification which confers a positive charge to polyacrylamide nanoparticles, as previously reported by Moore and others [109,125]. The introduction of increasing concentrations of quaternary ammonium ion functionalities into polyacrylamide nanoparticles aimed for the modulation of the net charge. Thus, as expected, the insertion of 2.5 % of trimethyl ammonium monomer in the reaction mixture for the synthesis of positively charged nanoparticles, generated a surface charge of $+13\text{ mV}$. The further increase to 5 % and 10 % of tetramethyl ammonium in the monomers mixture was also accompanied by an increase in surface charge, to $+18\text{ mV}$ and $+28\text{ mV}$, respectively. Therefore, zeta potential results indicated that nanosystems carrying increased levels of net charge were generated. The results were consistent with the work previously developed by Sun, *et al.*, who also investigated the development of positively charged polyacrylamide nanoplateforms [59].

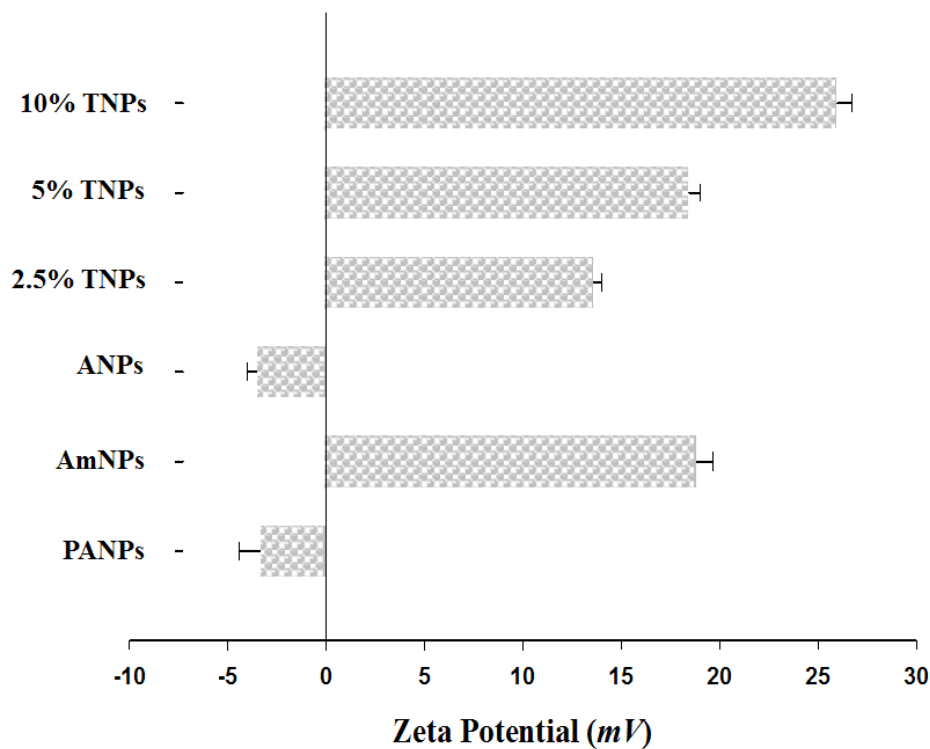


Figure 3.11: Surface charge of functionalised polyacrylamide nanoparticles. The results were mean \pm SD of three independent measurements.

3.2.3.1 Comparison of nanoparticle sizes

The size distributions of the functionalised and non-functionalised nanoplatforms were shown in Figures 3.7, 3.8, 3.9, 3.10. Figure 3.12 shows and compares the average size diameters for the various nanoplatforms developed.

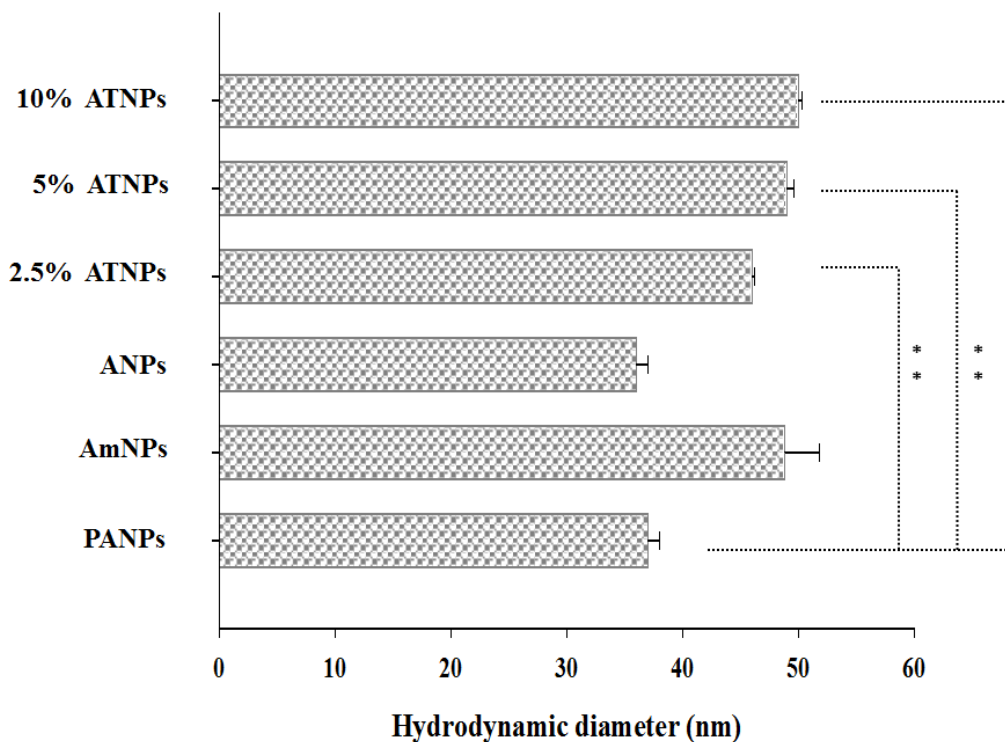


Figure 3.12: Comparison of size variation in polyacrylamide functionalised nanoparticles by DLS. The results were mean \pm SD of three measurements. Control (polyacrylamide NPs) vs. 2.5 %; 5 % and 10 % TNPs:** $p < 0.001$. Student's-*t*-test.

The introduction of an alkyne moiety did not produce significant alterations in size distributions when compared with non-functionalised systems ($p > 0.05$).

For the amino-functionalised nanoplateforms, an increased z-average was obtained, even though that value was not significant ($p > 0.05$) when compared with its non-functionalised counterparts. As mentioned above (Chapter 2), DLS intensity distributions are prone to be misled by the presence of a small amount of larger particles. Thus, as stated above, the characteristic aggregation associated with amino-functionalised NPs originated larger size distributions for these systems. The increased z-average is hypothesized to result in small aggregation, which would explain the larger size distributions and, consequently, overestimation of

this value.

On the other hand, dual functionalised nanoplateforms (alkyne/TNPs) showed statistically different hydrodynamic diameters when compared with the non-functionalised particles ($p < 0.001$).

In order to further investigate the variations in nanoparticle size, measurements using differential centrifugation sedimentation (CPS) were compared with those obtained from DLS. Both methodologies resulted in monomodal distributions for all analysed systems, previously reported as essential conditions for accurate nanoparticle size determination by these instruments [126].

3.2.3.2 Size distribution of nanoparticles: Dynamic light scattering (DLS) vs. differential centrifugation (CPS).

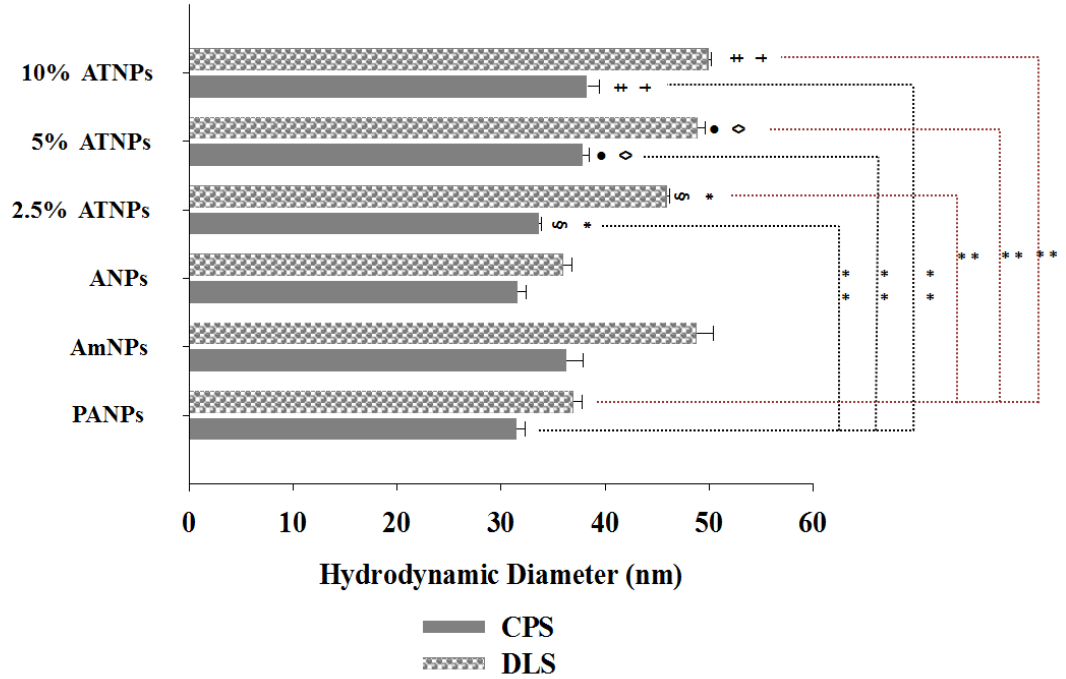


Figure 3.13: Size characterisation of functionalised and non-functionalised polyacrylamide nanoparticles by dynamic light scattering (DLS) and differential centrifugation (CPS) (t=0 day). The results were median \pm SD of three independent measurements. Control vs. 2.5 %; 5 % and 10 % TNPs: ** $p < 0.001$; 2.5 % TNPs vs. 5 % TNPs: * $p < 0.001$; 2.5 % TNPs vs. 10 % TNPs: § $p < 0.001$; 5 % TNPs vs. 2.5 % TNPs: ◇ $p < 0.001$; 5 % TNPs vs. 10 % TNPs: ● $p < 0.001$; 10 % TNPs vs. 2.5 % TNPs: † $p < 0.001$; 10 % TNPs vs. 5 % TNPs: ‡ $p < 0.001$. Student's-*t*-test and One-Way ANOVA.

Figure 3.13 shows the hydrodynamic diameter of functionalised nanoparticles determined by dynamic light scattering (DLS) and differential centrifugation sedimentation (CPS). Particle size analysis by CPS produced consistently lower diameters for all nanoparticle systems when compared with DLS. This was in agreement with observations reported by Elizalde, *et al.*, for polymeric dispersions [126, 127]. Furthermore, it was possible to verify a consistent difference of 5 nm between the two methodologies for particle size for non-functionalised and

alkyne NPs. For nanosystems containing positive charges a higher difference of 12 nm and 16 nm for 10 % ATNPs NPs was obtained. It is hypothesized that the variations produced by the two methodologies are due to differences in the approaches used by the two techniques to determine the particle size (e.g. particle density). In addition, the higher differences observed for positively charged nanoparticles could be due to the swelling effect, as mentioned above (Section 3.2.2.4) and reported by other groups [59]. The swelling effect appears mainly to be present in samples analysed by DLS.

In sum, the results of particle size characterisation by the two different techniques presented similar results. However, differential centrifugation sedimentation appears to produce higher similarity for the different functionalised systems than DLS, especially for positively charged nanosystems. This difference could be associated with the fact that DLS intensity distributions are highly affected by the presence of even small number of larger particles (therefore, prone to errors). Moreover, CPS allowed a better resolution of smaller particles since it distinguished sizes differing by as little as 2 %. However, it is necessary to note that a good resolution of small particle sizes requires high disk speeds, as the sedimentation velocity increases with the square of particle size diameter (Chapter 2; Section 2.1.1.2). Thus, to acquire a good resolution it would be necessary to involve several hours per sample, which could become problematic due to the issue of background noise.

3.2.3.3 Nanoparticles stability over time: DLS characterisation.

Evaluation of the nanoparticle size over a long period of time was performed by dynamic light scattering. The study was performed for nanoparticles which were stored at -18°C for a period of 10 months. Figure 3.14 shows the comparison

between particle size measured at the time of synthesis and after 10 months of storage at -18°C . In general, the systems presented a monomodal distribution before and after storage. However, a significant difference was seen for amine functionalised NPs and 10 % ATNPs NPs.

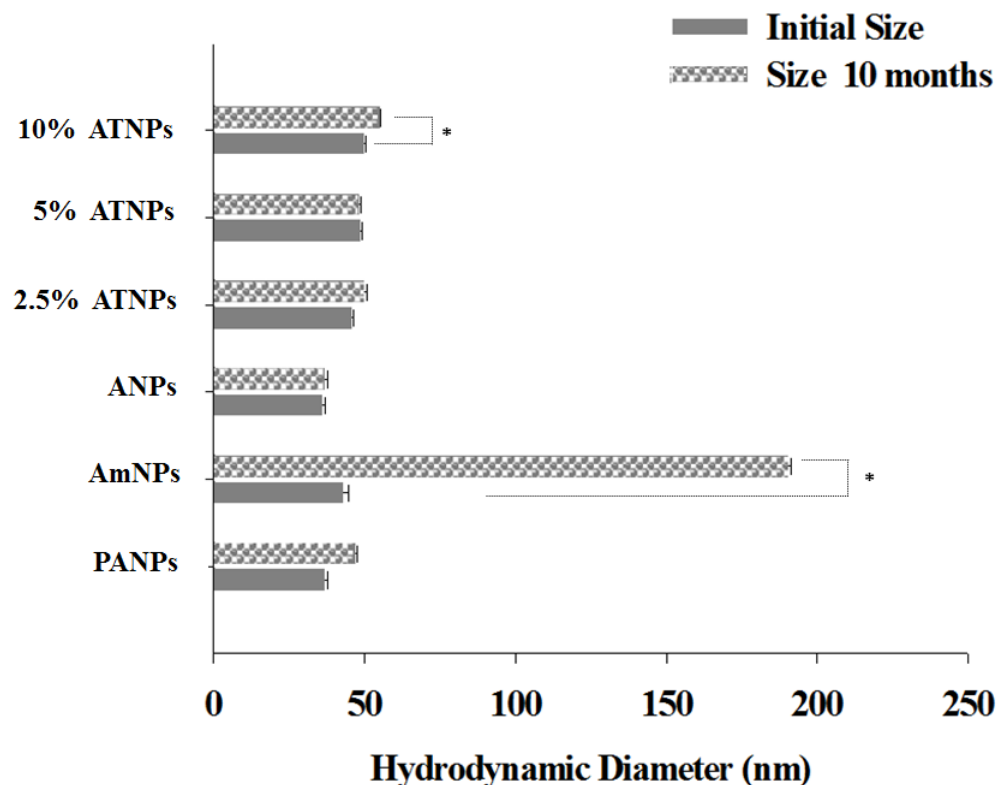


Figure 3.14: Time-dependent size characterisation of polyacrylamide functionalised nanoparticles by DLS. The results were mean \pm SD of three measurements: amino NPs ($t=0$) vs. amino NPs ($t=10$ months):* $p < 0.05$; 10 % TNPs ($t=0$) vs. 10 % TNPs ($t=10$ months):* $p < 0.05$: Student's- t -test.

The amino functionalised nanoparticles exhibited a significant increase in particle size after storage. This was expected and, indeed, particle size increases of amino modified NPs associated with aggregation have previously been reported by others [2, 70, 87, 109, 122, 123]. Moreover, it is important to note that, after storage amino functionalised NPs presented a monomodal distribution, but only an increased polydispersion index ($\text{PDI}=0.475$) was observed. Positively

charged and alkyne functionalised polyacrylamide nanoparticles at low TNPs concentrations (2.5 % ATNPs, 5 % ATNPs) were found to be stable after 10 months of storage without significant variations in hydrodynamic diameter ($p > 0.05$). The 10 % ATNPs modified nanoparticles exhibited an increase 5 nm in particle size, which was found to be statistically significant, though much less obvious than the amino functionalised NPs ($p < 0.05$). It was found that the functionalised nanosystems were stable after a long period of storage with a maximum increase in hydrodynamic diameter of 5 nm.

3.3 Conclusions

For the development of nanoplateforms capable of inducing the generation of ROS in cellular systems, free radical polymerization in reverse microemulsions was used. Polyacrylamide matrix can be used to incorporate chemically reactive functional groups by reacting monomers containing those groups in the free radical polymerization. Chemical tailoring of nanoparticles is important to alter the physicochemical characteristics of the resultant systems. This methodology is frequently used to allow attachment of cargo molecules, but also to control cellular uptake and sub-cellular localszation. In the present research, three types of functionalised nanoplateforms were investigated.

Nanosystems containing amino or alkyne functionalities were investigated to develop stable platforms to further conjugate an ROS generator moiety. Successful tailoring of nanoparticles with amino or alkyne functional groups was investigated by zeta potential analysis. Amino functionality had been previously associated with positive net charge at the surface of the nanoplateforms, thus was easily confirmed by zeta potential. On the other hand, alkyne chemical modifications were more challenging to determine owing to the fact that this functionality originates a slight negative charge, as observed for non-functionalised nanoparticles. Dynamic light scattering and differential centrifugation were used to investigate the diameter of the resultant nanosystems. Size analysis of the resultant nanosystems presented very promising results; DLS data have shown nanoplateforms with hydrodynamic diameters of 49 (amino groups) and 36 (alkyne groups) nm, values compatible with biological applications (cellular uptake <100

nm). Further studies on the functionalised nanosystems stability indicated that amino tailoring was limiting for further studies, size increase over time indicated that this approach shows aggregation over time. Mainly, it was found that dispersion of these nanoparticles was only possible immediately after synthesis. As for alkyne functionalised systems, great stability over time was found with no size alterations even after 10 months storage. Alkyne functionalised nanoparticles were promising approaches for conjugation.

The cellular uptake of polyacrylamide nanoparticles has previously been reported as inefficient and, several approaches have been demonstrated (e.g. gene gun, microinjection) to overcome this. Lately, physicochemical engineering of the nanoparticle surface has been reported effective for facilitated uptake. The presence of positive surface charge was previously reported to facilitate uptake by conferring interaction between nanoparticles and biological membranes. Trimethyl ammonium functional groups have been previously applied to confer positive charge to polyacrylamide nanoparticles. This approach was developed in this project to produce a dually functionalised nanosystem, a trimethyl ammonium functionality to facilitate uptake and alkyne functionality for cargo molecules conjugation. This methodology allowed the development of three types of nanosystems and, size analysis confirmed the stability of these nanosystems with diameters between 46 and 50 nm, even after 10 months of storage. As for net surface charge, values between +13 and +20 (mV) were achieved, representing very promising approaches for the ongoing work.

The major limitations of the present work was to verify the presence of alkyne functionalities, future work will be developed to confirm the presence of such functional group. In general, the present research allowed the development of stable functionalised nanoplateforms with favorable physicochemical characteristics and for the development of ROS generating nanosystems.

Chapter 4

Development of Porphyrin

Polyacrylamide Nanoparticle

Systems.

4.1 Introduction

The advances in nanoparticle engineering have led to the creation of versatile tools with multiple applications in biomedical therapeutic/diagnostic research, as well as the study of biological processes and interactions. These advances were based on transformations of the nanoparticle interface to accommodate surface chemically reactive moieties that provide proper linkage of biomolecules under physiological conditions [47, 128, 129].

There are several important points to consider when designing a conjugation reaction, the most important being that: the process of conjugation should not

affect the activity of the molecule or interfere with nanoparticle functionality. A more challenging requirement control, over the number of linkage sites available for the molecules binding. The conjugation reaction should proceed under mild conditions and not be subject to competing reactions (e.g. hydrolysis) [129].

The development of conjugates that obey the characteristics cited above led to the development of several coupling mechanisms. Figure 4.1 shows some examples of the most common.

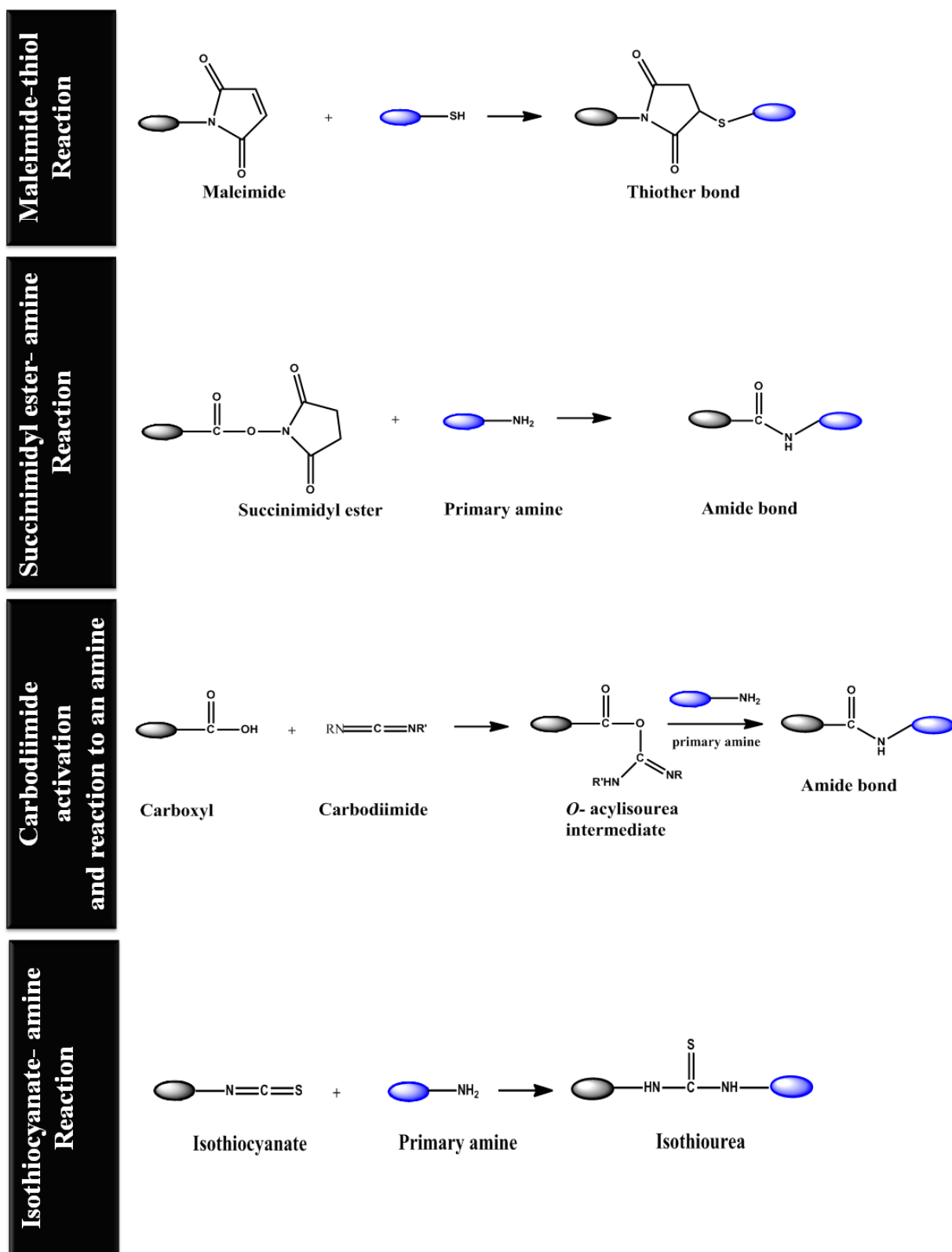


Figure 4.1: Common coupling mechanisms used for conjugation.

4.1.1 “Click chemistry”

In 2001 Torne and Meldal first introduced the concept of “click chemistry”, otherwise known as the Huisgen 1,3-dipolar cycloaddition reaction of organic azides and alkynes (CuAAC) [130]. Click reactions were defined as “... powerful, highly reliable and selective reactions for the synthesis of new compounds...” [130]. In the context of Huisgen 1,3-dipolar cycloaddition, the alkyne/azide is a metal-catalysed variant between C-C triple and C-N triple bonds [130,131]. This reaction leads to the formation of 1,2,3- triazoles. The attractiveness of Cu (I) catalysed reactions is the fact that they are very robust, regioselective, of wide scope, insensitive to solvent, can be performed at room temperatures, and produce, very high yields [130–132]. It is also worth noting that the triazole formed is chemically stable and inert to reactive conditions (e.g. oxidation, reduction, hydrolysis, etc) [87,130–136].

4.1.1.1 The mechanism of Alkyne-Azide CuAAC.

Briefly, the mechanism of alkyne/azide CuAAC, Figure 4.2, is initiated by the π complexation of a CuI dimer to the alkyne, which lowers the pka of the terminal alkyne (Fig. 4.2 (1)). According to Sonogashira coupling, CuI can be directly inserted in alkynes [133,137].

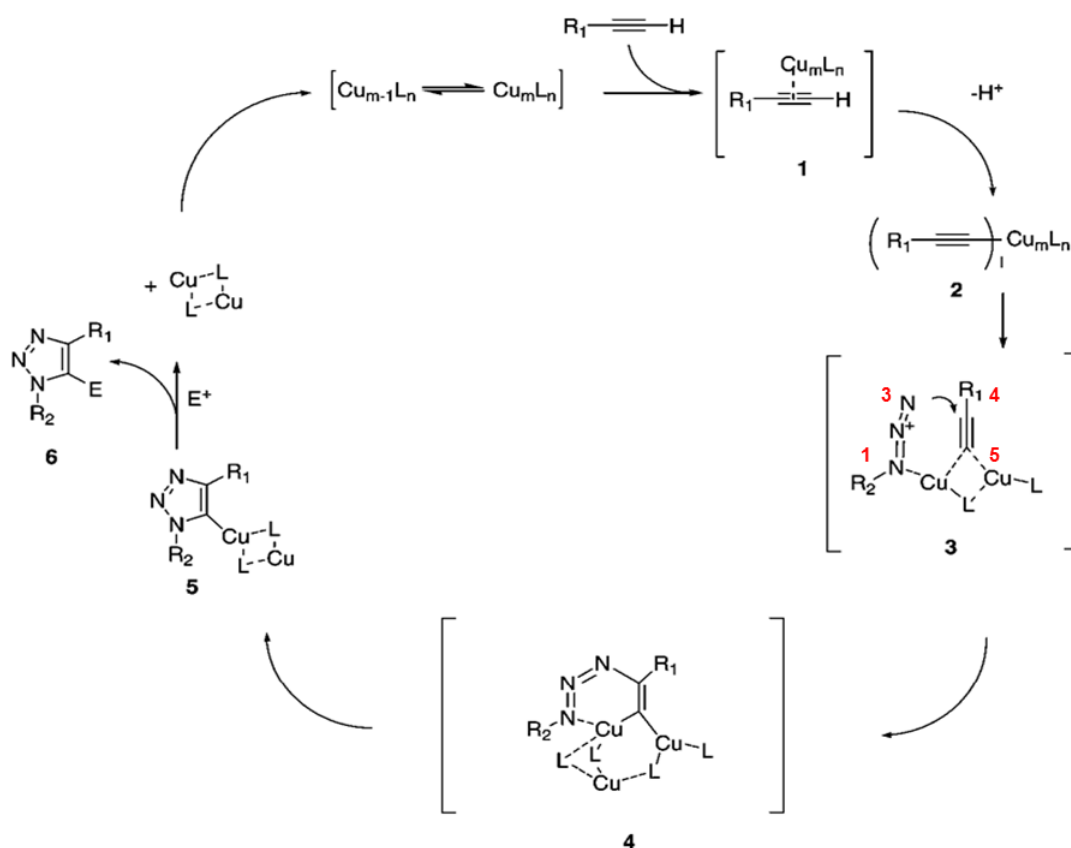


Figure 4.2: Click chemistry: accepted mechanisms for Cu(I) catalysed reaction between azides and terminal alkynes. Adapted from [130]

A deprotonation of the terminal hydrogen leads to the formation of the Cu-acetylide complex (Fig. 4.2 (2)). Thereafter, one of the ligands is displaced by N (1) in the Cu-acetylide complex forming (3). Subsequently, the azide reacts with C(5) through nucleophilic attack. On the other hand, proximity and electronic factors favours the attack to C (4), forming a metalocycle (Fig. 4.2 (4)). Thereafter, due to the contraction of the metalocycle, as consequence of a lone pair of electrons, N (1) attacks C (5) with the release of the triazole (Fig. 4.2 (5)). The ligand denoted by (**L**) can be represented by a variety of compounds, in the case of CuBr, the ligand is bromide.

4.1.1.2 Sources of Cu(I).

Several conditions have been established to achieve the active catalyst for cycloaddition reactions. The most popular approach is the reduction of Cu^{II} salts *in situ* to form Cu^I (e.g. CuSO₄ · 5H₂O) mediated by a reducing agent (e.g. sodium ascorbate). This methodology brings several advantages; low cost, aqueous conditions, does not require an inert atmosphere. The main disadvantage is that the reducing agent might convert Cu^{II} to Cu⁰; however, this can be resolved by the use of an appropriate ratio of the reducing agent [130, 131, 133].

Another methodology is the use of Cu^I salts which does not require the use of a reducing agent. However, it is important to protect the Cu^I from oxidation when in contact with oxygen; thus, an inert atmosphere is normally required when using this catalyst source. In addition, tetravalent ligands, such as (tris-(benzyl-triazolylmethyl)amine) (TBTA) [21, 138], triethylamine hydrochloride [139], and sulfonated bathopenantrolone [140], were also found to confer protection of Cu^I against oxidation and increase the reaction efficiency [130–133].

Aims

The purpose of the present chapter was the development and characterization of stable nanoconjugates through the linkage between ROS generator moiety (porphyrins) and functionalised nanosystems as developed in Chapter 3. The efficient attachment between NPs and porphyrins was studied by several methods; the focus is to ensure only the linkage between the two portions and the absence of physical adsorption. The present research also aimed to investigate the impact of conjugation on the characteristic profile of metal complexes of porphyrins. Furthermore,

the physicochemical characteristics of the resultant porphyrin-nanosystems were evaluated to ascertain compatibility with biological applications.

4.2 Results and Discussion

One of the main challenges in the conjugation of nanoparticles with biomolecules is the quantification of the number of ligands attached to the NP and where they are attached. For this reason is difficult to achieve uniform distribution of molecules conjugated at the surface of the nanoparticles. For the development of the present project it was necessary to ensure that the amount of porphyrin coupled with nanoparticles would be enough to promote a photosensitizing effect. Therefore, several conjugation reactions were investigated and optimized to attain maximal porphyrin conjugation whilst maintaining a stable system.

4.2.1 Spectroscopic characterisation of porphyrins

The fluorescent emission spectrum of porphyrins has been widely reported to be sensitive to metallation, dimerization and hydrolysis [141,142]. In order to anticipate any alterations resulting from the coupling reactions, spectroscopic characterisation of porphyrins was performed. Figure 4.3 shows the absorption spectras of five porphyrins that were used for conjugation with functionalised nanoparticles, (for the sake of simplicity, the porphyrins used are labelled according to their metal centre and functional group).

Metallated porphyrins, ZnPNCS (**XII**) and ZnPN₃ (**XIII**), exhibit a maximum (soret band) at 435 nm and two Q-bands of less intensity at 565 nm and 610 nm (**F**), characteristic of zinc metalloporphyrins. Similarly, for ZnPMA (**XIV**), the same pattern of absorption is observed; however, a red shift (4 nm) is seen for the soret band. Copper metallated porphyrins present a maximum at 425 nm (Soret band); however, in terms of Q-band, only one is distinguishable by its absorption

spectra 555 nm. For the corresponding porphyrin free base (i.e. non metallated (**X**)), the solet band at 420 nm and 4 maxima of lower energy transitions (Q bands) are evident. The resultant spectra are a consequence of the highly conjugated skeleton of porphyrins showing maximums of absorption (solet band) between 420- 439 nm resulting from ground state to the second excited state ($S_0 \rightarrow S_2$) transitions.

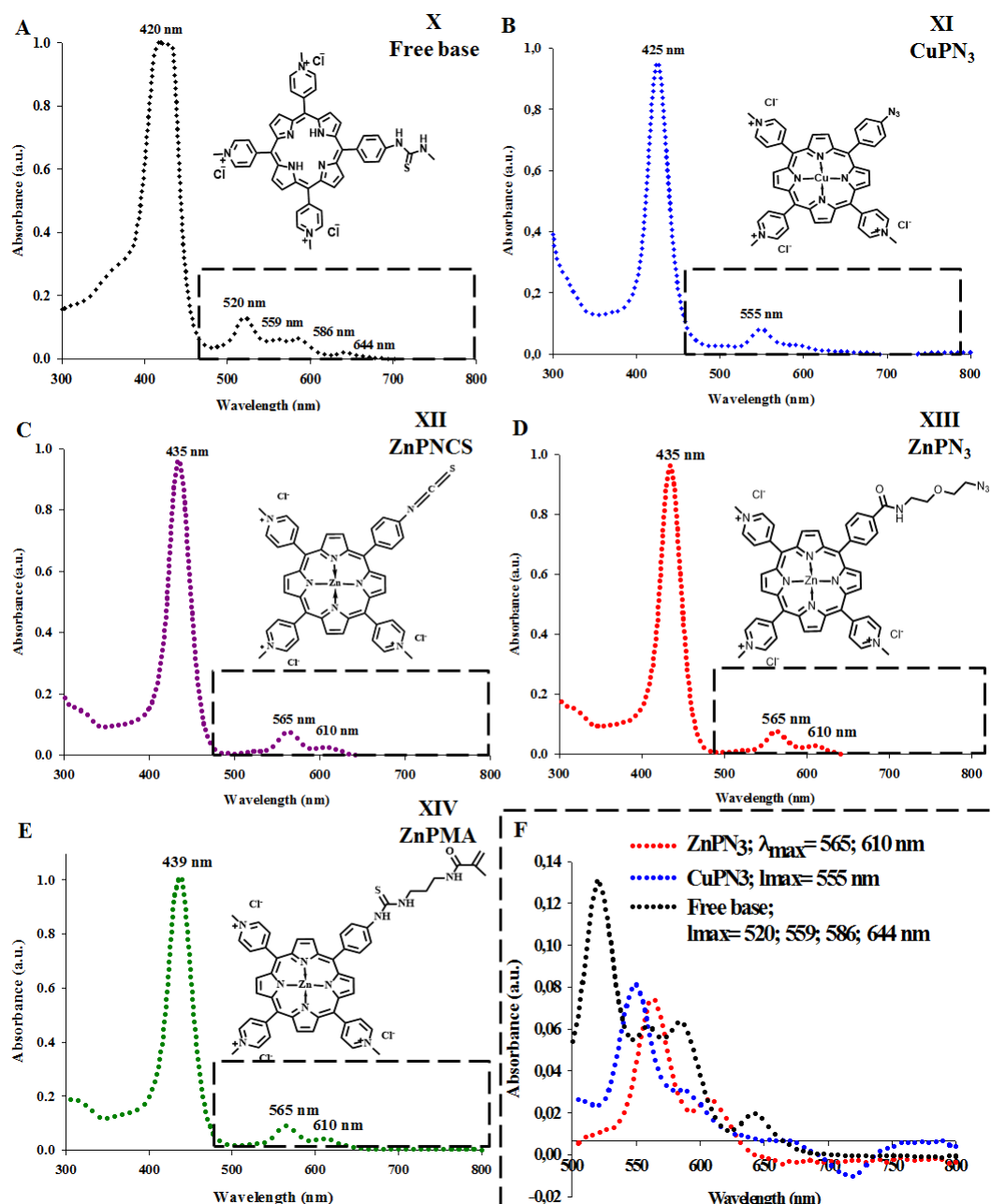


Figure 4.3: Absorption spectra of porphyrins in dH₂O: (A)- 5-(4-isothiocyanatophenyl)-10,15,20-(4-N-methylpyridiniumyl) porphyrin trichloride (X-free base); (B)- 5-(4-azidophenyl)-10,15,20-tris-[(4-N-methylpyridiniumyl)] porphyrinato copper(II)trichloride (XI- CuPN₃); (C)- 5-(4-isothiocyanatophenyl)-10,15,20-tris-[(4-N-methylpyridiniumyl)] porphyrinato zinc(II)trichloride (XII- ZnPNCS); (D)- 5-[4-[2-(azidoethoxy)ethyl]phenyl]-10,15,20-tris-[(4-methylpyridiniumyl)] porphyrinato zinc(II)trichloride (XIII- ZnPN₃); (E)- 5-4-(3-(3-methylthioureido)propyl methacrylamide)phenyl)-10,15,20-tris-[(4-methylpyridiniumyl)]porphyrinato zinc(II) trichloride (XIV- ZnPMA); (F)- detailed absorbance spectra for Q- bands regions (500-650 nm) of ZnPN₃; CuPN₃ and ZnPNCS.

Subsequently, the lower intensity bands (Q-bands) result from weak transitions to the first excited state, ($S_0 \rightarrow S_1$) [143]. The different pattern between Q- bands

of the free base (**F**) and metallated porphyrins were previously reported and result from different vibrational components of the same electronic transition (x and y , 2 for each). However, for zinc metalloporphyrins, the presence of the metal ion in the macrocycle cavity leads to a higher rigidity of the porphyrin ring structure and, consequently, its symmetry. Therefore, the dipole transitions along x and y are of now of identical energy, which results in an overlap reducing the number of Q bands from four to two [143,144].

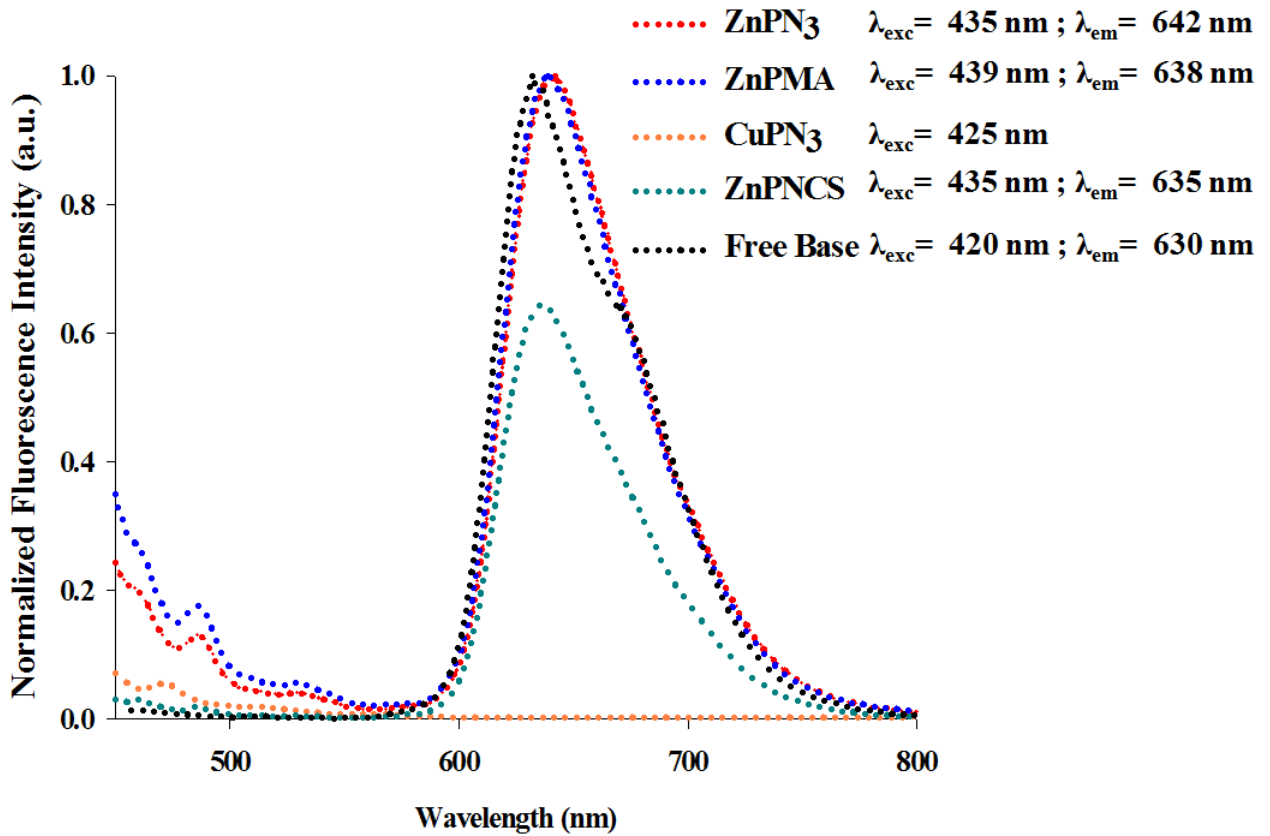


Figure 4.4: Emission spectra of porphyrins.

4.2.2 Development of porphyrin polyacrylamide systems *via* amino-isothiocyanate conjugation.

4.2.2.1 Optimisation of conjugation reaction conditions.

In chapter 3, the synthesis of amino functionalised nanoplateforms was described and characterised. This procedure allowed the creation of a nanosystem which carries an exposed amino group, firstly identified by its characteristic positive surface net charge. Subsequent identification of these chemically reactive moieties in nanoparticles was confirmed by the use of fluorescence analysis. Fluorescamine (Figure 4.5 (1)) is a highly reactive heterocyclic dione which is characteristically non-fluorescent; however, it becomes fluorescent when it reacts with primary amines. Fluorescamine (4-phenylspiro-[furan-2(3H),1-phthalan]-3,3'-dione) has previously been reported for the labelling of proteins, peptides, amino acids and primary amines [145–147].

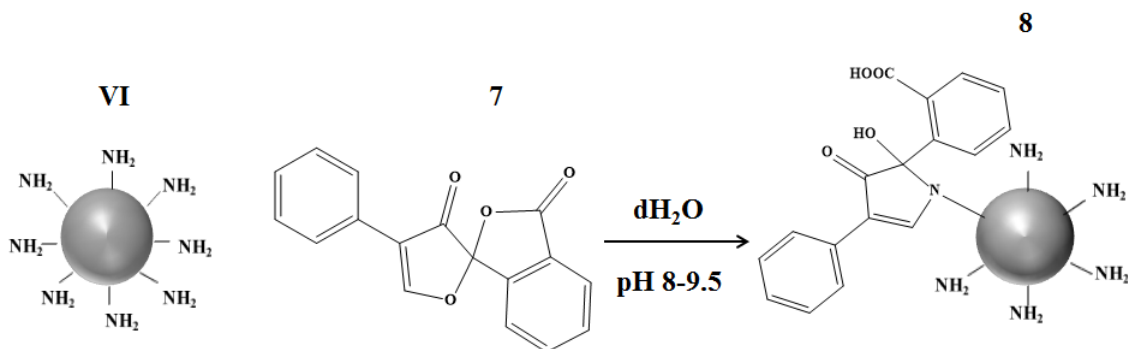


Figure 4.5: Mechanism of reaction fluorescamine with amino functionalised nanoparticles. (VI)- amino functionalised nanoparticles; (7)- fluorescamine; (8)- conjugates with fluorescamine ligand (fluorescent form).

The addition of this reagent (Figure 4.5 (7)) to amino functionalised nanoparticles (VI) led to an activated form of fluorescamine as a consequence of its reaction with the amino functionalisation present at the nanoparticles interface,

thus conferring a methodology for the identification of these functional groups. This was confirmed by measuring the fluorescence spectrum of activated fluorescamine ($\lambda_{\text{exc}} = 390 \text{ nm}$; $\lambda_{\text{em}} = 465\text{-}475 \text{ nm}$).

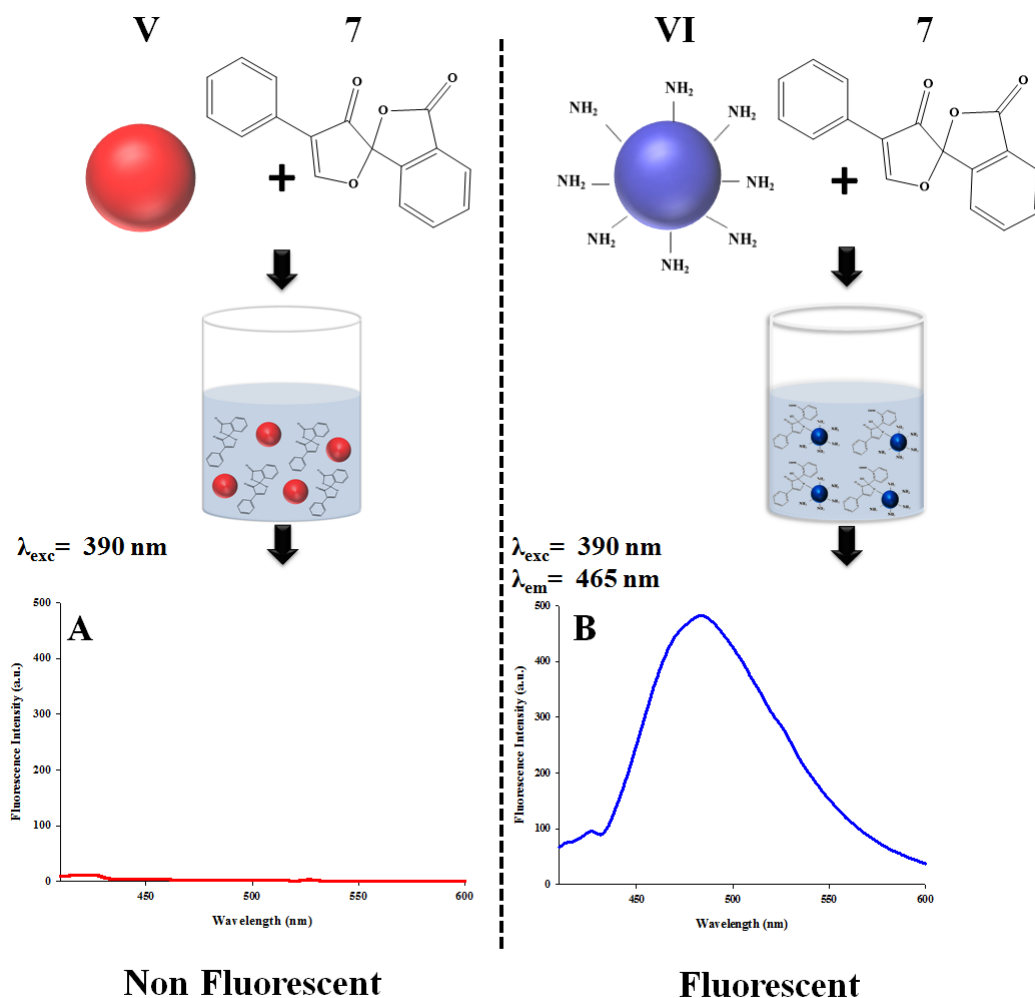


Figure 4.6: Emission spectrum of amino and non- functionalised nanoparticles upon reaction with fluorescamine. Non- functionalised NPs (**V**) were reacted with fluorescamine (**7**) in aqueous conditions. In parallel, amino functionalised NPs (**VI**) were also incubated with fluorescamine(**7**). The emission spectrum of amino and non-functionalised NPs upon reaction with fluorescamine was collected. (**A**)- fluorescamine reacted with non-functionalised NPs did not show any fluorescence (red plot); (**B**)- fluorescamine-amino NPs showed fluorescence at 465 nm (blue plot). $\lambda_{\text{exc}} = 390 \text{ nm}$; $\lambda_{\text{em}} = 465\text{-}475 \text{ nm}$.

Figure 4.6 shows the schematic representation of the experiment performed to identify the presence of amino functionalisations in polyacrylamide nanoparticles. It is important to note that the evaluation of fluorescamine reactivity was made

directly for both samples without any purification process prior to fluorescence analysis. Therefore, as expected, the complete absence of fluorescence was observed for non-functionalised nanoparticles (**V**) incubated with fluorescamine (**7**), due to the lack of primary amino groups. Furthermore, for amino functionalised nanoparticles (**VI**) the presence of fluorescence was observed, which suggests successful introduction of this functionality to the nanoparticles.

4.2.2.2 Spectroscopic characterisation of NP-porphyrin conjugates.

4.2.2.2.1 Capped porphyrin-nanoparticle conjugates (XVI- Zn-PCNPC). Amino functionalised polyacrylamide nanoparticles were previously reported to be prone to aggregation with a very short lifetime, ≤ 1 week. Moore, *et al.* suggested that the reaction between *N*-(3-aminopropyl) methacrylamide and unreacted *N,N'*-methylene bisacrylamide was the mechanism responsible for aggregation of amino functionalised nanosystems [109]. In the development of porphyrin polyacrylamide systems *via* amino-isothiocyanate (ZnPNPC) conjugation, Josefsen, *et al.* reported diameters of 195 nm, suggesting aggregation; it was reasoned that unreacted amino groups would lead to aggregation [2]. In order to overcome this, a protocol was developed where the amino groups were inactivated by reaction with acetic anhydride after porphyrin conjugation. Figure 4.8, schematically shows the reaction of capping amino functionalised nanoparticles with acetic anhydride [129, 148].

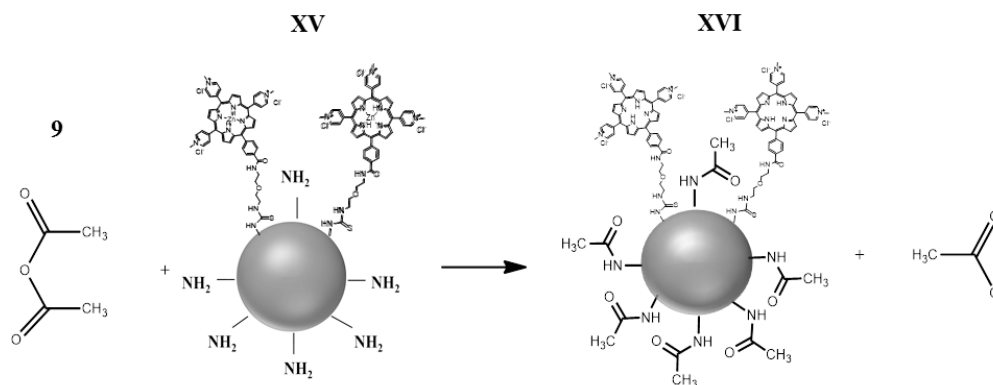


Figure 4.7: Reaction of porphyrin-amino nanoparticles with acetic anhydride. Acetic anhydride (**9**) was reacted with porphyrin-amino nanoparticle conjugates (**XV**)

In order to investigate whether it was possible to block off amino groups at the surface of polyacrylamide nanoparticles, the compound fluorescamine, was used, as referred to in Section 4.2.2.1. To ensure the full capping of amino groups, an excess of acetic anhydride was used. Figure 4.8 shows the fluorescence emission spectra of capped polyacrylamide nanoparticles.

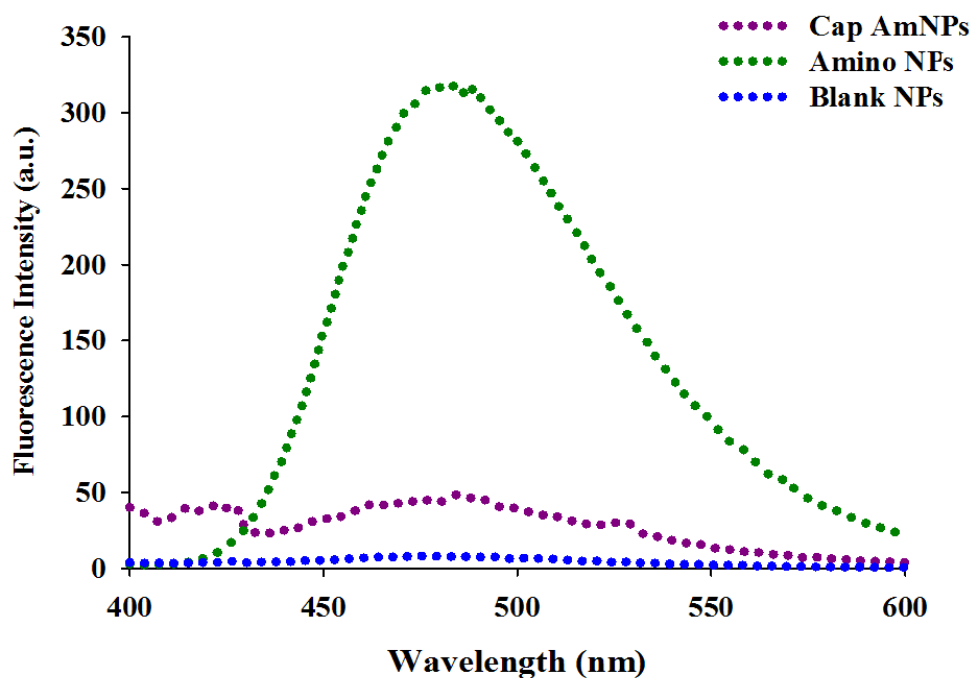


Figure 4.8: Emission spectra of porphyrin-amino nanoparticles upon reaction with fluorescamine.

It can be observed that fluorescamine fluorescence ($\lambda_{\text{exc}} = 390 \text{ nm}$; $\lambda_{\text{em}} = 465\text{--}475 \text{ nm}$) in NPs had amino functionality (green dotted line) whilst particles without amino functionality (PANPs, blank blue dotted line) did not show any fluorescence. In addition, for capped amino NPs a low fluorescence was observed (purple dotted line), suggesting that the cap of amino groups was not complete.

4.2.2.2.2 Porphyrin nanoparticles (XVII-ZnPNPs) Once it was established that it was not possible to completely block reactive amino groups on nanoparticles, a porphyrin monomer with a reactive acrylamide was developed. This approach involved the reaction of the monomer *N*-(3-aminopropyl)methacrylamide with isothiocyanate porphyrins, as shown in Figure 4.9.

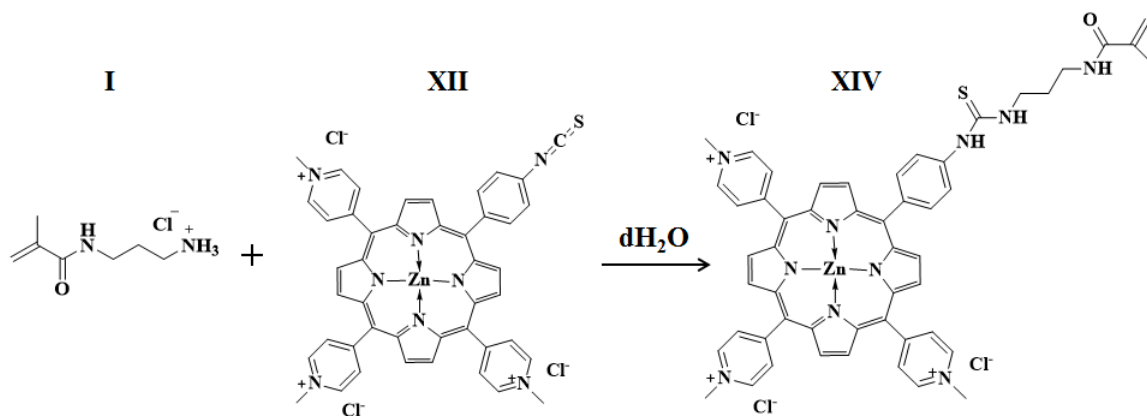


Figure 4.9: Synthetic scheme to afford 5-4-(3-(3-methylthioureido)propyl methacrylamide)phenyl)-10,15,20-tris-[(4-methylpyridinium)yl] porphyrinato zinc(II) trichloride (APMAP).

For this approach, the monomer was directly incorporated into the matrix of nanoparticles, thereby avoiding the presence of unreacted amino groups that facilitate aggregation. Therefore, an excess of ZnPNCS (**XII**) was reacted with the monomer *N*-(3-aminopropyl)methacrylamide hydrochloride (**I**). The excess of porphyrin aimed to exclude the presence of unreacted amino groups, which also avoided time consuming purifications as it is a very straightforward reaction without by-products. The reaction produced the porphyrin ZnPMA (**XIV**) characterised in Section 4.2.1. Therefore, any unreacted porphyrin would be collected after nanoparticles synthesis, along with the washing/purification step. Figure 4.10 shows the absorption and emission spectra of porphyrin-nanoparticles (**XVII**-ZnPNPs).

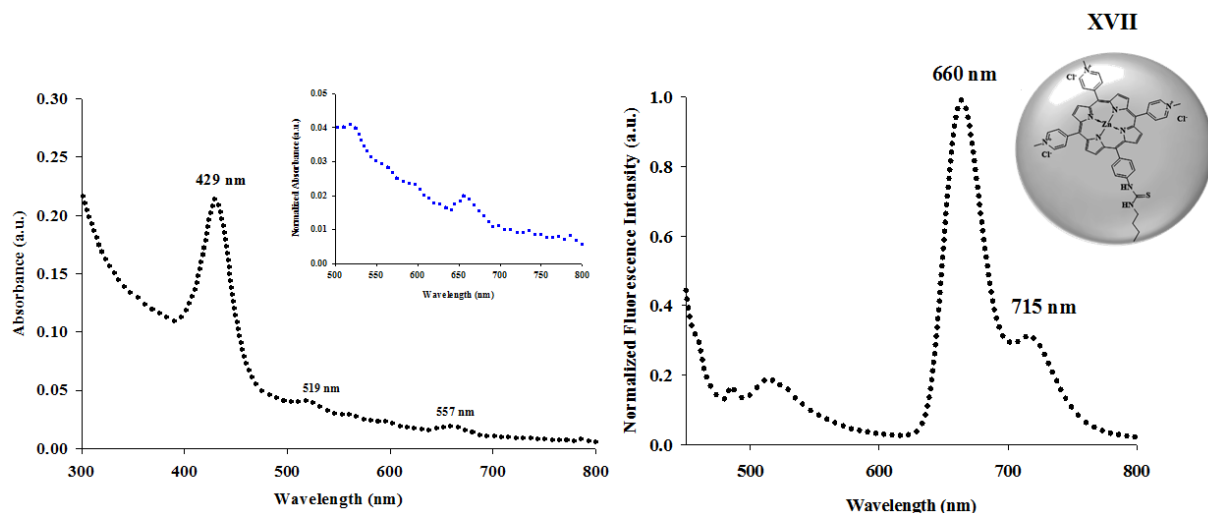


Figure 4.10: Absorption and emission spectra of ZnPNP (**XVII**).

It is possible to identify an absorption emission spectrum characteristic of free base porphyrin when compared to that in Section 4.2.1. Although, it verified changes in the absorption pattern, red shifted (4 nm) in relation to the soret-band and blue shifted in relation to the Q-bands, these results could have arisen from interactions of the porphyrin and the polyacrylamide matrix, such as entrapment of the porphyrin in the polymeric matrix.

4.2.2.2.3 Porphyrin trimethylammonium nanoparticles (**XVIII**- ZnPT-NPs)

Following the above results, Section 4.2.2.2.2, and knowing the present research aimed to exploit surface charge as a means for nanoparticle facilitated cellular uptake and targeting, NPs with porphyrin (**XIV**- ZnPMA) and trimethyl ammonium functionalities (**II**), were developed. The new nanosystem provided the development of constructs with porphyrin and trimethyl ammonium ligands covalent-linked to the polymeric matrix. Figure 4.11 shows the absorption and emission spectra of porphyrin trimethyl ammonium nanoparticles (ZnPTNP).

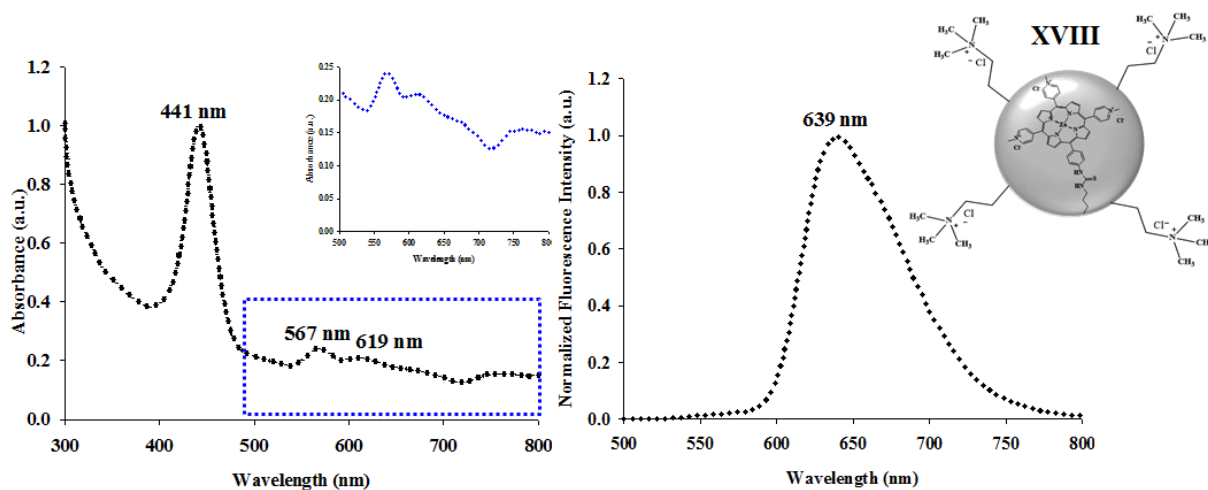


Figure 4.11: Absorption and emission spectra of ZnPTNPs (XVIII).

It is possible to identify an absorption and emission spectrum characteristic of porphyrin when compared to that in Section 4.2.1 (XIV). Although, it verified changes in the absorption pattern, red shifted in relation to the solet-band and the Q-bands. Once again, the results suggest a possible interaction between the porphyrinic ligand and the polyacrylamide matrix.

4.2.2.3 Size characterisation of porphyrin-NP conjugates.

Particle size of porphyrins-nanoparticle conjugates was investigated by dynamic light scattering (DLS). Figure 4.12 shows the hydrodynamic diameters of the nanosystems developed.

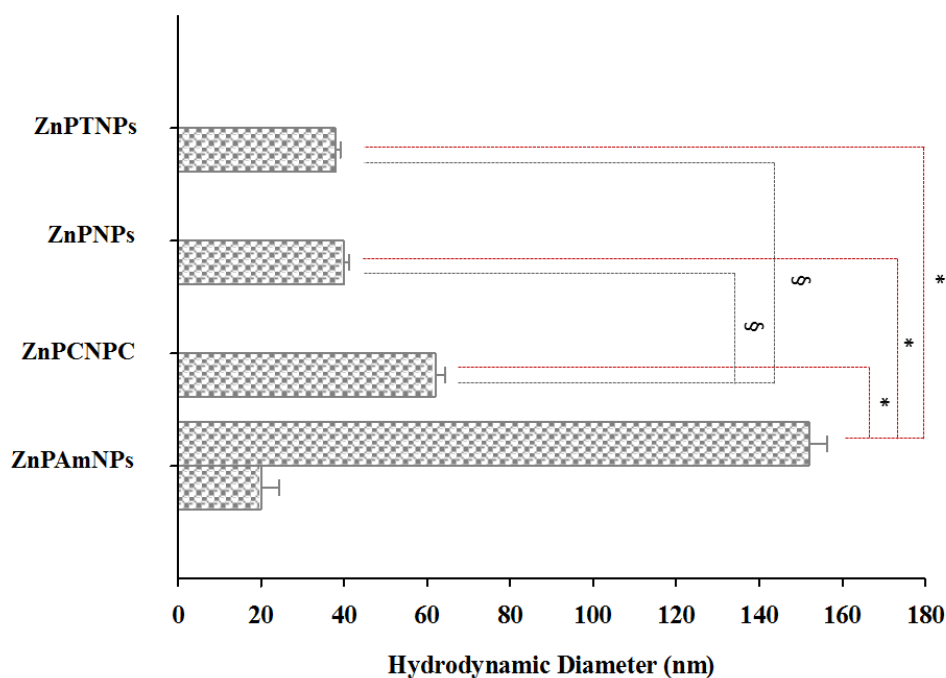


Figure 4.12: Hydrodynamic diameter of porphyrin nanosystems measured by dynamic light scattering. PAmNPC (Figure 4.7; **XV**)- porphyrin nanoparticle conjugates *via* amino functionalisation. ZnPCNPC (**XVI**)- porphyrin nanoparticle conjugates *via* amino functionalisation with unreacted amino groups capped. ZnPNP (**XVII**)- porphyrin functionalised nanoparticles. ZnPTNP (**XVIII**)- porphyrin/ trimethyl ammonium functionalised nanoparticles. The hydrodynamic diameter presented is a result of is an average 3 independent batches \pm SD. ZnPAmNPC vs. ZnPCNPC/ZnPNP/ZnPTNP: * $P < 0.05$; ZnPCNPC vs. ZnPNP/ZnPTNP: § $P < 0.05$ were considered statistically different, all pairwise comparison One way ANOVA.

In general, monomodal distributions were observed for capped porphyrin nanoparticles conjugated *via* amine functionalisation (ZnPCNPC) and for porphyrin (ZnPNP) and porphyrin/trimethylammonium (ZnPTNP) functionalised nanoparticles. In addition, for porphyrin nanoparticles conjugated *via* amino functionalisation, a bimodal distribution was observed. The porphyrin nanosystems attained by conjugation with amino functionalised have shown higher hydrodynamic diameters of $152/20 \pm 4.3$ nm and 62 ± 2.3 nm for PAmNPC and ZnPCNPC, respectively. Furthermore, the hydrodynamic diameter of PAmNPC was significantly ($p < 0.05$) higher than ZnPCNPC, suggesting that amino capping

prevented aggregation of ZnPCNPC. Previously, Josefsen, *et al.* characterised the development of porphyrin-amino nanoparticles (PAmNPC) and found a hydrodynamic diameter of 195 nm for PAmNPC, in agreement with the results presented here [2, 70].

For porphyrin functionalised nanosystems, ZnPNP (38 ± 1.2 nm) and ZnPTNP (40 ± 1.2 nm), independent of the number of functionalisations similar hydrodynamic diameters were observed. The results indicated that using porphyrin monomers avoid aggregation.

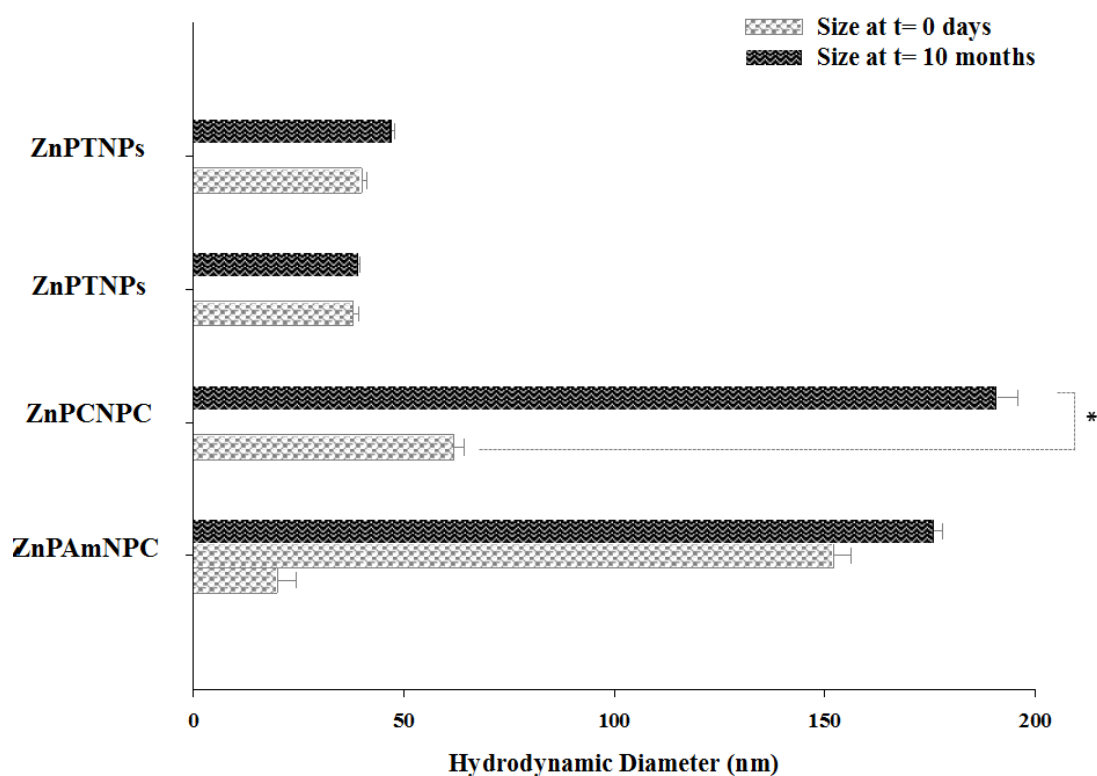


Figure 4.13: Hydrodynamic diameter of porphyrin nanosystems after 10 months of storage at -18° C. measured by dynamic light scattering. PAmNPC- porphyrin nanoparticle conjugates *via* amino functionalisation. ZnPCNPC- porphyrin nanoparticle conjugates *via* amino functionalisation with unreacted amino groups capped. ZnPNP- porphyrin functionalised nanoparticles. ZnPTNP- porphyrin trimethyl ammonium functionalised nanoparticles. The hydrodynamic diameter presented is a result of an average three independent batches \pm SD. PAmNPC vs. ZnPCNPC: * $P < 0.05$ were considered statistically different, all pairwise comparison One way ANOVA.

Further analysis of hydrodynamic diameter after 10 months of storage aimed to evaluate the stability of the nanosystems developed. For PAmNPC, no significant alterations in hydrodynamic diameter ($\text{size}_{10\text{ mo}} 176 \pm 2\text{ nm}$) were found. Surprisingly, ZnPCNPC showed higher significant variations ($p < 0.05$) than the one PAmNPC after 10 months of storage (ZnPCNPC $\text{size}_{10\text{ mo}} 191 \pm 5\text{ nm}$). These results suggest that the incomplete capping of amino groups is not enough to reduce the aggregation of ZnPCNPC. On the other hand, porphyrin functionalised nanosystems, ZnPNP and ZnPTNP, showed high stability after 10 months storage with sizes of $39 \pm 1\text{ nm}$, and $47 \pm 1\text{ nm}$, respectively.

Taken together, the results of porphyrin nanoparticles attained *via* amino conjugation suggested that it was not possible overcome nanoparticle aggregation due to amino functionalisation; however, PCNPC presented a lower diameter at the time of synthesis. The use of porphyrin monomers attached to the polyacrylamide matrix produced systems with considerable lower diameters than the porphyrin conjugates and were highly stable after a long period of storage.

4.2.2.4 Surface characterisation of NP-conjugates.

The porphyrin nanoparticles aimed to attain characteristics that promote passive cellular uptake. In order to characterise the surface charge, zeta potential of the resultant nanosystems was measured. It is important to note that porphyrins as tricataionic molecules contributed with three positive charges each. In addition, unreacted amino functionalities and trimethyl ammonium functionalities also conferred a net positive charge. The analysis of surface charge in the resultant nanosystems is represented in Figure 4.14.

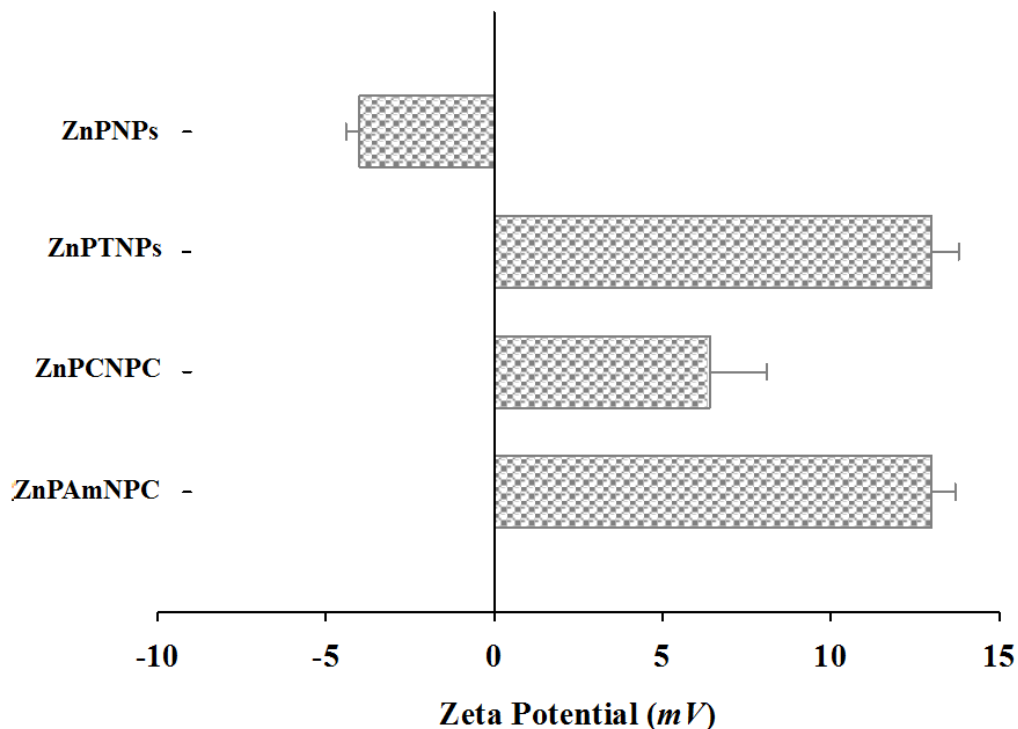


Figure 4.14: Porphyrin nanosystems surface charge characterisation, zeta potential. PAmNPC (Figure 4.7; **XV**)- porphyrin nanoparticle conjugates *via* amino functionalisation. ZnPCNPC- porphyrin nanoparticle conjugates *via* amino functionalisation with unreacted amino groups capped. ZnPNP- porphyrin functionalised nanoparticles. ZnPTNP- porphyrin trimethyl ammonium functionalised nanoparticles. The zeta potentials presented are a result of an average three independent batches \pm SD.

For porphyrin- nanoparticle conjugates, PAmNPC (**XV**) and ZnPCNPC (**XVI**), zeta potentials of $+13 \pm 1$ mV and $+6 \pm 2$ mV were observed. As expected, the capping of unreacted amino functionalisations led to a decrease in surface charge of ZnPCNPC (**XVI**). By contrast, ZnPNP (**XVII**) showed a negative surface charge (-4 ± 1 mV), which, indicates that the functionalization of polyacrylamide NPs with porphyrins monomers results in the entrapment of porphyrin molecules. As porphyrins are tricationic molecules, it was expected to observe positive charge on those nanosystems if these ligands were to be exposed at the surface of the NPs. Furthermore, the surface charge of ZnPNP (**XVII**)

is consistent with non-functionalised polyacrylamide nanoparticles. As expected, functionalization of polyacrylamide NPs with porphyrin and trimethyl ammonium monomers ZnPTNP (**XVIII**) had led to an increase of surface charge to $+13 \pm 1$ mV. Due to the newness of this system, it was not possible to achieve a comparison.

The results obtained suggest that it is possible to synthesize stable porphyrin nanosystems through the use of porphyrin monomer (ZnPNP). In addition, conferring a positive charge was also attained by the incorporation of a trimethyl-ammonium functionality (ZnPTNP). By contrast, conjugation of porphyrins *via* amino functionalities (PAmNPC) was revealed to be inefficient due to aggregation. Capping of unreacted amino groups was not complete, therefore did not allow the control of aggregation of PCNPC.

4.2.3 Development of porphyrin polyacrylamide systems *via* click chemistry methodologies.

In the previous section, the development of porphyrin-nanoparticles through amino functionalisation led to aggregation. Subsequently, it was found that stable nanosystems could be achieved by the use of porphyrin monomers. Although, stable nanosystems were possible to achieve, the porphyrin was found to be entrapped in the polymeric matrix, therefore the photodynamic efficiency of porphyrins could have been compromised. Thus, porphyrin-nanoparticle conjugates were developed through an alkyne functionality, the advantages of which were referred to in the introductory Section 4.1.1. The nanosystem described in this section aimed to attain porphyrin conjugated at the surface of nanoparticles.

4.2.3.1 Optimisation of conjugation click reaction conditions.

As referred to in the introductory section of the present chapter, there are several approaches described in the literature for efficient copper-catalysed triazole formation. These approaches rely on a high concentration and constant presence of copper (I) while the other reaction conditions can be adjusted according to the final aim (e.g. temperature, solvent, etc). From these approaches, a number of possible methodologies have been generated with CuI; CuBr and CuSO₄ being the most popular source of Cu(I) ions. The main difference between these copper salts are that CuI and CuBr are Cu(I) sources that immediately forms Cu-acetylides whereas CuSO₄ is a copper (II) source which requires the presence of a reducing agent to perform the conversion of copper (II) to copper (I) prior to formation of Cu-acetylides. The advantage of using a copper (II) salt is the protection against

oxidation from contact with oxygen. Prior to the establishment of a protocol for copper(I)- Huisgen catalyzed 1,3, cycloaddition an initial evaluation of the impact of the reagents on the hydrogel matrix and final yields was undertaken. In the present study, all three sources (CuI, CuBr and CuSO₄) were investigated by incubation with functionalised nanoparticles in aqueous conditions. For the removal of catalyst excess, upon reaction completion the resultant NPs were purified by gel filtration sephadex (SEC columns, as shown in Figure 4.18). It was found that using CuSO₄ catalyst in the presence of sodium ascorbate as the reducing agent led to an alteration in coloration of the blank polyacrylamide nanoparticles (from white to yellowish), even after purification, the colouration remained and the recovered yield was below 50 %. Although CuSO₄ has been a popular choice for copper-catalysed triazole formation, it was not possible to justify this reagent based on its coloration and yield therefore it was abandoned as a catalyst for further studies. The use of CuI and CuBr, however, induced no alterations when introduced to non-functionalised nanoparticles and the final yields of recovery were found to be, 72 % and 85 % respectively. The effects of CuBr on the whole system in the study were tested and are reported in the final characterisation of the resultant systems.

4.2.3.1.1 Click reaction of NPs with azidocoumarin. Previously, Welser, *et al.* reported the development of alkyne functionalised nanoparticles, whose characterisation by FT-IR at 3300 cm⁻¹ (indication alkyne functionality) was found to be difficult due to the strong absorbance of the polymer backbone [87,114]. In order to show the presence of alkyne groups in alkyne functionalised nanoparticles,

fluorescence analysis was used. Similarly with amino functionalised nanoparticles (Section 4.2.2.1), the introduction of alkyne functionalisation into polyacrylamide nanoparticles was evaluated by an intrinsically non-fluorescent probe that becomes fluorescent upon azide-alkyne reaction, with formation of 1,2,3 triazole product. Sivakumar, *et al.* reported on the ability of 3-azidocoumarin to become fluorescent upon reaction with alkyne moiety mediated by the catalyst copper (I) [85]. Hence, the evaluation of the presence of alkyne functionalisations at the nanoparticle interface was investigated by its reaction with 3- azidocoumarin through CuAAC the reaction of which is represented in Figure 4.15. It is important to note that, as the reaction was performed with a copper (I) catalyst, it was necessary to avoid contamination with oxygen that would lead to oxidation; therefore all reactions were performed with an excess of CuBr and in sealed vials.

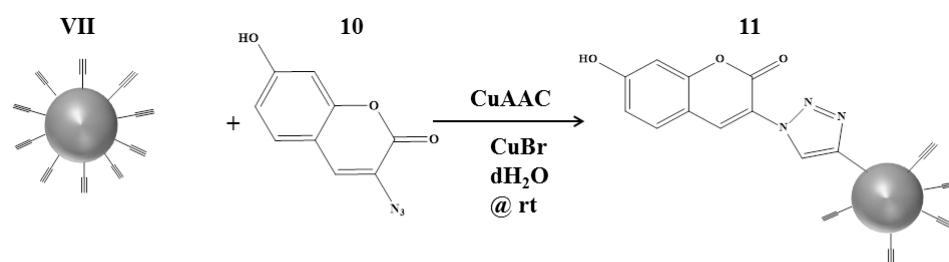


Figure 4.15: Reaction that occurs from incubation of fluorescamine with alkyne functionalised nanoparticles. (VII) alkyne functionalised nanoparticles; (10) 3-azidocoumarin; (11) azidocoumarin-alkyne nanoparticle conjugates.

In order to evaluate the efficiency of the CuAAC between 3-azidocoumarin-alkyne nanoparticles, the emission spectra of the resultant conjugates were analysed, as shown in Figure 4.16.

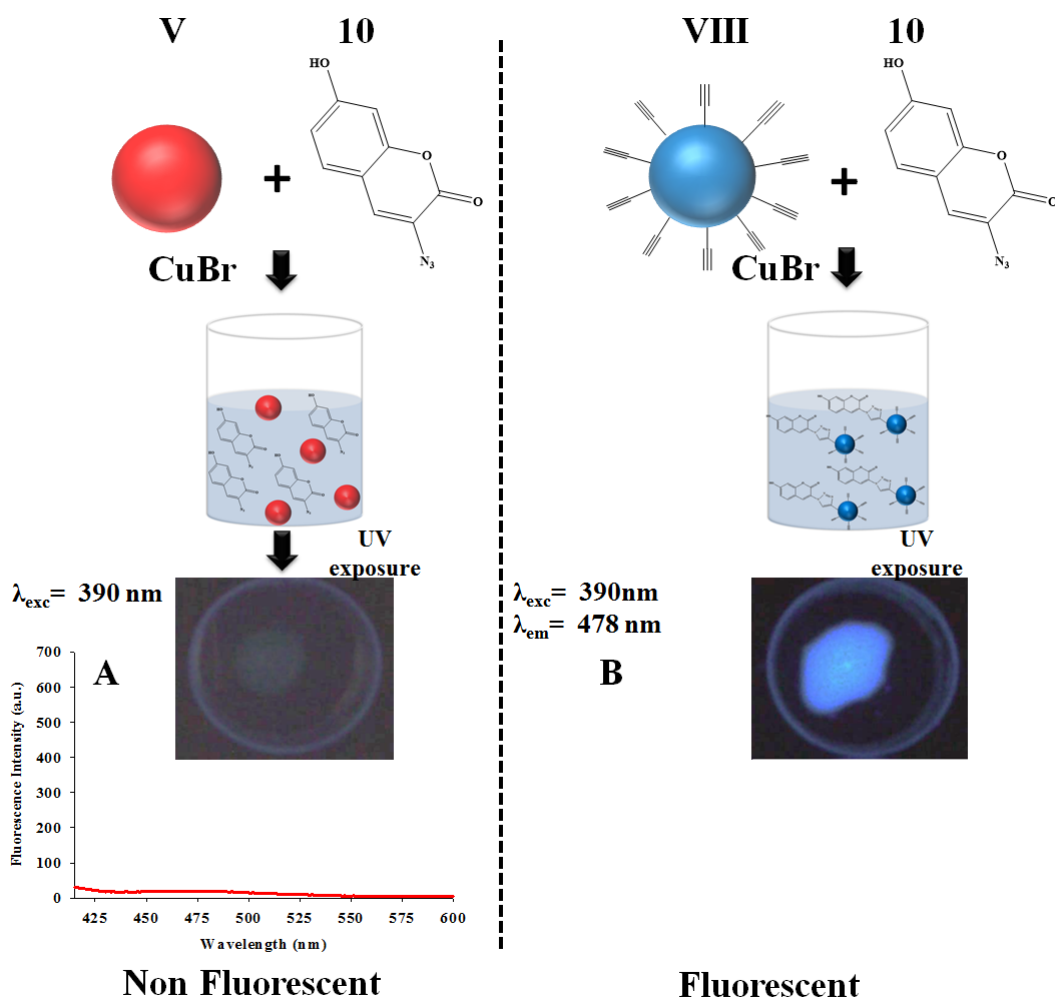


Figure 4.16: Emission spectrum of alkyne and non-functionalised nanoparticles upon reaction with 3- azidocoumarin. Non-functionalised NPs (V) were reacted with 3- azidocoumarin (10) in aqueous conditions. In parallel, alkyne functionalised NPs (VIII) were also incubated with 3- azidocoumarin (10). The emission spectrum of alkyne and non-functionalised NPs upon reaction with 3- azidocoumarin was collected. (A)- fluorescamine reacted with non-functionalised NPs did not show any fluorescence (red plot); (B)- 3-azidocoumarin-amino NPs showed fluorescence at 478 nm (blue plot) which could also be observed under UV light (blue spot). $\lambda_{\text{exc}} = 390 \text{ nm}$; $\lambda_{\text{em}} = 478 \text{ nm}$.

The reaction mixtures correspondent to products (A) and (B) were analysed without any purification. As expected, non-functionalised NPs did not react with 3-azidocoumarin, therefore no fluorescence was observed. The emission spectra

in Figure 4.16 reveals that the reaction product of **(B)** showed a fluorescence maximum at 478 nm, confirming the presence of alkyne groups. In addition, alkyne functionality was also confirmed by the exposure of both suspensions to UV light only the conjugates exhibit a blue colouration **(ii)**. These results clearly demonstrate the presence of alkyne functionalisation and indicate the success of the copper catalysed reactions.

4.2.3.1.2 Effect of copper (I) bromide in the absorption of metallated porphyrins. Once the studies in the present work required the use of metallated porphyrins, it was important to investigate the effect of copper (I) bromide on their absorption spectra. This study aimed to verify whether the copper would become entrapped in the cavity of the macrocycle. The impact of copper bromide on the porphyrinic molecule was investigated by UV-vis spectroscopy. Entrapment of copper ions in the macrocycle cavity results in a blue shift of the solet-band and loss of the Q-band, thus Zinc porphyrin was incubated with CuBr (in the absence of nanoparticles) and evaluated for a period of 20 hours. Figure 4.17 represents the absorption spectra of ZnPN₃ collected at different time points, where it is possible to see the presence of three maxima of absorbance; one stronger correspondent to the solet band at 435 nm and two others of weaker absorption correspondent to the Q-bands at 565 and 610 nm, respectively. Therefore, by comparison with the absorption spectra of ZnPN₃ present in Figure 4.3 (page 117), no changes were observed. The results obtained indicate that the protocol developed for azide-alkyne linkage did not affect the structure of zinc porphyrins.

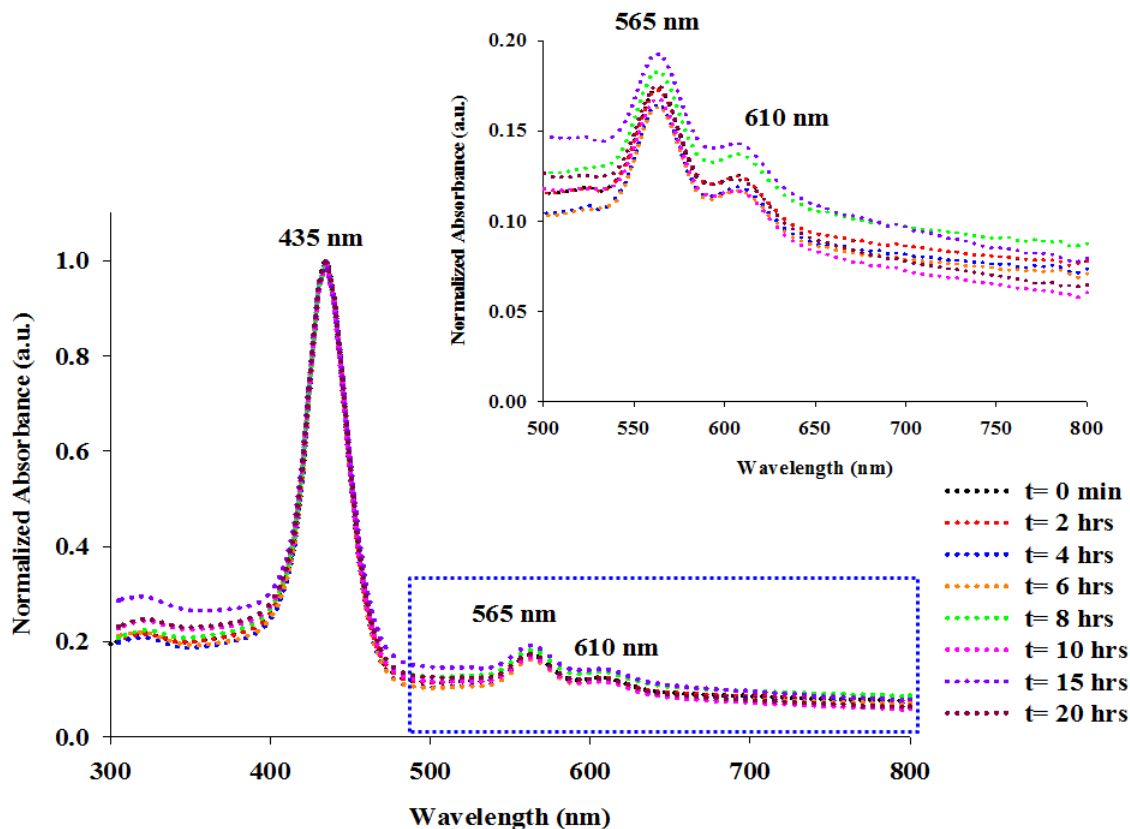


Figure 4.17: Absorption spectra of ZnPN_3 in presence of CuBr along 20 hours of incubation.

Once the optimal reaction conditions for the covalent linkage between azide porphyrins and alkyne polyacrylamide nanoparticles were established, an experiment was carried out to investigate whether any adsorption between the polyacrylamide nanoparticles and the porphyrin was observed. To achieve this, non-functionalised NPs were mixed with porphyrin, followed by the addition of CuBr .

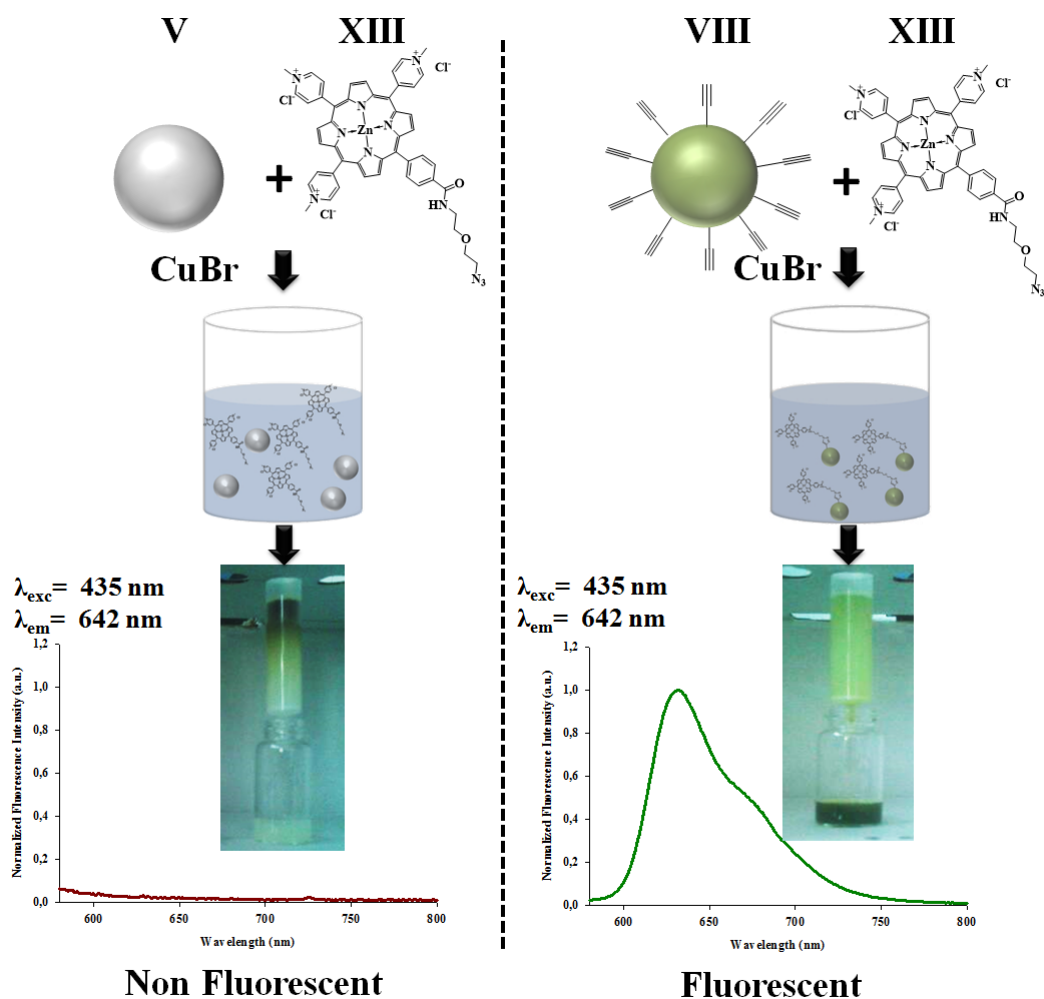


Figure 4.18: Fluorescence characterisation of alkyne modified nanoparticles and its non-functionalised counterparts after CuAAC reaction with ZnPN₃: **(A)**- non-functionalised polyacrylamide nanoparticles after reacting with ZnPN₃; **(B)**- covalent attachment of ZnPN₃ to alkyne modified polyacrylamide nanoparticles. **i**- non-functionalised nanoparticle eluted from a SEC is shown by a translucent suspension of NPs, while porphyrin remained in the top of the column; **ii**- suspension of porphyrin-nanoparticles conjugates eluted from a SEC column is shown by the green colouration of the resultant suspension.

Concurrently, an experiment was run where the porphyrins were mixed with alkyne functionalised nanoparticles. The results are presented in Figure 4.18, where it can be seen that the alkyne functionalised NPs **VIII** exhibit intense colouration indicating efficient conjugation (**B**), shown by the eluted (**ii**) fraction and fluorescence spectra (**B**). In contrast the non-functionalised NPs do not show colouration (**A**; **i**), which was to be expected.

4.2.3.2 Spectroscopic characterisation of NP-porphyrin conjugates.

Upon coupling of alkyne/trimethyl ammonium functionalised nanoparticles with ZnPN₃ it was necessary to evaluate the stability and characteristics of the resultant systems. The effects of porphyrin nanoparticle conjugation were evaluated by differences present in the absorption and emission spectrum of the conjugates.

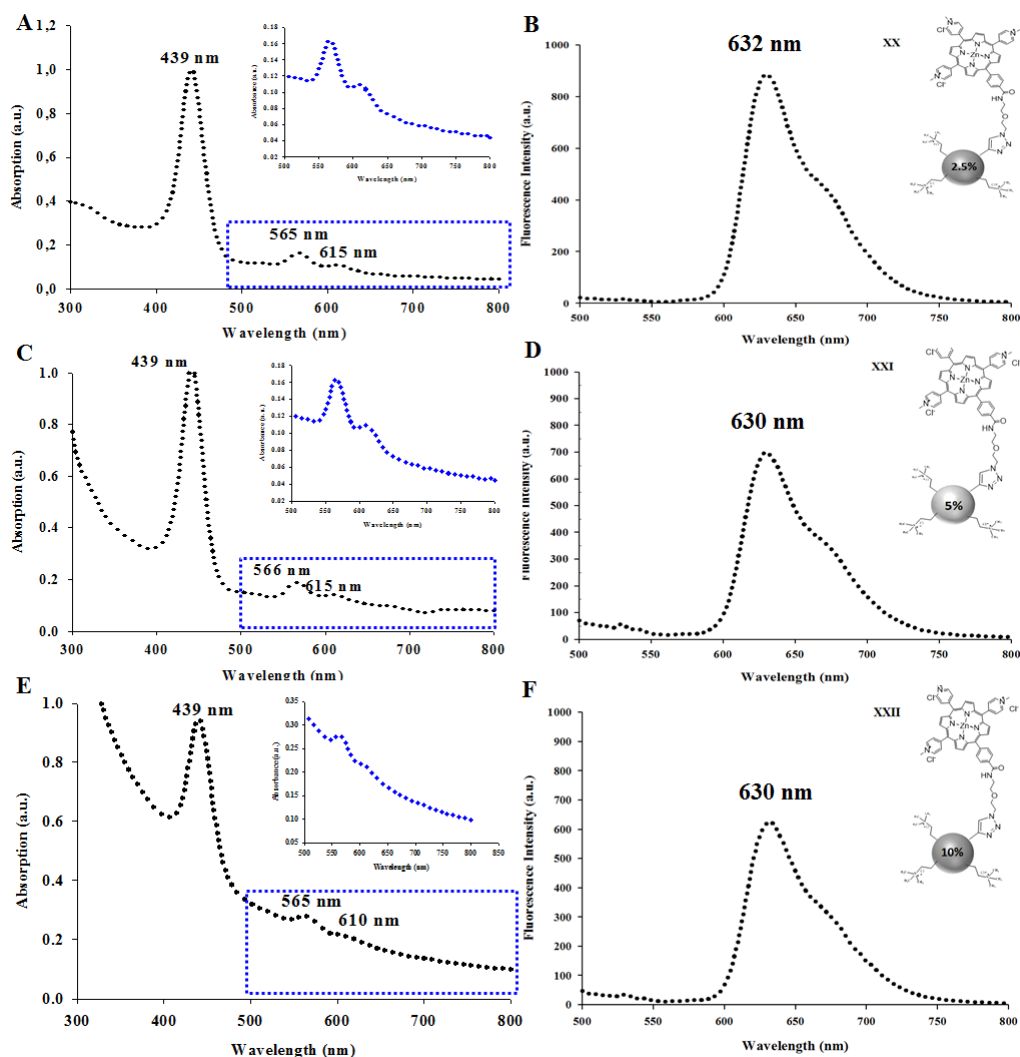


Figure 4.19: Representative absorption and emission spectrum of porphyrin-alkyne/(2.5 %)trimethylammonium nanoparticle conjugates (2.5 % ZnPTNPC). (A) absorption and (B) emission spectra of porphyrin-alkyne nanoparticle conjugates; (C)absorption and (D) emission spectra of porphyrin-alkyne/(5 %)trimethylammonium nanoparticle conjugates (5 % ZnPTNPC); (E) absorption and (F) emission spectrum of porphyrin-alkyne/(10 %)trimethyl ammonium (10 % ZnPTNPC).

In Figure 4.19; the spectrum of the three types of porphyrin-trimethyl am-

monium nanoparticle conjugates are shown. The investigation of ZnPN₃ conjugation with alkyne/trimethylammonium nanoparticles (2.5 %; 5 % and 10 %) showed a characteristic spectra of metalloporphyrins. The results suggest that the conjugation of porphyrins with trimethyl ammonium nanoparticles did not impact on the characteristics of the porphyrins.

4.2.3.3 Size characterisation of NP-porphyrin conjugates.

Porphyrin-alkyne trimethyl ammonium nanoparticle conjugates were characterised by dynamic light scattering. Figure 4.20 shows the hydrodynamic diameters of the resultant conjugates.

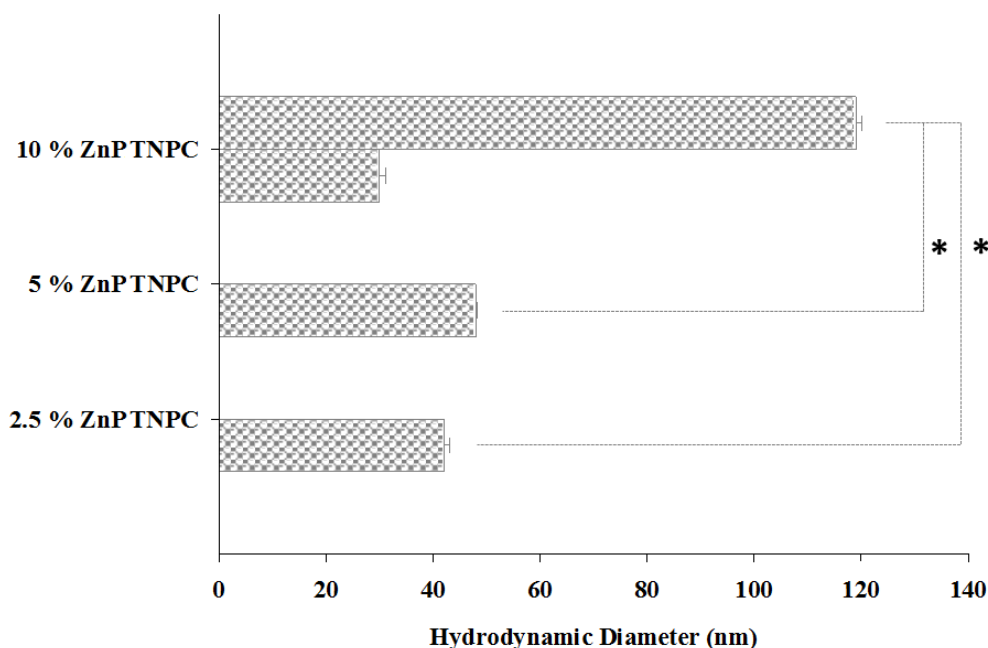


Figure 4.20: Hydrodynamic diameter of porphyrin nanosystems measured by dynamic light scattering. Porphyrin- alkyne/2.5 % trimethylammonium nanoparticle conjugates (2.5 % ZnPTNPC); porphyrin-alkyne/5 % trimethylammonium nanoparticle conjugates (5 % ZnPTNPC); porphyrin-alkyne/10 % trimethyl ammonium (10 % ZnPTNPC). The hydrodynamic diameter presented is a result of is an average three independent batches \pm SD. 10 % ZnPATNPC vs. 2.5 % ZnPATNPC/ 5 % ZnPATNPC: * $P < 0.05$; were considered statistically different, all pairwise comparison One way ANOVA.

The results showed monomodal distributions for 2.5 % and 5 % ZnPATNPC with hydrodynamic diameters of 42 ± 1 nm and 48 ± 1 nm, respectively. The difference in nanoparticle size for these conjugates was not too significant ($p > 0.05$). For 10 % ZnPATNPC, a bimodal distribution was observed with sizes of 30 ± 2 nm and 119 ± 2 nm. These results suggest that surface charge might be involved. Others have previously reported on the size increase of trimethyl ammonium functionalised polyacrylamide nanoparticles noting an increase in nanoparticle size as the trimethyl ammonium functionality increased [59, 124, 149]. Sun, *et al.* found that for 24 % of trimethyl ammonium functionality, 139 nm in hydrodynamic diameter was achieved. This increase was suggested to be associated with a positive charge linked to the polymer matrix, leading to hydrogel swelling as a consequence of increased osmotic pressure [119].

Further analysis on the hydrodynamic diameter after 10 months of storage at -18° C aimed to investigate the stability of the aforementioned nanosystems. Figure 4.21 shows the hydrodynamic diameters.

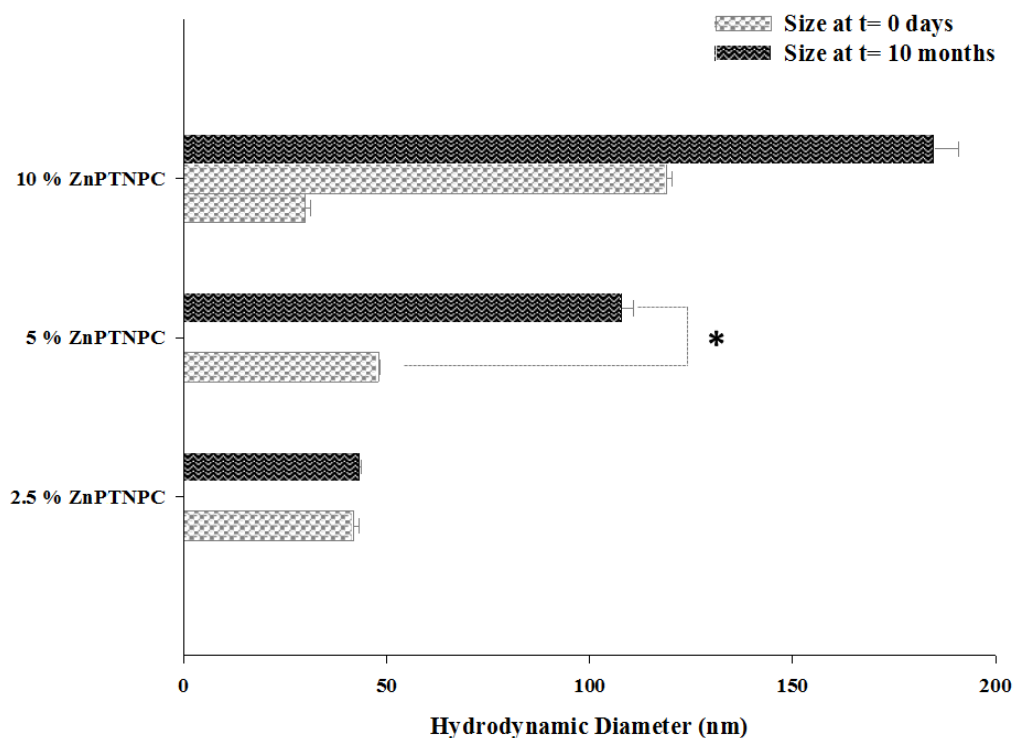


Figure 4.21: Hydrodynamic diameter of porphyrin nanosystems measured by dynamic light scattering after 10 months storage. Porphyrin- alkyne/2.5 % trimethylammonium nanoparticle conjugates (2.5 % ZnPTNPC). Porphyrin- alkyne/5 % trimethylammonium nanoparticle conjugates (5 % ZnPTNPC). Porphyrin- alkyne/10 % trimethyl ammonium (10 % ZnPTNPC). The hydrodynamic diameter presented a result of is an average three independent batches \pm SD. 5% ZnPATNPC (t= 0) vs. 5 % ZnPATNPC (t= 10 mo): * $P < 0.05$; were considered statistically different, all pairwise comparison One way ANOVA.

4.2.3.4 Surface characterisation of NP-conjugates.

Porphyrin alkyne/trimethyl ammonium nanoparticles surface charge were characterised by zeta potential. In order to confer a positive surface coating on nanoparticles, trimethyl ammonium functionalisations and conjugation of tricationic porphyrins were used. These manipulations aimed to produce a nanosystem with characteristics for passive cellular uptake and specific sub cellular co-localisation. Figure 4.22 shows the zeta potential of the nanosystems in study.

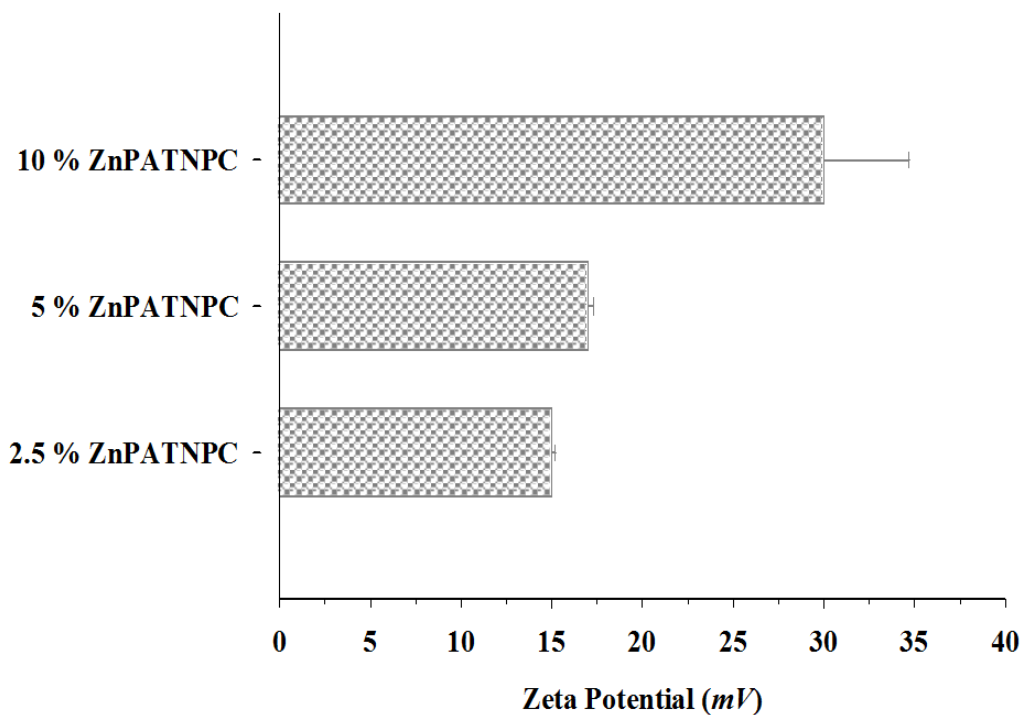


Figure 4.22: Zeta potential characterisation of ZnPATNPC. Porphyrin- alkyne/2.5 % trimethylammonium nanoparticle conjugates (2.5 % ZnPTNPC). Porphyrin- alkyne/5 % trimethylammonium nanoparticle conjugates (5 % ZnPTNPC); porphyrin- alkyne/10 % trimethyl ammonium (10 % ZnPTNPC). .

As expected, an increased trimethyl ammonium functionality led to a higher surface charge. For 2.5 % and 5 % ZnPTNPC, surface charges of $+15 \pm 0.3 \text{ mV}$ and $+17 \pm 0.5 \text{ mV}$ were observed. In addition, for 10 % ZnPTNPC, higher zeta potential value was attained of 30 ± 4.7 . These values showed a slight increase in positive charge when compared with the trimethyl ammonium functionalised nanosystems developed in Chapter 2.1, Section 3.2.3. It is hypothesized that the differences obtained were a result of the positive charge carried by the porphyrin conjugated at the surface of the nanoplatforms.

4.3 Conclusions

The present chapter focused on the development of stable linkage between polyacrylamide nanoparticles and porphyrins for the construction of an ROS generator nanosystem. Conjugation methodologies were exploited to achieve stable monodisperse porphyrin-nanoparticle conjugates compatible with biological systems. Firstly, the effect of linking porphyrins with amino functionalised nanosystems was studied; as expected, these conjugates produced aggregates. This result showed that not even reacting an excess of porphyrin was sufficient to overcome the aggregation patterns of these NPs, as a result of unreacted amino groups. In order to overcome these effects, a cap of unreacted amino groups was investigated; a remarkable lowering size was found. Unfortunately, DLS stability studies of these porphyrin-NPs over time have shown formation of aggregates. Therefore, amino functionalised nanoparticles were abandoned as an approach for porphyrin conjugation.

A new strategy involved the covalent linkage of porphyrin monomers to the polyacrylamide matrix of nanoparticles. This approach was found very attractive and stable, surface charge analysis was consistent with non-functionalised NPs, suggesting porphyrin entrapment in the polymeric matrix. The main limitations of porphyrin entrapped NPs were the unknown photodynamic effects of porphyrin entrapment and the unfavorable surface characteristics. These disadvantages led to the design of two new constructs: the first originated to improve the biological compatibility of porphyrin entrapped NPs conferred by introducing a positive surface charge by a trimethyl ammonium ligand. The resultant nanosystems were shown to be very promising candidates for ROS generating nanoplateforms.

In parallel, a second successful approach was explored by the surface linkage of porphyrins moieties with alkyne/trimethyl ammonium dually functionalised NPs through copper-catalysed triazole formation. This second construct allowed porphyrin surface exposure and conferred great stability over time.

Although many obstacles were found in the development of nanoparticle-porphyrin conjugates, two promising constructs were attained: both contain positive charges compatible with cellular uptake (conferred by trimethyl ammonium functionalities), with a difference in porphyrin location (either entrapped or at the surface).

Chapter 5

Delivery of nanoparticles to human Mesenchymal Stem Cells

5.1 Introduction

The potential of nanotechnology as a vehicle for improved therapeutic delivery, imaging, biosensing, diagnosis and basic mechanistic studies *in vivo* and *in vitro* is widely recognised. This mainly arises in consequence of the variability and flexibility of these materials architecture to accommodate specific physicochemical characteristics (e.g. shapes, sizes, surface charge, chemical reactive groups, etc) for optimal biodistribution, cellular internalisation and intracellular trafficking. As a consequence, several advances have been made in the characterisation and establishment of mechanisms for nanoparticle uptake and their cellular fate. However, and despite the extensive literature, it is not yet possible to draw an optimal general pattern for nanoparticle uptake or intracellular localisation. There has mainly been found an interdependency between uptake and nano-

particle size, surface charge (among others physiochemical characteristics) and cell-type [50, 73, 150].

For cellular entry, the first obstacle nanoparticles face is the plasma membrane, which creates a barrier between the intracellular (cytoplasm) and the extracellular environment, and which dynamically acts on the regulation and coordination of the entry and exit of small and large molecules [35]. Small molecule, can cross the plasma membrane through membrane protein pumps or channels (e.g. ions, sugars, aminoacids). Macromolecules are internalised through membrane-bound mechanisms involving the invagination and pinch-off of the cell membrane for internalisation in a process known as endocytosis. Based on the nature of nanoparticles, it has been found that endocytic mechanisms arise as the most important in nanoparticle uptake. The main endocytic mechanisms involved in nanoparticle cellular uptake and their characteristics are briefly described below.

5.1.1 Endocytic mechanisms for cellular uptake of nanoparticles and size effect

The mechanism of endocytosis itself comprises several mechanisms which fall into two main categories, phagocytosis, also known as “cell eating”, and pinocytosis, also known as “cell drinking”. Phagocytosis mainly occurs in specialised mammalian cells (e.g macrophages, monocytes, neutrophils, endothelial cells, dendritic cells) [151, 152]. On the other hand, pinocytosis occurs in almost all cells and is further subdivided into four main mechanisms: macropinocytosis, clathrin- and caveolae- mediated endocytosis and clathrin- and caveolae-independent endocyt-

osis as schematically shown in Figure 5.1.

5.1.1.1 Phagocytosis

The uptake of nanoparticles through the phagocytic pathway occurs through three steps: recognition of the nanoparticle by opsonisation, adhesion of the opsonised particles to the macrophage and ingestion of the particles. The step of opsonisation comprises the labelling of nanoparticles with opsonins (proteins), leading to a visible form of the macrophages which further establishes specific receptor-ligand binding at their surface. Once binding to the macrophage surface is established, signalling cascade responses mediated by Rho family GTPases trigger the assembly of actin with the formation of cell surface extensions (pseudopodia; Figure 5.1; **i**) that surround the particle, which is finally engulfed, originating the phagosome (Figure 5.1, **A 1**). In biological systems, the phagocytic process aims for clearance of foreign material (e.g. bacteria, yeast, cellular debris, etc) and it is known that, through phagocytosis nanoparticles in the range of $0.5\ \mu\text{m}$, up to $10\ \mu\text{m}$ are taken up [63, 153].

5.1.1.2 Pinocytosis

Macropinocytosis

In a similar manner to phagocytosis, macropinocytosis involves the formation of membrane protrusions which collapse onto and fuse with the plasma membrane, as schematically shown in Figure 5.1; (**B, ii**). These membrane protrusions are formed through a similar mechanism to phagocytosis, in which the activation of the Rho-family GTPases leads to the assembly of actin. Furthermore,

the collapse of these membrane protrusions with the plasma membrane leads to the formation of large vesicles called macropinosomes, Figure 5.1; (2) [152,154].

Clathrin-mediated endocytosis

Clathrin-mediated endocytosis (Figure 5.1; C iii) is the most intensively studied endocytic mechanism and is present in all mammalian cells where it plays a central role in the continuous uptake of essential nutrients (e.g. low-density lipoprotein (LDL) and transferrin, epidermal growth factor (EGF)). Endocytosis proceeds through the recognition of nanoparticles by a membrane receptor (adapter protein complexes) which recruits clathrin, a main cytosolic coat protein. Polymerisation of clathrin units (triskelion polyhedral structure) helps to deform the membrane into a coat pit, which leads to a vacuole formation holding the nanoparticle [63, 152, 154, 155].

Clathrin-and caveolae- independent pathways

Cellular uptake can also be mediated by independent clathrin- and caveolin-processes. These mechanisms involve cholesterol-rich microdomains present on the plasma membrane, also known as lipid rafts of 40 up to 50 nm length.

The clathrin- and caveolin- mechanism's independent pathways are still poorly understood, largely because of the lack of inhibitors needed to study these specific mechanisms presents a major challenge in the characterisation of these pathways [75, 152, 154].

Caveolae-mediated endocytosis

Caveolae-mediated endocytosis (Figure 5.1; **E V**) (caveolae from the Latin little caves) is characterised by flask-shape invaginations displayed by the plasma membranes in many types of eucariotic cells. It was previously demonstrated that caveolae is localised to lipid rafts, which are areas of the membrane highly concentrated in sphingolipids [152,156]. In addition, caveolae membranes are also rich in caveolin-1 (muscle cell analogous caveolin-3) and caveolin-2. Caveolins are proteins (21 kDa) anchored to the cell membranes through a hydrophobic sequence on the cytosol side [152,154,157–159]. It is known that caveolin-1 is responsible for the structural formation of the caveolae. However, the exact function of, caveolin-2 exact mechanism remains unresolved.

To date, the exact mechanism of caveolae-mediated endocytosis is still unclear and the link of cargo molecules and caveolae-receptors remains a matter of study [157,159].

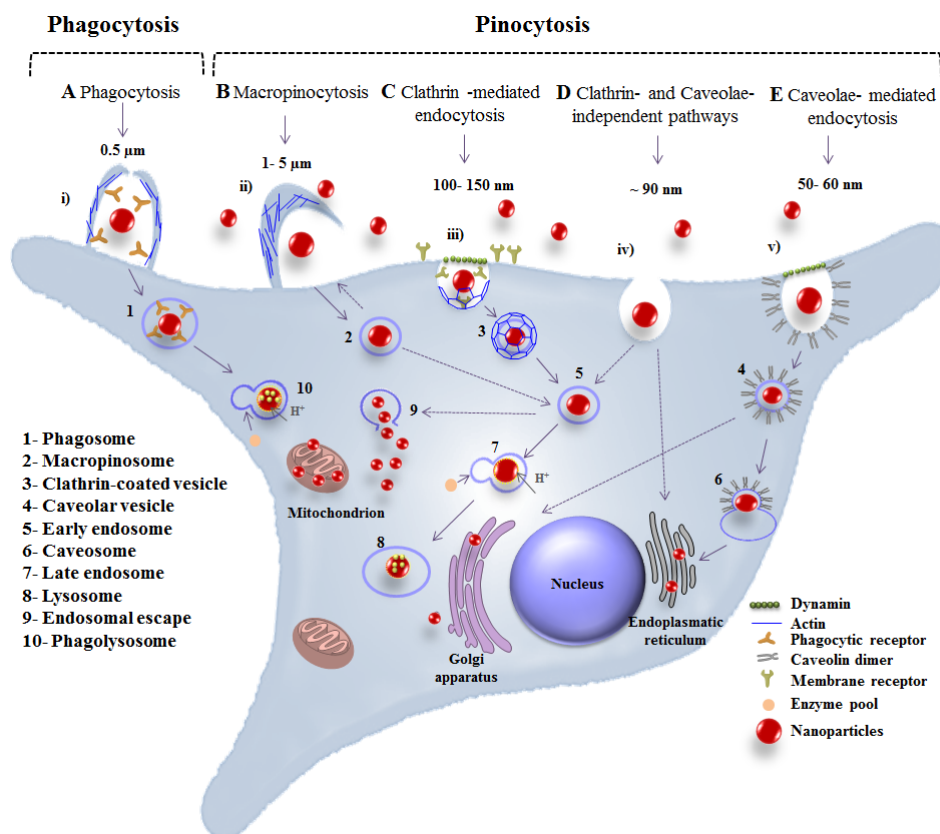


Figure 5.1: Intracellular mechanisms of nanoparticle uptake.

5.1.1.3 Surface charge and cellular uptake

After nanoparticle size, the surface chemistry of nanoparticles is another area of intense research. It has been found that the way nanoparticles interact with each other, and also with the surrounding environment, determines their applications. Surface charged nanosystems have been widely explored as a means to promote cellular uptake and intracellular targeting. Cationic nanosystems have been associated with enhanced cellular internalisation compared to anionic ones. The rationale behind facilitated uptake for positively charged systems relies on their electrostatic interaction with the negatively charged proteoglycans present on the membrane [45, 51, 72, 160–162]. Between cellular transporters approaches, the most popular are the short polycationic or amphiphilic peptides,

cell penetrating peptides (CPPs) [89, 150, 160, 163]. However, many other synthetic molecules have also been introduced, such as triphenyl phosphonium and trimethylammonium [59, 164].

Several studies have tried to clarify the mechanisms and interactions established between positively charged systems and cells. Although it is not possible to draw a general pattern of cellular internalisation for all the positively charged nanoparticles, which are extremely affected by other physico-chemical characteristics (e.g. size, shape, nanoparticle composition, morphology, geometry) [51], it is believed that endocytic mechanisms are the main operators of spherical cationic nanosystems internalisation in mammalian cells.

Endocytic mechanisms include absorptive-type endocytosis, transcytosis, and endocytic processes which are clathrin- and caveolin independent [45, 51, 161, 165, 166]. Literature mainly suggests that internalisation of cationic nanosystems follows clathrin- mediated mechanisms. However, it has also been reported that, upon pharmacological inhibition of this pathway, nanoparticles follow alternative mechanisms of internalisation, such as macropinocytosis, which leads to an increased concentration of nanoparticles inside the cell [160–162].

5.1.2 Nanoparticle engineering and sub-cellular fate

A major disadvantage in the development and effectiveness of cellular targeted delivery of nanosystems is endo/lysosomal degradation. Therefore, several methodologies have been developed to overcome endosomal sequestration. In recent years, nanoparticle engineering has been applied to confer physico-chemical

specificity and biological compatibility for more effective cargo delivery.

Surface charge was previously associated with facilitated kinetics of uptake; however, it has also been associated with intracellular trafficking and endosomal escape. One mechanism of endosomal escape relates to the formation of membrane pores. The interaction between amphiphilic cationic agents (e.g. polyethyl-enimine (PEI) and the lipid bilayer of the endosome membrane results in the formation of pores due to internal stress and/or membrane tension, with release of the sequestered molecules [167–170]. This mechanism has been previously exploited for several nanomaterials, such as, polyplex [171]; Gold NPs [172] and Chitosan NPs [173].

Another mechanism for endosomal escape is the "proton sponge effect", which involves the presence of agents with buffering capacity; examples of cationic materials include poly(L-lysine), *N*[1-(2,3-dioleyloxy)propyl]-*N,N,N*-trimethyl ammoniumchloride (DOTMA) and poly(amidoamide)dendimers [153, 167] among many others [167]. The exact mechanism of endosomal escape remains elusive. It is hypothesised, that the presence of unprotonated amines is involved, as they can absorb protons pumped into the endosomes, leading to an increase of proton being pumped into the endosome. In addition, an increase in Cl^- and water arises from the increased proton pumping. The osmotic swelling of endosomal membrane emerges, with subsequent rupture and release of the contents to the cytoplasm [153, 167, 174].

A slightly different approach that promotes endosomal escape, is the process of photochemical internalisation, which offers improved internalisation of macromolecules to access the cytosol [163,175–180]. The mechanism by which this access is conceded, relies on the photodynamic activity of photosensitizer molecules upon light activation of appropriate wavelength, as detailed in section 1.2. The ROS generated through photosensitizer activation is then responsible for the destruction of the endosomal/lysosomal membrane, with the release of its contents to the cytoplasm [175]. The cytotoxic activity of ROS is limited by their short-lifetimes and range of action and is confined to endosomal compartments.

5.1.2.1 Cationic nanosystems and associated cytotoxicity.

The main disadvantage of cationic nanosystems is the detrimental effects on the cells. Cytotoxic effects induced by cationic nanosystems are primarily related to its size, morphology and shape [51]. Nanoparticle positive surface charge facilitates the association with the cellular membrane and the internalisation of nanomaterials. However, highly charged nanosystems have been related with cytotoxicity [45,180,181]. Excess of positive charge in the blood stream is known to promote nanoparticle opsonisation aggregation. Furthermore, extracellularly, the cytotoxic effects of these systems are a consequence of complement activation, which leads to its clearing from circulation by the reticuloendothelial system (RES) [45,51,153]. Cationic nanosystems have been associated with toxicity and immunogenicity which limits its clinical applications [153,167].

Aims

This chapter aims to investigate the cellular uptake of trimethyl ammonium functionalised nanoplateforms and porphyrinic/trimethyl ammonium nanosystems developed in Chapters 3 and 4. In addition, it was also intended to evaluate the internalization profile and sub-cellular co-localisation of these nanosystems. The impact of these nanoplateforms was also studied for cellular toxicity in hMSCs. In order to achieve this, fluorescent microscopy and flow cytometry analysis were used.

5.2 Results and Discussion

For the present work, a system capable of inducing controlled toxic responses in hMSCs mediated by ROS generation was required. Mitochondrion is known as the major source of ROS, which are involved in the fundamental signalling process and are also mediators of pathological oxidative damage [3, 182–185]. In order to develop a tool to trigger the controlled production of ROS in hMSCs, it was reasoned that the mitochondrion would be a preferential target for nanoparticle systems. Mitochondrion targeting strategies often involve the use of cationic systems, exploiting the intrinsically negatively charged mitochondrial inner membrane [122, 186–188]. Although, in theory, cationic systems accumulate preferentially at mitochondria, some cationic systems have previously been reported to remain entrapped in endosomes/lysosomes [89, 189]. It was anticipated that, even though endosomal/lysosomal would be a possible outcome for the intracellular fate of porphyrinic nanoplateforms developed, photochemical internalisation could be applied in order to facilitate its release to the cytosol. As referred to in Section 5.1.2, light activation (specific wavelength) of nanoplateforms containing photosensitizers led to $^1\text{O}_2$ production, reported as a mechanism for rupture of the endocytic/lysosomal membranes and nanoplateform’s cytoplasmic release. It is note-worthy that lack of cellular toxicity was associated with this mechanism of internalisation as consequence of nanoplateform endocytic/lysosomal entrapment and the $^1\text{O}_2$ short-range phototoxic effect [190–194].

The delivery of polyacrylamide nanoparticles developed in Chapters 3 and 4, to hMSCs was investigated by flow cytometry and fluorescent microscopy using

the fluorescent signal of porphyrin or FITC-dextran. Porphyrin emission (red λ_{em} 630 nm) resulted from covalent linkage of these molecules to functionalised polyacrylamide nanoparticles. The fluorescence of FITC-dextran (green λ_{em} 520 nm) was present due to entrapment of these molecules in the matrix of polyacrylamide nanoparticles at the time of synthesis. The process and feasibility of the physical entrapment of FITC-dextran has been previously reported by many studies [37, 55, 58, 89, 109]. It was generally reported that the covalent linkage between the fluorophore, fluorescein isothiocyanate and an inert large molecule such as dextran (10 000 Mw) would confer protection against fluorophore leaching out of the polymeric matrix [37, 55]. Moreover, entrapped FITC-dextran in polymeric matrices has been previously associated with high stability and the capability to sense pH variations, and has been described as a potential tool for intracellular pH sensing [58].

5.2.1 Cellular uptake of positively charged polyacrylamide nanosystems

5.2.1.1 Internalisation of positively charged nanoplateforms.

Although nanoparticle engineering seems to be a feasible approach to confer specific chemical characteristics to nanoparticles, allowing it to be efficiently internalised and redirected to specific sub-cellular compartments, some disadvantages still exist.

In order to investigate the internalisation of positively charged nanosystems, polyacrylamide nanoparticles were synthetically manipulated to incorporate

different percentages of trimethyl ammonium functionalities. The trimethyl ammonium modified polyacrylamide nanosystems under study presented zeta potentials between $+13\text{ mV}$ and $+25\text{ mV}$ and were incubated with hMSCs for a 15 hour time period. The internalisation of the positively charged nanosystems was then visualised through fluorescent microscopy. Due to the small size of the nanosystems studied and the resolution limit of the microscope, visualisation of individual nanoparticles was not possible and images show an ensemble of nanoparticles. For all the experiments, images were collected in z-stack mode and only by reaching the centre of the cell was possible to visualise nanoparticle fluorescence (green λ_{em} 520 nm), unless stated otherwise.

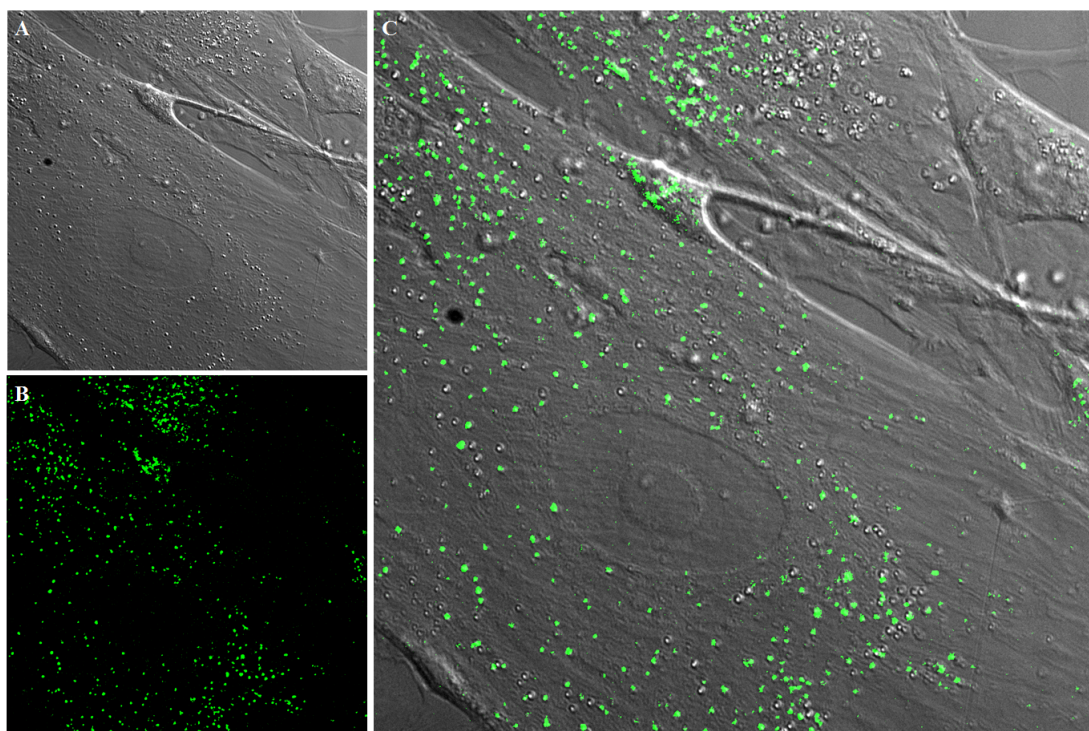


Figure 5.2: Representative *live-cell* imaging of hMSCs treated with 5 mg/ml of 2.5 % TNPs. A- Differential interference contrast image of hMSCs; B- 2.5 % TNPs (FITC $\lambda_{\text{em}} = 520\text{ nm}$); C- Overlay of Differential interference contrast and 2.5 % TNPs. Imaging performed with widefield Olympus Deltavision elite deconvolution fluorescent microscope, Olympus U-plan S- Apo 60x/NA 1.42. Scale= $17\text{ }\mu\text{m}$.

Figure 5.2, shows a representative image of hMSCs treated with 2.5 % TNPs. As can be observed, nanoparticles were passively uptaken by hMSCs; see (Fig. 5.2 (C)) Nanoparticles appear as punctated and granular structures distributed through the cytoplasm. Moreover, it was also possible to observe the absence of particles associated with the cellular membrane. This was verified by the absence of green emission at the top and bottom of the cell (Z-stack, data not shown).

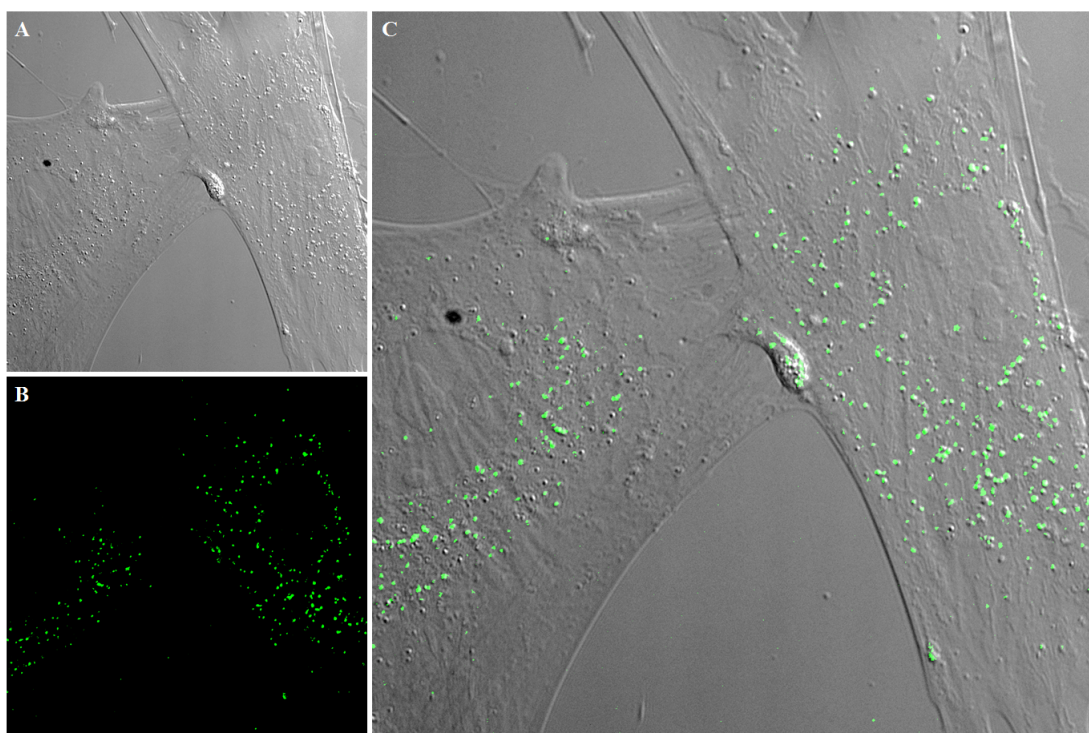


Figure 5.3: Representative *live-cell* imaging of hMSCs treated with 5 mg/ml of 5 % TNPs. A- Differential interference contrast image of hMSCs; B- 5 % TNPs (FITC λ_{em} = 520 nm); C- Overlay of differential interference contrast and 5 % TNPs. Imaging performed with widefield Olympus Deltavision elite deconvolution fluorescent microscope, Olympus U-plan S- Apo 60x/NA 1.42. Scale= 15 μ m.

Similarly, 5 % TNPs NPs also shows the presence of punctated/granular structures distributed throughout the cytoplasm. Figure 5.3 (C) shows the overlay of

phase contrast and green emitted light, where it is possible to observe the distribution of nanoparticles in the area surrounding the nucleus.

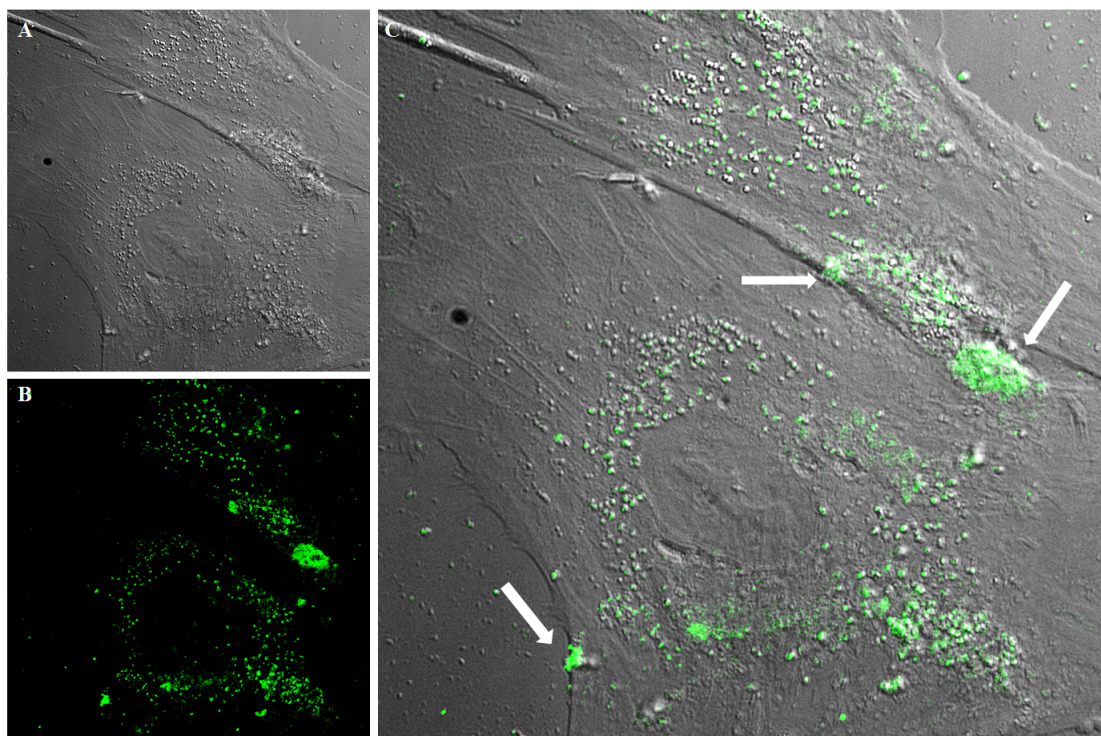


Figure 5.4: Representative *live-cell* imaging of hMSCs treated with 5 mg/ml of 10 % TNPs functionalised nanoparticles. A- Differential interference contrast image of hMSCs; B- 10 % TNPs nanoparticles (FITC $\lambda_{em}= 520$ nm); C- Overlay of differential interference contrast and 10 % TNPs NPs. Imaging performed with widefield Olympus Deltavision elite deconvolution fluorescent microscope, Olympus U-plan S- Apo 60x/NA 1.42. Scale= 17 μ m.

In addition, the treatment of hMSCs with 10% TNPs NPs also revealed the presence of punctate/granular structures emitting green light; see Figure 5.4 (B);(C). However, contrary to the 2.5 % and 5 % of positively charged systems described earlier, 10 % TNPs NPs showed the presence of green emitted light from the top to the bottom of the cell in the areas indicated by white arrows; see Figure 5.4 (C). The results suggest the presence of nanoparticles adherent to the

cell membrane. It is important to note that cells under analysis were extensively rinsed with phenol red free medium prior to analysis. Furthermore, the same evidence was present in several cells within the same sample and also in independent experiments.

The cellular uptake for positively charged nanosystems suggested the successful internalisation of all three systems, as expected. The results obtained are in accordance with those previously reported by Sun, *et al.* for trimethyl ammonium functionalised nanoparticles and many other studies for other positively charged nanosystems [51, 59, 160, 161, 195]. Furthermore, in accordance with the work developed by Jiang, *et al.*, nanoparticles with a surface charge $>+25$ mV showed a small percentage of nanoparticulates associated with the cellular membrane [73, 196].

5.2.1.2 Sub-cellular co-localisation of internalised positively charged nanosystems.

The internalisation of cationic systems was evaluated by high resolution widefield fluorescent microscopy. In Figure 5.5, the intracellular co-localisation of 2.5 % TMA NPs, either with mitochondria or endo/lysosomes in hMSCs, was evaluated. The overlaid images between mitochondrion and FITC labelled 2.5 % TNPs, (see Figure 5.2 (E)), shows partial points of co-localisation between nanoparticles and mitochondria. At those regions where mitochondria and nanoparticles coincide, a yellow fluorescence was obtained, as can be observed in regions R1 and R2. Similarly, co-localisation with endo/lysosomal vesicles was detected by the overlay between blue endo/lysosomal staining and the FITC labelled NPs originating a light blue fluorescence for co-localised points. Therefore, as seen in

Figure 5.2 (F), for regions R3 and R4 minimal co-localisation of nanoparticles with endo/lysosomes was observed from each other.

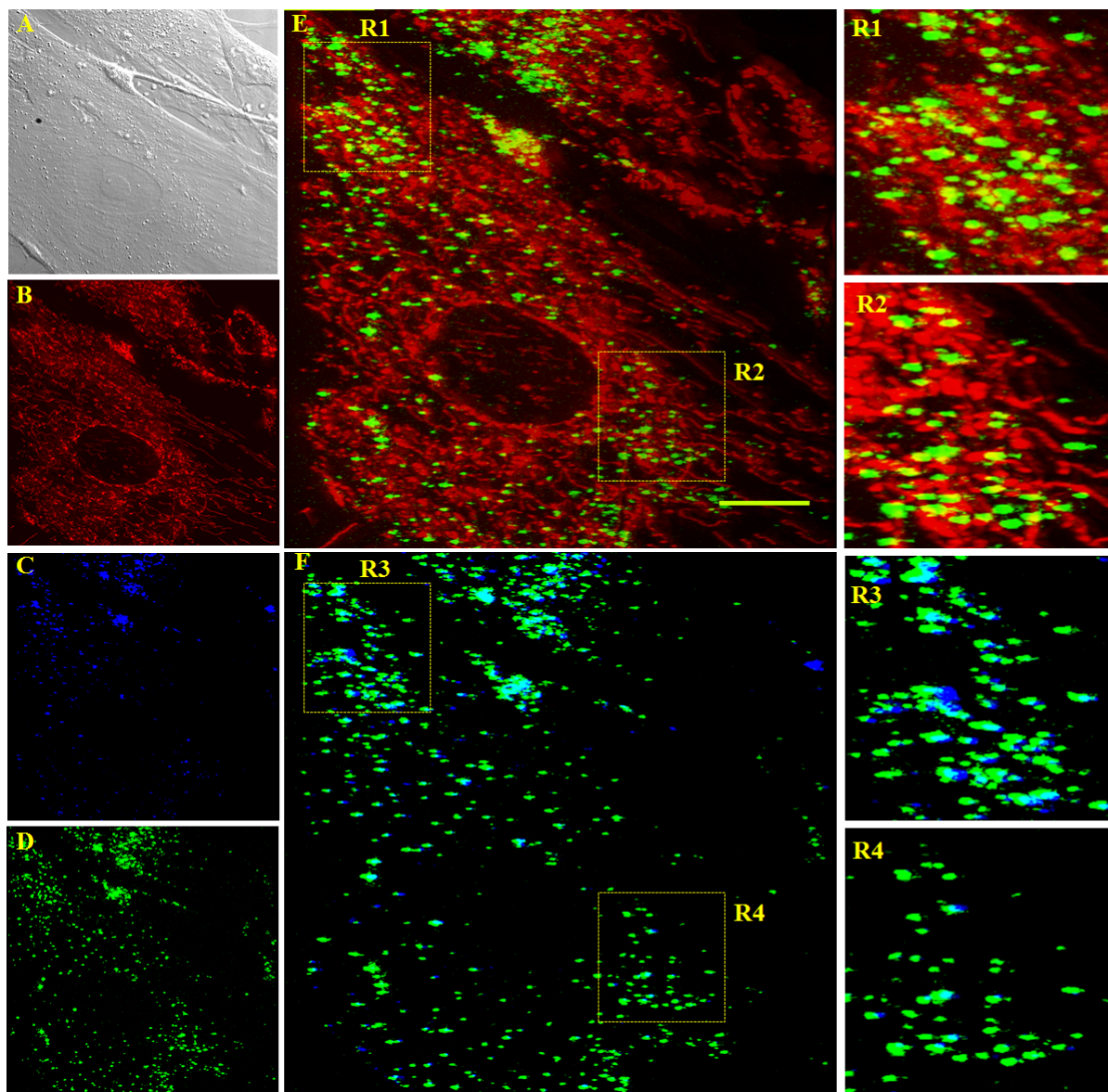


Figure 5.5: Representative analysis of intracellular co-localisation of 2.5 % TNPs (5mg/ml) with mitochondria and endo/lysosomal vesicles by widefield Olympus Delta-vision elite deconvolution fluorescent microscopy. (A)- Differential interference contrast of hMSCs. (B)- hMSCs mitochondrial staining with mitotracker red; $\lambda_{exc}=594$ nm, $\lambda_{em}=610$ nm. (C)- endosomal/lysosomal staining with lysotracker blue; $\lambda_{exc}=399$ nm, $\lambda_{em}=457$ nm. (D)- FITC fluorescence 2.5 % TNPs; $\lambda_{exc}=488$ nm, $\lambda_{em}=526$ nm. (E)- mitochondrial and FITC overlaid images; **R1** and **R2**- zoom of regions R1 and R2 in E to show co-localisation of nanoparticles with mitochondria. (F)- endo/lysosomal and FITC overlaid images showing sub-cellular localisation of 2.5 % TNPs; **R3** and **R4**- zoom of regions R3 and R4 in F to show co-localisation of nanoparticles with endosomes/lysosomes. Olympus U-plan S- Apo 60x/NA 1.42. Scale= 17 μ m.

The analysis of 5 % TNPs internalised co-localisation with mitochondria or

endosomes/lysosomes showed a similar trend to 2.5 % TNPs, and is shown in Figure 5.3(**E**), (**F**). As can be observed in regions R1 and R2, partial points of co-localisation were identified by the yellow fluorescence (nanoparticle concentrated at the mitochondrion). Furthermore, lyso/endosomal co-localisation was minimal for 5 % TNPs as shown in regions R3 and R4 where blue and green fluorescence was found isolated .

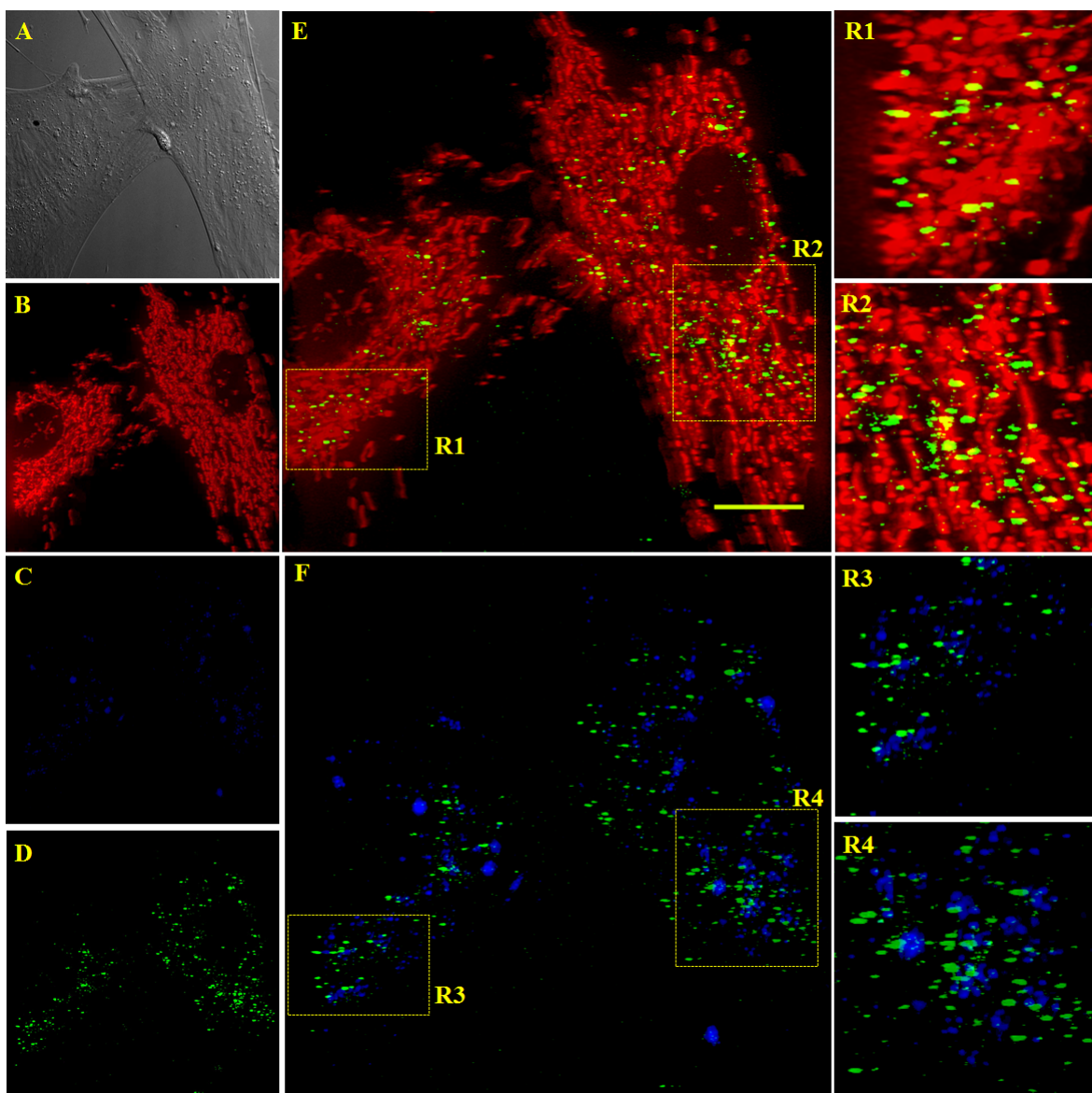


Figure 5.6: Representative analysis of intracellular co-localisation of 5 % TNPs (5mg/ml) with mitochondria and endosomal/lysosomal vesicles by widefield Olympus Deltavision elite deconvolution fluorescent microscopy. (A)- Differential interference contrast of hMSCs. (B)- hMSCs mitochondrial staining with mitotracker red; $\lambda_{exc}=575$ nm, $\lambda_{em}=632$ nm. (C)- endosomal/lysosomal staining with lysotracker blue; $\lambda_{exc}=390$ nm, $\lambda_{em}=435$ nm. (D)- FITC fluorescent 5 % TNPs; $\lambda_{exc}=475$ nm, $\lambda_{em}=523$ nm. (E)- mitochondrial and FITC overlaid images; **R1** and **R2**- zoom of regions R1 and R2 in E to show co-localisation of nanoparticles with mitochondria. (F)- endosomal/lysosomal and FITC overlaid images; **R3** and **R4**- zoom of regions R3 and R4 in F to show co-localisation of nanoparticles with endo/lysosomes. Olympus U-plan S- Apo 60x/NA 1.42. Scale= 15 μ m.

Contrary to the 2.5 % and 5 % cationic nanosystems described above, the analysis of 10 % TNPs co-localisation with mitochondrial and endosomal/lysosomal organelles showed a low co-localisation with mitochondria. Higher co-localisation

was observed with stained endosomes/lysosomes.

Furthermore, mitochondrial staining for 10% TNPs was generally dimmer than that observed for the systems 2.5 % and 5 % TNPs. It is important to note that mitochondrial staining with mitotracker red was previously reported to be sensitive to variation in mitochondrial membrane potential [197]. Thus, a decrease in mitochondrial staining was previously associated with a decrease in membrane potential and, consequently, is also an indicator of diminished cellular viability [197, 198]. Therefore, the lower viability found for hMSCs incubated with 10 % TNPs, was consistent with the viability studies described in Section 5.2.1.3. Cytotoxicity associated with cationic systems is mainly correlated with the interaction of these systems and the phospholipidic membrane. However, it has also been reported that these systems can also exert cytotoxic actions, even if entrapped in lysosomes. This is mainly due to the swelling and disruption of these organelles as the consequence of a buffering of H^+ , with release of hydrolytic enzymes that subsequently degrade intracellular macromolecules [51].

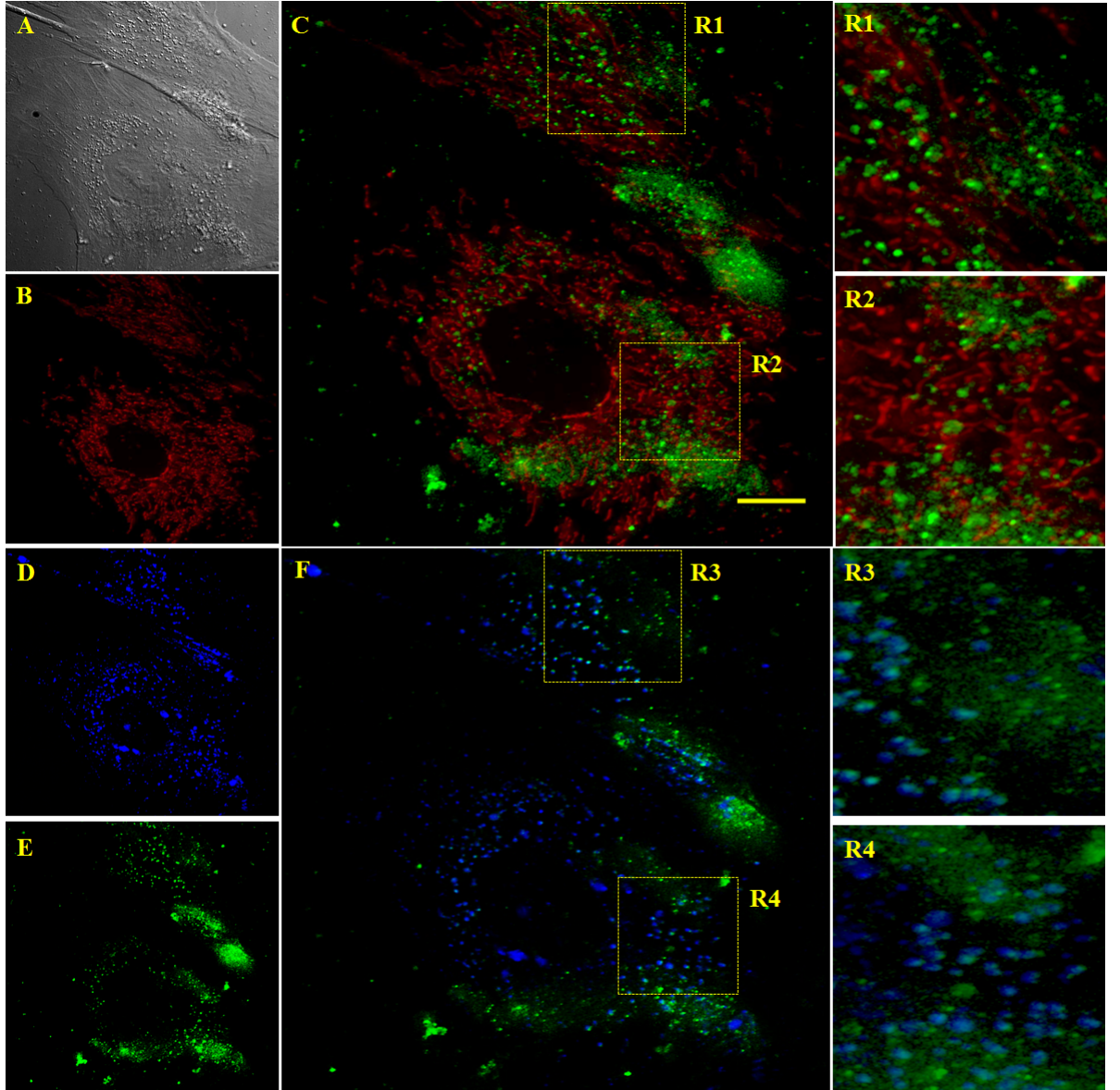


Figure 5.7: Representative analysis of intracellular co-localisation of 10 % TNPs (5 mg/ml) with mitochondria and endo/lysosomal vesicles by widefield Olympus Deltavision elite deconvolution fluorescent microscopy. **(A)**- Differential interference contrast of hMSCs. **(B)**- hMSCs mitochondrial staining with mitotracker red; $\lambda_{exc}=575$ nm, $\lambda_{em}=632$ nm. **(C)**- endosomal/lysosomal staining with lysotracker blue; $\lambda_{exc}=390$ nm, $\lambda_{em}=435$ nm. **(D)**- FITC fluorescent 10 % TNPs; $\lambda_{exc}=475$ nm, $\lambda_{em}=523$ nm. **(E)**- mitochondrial and FITC overlaid images; **R1** and **R2**- zoom of regions R1 and R2 in E to show co-localisation of nanoparticles with mitochondria. **(F)**- endosomal/lysosomal and FITC overlaid images; **R3** and **R4**- zoom of regions R3 and R4 in F to show co-localisation of nanoparticles with endosomes/lysosomes. Olympus U-plan S- Apo 60x/NA 1.42. Scale= 15 μ m.

5.2.1.3 Impact of positively charged nanoparticles on hMSCs: Viability versus particle uptake.

In order to achieve a better understanding of the cellular uptake of the different positively charged systems, flow cytometry (FCM) was used as a complementary technique to fluorescence imaging. The enhanced uptake of positively charged systems has been associated with toxic effects in treated cells; this technique was also used to evaluate the level of toxicity associated with the nanosystems being studied [188].

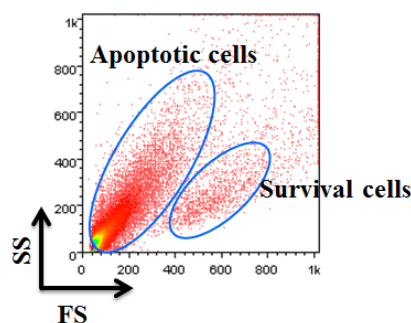


Figure 5.8: Representative bi-variate plot of cell survival/apoptosis analysis by flow cytometry [199].

The assessment of nanoparticle uptake by flow cytometric analysis is well established [89,199–202]. Flow cytometric analysis of cellular uptake and the toxicity of the positively charged nanosystems was performed according to the scheme shown in Figure 5.8. Bi variate scatter plots of healthy hMSCs were used to isolate (gate) live cell populations and to provide a comparison model to other populations (treated cells). Forward scatter provides information about the cell size, which should be positive for viable cells. Side scatter provides evidence about the complexity/granularity of the cell. Apoptotic cells present a decrease in size

(cell shrinking) and increased granularity (formation of apoptotic bodies- nuclear spherulic follicles) [78, 79, 199]. Forward and side scatter bi-variate plots were used to isolate (gate) the region of cell survival.

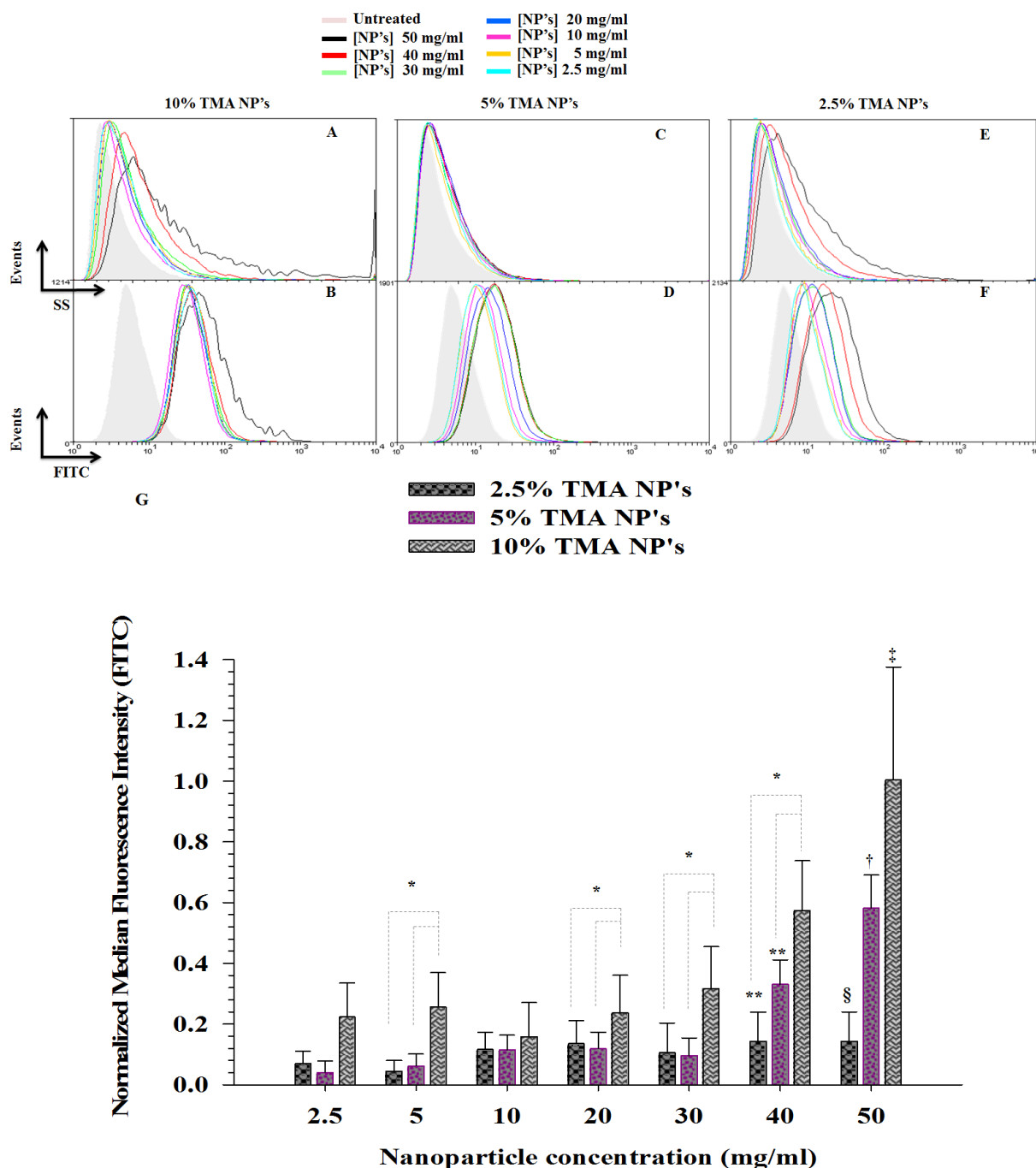


Figure 5.9: Analysis of cellular uptake of positively charged nanoparticles by flow cytometry. hMSCs were treated overnight (≈ 15 hours) with several doses (2.5, 5, 10, 20, 30, 40, 50 mg/ml) of TNPs (2.5 %, 5 % and 10 %). (A)- FCM histogram of events vs SS for 10 % TNPs. (B)- Dose-dependent comparison of events vs FITC for 10 % TNPs. (C)- FCM histogram of events vs. SS for 5 % TNPs. (D)- Dose-dependent comparison of events vs. FITC for 5 % TNPs. (E)- FCM histogram of events vs. SS for 2.5 % TNPs. (F)- Dose-dependent comparison of events vs. FITC for 2.5 % TNPs. (G)- Graphical representation of dose-dependent comparison of FITC normalised median fluorescence intensity. Medians were calculated from two independent experiments conducted in triplicate. Error bars represent mean \pm SD (n=6). 10 % vs. 5 and 2.5 % TNPs: * $p < 0.05$; 40 mg/ml 5 % vs. 2.5 % TNPs: ** $p < 0.05$; 50 mg/ml 2.5 % vs 5 % TNPs: § $p < 0.05$; 50 mg/ml 5 % vs 10 % TNPs: † $p < 0.05$; 50 mg/ml 10 % vs 2.5 % TNPs: ‡ $p < 0.05$ were considered statistically different, One Way ANOVA.

Figure 5.9 shows the internalisation of positively charged nanoparticles in hMSCs in a dose-dependent manner. From side scatter histograms, it was possible to observe discrete granularity variations in hMSCs with the increase in dose and charge of nanoparticles (**A**), (**C**) and (**E**). Forward scatter histograms were found to be constant with the different nanoparticle dosages (data not shown). The results indicate the successful internalisation of cationic nanosystems in hMSCs. Similarly, Coupland, *et al.* investigated the uptake of TAT- functionalised polyacrylamide nanoparticles in hMSCs by flow cytometry. They found that internalised NPs contributed to slight variations in cell granularity (increased) due to nanoparticle internalisation (increase in cellular complexity) [89,203]. Furthermore, they also obtained an invariable pattern in the forward side histograms for treated and non-treated cells, indicators of unaltered morphology and viability [89,199]. Additionally, the analysis of FITC fluorescence intensity resulted in increased fluorescence (uptake) for 10 % >5 % and >2.5 % TNPs, respectively. The results suggest that higher nanoparticle uptake is associated with increased positive charge on the nanoparticles.

Graphical analysis of the FITC fluorescence intensity versus nanoparticle concentration (see Figure 5.9 (**G**)), showed non-significant variations in uptake for 2.5 % and 5 % TNPs in the range of concentrations from 2.5 mg/ml to 30 mg/ml. For concentrations above 30 mg/ml, significant increase of nanoparticle uptake for cells treated with 5 % TNPs was found. More significant variations were found for cells treated with 10 % TNPs NPs on a concentration range of 5 mg/ml to 50 mg/ml. However, it was reasoned that variations in the 10 % TNPs uptake were partially affected by the presence of these systems interacting with the cellular

membrane, as demonstrated by microscopic analysis (Section 5.2.1.2). Unfortunately, flow cytometric analysis did not allow differentiation between nanoparticles internalised and associated with the cellular membrane, as flow cytometry provides information on the total fluorescence of each cell.

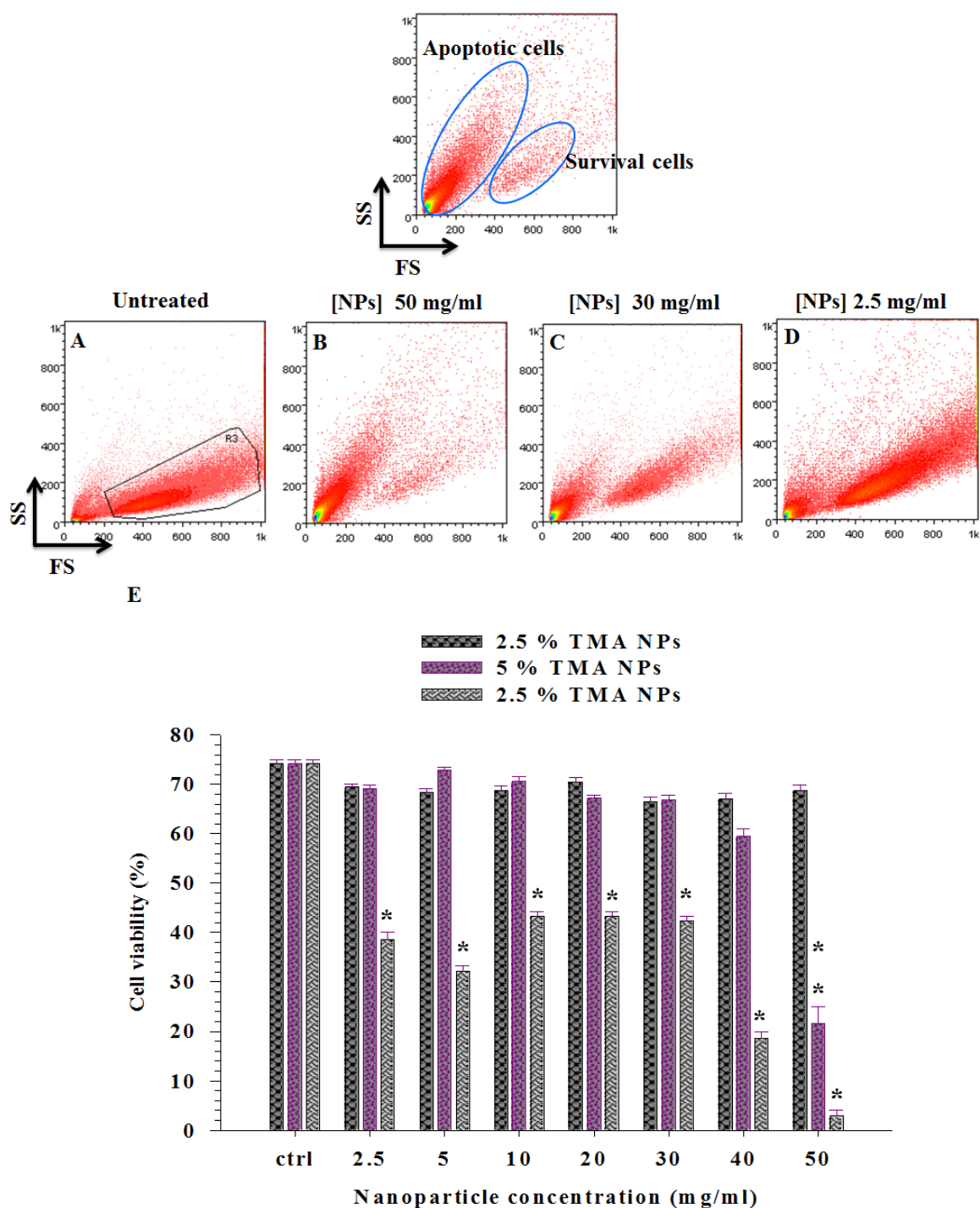


Figure 5.10: Analysis of cellular viability in hMSCs treated overnight with 2.5 %, 5 % and 10 % TNPs by flow cytometry. hMSCs were treated overnight with several doses (5, 10, 20, 30, 40, 50 $\mu\text{g/ml}$) of TNPs. Representative bi-variate plots: (A)- untreated cells; (B)- cells treated with 50 $\mu\text{g/ml}$; (C)- cells treated with 30 $\mu\text{g/ml}$; (D)- cells treated with 5 $\mu\text{g/ml}$, show alterations in population density for treated and un treated cells. Graph (E) shows the impact of 2.5 %, 5 % and 10% TNPs in hMSCs viability, demonstrating that 10 % TNPs have high impact on hMSCs survival. Percentage of viability was calculated from two independent experiments conducted in triplicate. Error bars represent mean \pm SD (n=6). Statistical analysis, control vs. [NPs]: * $p < 0.05$, all pairwise comparisons:** $p < 0.05$ were considered statistically different, One Way ANOVA.

Cationic nanoparticle systems are often associated with a high level of toxicity [71,74,204,205]. In order to evaluate the toxicity associated with cationic nanosystems flow, cytometric analysis of treated *live* hMSCs was performed and compared with healthy cells (non-treated). Cellular viability was assessed by the comparison between bi-variate scatter plots in healthy and treated cells. Figure 5.10 shows the resultant scatter plots, where healthy cells were gated Figure 5.10 (A) provide a reference for comparison with treated cells. As can be observed in the scatter plots of treated hMSCs, the number of cells in the gated area (viable cells) are small at higher concentrations of cationic nanoparticles (B), meaning that the survival rate is low. The low rate of survival is visualised by the increase in number of cells with low forward scatter and high granularity. Furthermore, the decreasing of nanoparticle dosage leads to an increase in hMSCs survival, as can be observed by the increased number of cells in the gated area (C,D).

The same trend was achieved for all three cationic nanosystems; however, for 2.5 % TNPs the cellular viability remained high throughout all the dosing concentrations. Figure 5.10 (E) shows cell viability as a function of nanoparticle dosing concentration. Significant impact in hMSCs viability was found for 10 % TNPs in the range of 2.5 mg/ml to 50 mg/ml compared to control cells ($p < 0.05$). Furthermore, cells treated with 5 % TNPs also showed significant deleterious effects in hMSCs survival at highest concentrations (50 mg/ml and 40 mg/ml) ($p < 0.05$).

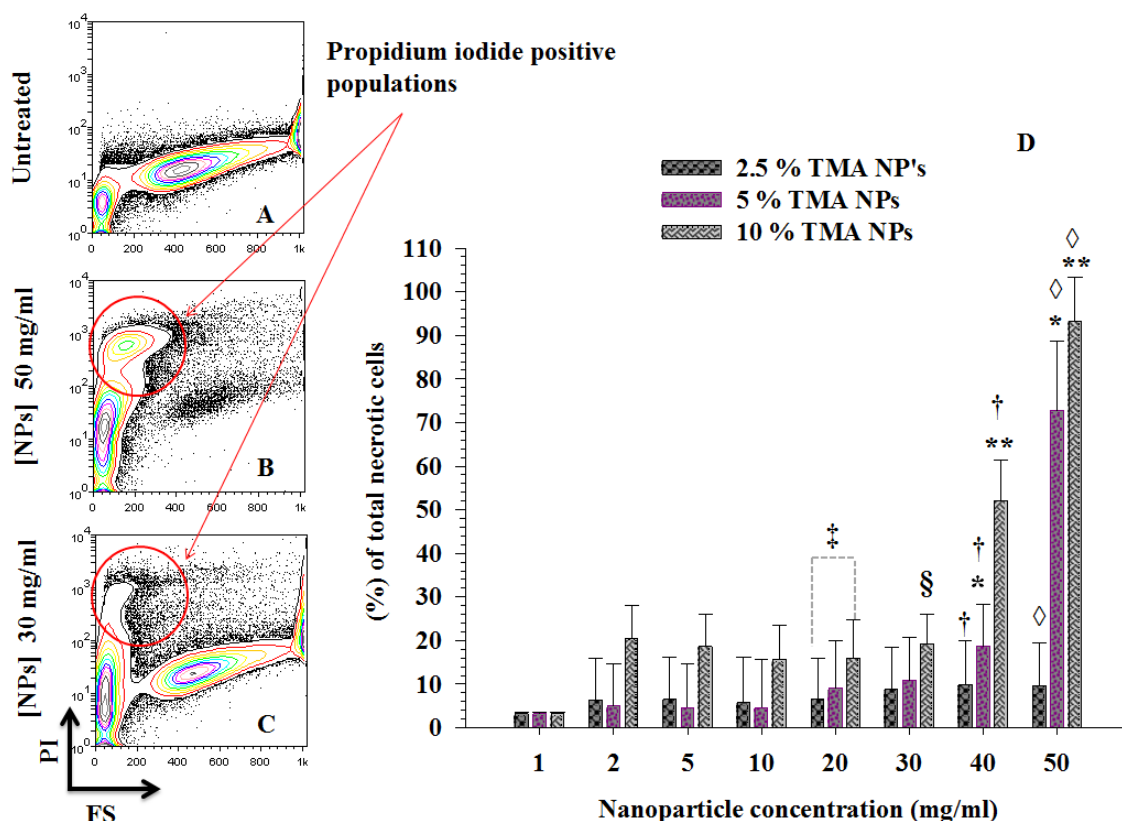


Figure 5.11: Analysis of necrotic/late apoptotic events in hMSCs treated with cationic nanosystems by flow cytometry. hMSCs were treated overnight (≈ 15 hours) with several doses (2.5, 5, 10, 20, 30, 40, 50 mg/ml) of TNPs (2.5 %, 5 % and 10 %). (A)- FCM contour plot of PI vs. FS for untreated hMSCs. (B)- FCM contour plot of PI vs. FS for hMSCs treated with 50 mg/ml of 10 % TNPs. (C)- FCM contour plot of PI vs FS for hMSCs treated with 30 mg/ml of 10 % TNPs. (G)- Graphical representation of percentage of total necrotic cells versus nanoparticle concentration. Medians were calculated from two independent experiments conducted in triplicate. Error bars represent mean \pm SD ($n=6$). 20 mg/ml 10 % vs. 2.5 % TNPs: $\ddagger p < 0.05$; 30 mg/ml 2.5 % vs. 5 % TNPs vs. 10 % TNPs: $\S p < 0.05$; 40 mg/ml 2.5 % vs 5 % vs. 10 % TNPs: $\dagger p < 0.05$; 40 mg/ml 10 % TNPs vs. 50 mg/ml 10 % TNPs: $** p < 0.05$; 50 mg/ml 2.5 % vs. 5 % vs. 10 % TNPs: $\diamond p < 0.05$; 40 mg/ml 5 % TNPs vs. 50 mg/ml 5 % TNPs: $* p < 0.05$; were considered statistically different, One Way ANOVA.

In order to further investigate the impact of cationic nanosystems on cellular viability, hMSCs were incubated with several dosages of cationic nanoparticles and stained with propidium iodide (PI), which leads to a highly fluorescent signal in necrotic or late apoptotic cells. Propidium iodide is a DNA intercalating dye; it intercalates with the major groove of double-stranded DNA. This agent is not able to cross intact cellular membranes, and only permeates compromised

membranes of dying or dead cells [78, 79, 199, 206].

Figure 5.11 (**A**; **B**; **C**) shows the PI versus forward scatter bi-variate contour plots of treated and untreated hMSCs. As can be seen, staining with PI is absent in untreated cells (**A**). For cells treated either with 50 mg/ml (**B**) or 30 mg/ml (**C**) of cationic nanoparticles, the portion of the population which stains positive for PI is more evident in cells treated with 50 mg/ml (red gated populations). The percentage of necrotic cells versus nanoparticle concentration for the three cationic systems studied is shown in Figure 5.11 (**D**), which reveals a significantly higher percentage of necrosis for hMSCs treated with 10 % TNPs ($p < 0.05$). Additionally, 5 % TNPs NPs present a significantly high number of necrotic events for nanoparticle concentrations from 20 mg/ml up to 50 mg/ml.

The results shown in Figures 5.10 and 5.11 are in good agreement with the literature, where cationic systems were often found to have a negative impact on the viability of several types of cells [71, 74, 188, 204, 205]. Previous studies on the effect of cationic systems on cellular viability have shown that polyelectrolytes (e.g. poly-(lysine)) exhibit toxicity *in vitro* due to interactions with the phospholipids in the cell membrane which results in its disruption [74, 188, 205].

The delivery of cationic polymeric nanosystems shows that, in general, charge confers enhanced internalisation while also conferring mitochondrial sub-cellular targeting. However, the results also suggest that for NPs with higher surface charge, pronounced cytotoxic actions and lower capability of specific sub-cellular targeting is observed. From these experiments it can be speculated that the

design of cationic systems needs to consider a tight balance between surface charge, sub-cellular targeting and cell viability.

It is note-worthy that, for 2.5% TNPs in the range of concentrations from 2.5 mg/ml up to 50 mg/ml, there was no significant impact on cell viability and that these NPs were internalised and localised to the mitochondria within hMSCs co-localisation. Similarly, 5 % TNPs were good candidates for enhanced uptake and mitochondrial targeting; although in a more restricted range of concentrations (up to 30 mg/ml). Contrary, 10 % TNPs showed high levels of toxicity. Moreover, major co-localisation with endo/lysosomes was also found for these systems, but also NPs/membrane interactions.

5.2.2 Cellular uptake of porphyrin nanosystems

Once the influence of positive NP charge on delivery and cellular viability of hMSCs was characterised, attention was directed at investigating the delivery of porphyrin-nanoparticle systems hMSCs.

As shown in the previous chapter (Chapter 4), porphyrin emission is collected at a 630 nm wavelength. Therefore, it was not possible to assess cellular viability using propidium iodide (λ_{em} 617 nm) due to the overlap in the emitted light fluorescence. Therefore, cellular viability was investigated by staining hMSCs with mitotracker green.

Similar to mitotracker red and due to its lipophilic cationic nature, mitotracker green accumulates in mitochondria by electrostatic interaction with the negatively charged inner mitochondrial membrane. This interaction leads to the fluorescent

form of the dye. Normally, mitotracker dyes are known to respond to variations in the mitochondrial membrane potential. Unlike mitotracker red, however, mitotracker green has previously been reported to be unaffected by variations in mitochondrial membrane potential [198].

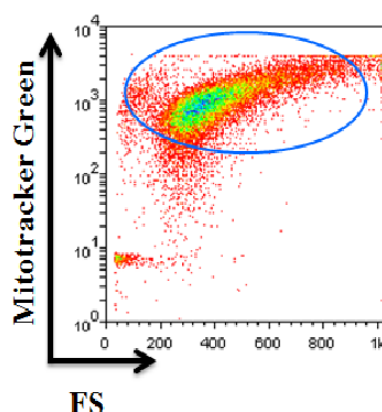


Figure 5.12: Representative image of hMSCs viability assessment by flow cytometric analysis of positive selection for mitotracker green.

Although mitotracker green is not a suitable dye to assess cellular viability in real time, it is capable of efficiently reporting relative changes in green fluorescence upon treatment. Figure 5.12 shows a representative bi-variate plot for viability assessment of hMSCs by mitotracker green. The positive selection for mitotracker green, blue gated area, was isolated for non-treated cells. Thus, a reference model was created to compare with treated populations.

5.2.2.1 Effects and internalisation of free porphyrin.

Porphyrins as photosensitizers are known to produce toxic effects in cells once activated by light; indeed, this is the basis of PDT. In order to anticipate possible

toxic effects as a consequence of imaging conditions, cell survival was first evaluated under bright field DIC light for a period of 16 hours.

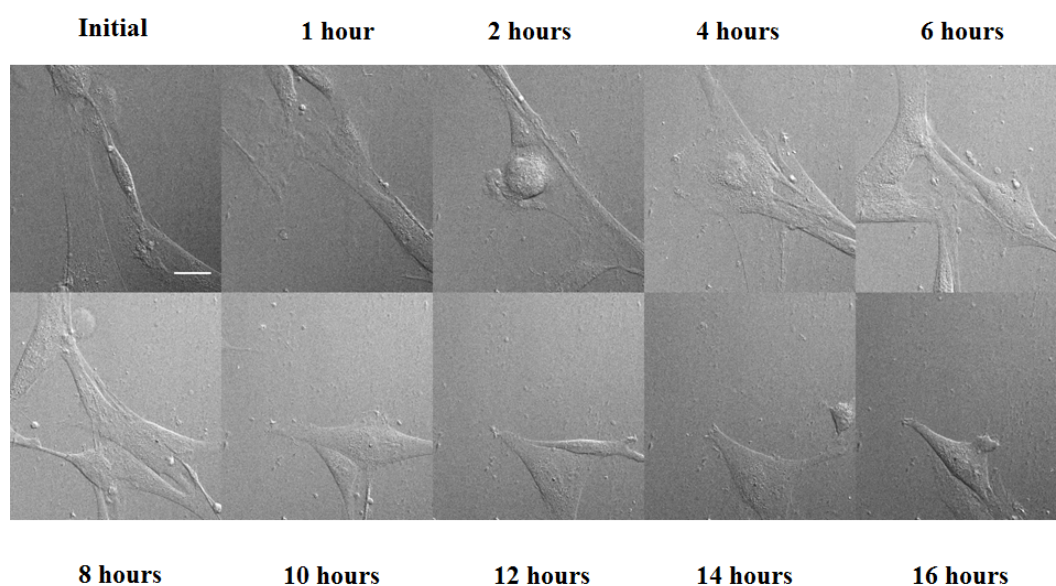


Figure 5.13: Representative timelapse *live cell* imaging of hMSCs treated with 5 $\mu\text{g}/\text{ml}$ of porphyrin. Differential interference contrast images were collected every 30 min for a total period of 16 hours. Imaging was performed with widefield Olympus Deltavision elite deconvolution fluorescent microscope, Olympus U-plan Apo 40x/ NA.0.95

Figure 5.13 shows the monitoring of morphology of hMSCs incubated with porphyrins; an initial point with cells was chosen and cells were imaged every 30 min. It is possible to observe that cells remained healthy for the full 16 hours of imaging; additionally, cell growth can be observed after two hours of imaging. The results were consistent throughout the entire culture and also in independent experiments. Therefore, they indicate that cellular viability remains unaffected throughout the time of imaging when incubated with the porphyrin dye.

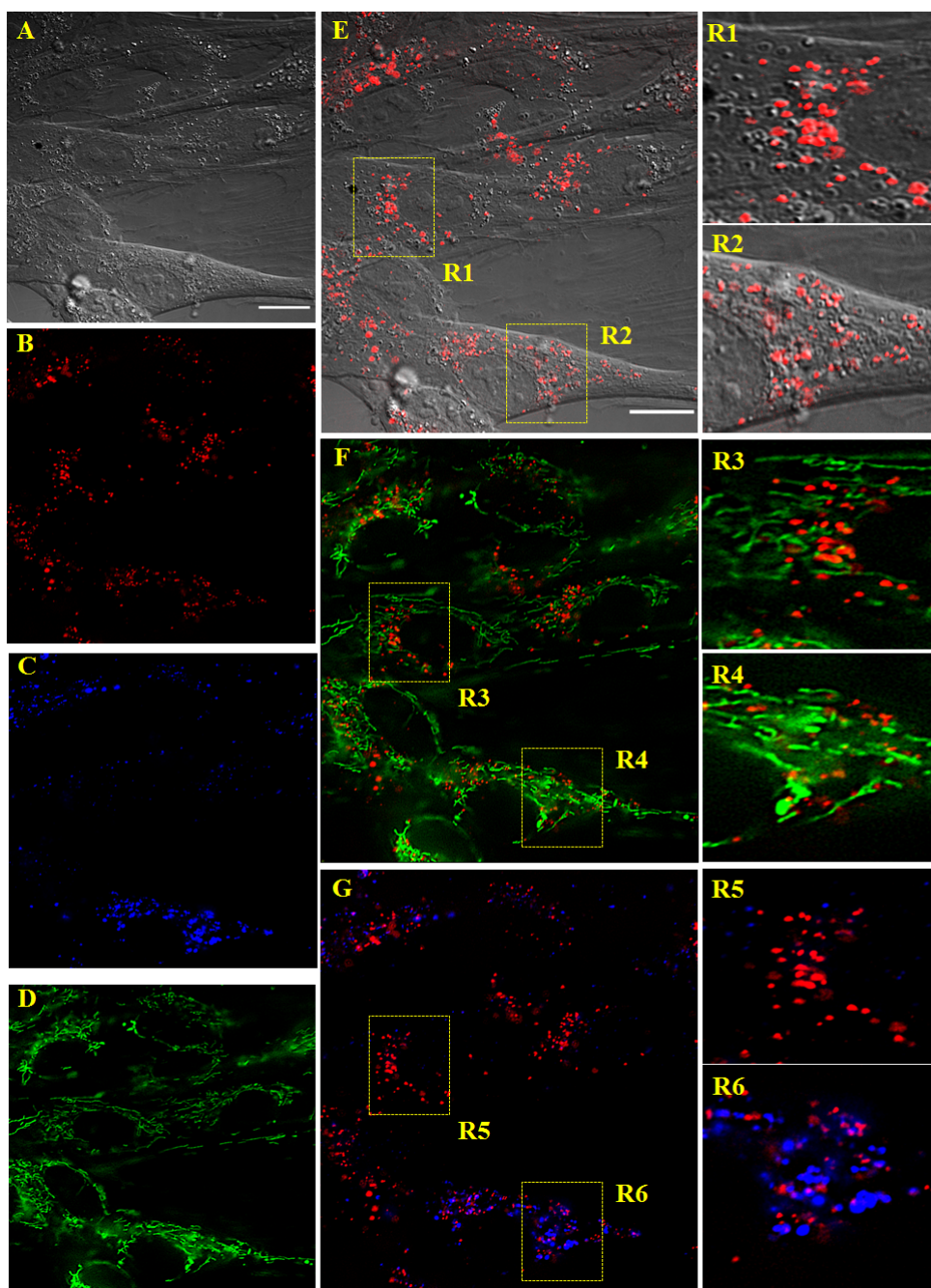


Figure 5.14: Representative analysis of intracellular co-localisation of porphyrin dye with mitochondria and endosomal/lysosomal organelles by widefield Olympus Delta-vision elite deconvolution fluorescent microscopy. (A)- Differential interference contrast of hMSCs. (B)- Porphyrin emission; $\lambda_{exc}=575$ nm, $\lambda_{em}=630$ nm. (C)- endosomal/lysosomal staining with lysotracker blue; $\lambda_{exc}=399$ nm, $\lambda_{em}=457$ nm. (D)- hMSCs mitochondrial staining with mitotracker green; $\lambda_{exc}=488$ nm, $\lambda_{em}=526$ nm. (E)- Differential interference contrast and porphyrin overlaid images showing that porphyrin is distributed throughout the cytoplasm ; **R1** and **R2**- zoom of regions R1 and R2 in E to show the distribution of porphyrin in the cell. (F)- mitochondrial and porphyrin images showing no interaction of porphyrins with mitochondrias **R3** and **R4**- zoom of regions R3 and R4 in F to show co-localisation of porphyrin with mitochondrium (G)- endosomal/lysosomal and porphyrin overlaid images showing low sub-cellular localisation of porphyrins in endosomes/lysosomes; **R5** and **R6**- zoom of regions R5 and R6 in G to show co-localisation of porphyrin with endosomes/lysosomes. Olympus U-plan S-Apo 60x/NA 1.42. Scale= 15 μ m.

The sub-cellular co-localisation of porphyrin dye was then evaluated in order to create a comparison model to subsequently understand the intracellular fate of porphyrin-polyacrylamide nanosystems. Similarly as for cationic nanosystems, the determination of porphyrin intracellular fate was evaluated by fluorescent microscopy.

Figure 5.14 shows the intracellular co-localisation of porphyrins. The internalisation of porphyrin was investigated by its red fluorescent light emission (λ_{em} 630 nm). As for cationic nanosystems (Section 5.2.2.1), the intracellular fate of porphyrin dye was studied in regard to two main compartments, the mitochondria and endo/lysosomes. Using mitotracker green for mitochondrial staining and lysotracker blue for endo/lysosomal staining, as can be seen in Figure 5.14 (B) and (E), it is possible to observe the intracellular distribution of porphyrin dye throughout the cytoplasm and outside of the nucleus. Moreover, no porphyrin dye was found to interact with the extracellular membrane. In addition, the analysis of porphyrin/ mitochondria interaction, (F), revealed that the porphyrin dye was not found co-localised with mitochondria. The analysis of porphyrin dye co-localisation with endo/lysosomes, (see Figure 5.14 (G)); R5, R6 also reveals low co-localisation patterns with these vesicles.

The results shown in Figure 5.14 contradict the general literature for cationic porphyrins, which states that the delocalised positive charge on porphyrins facilitates their interaction (all porphyrins have three positive charges) with the charged lipids on the extracellular membrane and facilitates diffusion and interaction with the negatively charged inner mitochondrial membrane [187, 207–209]. Pavani, *et al.* reported on the efficiency of several porphyrins to target mitochondria

through their charge-facilitating mitochondrial co-localisation [187]. Their study showed that porphyrins targeting mitochondria are not only dependent on the overall charge of the porphyrin, but also on the metal centre. They found that metallated cationic porphyrins would present lower interaction with mitochondria than the free base. In addition, it was suggested that incorporation of a zinc metal on the cavity of the macrocycle increases the hydrophilicity of porphyrins, diminishing their ability to interact with the hydrophobic membranes [187, 210]. Although it was found that the zinc insertion decreased the porphyrin mitochondrial interaction, it was also found that zinc increased intracellular interaction with membranes. In addition, it was stated that the photodynamic efficiency of zinc porphyrins was independent of the photosensitizer intracellular co-localisation [187].

Additionally, to investigate the toxicity of porphyrins in hMSCs in the absence of light activation (dark toxicity), cells were incubated with porphyrin dye for 15 hours and analysed by flow cytometry (Figure 5.15).

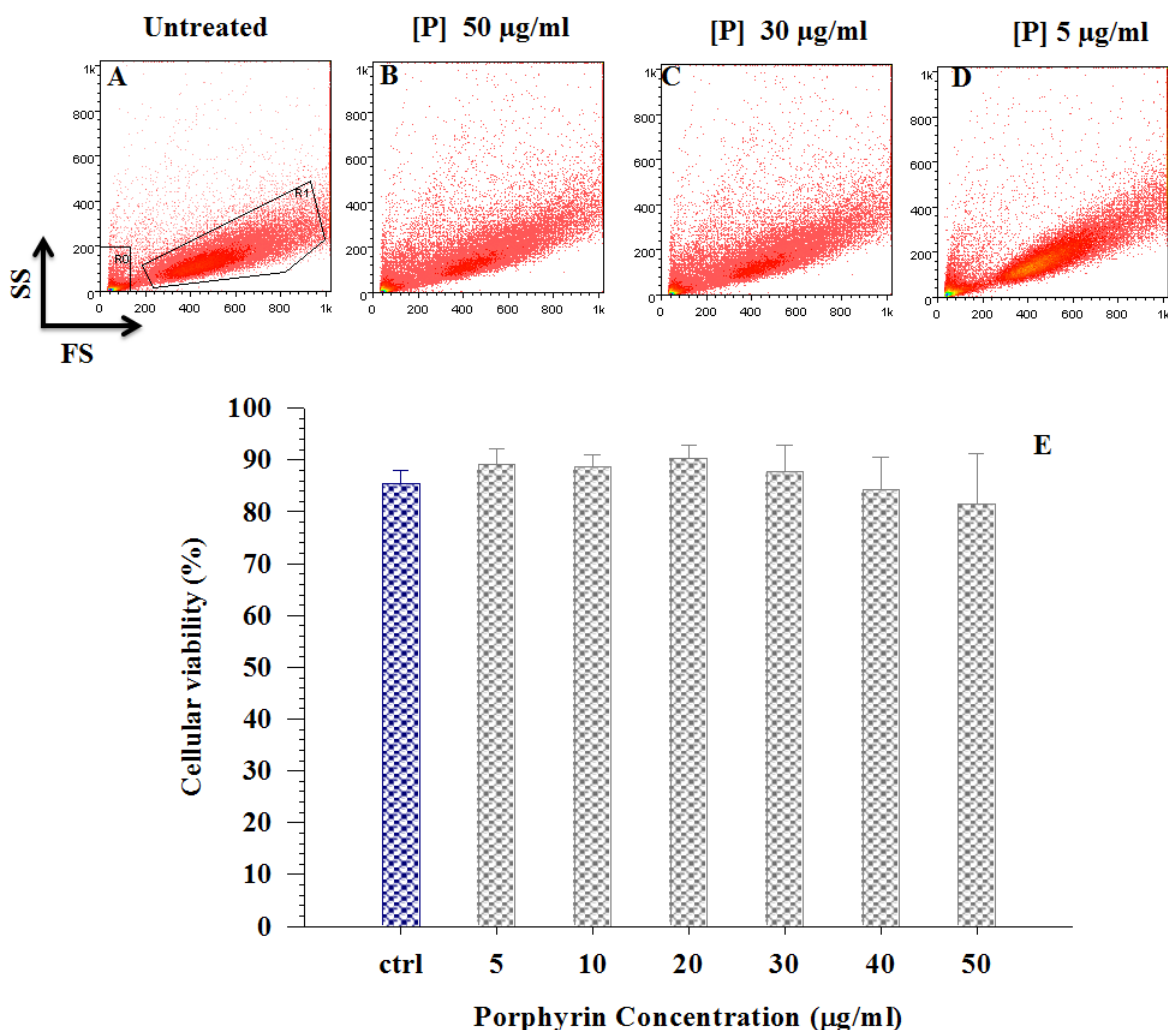


Figure 5.15: Analysis of cellular viability in hMSCs treated with porphyrins by flow cytometry. hMSCs were treated overnight with several doses (5, 10, 20, 30, 40, 50 µg/ml) of porphyrin. Representative bi-variate plots: (A)- untreated cells; (B)- cells treated with 50 µg/ml; (C)- cells treated with 30 µg/ml; (D)- cells treated with 5 µg/ml, show no alteration in population density for treated and untreated cells. Graph (E) shows the impact of porphyrin in cellular viability; no alterations were found in viability. Percentage of viability was calculated from two independent experiments conducted in triplicate. Error bars represent mean \pm SD (n=6). Statistical analysis, $p > 0.05$ not statistically different, One Way ANOVA.

The bi-variate plots in Figure 5.15, show no alterations in population density (gated area A) for treated (B), (C) or (D) and non-treated (A) hMSCs. Additionally, the analysis of percentage of cellular viability did not show significant alterations in hMSCs.

The results obtained suggested that the porphyrins in study do not present signi-

ficant dark toxicity.

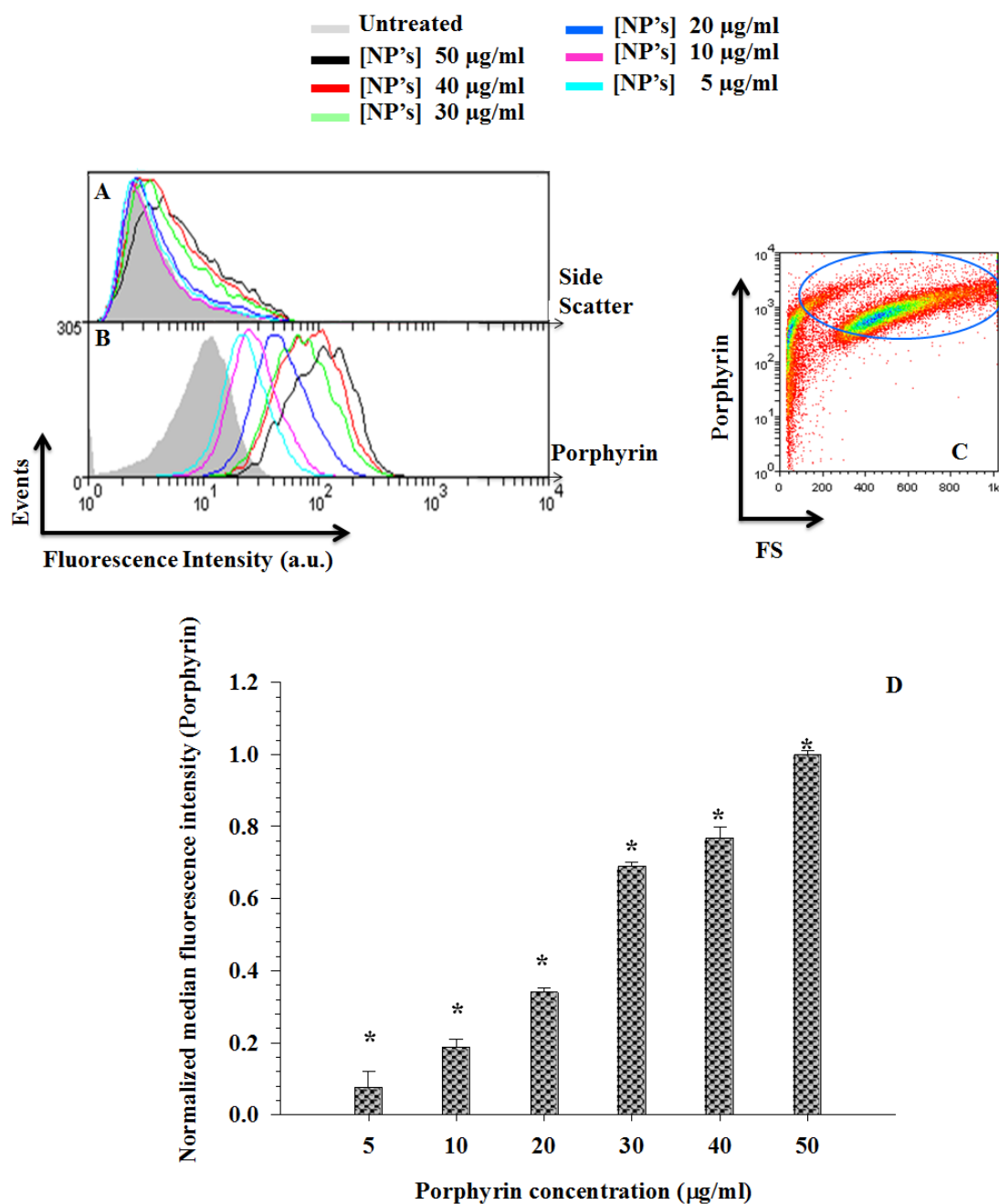


Figure 5.16: Analysis of cellular uptake of porphyrin in hMSCs treated by flow cytometry. hMSCs were treated overnight with several doses (5, 10, 20, 30, 40, 50 $\mu\text{g/ml}$) of porphyrin. Representative histogram of porphyrin uptake: (A)- Side scatter analysis showing increase in cellular complexity with the increase of porphyrin concentration. (B)- Porphyrin fluorescence intensity increases with the concentration of porphyrin. (C)- Representative bi-variate plot analysis of cell populations positive for porphyrin. (D)- Graph of porphyrin median fluorescence intensity with the concentration of porphyrin. It can be observed that the fluorescence intensity increases with the dosage of porphyrin. Error bars represent mean \pm SD (n=6). Statistical analysis, * $p < 0.05$ were considered statistically different, One Way ANOVA.

The porphyrin uptake studies reveal that porphyrins are passively uptaken by hMSCs. As shown in Figure 5.15 (A), the increased internalisation of porphyrins leads to an increase in cellular complexity/granularity in a dose-dependent manner, as seen by the variation in side scatter intensities for treated and non-treated cells. Furthermore, as shown in B, the variation in dosage of porphyrin leads to different patterns of uptake. As the dosage of porphyrin increases, a significant increase in uptake was verified, as shown by the graph in Figure 5.15 (D). Similarly, Peng *et al.* have shown an increased uptake of cationic porphyrins by HeLa cells [211]. Therefore, the results obtained suggest that porphyrins are efficiently internalised.

Taken together, the results indicate that the porphyrins in study were internalised in cells. Additionally, when investigating their cellular fate, a cytoplasmic concentration (Figure 5.14) was found. However, it was not possible to determine their specific sub-cellular fate, as co-localisation with mitochondria or endo/lysosomes was not observed.

5.2.2.2 Effects and internalisation of porphyrin-nanoparticle conjugates (ZnPATNPCs).

In order to investigate the delivery of porphyrin-nanoparticle conjugates to hMSCs, cell survival under a bright field light was firstly analysed. Below are shown the time-lapse images for a total of 16 hours (acquired every 30 min) of hMSCs treated with porphyrin-nanoparticles conjugates. Figure 5.17 shows that hMSCs were able to survive for the full period of imaging without any deleterious effects.

The results indicate that it is possible to proceed to real time imaging of hMSCs under experimental conditions. Furthermore, it was also possible to verify that no activation of porphyrins was achieved.

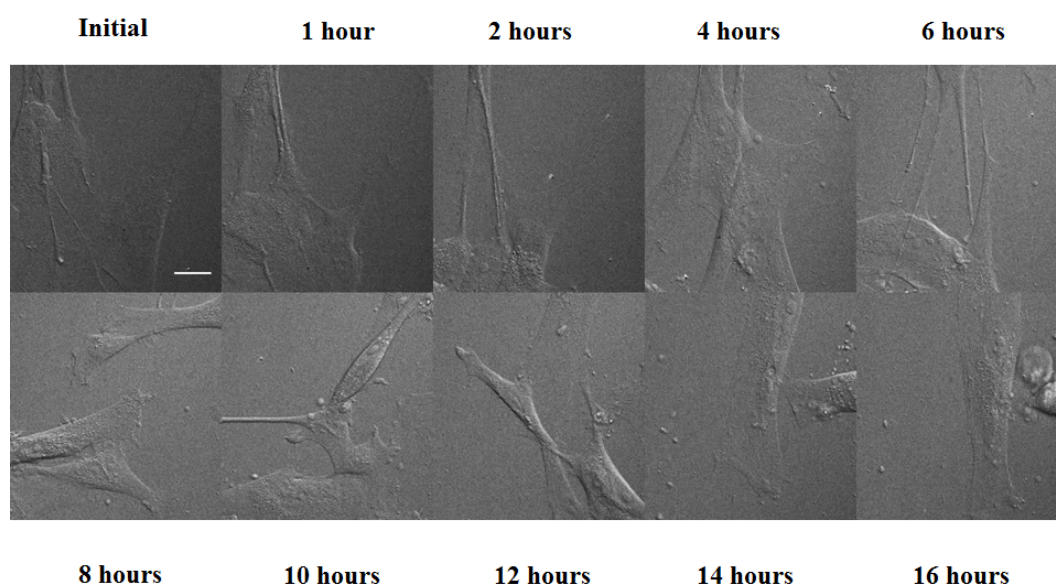


Figure 5.17: Representative timelapse *live cell* imaging of hMSCs treated with 5 mg/ml of ZnPATNPCs. Differential interference contrast images were collected every 30 min for a total period of 16 hours. Imaging performed with widefield Olympus Deltavision elite deconvolution fluorescent microscope, Olympus U-plan Apo 40x/ NA.0.95

The intracellular fate of ZnPATNPCs in hMSCs by fluorescence microscopy was then investigated. The internalisation of ZnPATNPCs was investigated by the red emitted light fluorescence of porphyrins ($\lambda_{\text{exc}}=575$ nm, $\lambda_{\text{em}}=630$ nm).

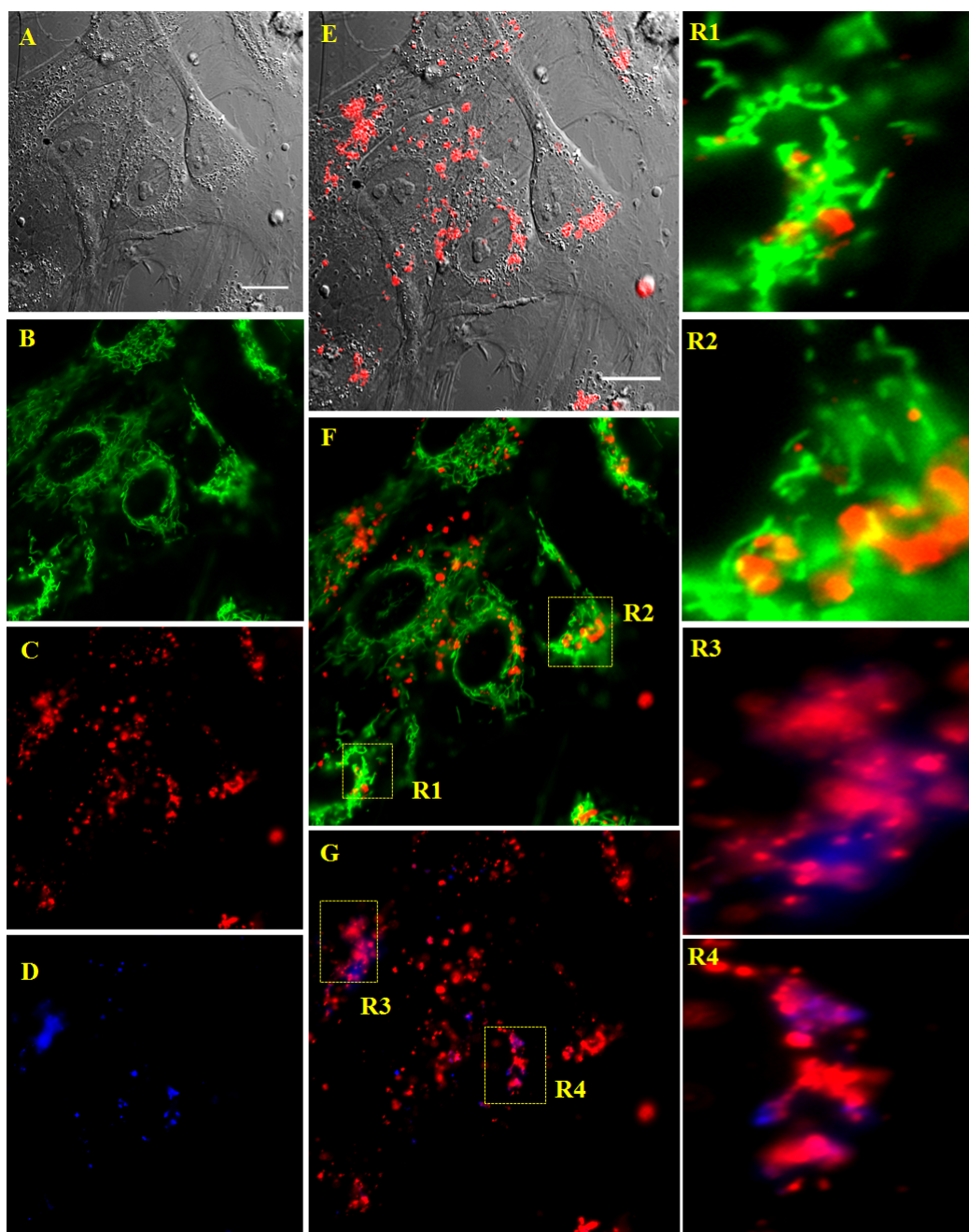


Figure 5.18: Representative analysis of intracellular co-localisation of ZnPATNPCs with mitochondria and endo/lysosomal vesicles by widefield Olympus Deltavision elite deconvolution fluorescent microscopy. (A)- Differential interference contrast of hMSCs. (B)- hMSCs mitochondrial staining with mitotracker green; $\lambda_{exc}=488$ nm, $\lambda_{em}=526$ nm. (C)- Porphyrin emission (ZnPATNPCs); $\lambda_{exc}=575$ nm, $\lambda_{em}=630$ nm. (D)- endo/lysosomal staining with lysotracker blue; $\lambda_{exc}=399$ nm, $\lambda_{em}=457$ nm. (E)- Differential interference contrast and ZnPATNPCs overlaid images showing that ZnPATNPCs are distributed throughout the cytoplasm. (F)- mitochondrial and porphyrin images showing partial concentration of porphyrins in mitochondrias **R1** and **R2**- zoom of regions R1 and R2 in F to show co-localisation of porphyrin with mitochondrium (G)- endosomal/lysosomal and porphyrin overlaid images showing low sub-cellular localisation of ZnPATNPCs in endo/lysosomes; **R3** and **R4**)- zoom of regions R3 and R4 in G to show co-localisation of porphyrin with endo/lysosomes. Olympus U-plan S- Apo 60x/NA 1.42. Scale= 17 μ m.

Figure 5.18 shows the analysis of co-localisation of ZnPATNPCs in hMSCs. The overlay of differential interference contrast (**A**) and porphyrin emission (**C**) images shows the distribution of nanoparticles in the cytoplasm and outside the nucleus. In addition, mitochondrial co-localisation studies, (**F**) R1 and R2, indicate that porphyrins present a partial co-localisation pattern with mitochondria. These results are different to those found for free porphyrin, where mitochondrial co-localisation was not attained. On the other hand, and also contrary to the results above (free porphyrin delivery) partial co-localisation was also found with endo/lysosomal vesicles. Endosomal/lysosomal co-localisation of porphyrin-nanoparticles was previously suggested by Kuruppuarachi, *et al.* however their study did not present any co-localisation studies to support the statement.

The intracellular fate of ZnPATNPC in hMSCs indicates that the covalent linkage of porphyrins to polymeric nanosystems changes the overall characteristics of the system. The free porphyrin delivery suggests that the presence of zinc in the cavity of the macrocycle tends to introduce a more hydrophilic character to porphyrins as also reported by Pavani, *et al.*, thus leading to lower concentration of these porphyrins in the mitochondrium [187]. The linkage of porphyrin to polyacrylamide vehicles seems to reverse that effect. Thus, and due to the limited number of studies in this matter, it was not possible to directly assume the use of polymeric vehicles would change the overall properties of zinc porphyrins. However, it is important to note (**F**) that no total co-localisation of ZnPATNPCs with mitochondria was achieved.

Taken together, the results above suggest that ZnPATNPCs were successfully passively internalised in hMSCs. Internalisation fate seems to be mainly directed to mitochondria, but not completely, as some co-localisation to endosomes/lysosomes was also observed. Although the present work did not aim to establish the exact mechanism of nanoparticle uptake, the results suggest the existence of more than one mechanism for ZnPATNPCs uptake. The first confers cytoplasmic access and a second would lead to vesicles entrapment.

As with free porphyrin and cationic nanosystems, the cellular toxicity resulting from nanoparticle delivery was investigated.

In Figure 5.17, the analysis of cellular viability through bi-variates plots comparing treated and non-treated hMSC populations clearly show alterations in cellular viability. In bi-variate plot (**B**), it is possible to observe a considerable increase in cell granularity/complexity and decrease in size, suggesting death; as previously reported by others [78,79,199].

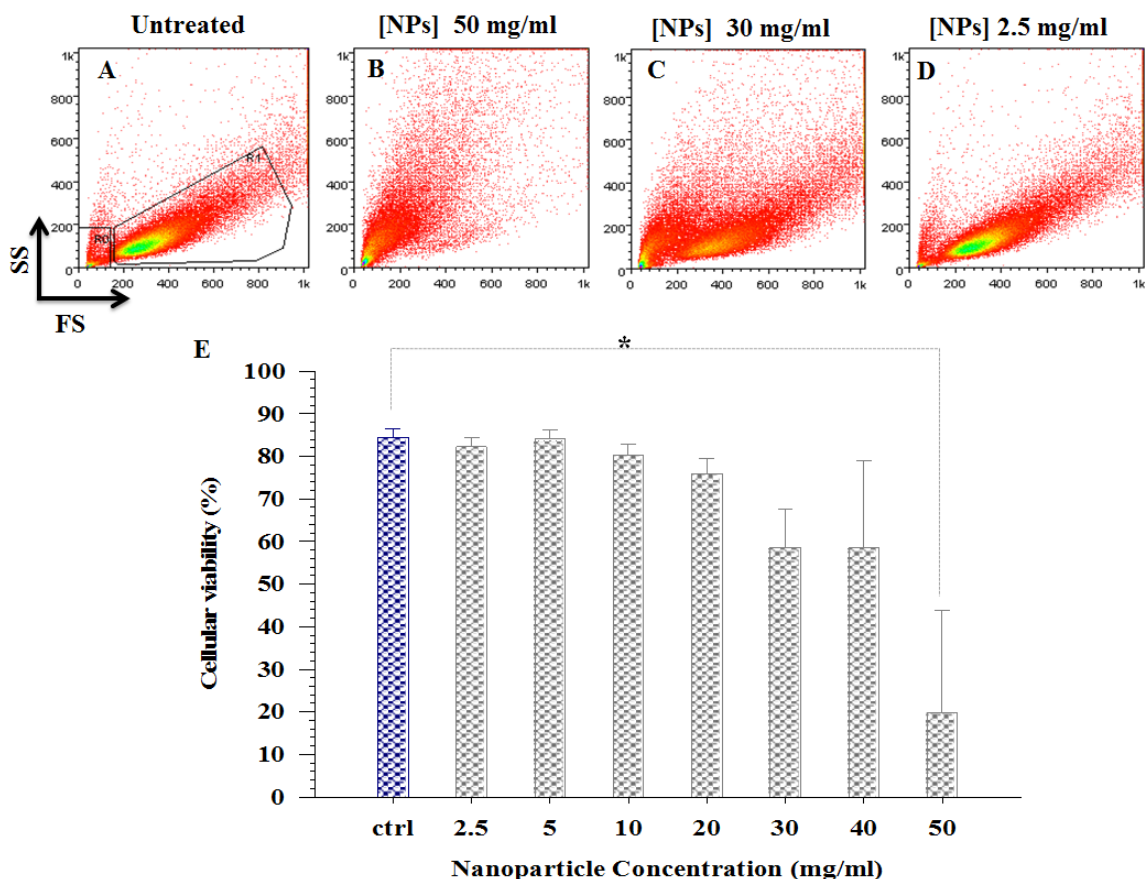


Figure 5.19: Analysis of cellular viability in hMSCs treated with ZnPATNPCs by flow cytometry. hMSCs were treated overnight with several doses (5, 10, 20, 30, 40, 50 mg/ml) of pophyrin-nanoparticle conjugates. Representative bi-variate plots: (A)-untreated cells; (B)- cells treated with 50 mg/ml; (C)- cells treated with 30 mg/ml; (D)- cells treated with 5 mg/ml, show alterations in population density (gated area) for treated and untreated cells in a dose-dependent manner. Graph (E) shows the impact of porphyrin-nanoparticle conjugates in cellular viability; it was observed that concentrations of nanoparticles of 50 mg/ml cause detrimental effects in hMSCs. Percentage of viability was calculated from two independent experiments conducted in triplicate. Error bars represent mean \pm SD (n=6). Statistical analysis, control vs. NPs 50mg/ml: * $p < 0.05$ were considered statistically different, One Way ANOVA.

Additionally, cell survival increases with the decrease in nanoparticle concentration. The comparison between treated and non-treated cells shows that only 50 mg/ml of ZnPATNPC present a significant deleterious effect on cellular viability ($p < 0.05$) with a reduction in viability observed at concentrations above 30 mg/ml.

The cellular uptake of ZnPATNPC in hMSCs was then analysed. Figure

5.19 presents the results associated with nanoparticle uptake. In (A) the histogram of side scatter analysis is shown, from which it was possible to attain subtle alterations in cells granularity/complexity in nanoparticle concentration dependence. The results suggest the increased nanoparticle uptake leads to an increase cellular complexity. Previously, Coupland, *et al.* had also reported that internalisation of polymeric nanoparticles in hMSCs resulted in an increased granularity pattern [89,203].

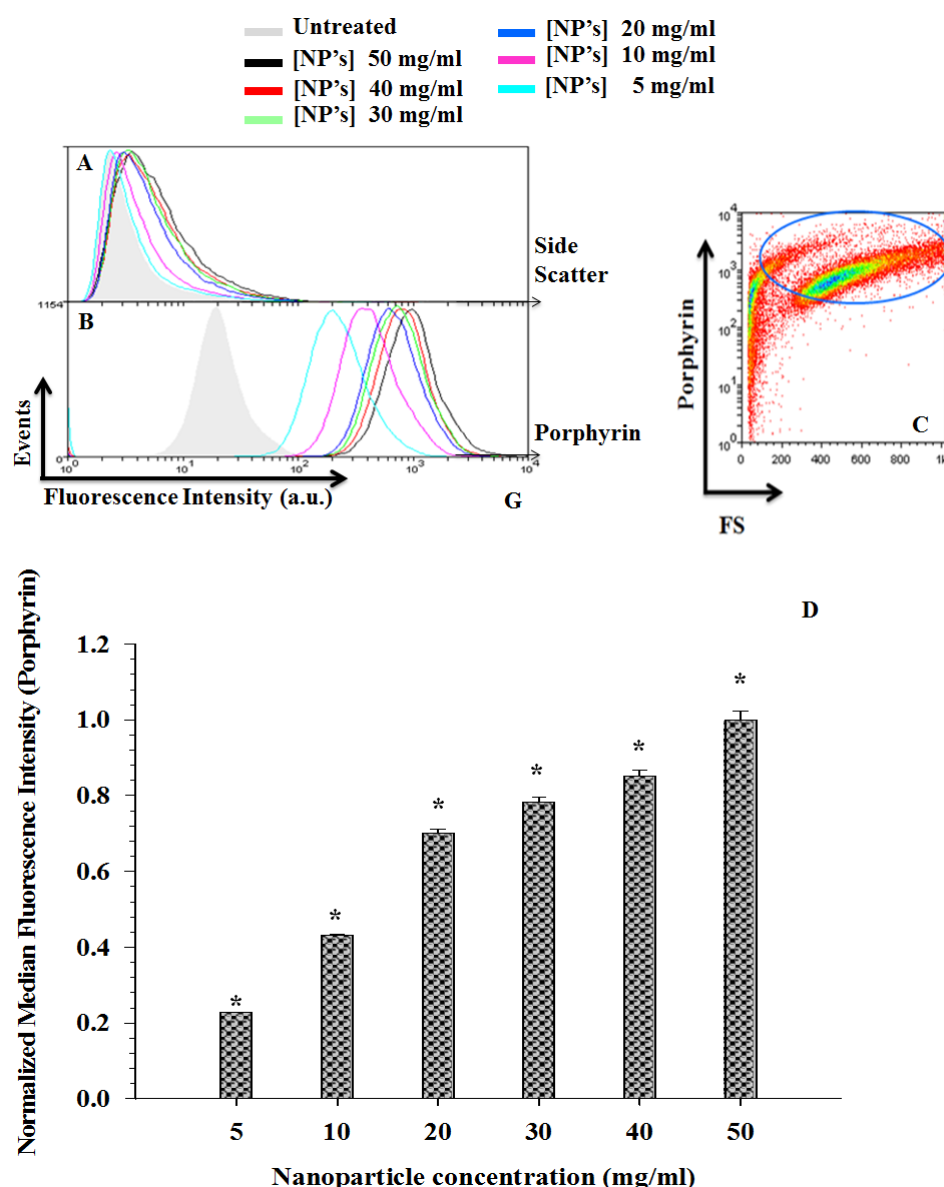


Figure 5.20: Analysis of cellular uptake of ZnPATNPCs in hMSCs by flow cytometry. hMSCs were treated overnight with several doses (5, 10, 20, 30, 40, 50 mg/ml) of ZnPATNPCs. Representative histogram of nanoparticle uptake: (A)- Side scatter analysis showing increase in cellular complexity with the increase of ZnPATNPC concentration. (B)- Porphyrin fluorescence intensity increases with the concentration of ZnPATNPC. (C)- Representative bi-variate plot analysis of cell populations is positive for ZnPATNPC. (D)- Graph of porphyrin median fluorescence intensity with the concentration of ZnPATNPC, It can be observed that the fluorescence intensity increases with the dosage of porphyrin. Error bars represent mean \pm SD (n=6). Statistical analysis, group comparison pairwise: * $p < 0.05$ were considered statistically different, One Way ANOVA.

In addition, the hypothesis of increase in granularity as a consequence of increased nanoparticle uptake can be also confirmed by the histogram of porphyrin fluorescence intensity. In (B) it is possible to observe that for higher NPs concen-

tations leads to increased porphyrin fluorescence intensity.

The graph in Figure 5.19 (D) shows the variation in median fluorescence intensity with nanoparticle concentration. The results show significant increase in porphyrin median fluorescence, significant for each increase in nanoparticle concentration.

5.2.2.3 Effects and internalisation of porphyrin nanosystems. (ZnPT-NPs)

ZnPTNPs were investigated for cell morphology under microscopic conditions. hMSCs treated with ZnPTNPs were shown to be unaffected by the imaging conditions for a period up to 16 hours, as can be observed from Figure 5.21.

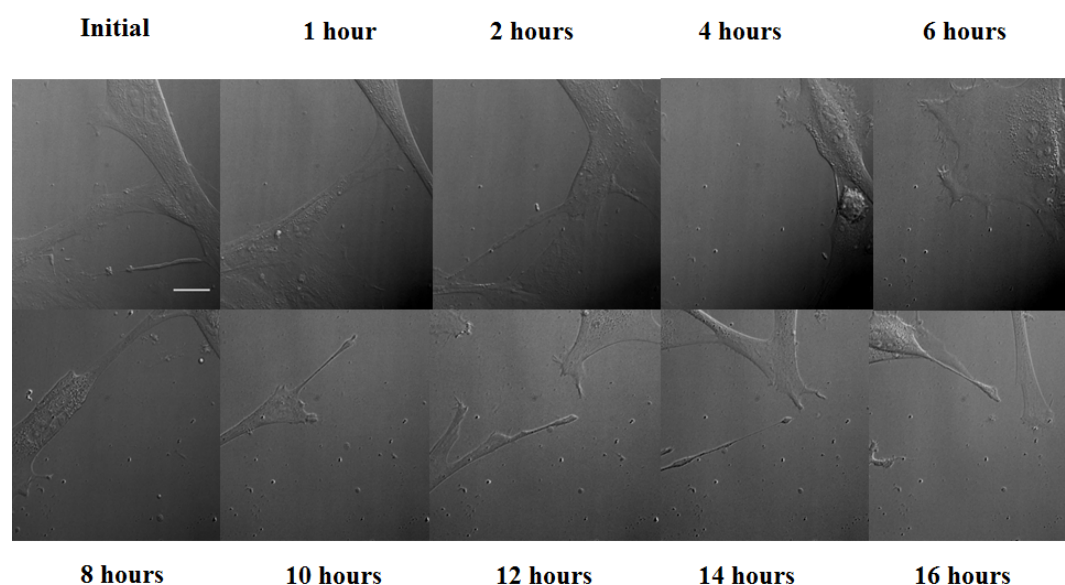


Figure 5.21: Representative timelapse *live cell* imaging of hMSCs treated with 5 mg/ml of ZnPTNPs. Differential interference contrast images were collected every 30 min for a total period of 16 hours. Imaging performed with widefield Olympus Deltavision elite deconvolution fluorescent microscope, Olympus U-plan Apo 40x/ NA.0.95

The intracellular fate of ZnPTNPs in hMSCs was then investigated. As with the nanosystems described in Section 5.2.2.2, the investigation of the sub-cellular fate of ZnPTNPs was performed by fluorescent microscopy. Figure 5.22, shows the co-localisation studies performed. The internalisation of ZnPTNPs was

followed by the detection of red emitted fluorescence (**C**) (λ_{em}). The merged differential contrast between interference image and the porphyrin emitted fluorescence showed that porphyrin was internalised in the cytoplasm of hMSCs (see Figure 5.22 (**A**);(**C**) and (**E**)) and outside the nucleus. To investigate the specific co-localisation of ZnPTNPs, the images of stained mitochondria and porphyrin were merged with the yellow fluorescence indicative of concentration of ZnPTNPs in the mitochondria (**F**). As can be observed in (**F**), and is more detailed in R1 and R2, partially ZnPTNPs co-localised with mitochondria. Studies of endosomal/lysosomal ZnPTNPs entrapment was performed by the overlay of porphyrin emission (**C**) and lysosomal/endosomal staining (**D**); the pink fluorescence was an indicator of lysosomal entrapment. The merged image, 5.22 (**G**), shows the presence of lysosomal entrapment (see zoom images R3 and R4); however, it is still possible to observe the presence of red fluorescence not co-localised with lysosomes. As for ZnPATNPCs, the results of ZnPTNPs intracellular fate also suggest the presence of more than one mechanism of nanoparticle internalisation.

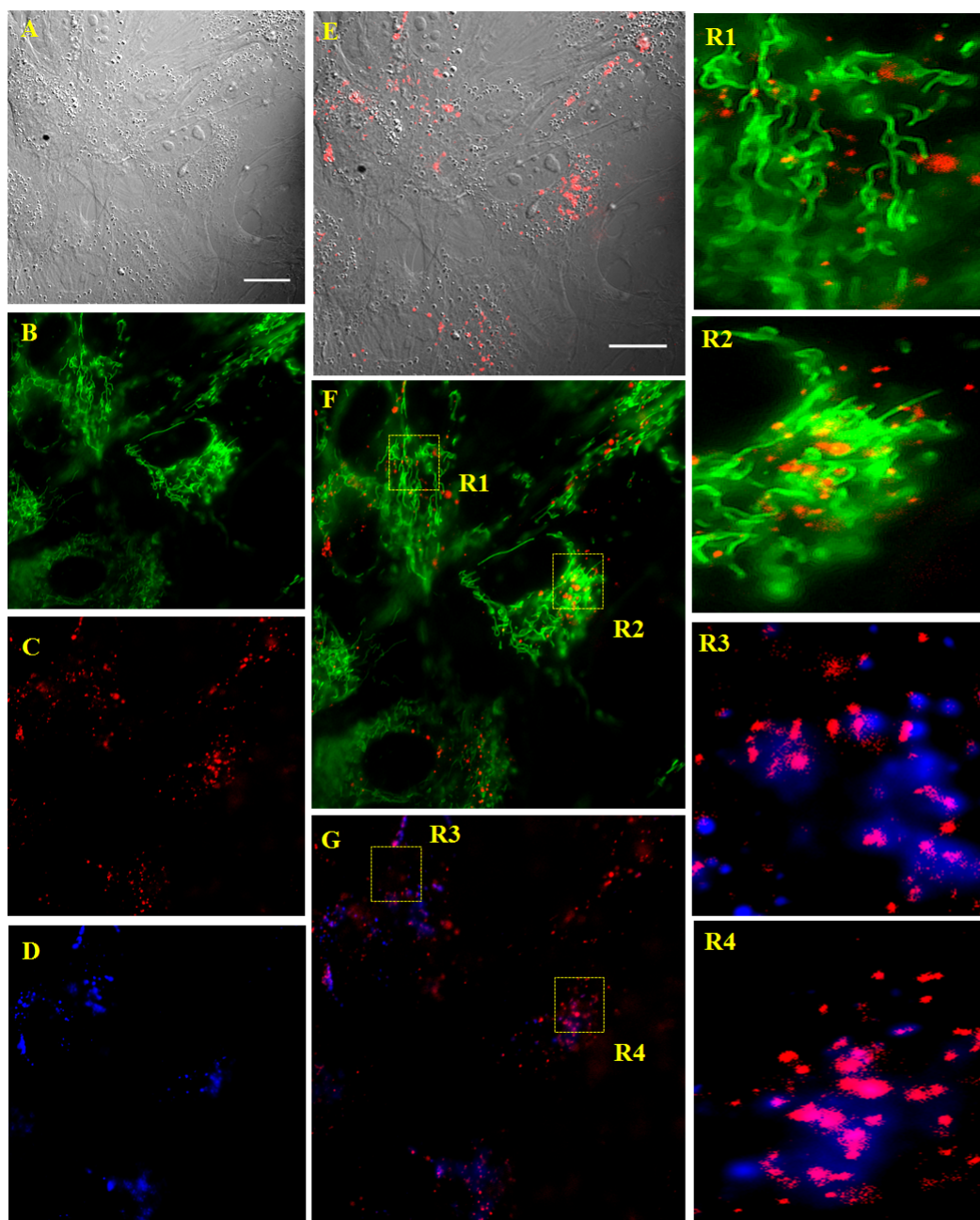


Figure 5.22: Representative analysis of intracellular co-localisation of ZnPTNPs with mitochondria and endo/lysosomal vesicles by widefield Olympus Deltavision elite deconvolution fluorescent microscopy. (A)- Differential interference contrast of hMSCs. (B)- Porphyrin emission; $\lambda_{exc}=575$ nm, $\lambda_{em}=630$ nm. (C)- endosomal/lysosomal staining with lysotracker blue; $\lambda_{exc}=399$ nm, $\lambda_{em}=457$ nm. (D)- hMSCs mitochondrial staining with mitotracker green; $\lambda_{exc}=488$ nm, $\lambda_{em}=526$ nm. (E)- Differential interference contrast and porphyrin overlaid images showing that porphyrin is distributed throughout the cytoplasm. (F)- mitochondrial and porphyrin images showing small concentration of porphyrins in mitochondria **R1** and **R2**- zoom of regions **R3** and **R4** in F to show co-localisation of porphyrin with mitochondria. (G)- endosomal/lysosomal and porphyrin overlaid images showing low sub-cellular localisation of porphyrins in endosomes/lysosomes; **R3** and **R4**- zoom of regions **R3** and **R4** in G to access co-localisation of porphyrin with endosomes/lysosomes. Olympus U-plan S- Apo 60x/NA 1.42. Scale= 12 μ m.

Analysis of hMSCs survival after incubation with increased concentrations of nanoparticles is shown in bi-variate plots in Figure 5.23. Variations in cell population density between treated (**B**),(**C**) and (**D**) and non-treated (**A**) hMSCs was observed. It was noticed that hMSCs treated with 50 mg/ml nanoparticles presented higher impact of cell viability. This can be seen, from a population (left side of the bi-variate plot) presenting low forward scatter (small cell size) and high side scatter (increase in cell complexity/granularity), which is an indicator of cellular death. That population disappears as the concentration decreases while cells treated with nanoparticles concentrations of 30 mg/ml present a significant decrease in dead cells and a more similar pattern to non-treated cells.

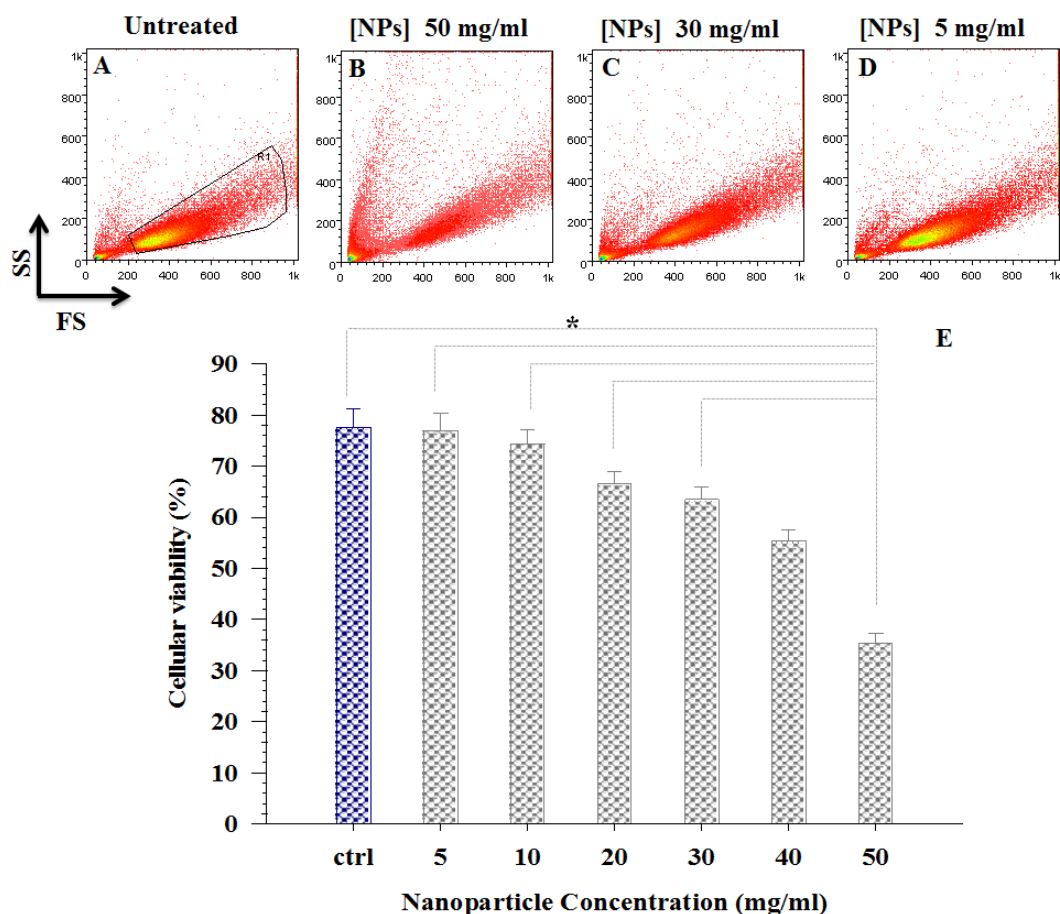


Figure 5.23: Analysis of cellular viability in hMSCs treated with porphyrin entrapped trimethyl ammonium nanoparticles by flow cytometry. hMSCs were treated overnight with several doses (5,10, 20, 30, 40, 50 mg/ml) of ZnPTNPs. Representative bi-variate plots: (A)- non-treated cells; (B)- cells treated with 50 mg/ml; (C)- cells treated with 30 mg/ml; (D)- cells treated with 5 mg/ml show small alterations in population density (gated area) for treated and untreated cells in a dose-dependent manner. Graph (E) shows the impact of porphyrin-nanoparticle conjugates in cellular viability, it was observed that concentrations of nanoparticles of 50 mg/ml caused detrimental effects in hMSCs. Percentage of viability was calculated from two independent experiments conducted in triplicate. Error bars represent mean \pm SD (n=6). Statistical analysis, all group comparison pairwise: * $p < 0.05$ were considered statistically different, One Way ANOVA.

Figure 5.23 (E) plots the percentage of cellular viability against the concentration of nanoparticles. The results support the observations iterated from the bi-variate plots; a significant difference in cellular viability was found for cell populations incubated with 50 mg/ml of ZnPTNPs ($p < 0.05$).

The results show that, as for ZnPATNPCs, high concentrations (50 mg/ml) of nanoparticles leads to deleterious effects in cell viability. It was found that for

the same concentration of nanoparticles (50 mg/ml), ZnPATNPCs (18 % cellular viability) present higher rates of cell death than for ZnPTNPs (35 % cellular viability), suggesting that ZnPATNPCs are more toxic for hMSCs.

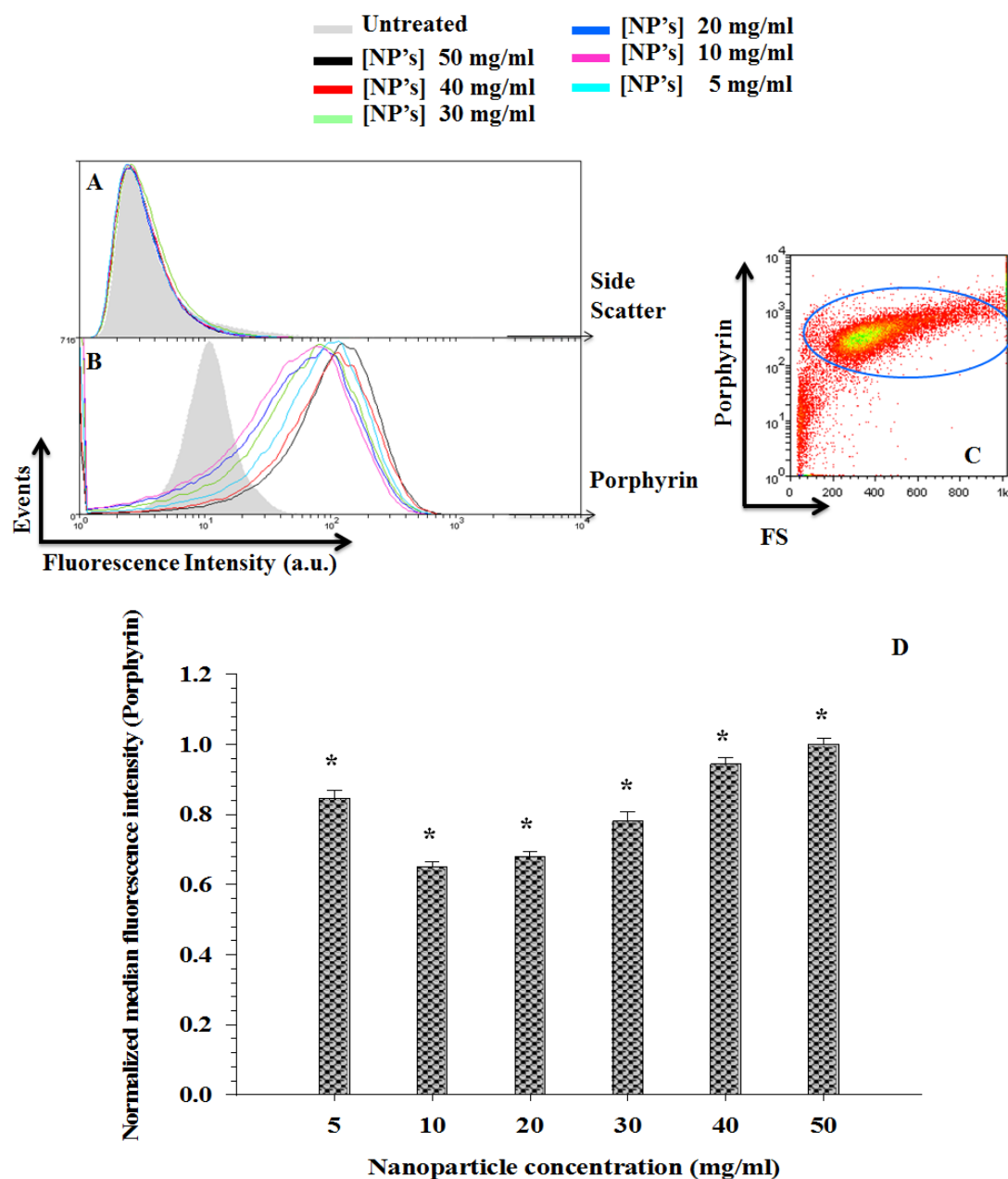


Figure 5.24: Analysis of cellular uptake of porphyrin entrapped trimethyl ammonium nanoparticles in hMSCs by flow cytometry. hMSCs were treated overnight with several doses (5, 10, 20, 30, 40, 50 mg/ml) of ZnPTNPs. Representative histogram of nanoparticle uptake: (A)- Side scatter analysis showing increase in cellular complexity with the increase of ZnPTNPs concentration. (B)- Porphyrin fluorescence intensity increases with the concentration of ZnPTNPs. (C)- Representative bi-variate plot analysis of cell populations positive for ZnPTNPs. (D)- Graph of porphyrin median fluorescence intensity with the concentration of PTNPs. It can be observed that the fluorescence intensity increases with the dosage of porphyrin. Error bars represent mean \pm SD (n=6). Statistical analysis, all group comparison pairwise: * $p < 0.05$ were considered statistically different, One Way ANOVA.

When investigating the cellular uptake of ZnPTNPs, variations in the side

scatter histogram were not found, meaning that no alterations in cell complexity/granularity were found as a consequence of nanoparticle uptake (see Figure 5.24(A)), which differs greatly from the previous nanosystems. Furthermore, from analysis of the histogram of porphyrin fluorescence intensity variations, it was found that the porphyrin intensity presented lower and less variations when compared with ZnPATNPCs. The same evidence can be observed in Graph (D) where smaller variations, although significant, were found for all the concentrations. Surprisingly, the lowest concentration (5 mg/ml) also presents higher porphyrin fluorescence intensity when compared with all other concentrations; the same evidences were found in independent experiments. These results might be a consequence of the porphyrin entrapment on the polymeric matrix, which could lead to partial quenching of the porphyrin fluorescence, justifying the lower variations in fluorescence intensity when compared with the systems above.

The results show that ZnPTNPs are efficiently delivered to hMSCs and its sub-cellular fate is mainly mitochondria while a small portion is also entrapped in endo/lysosomes. As with the previous findings for ZnPTNPs uptake by flow cytometry, fluorescence microscopy found a decreased fluorescence emission of porphyrins when compared with ZnPATNPCs. Those findings again suggest that porphyrin entrapment into the polymeric matrix might lead to some level of fluorescence quenching.

5.3 Conclusions

The present work showed the successful uptake of positively charged and porphyrinic nanoparticles in hMSCs, using live cell fluorescence imaging and flow cytometry analysis.

Positively charged nanoplateforms clearly showed an uptake on a charge dependent manner. Nanoplateforms with low levels of surface charge were seen as the most promising route for the facilitated uptake and mitochondrial co-localisation of polymeric nanoparticles in hMSCs. This study showed that it is possible to engineer nanoparticles surface with trimethyl ammonium and create specific conditions for facilitated delivery and targeting without compromising the viability of the cellular system. Although not being possible to draw a mechanism of cellular uptake, the presence of positive charge seems to be involved with endosomal escape and mitochondrial co-localisation.

In general, this project was most concerned with the development of a non-invasive nanotool that could in turn accumulate at the mitochondria, this system was achieved by multifunctional nanoplateforms containing trimethyl ammonium/porphyrin functionalities. Although, porphyrins (free state) were not accumulated to endosomes/lysosomes or mitochondria. Porphyrinic nanoplateforms, encapsulated or conjugated, were successfully delivered and preferentially accumulated in mitochondria. The above indicates that most likely the mitochondrial accumulation occurs as a result of trimethyl ammonium functionalization. The uptake of these nanosystems did not show impact in hMSCs viability up to 40 mg/ml. The main limitation was to promote a complete accumulation of

nanoplatforms at mitochondria. Further studies on the mechanisms of internalization would provide a better understanding on how to manipulate nanoplatforms surface to attain full mitochondrial association.

These results were very encouraging towards the development of a non-invasive nanotool to investigate the real time effects of ROS in hMSCs.

Chapter 6

Porphyritic nanoplatforms for the controlled generation of ROS in stimulated human Mesenchymal Stem Cells

6.1 Introduction

Oxidative stress has been correlated with several conditions such as, inflammation, cancer, Parkinsons and, Alzheimers among others neurodegenerative diseases. Oxidative stress arises from the incapacity of antioxidant systems for ROS removal. Accumulation of ROS leads to toxicity due to their high reactivity towards DNA, proteins and lipids. Despite the widespread postulation of ROS mechanisms, little is actually known about the immediate response in living cells to the generation of these highly reactive compounds. The study of the precise mechanisms responsible

for ROS pathology is challenging due to ROS high reactivity, short lifetime and difficult detection. Therefore, the development of specific tools and methodologies that could enable a deeper knowledge of its action and mechanisms would be important for the prevention and therapeutics of ROS related diseases.

6.1.1 Porphyrins: production of reactive oxygen species

Photosensitizers are molecules that absorb energy from light, at specific wavelengths, and transfer this energy to molecular oxygen, leading to production of ROS [16, 28, 212, 213]. Photosensitizers can exert its toxicity through two main mechanisms. Reactions type I, occur through electron/hydrogen transfer from the photosensitizer, which results in the production of ions, or by the removal of electron/hydrogen from the substrate molecules [1, 16, 214, 215]. Further reaction of these radicals with oxygen leads to ROS production (hydrogen peroxide, superoxide radical and hydroxyl radicals). Reactions type II, involve energy transfer from the photosensitizer to molecular oxygen, with formation of singlet oxygen. The mechanism involved in ROS production depends mainly on the type of photosensitizer [1, 16, 214, 215]. Photodynamic reactions induce oxidative stress *via* type I and type II reactions, which operate simultaneously. The prevalence ratio of these two mechanisms in cellular systems is conditioned by the photosensitizer location, target molecule and efficiency of energy transfer to molecular oxygen, consequently oxygen concentration also plays an essential role [215–217]. However, evidences exists that type II reactions are the most important in photodynamic therapy.

The amount of ROS produced through the mechanisms above, will lead to oxid-

ative stress and consequently cell death (apoptosis, necrosis or autophagy). As a result of ROS short lifetime and therefore low diffusion, the sub cellular structures damaged by these mechanisms are restricted to an area surrounding the locale of its generation and the location of the photosensitizer [30, 218–220].

6.1.2 Zinc and copper porphyrins as photosensitizers

Photophysical properties of porphyrins can be greatly impaired according to the nature of the central metal ion [221]. Metalation of porphyrins is known to primarily contribute to the strength of the porphyrinic ring through the stabilisation of its symmetry. However, metalation has additional effects on the porphyrin, which is mainly depending on the ligand structure, the type of axial ligation, the electronegativity of the metal and also the spin state of the central metal ion. The major difference between metalloporphyrins relies on their classification; they can be classified as open-shell or closed-shell in relation to the centre ion metal, which mainly influences their luminescence patterns. In the closed shell group, diamagnetic metal ions can be found as Cd(II); Mg(II); Zn (II), which are characterised by its strong fluorescence. On the other hand, open-shell paramagnetic metalloporphyrins present centers such as Cu(II); Fe(II); Mn(II) whose fluorescence is not observed [222].

In the group of closed-shell metalloporphyrins, zinc porphyrin shows up as an important model of photosensitizers. The zinc insertion on the porphyrin ring seems to provide stabilization of the porphyrinic ring, improving its action as a photosensitizer. Furthermore, the zinc metal centre was also reported as improving the interactions of the photosensitizer with membranes, thus improving the

photosensitizing activity by the oxidation of membrane lipids, which leads to the activation of chain oxidative reactions and decomposition into free radicals [187] .

On the other hand, in paramagnetic copper porphyrins, the existence of an unpaired electron in the upper orbital of the central metal ion, which interacts with the porphyrin π system, induces the formation of tri-multiplet states [223–226]. Therefore, a spin allowed transition for relaxation is enabled by the fact that the tri-multiplet state at higher energy has formally the same spin multiplicity as the ground state molecule, leading to quenching of the triplet excited state [222–226].

Aims

The present chapter aims to establish the development of a nanotool for the controlled endogenous generation of ROS in light stimulated hMSCs. It was aimed to investigate the photodynamic effects in hMSCs of activated porphyrinic nano-platforms, as developed in Chapter 4. High levels of oxidative stress induced by singlet oxygen generation are known to be lethal for cells (e.g. PDT). Therefore, multifunctional porphyrinic nanosystems were investigated and redesigned in order to reach controlled generation of ROS by cumulative exposure to light (of appropriated wavelength). It was also intended to evaluate in real time the impact of increasing oxidative stress in treated hMSCs submitted to cumulative light dosages. Thus, real time impact of ROS in cellular viability and hydrogen peroxide response was evaluated by fluorescent time-lapse microscopy.

6.2 Results and Discussion

The present chapter introduces the development of a nanoscale tool for single cell studies of ROS effects in hMSCs. Therefore, porphyrinic nanoplatforms were delivered to hMSCs. The principle of this system was to use porphyrinic moieties linked to polymeric matrices to induce the endogenous production of ROS in a controlled manner. The porphyrinic moiety acts as an ROS generator, upon light exposure of appropriate wavelength. The effects of ROS on hMSCs were then investigated using the porphyrin nanoplatforms developed in Chapter 4 (Fig. 6.1) and whose delivery to hMSCs was demonstrated in Chapter 5.

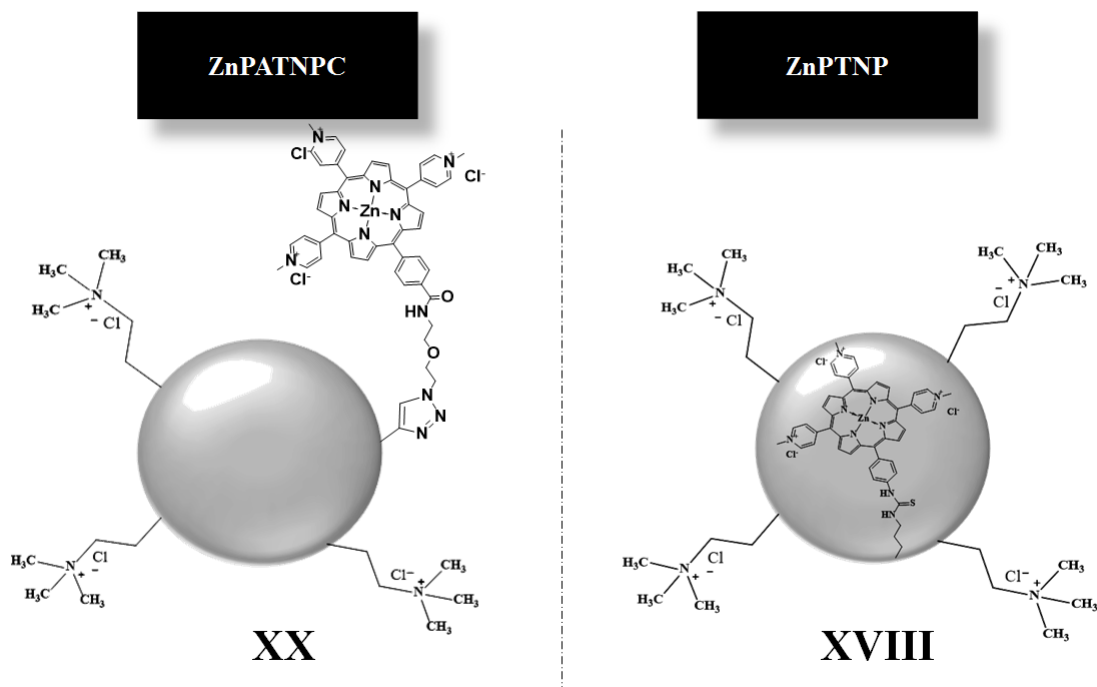


Figure 6.1: Schematic representation of the porphyrinic nanoplatforms in study. ZnPATNPC- zinc porphyrin nanoparticle conjugates and ZnPTNP- zinc porphyrin entrapped nanoparticle conjugates.

For the porphyrinic nanoplatforms in study, the exact amount of photosensitizer conjugated at the surface or entrapped is unknown. The functionalization of

nanoparticles is hampered by the random nature of the free radical polymerisation of polyarylamide, making it impossible to establish the number of functionalities introduced in the synthesis of the nanoparticles or the concentration of porphyrin. Thus, in the development of both nanoplateforms (ZnPTNPC and ZnPTNP), a maximum of porphyrin was reacted, achieved by adding an excess of porphyrin. The presence of porphyrin fluorescence on the supernatants during the purification step confirmed that an excess of photosensitizer molecules was used. In order to introduce similar amounts of photosensitizer in both nanosystems, the same number of moles were reacted with ATNPs (ZnPATNPC) and polymerised in ZnPTNPs. However, it is worth noting that this methodology only aimed to approximate the amount of photosensitizer and differences were expected in both nanosystems, due to the interactions and reactivity of photosensitizers and reaction components.

6.2.1 Porphyrin-NPs:ROS generation in hMSCs

6.2.1.1 Detection of ROS

To study the oxidative response in hMSCs, as a consequence of photosensitizer activation, a fluorescent reporter molecule toward ROS was used. The major limitations in the detection of ROS are associated with their short lifetime and high reactivity (in the order of ns); most of the commercially available probes do not respond specifically to one type of ROS and/or are affected by other nonspecific chemical interactions [227, 228].

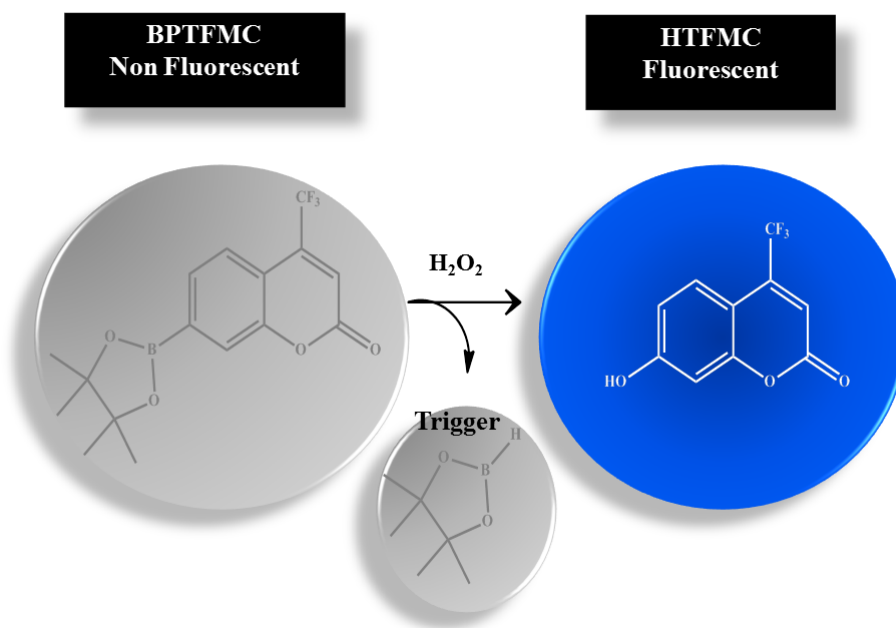


Figure 6.2: Detection of H_2O_2 through its reaction with 4-trifluoromethyl coumarin pinacol boronate (BPTFMC) with the release of pinacolborane (trigger) leading to the release of the fluorophore active form, 7- hydroxy-4-(trifluoromethyl) coumarin (HTFMC).

The present study chose a fluorescent reporter towards H_2O_2 developed by Alhaj Zen, (as part of his PhD project, Nottingham University, 2013). The molecule BPTFMC is a modified coumarin based fluorophore whose fluorescence is masked by the presence of a boronate group, as represented in Figure 6.2. In the presence of H_2O_2 , the trigger is cleaved, affording the fluorescent reporter molecule HTFMC.

6.2.1.2 Imaging hMSCs: Multichannel fluorescence stitching

To study the effects of porphyrin activation on hMSCs, the wavelength of its activation was determined. Porphyrins spectra presented several absorption points which could be used. However, it was anticipated that lower wavelengths (<550 nm) would lead to inefficient photosensitization due to competitive absorption with

other molecules which lead to reduced photosensitization [16,28]. In order to avoid compromising the photosensitizer activity and ROS modulation, a wavelength of diminished absorption, 575 nm, was chosen. Characteristically, the action of photosensitizers is limited to the area of irradiation, this being one of the main advantages of photosensitizers in therapeutic applications (avoiding side effects in non-diseased cells). This localised activity has been reported to be a consequence of the high reactivity of ROS and low diffusion patterns [1, 16, 18, 25, 30, 229]. In order to evaluate the cytotoxic effects of activated porphyrinic nanoplateforms, a multichannel fluorescence imaging was performed. Due to the damage of photosensitizers being restricted to the irradiated area, the imaging was performed in irradiated and surrounding areas. As schematically represented in Figure 6.3, the LED light source for photosensitizer activation was achieved by transmitted LED light at 575 nm from an Olympus inverted microscope. The experimental design was aimed to allow a real time observation of the effects of photosensitizer activation.

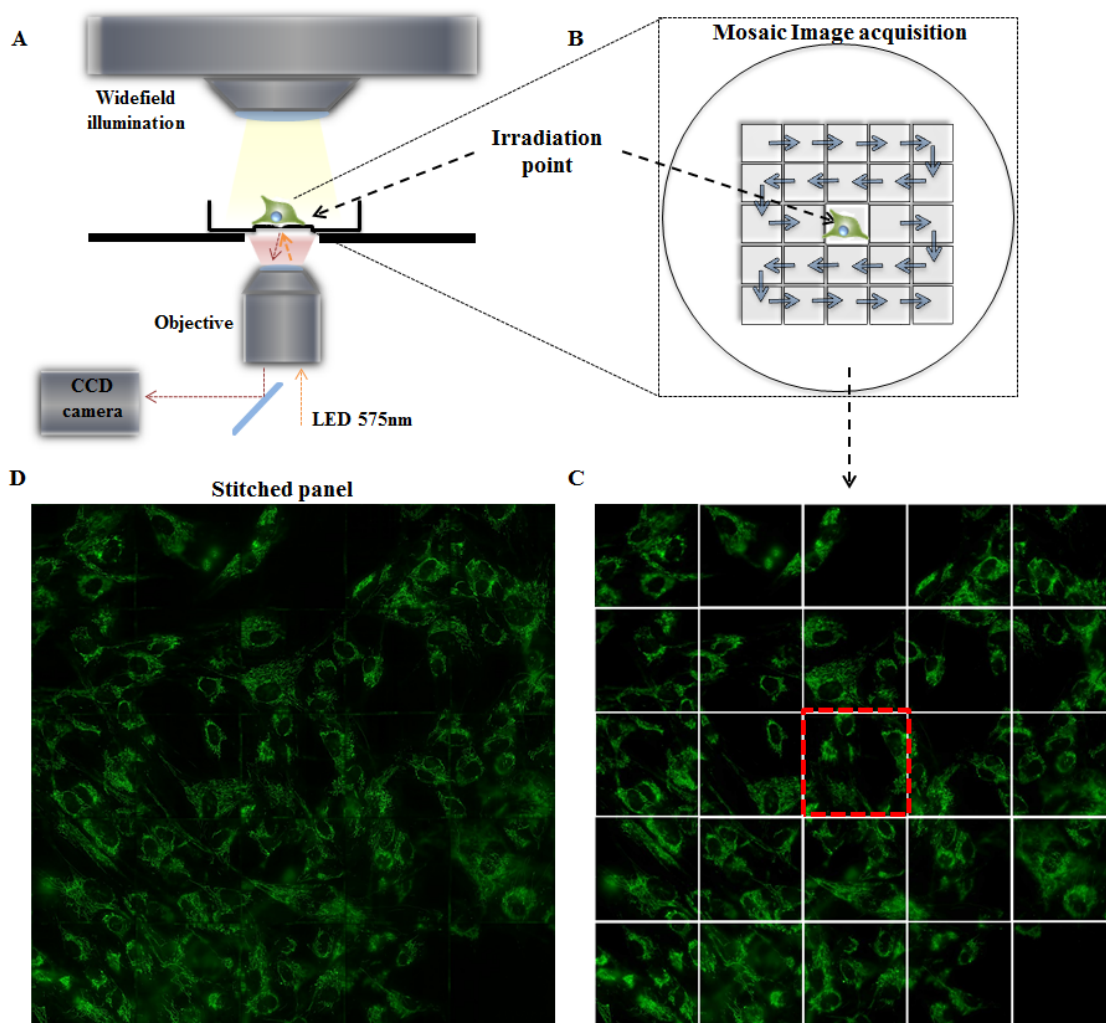


Figure 6.3: Schematic representation of live cell experimental design for studying photosensitizer activation. Untreated cells were irradiated with LED light from a widefield Olympus delta vision elite deconvolution fluorescent microscope, Olympus U-lan S- Apo 60x/NA 1.42. hMSCs stained with mitotracker green $\lambda_{exc}=488$ nm ; $\lambda_{em}=511$ nm. (A): experimental design of cell irradiation. (B): multichannel mosaic image acquisition to observe effects of porphyrin activation on the surrounding cell population. (C): mosaic of collected images, irradiation point at image 13 (red dotted line- central image) of 25 acquired images. (D): combination of mosaic images into a single panel, stitching performed by software *softWoRx*.

For this experiment, and due to photosensitizer activation, it was necessary to establish a fluorescence method to visualize the cellular effects of ROS (e.g. cell viability). In addition, considering the photosensitizer activation wavelength (575 nm), it was necessary to consider a viability fluorochrome that would not absorb light at any of the porphyrin excitation points (430 nm; 575 nm; 610 nm).

Therefore, hMSCs were stained with a cationic membrane-permeant fluorochrome which accumulates preferentially in the mitochondrial matrix by differential potential (staining mitochondria). In this experiment, mitochondrial alterations due to ROS toxic effects were visualized by the use of mitotracker green (MTG).

6.2.1.3 Effect of porphyrin-NPs on cells when irradiated with light

Porphyrin activation was achieved by exposure of treated hMSCs, (whith either ZnPATNPC or ZnPTNP), to a single light dosage of 512 μ W/2 sec at 575 nm wavelength, as shown in Figure 6.4.

For non-treated hMSCs (control; top panel) toxic effects by light exposure were not observed, suggesting that the chosen wavelength did not affect hMSCs. Absence of HTFMC fluorescence also indicates the absence of H₂O₂ generation when cells were exposed to this level of light. In addition, it was also possible to observe that the fluorochrome HTFMC was unresponsive to the intracellular environment of hMSCs.

For hMSCs incubated with ZnPATNPC, alterations in cellular morphology were observed, represented by white arrows in the DIC image (middle panel; **D**). Likewise, a "blast zone" is visible at the centre of the image in the proximity of irradiation, indicated by the absence of MTG staining. The blurred fluorescence of mitotracker green suggests the loss of mitochondrial integrity, as previously reported by Pendergrass, *et al.* [198]. In addition, an increase in fluorescent emission of HTFMC (blue fluorescence; **F**), a consequence of BPTFMC activation, is indicative of H₂O₂ production.

Similarly with the control cells, hMSCs incubated with ZnPTNPs did not show

alterations either in cellular morphology or viability (bottom panel; **G/H**), indicating that entrapment of photosensitizers in the polymeric matrix depresses photosensitizer activity. As for HTFMC fluorescence, different levels of response (bottom panel; right) were observed. Low fluorescence intensity of HTFMC suggests low production of H_2O_2 , thus small photodynamic effect at the irradiation point was found. Mitotracker green also shows the staining of individual mitochondria, which indicates integrity of the organelle [198].

At this stage it was not possible to use a fluorescent dye responsive to variations in mitochondrial membrane potential, which would have given a better idea of cell viability, (MMP) due to the absorption and emission points of porphyrin and spectral overlap with most MMP sensitive dyes (i.e. mitotracker red).

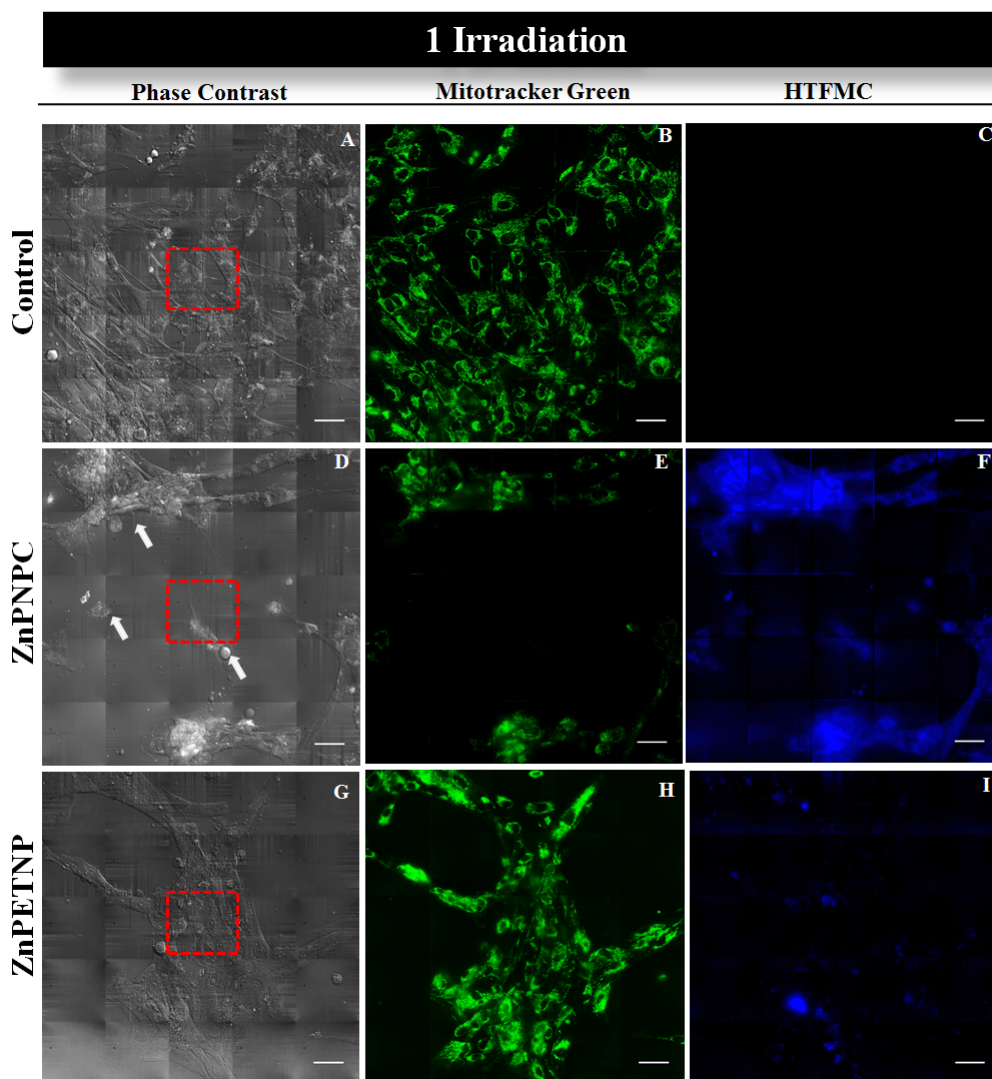


Figure 6.4: Multichannel 2D mosaic imaging. hMSCs were stained with mitotracker green, incubated with BPTFMC, single irradiated and visualized by a widefield Olympus delta vision elite deconvolution fluorescent microscope, Olympus U-lan S- Apo 60x/NA 1.42. hMSCs were incubated overnight with porphyrinic nanoplateforms (ZnPATNPC or ZNPTNPs), incubated with BPTFMC $\lambda_{exc} = 390$ nm and $\lambda_{em} = 435$ nm for its active form HTFMC and stained with mitotracker green $\lambda_{exc} = 488$ nm ; $\lambda_{em} = 511$ nm. Scale= $51\mu\text{m}$. Stitched mosaic image generated from 25 microscopic fields. Point of irradiation represented by the dotted red line. Control cells (top panel) do not show alterations in the pattern of cell morphology (A) or mitotracker green staining (B) it also shows the absence of BPTFMC activation by ROS, H_2O_2 , thus the absence of blue fluorescence (C). On the other hand, cells incubated with ZnPATNPC (middle panel) indicate high cellular damage upon single light stimulation visualised by phase contrast (D), loss of mitochondrial delimited staining (E) and conversion of BPTFMC into the active form HTFMC with the consequent appearance of blue fluorescence (F). hMSCs incubated with ZnPTNPs (bottom panel) on phase contrast image show little response to single light dosage (G), which can be further confirmed by mitotracker green staining (H), non specific and little response to BPTFMC activation is present (I).

The previous results, as expected, suggest that the amount of photosensitizer

conjugated to polyacrylamide nanoparticles leads to immediate cellular damage at the irradiation point and surrounding areas, which is hypothesized to be a consequence of a burst of ROS. Subsequently, it was also possible to anticipate that ZnPATNPC would be a better system to modulate ROS generation in hMSCs, given that ZnPTNPs have not demonstrated a homogeneous response of HTFMC. These results contradict the previous reports of Gao, *et al.* [69, 230], which stated that encapsulation of photosensitizers does not alter their photosensitizing activity. However, random cellular damage and low photosensitizing activity was also present in their results [69, 230]. Other studies reported the non-interference of polyacrylamide matrix in the singlet oxygen production [62, 230]. It is hypothesized that porphyrins covalently linked to the polyacrylamide matrix might not produce a homogeneous distribution of porphyrin throughout the nanoplateforms, leading to a lower photodynamic activity.

6.2.2 ZnPATNPC for the controlled generation of ROS in hMSCs.

Based on the previous results (Section 6.2.1), ZnPATNPC was selected as the model system to be used in the modulation of ROS generation in hMSCs. It was anticipated that to achieve that system it would be necessary to adjust light dosage or the amount of photosensitizer conjugated at the surface of nanoplateforms. The adjustment of light dosage was not considered to be a valid approach given that, for live cell studies, the exposure conditions were already minimal. Therefore, the adjustment of the photosensitizer at the surface of the nanoparticles was selected, as the best approach to control the amount of ROS generated by stimulated

hMSCs. At this point, in order to achieve a nanoplatform capable of inducing intracellular ROS generation in a controlled manner, it was firstly necessary to develop porphyrinic-nanoplatforms unresponsive to single light dosage upon photosensitizer activation. The rationale behind this approach was to decrease the amount o photosensitizer to a level that confers little production of singlet oxygen, upon single light dosage. Subsequently, an increase in the intracellular amounts of ROS would be achieved by the administration of increasing light dosages.

6.2.2.1 ZnPATNPC: Modulation of conjugated porphyrin

The present section concerns the development of porphyrinic nanoplatforms unresponsive to single light dosage. As previously discussed in Section 6.2 the photosensitizer concentration conjugated with ATNPs was difficult to attain due to the random nature of free radical polymerisation and functionalisation of these nanosystems. Therefore, for the development of a new nanosystem, ATNPs were titrated with photosensitizer. The original porphyrinic nanoplatform previously investigated (Section 6.2) was used as a reference and labelled as 100% ZnPATNPC.

For the design of a new porphyrinic nanoplatform, it was considered necessary to maintain the physico-chemical characteristics of the previous systems. Therefore, it was reasoned that the trimethyl ammonium functionality (2.5 %) would confer a positive net charge necessary to maintain passive cellular uptake and mitochondrial co-localisation. In addition, decreased amounts of porphyrin would be conjugated to the NPs.

6.2.2.1.1 Size and surface charge characterisation of ZnPATNPC.

For the adjustment of particle surface charge for titrated porphyrin, the knowledge achieved in the third and fifth chapters was used. It was found that for mitochondrial co-localisation would need a total net charge between $+12\text{ mV}$ and 20 mV . Therefore, alkyne/trimethyl ammonium NPs (ATNPs) were developed with net surface charge of approximately $+13\text{ mV}$. Further increase in surface charge would be conferred by the conjugation of the tricationic porphyrin, which contributes with three positive charges each.

Figure 6.5 shows the surface charge (**A**) and size characterisation (**B**) of NPs titrated with porphyrin. Surface charge results show ATNPs present a zeta potential of approximately $+13\text{ mV}$. Further conjugation with an excess of Zn porphyrin (100 % ZnPATNPC) leads to an increase in surface charge to $+23\text{ mV}$. This system had been previously shown to generate a burst of ROS in hMSCs upon a single light irradiation. For nanosystems containing 75 % to 25 % of Zn porphyrin coating, zeta potentials of approximately $+20\text{ mV}$ were observed. As expected, lower zeta potential values for nanosystems titrated with 10 and 5 % of Zn porphyrin ($+15\text{ mV}$) was achieved.

Taken together, the results showed it to be possible to generate nanosystems with surface charges in the range of $+12\text{ mV}$ up to $+20\text{ mV}$ which were found to confer mitochondrial co-localisation. In addition, surface charge variations in the new porphyrin nanoplatform developed suggest the successful titration of porphyrin with ATNPs.

Hydrodynamic diameter of titrated porphyrin nanoplateforms indicated that all the systems presented size compatible with cellular uptake, below 100 nm. Figure 6.5 (**B**) shows the hydrodynamic diameters of porphyrin titrated nanoparticles. For nanosystems containing a dual functionalisation (**B2**; 45 nm) compared with their non-functionalised counterparts (**B1**; 37 nm), significant variation in size was observed.

The size analysis for porphyrin conjugated nanosystems observed an increased hydrodynamic diameter compared to their functionalised counterparts. For the different titrated porphyrin conjugates, low variations in size were identified, a hydrodynamic diameter of around 80 nm.

With regards to zeta potential, variations in surface charge of the titrated porphyrin conjugates were observed as expected. Higher surface charge was obtained for alkyne trimethyl ammonium nanoparticles reacted with an excess of porphyrin (100 % ZnPATNPCs) whilst decrease in porphyrin conjugated at the surface led to proportional reductions for the remaining porphyrin titrated conjugates.

It is hypothesized that the increase in size upon porphyrin conjugation might be associated with the variations in surface charge. The same evidences was previously reported by Rubinstein, *et al.* and others [59, 124] for cationic polymeric nanosystems. One of the suggestions from these observation related to positive charge covalently bonded to the hydrogel matrix (trimethyl ammonium functionalisation) increasing the osmotic pressure in consequence of dissociated counterions, leading to hydrogel swelling.

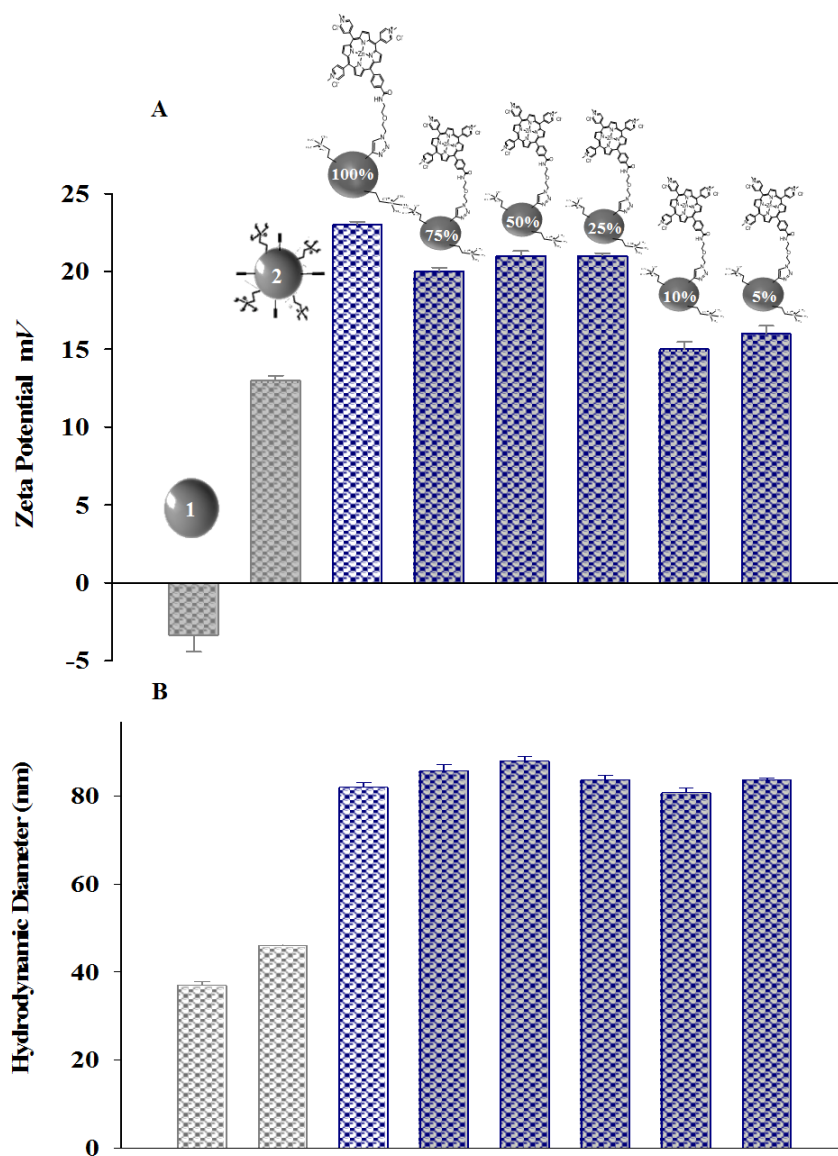


Figure 6.5: Characterisation of functionalised nanoplateforms comparison with their porphyrin conjugated counterparts. **A.** shows the zeta potential results. **B.** hydrodynamic diameter of the resultant systems (1) control PANPs, (2) dually functionalised (ATNPs); (100%) ZnPATNPCs, (75- 5 %) PATNPCs.

6.2.2.1.2 Fluorescence characterisation of ZnPATNPC Variations in photosensitizer conjugated with ATNPs in titrated nanosystems was evaluated by fluorescence characterisation. Figure 6.6 shows the emission spectras of the conjugates resultant from the titration of porphyrin with ATNPs. The first emission spectra of 100% Zn PATNPC refers to the system which had been shown above to induce immediate toxic effects (Section 6.2.1.3). The derived systems, from

75 % to 5%, correspond to polyacrylamide nanoplateforms with titrated amounts of porphyrin at the surface. The results obtained clearly show that decreasing the proportion of photosensitizer reacted with ATNPs led to a decrease in the fluorescence intensity. The results obtained suggest that it was possible to develop porphyrin-nanoplateforms containing different amounts of photosensitizer conjugated.

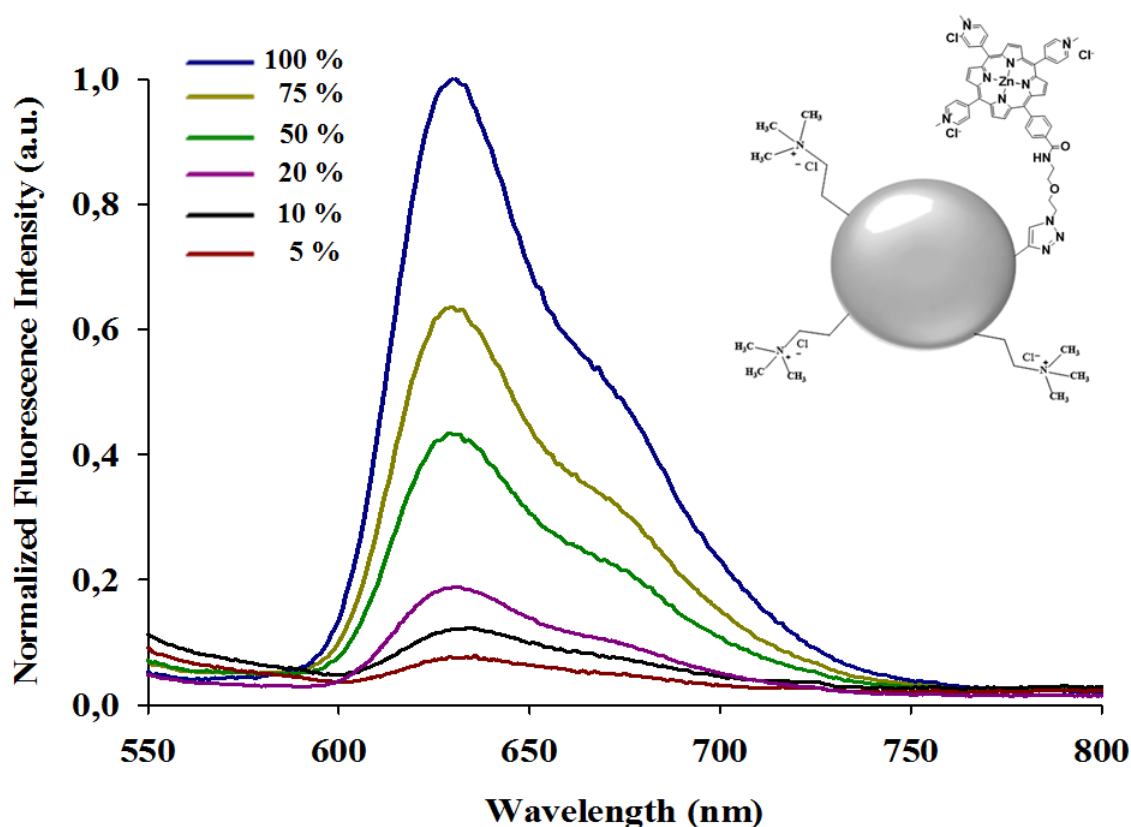


Figure 6.6: Fluorescence emission spectra of titrated porphyrins at the surface of polyacrylamide nanoparticles.

6.2.2.2 Cellular effects of porphyrin modulated nanosystems.

The real time effect of photosensitizer activation in treated hMSCs was evaluated by fluorescent microscopy. Thus, hMSCs treated with the new porphyrin-nanoparticle conjugates (75 %- 5 % ZnPATNPC) were exposed to a single light dosage and the effects were evaluated. For cells treated with ZnPATNPC,

photosensitizers ranging from 75 % up to 20 % have shown high impact on cell viability. Furthermore, similar to 100 % ZnPATNPC, a "blast zone" was also observed in hMSCs incubated with 75 %- 20 % ZnPATNPC. Figure 6.7, shows the effects of photosensitizer activation in hMSCs treated with 20 % ZnPATNPC (**K-M**); alterations in cell morphology were observed.

In consequence of the decreased amount of porphyrin conjugated to 20 % to 5 % ZnPATNPC, a fluorescent signal of porphyrins was not observed when excited at 575 nm, thus it was possible to stain hMSCs with an MMP sensitive fluorochrome. As previously demonstrated by Pendergrass, *et al.*, mitotracker red (CMXRos), which responds to relative changes in MMP, was chosen for the subsequent experiments.

Figure 6.7 presents the effects in hMSCs of nanoplateforms containing 20 %, 10 % and 5 % of porphyrin conjugation exposed to single light dosage of 512 μ W/2 sec at 575 nm wavelength. As can be observed, at these levels of photosensitizing effect it was not necessary to proceed to multichannel mosaic imaging to achieve cellular viability (Imaging Olympus U-plan S-Apo 40x/ NA 0.90). It was possible to visualize that hMSCs treated with 20 % ZnPTNPC still presented a high level of H₂O₂ production upon light stimulation (**L**), with decreased cellular viability at irradiation point (**M**). Higher cellular viability was obtained for 10 % ZnPTNPC with augmented mitotracker red fluorescence(**I**) and lower fluorescence of HTFMC. For hMSCs incubated with 5 % ZnPATNPC (**F**), HTFMC remained unresponsive (**E**) and increased cellular viability was observed.

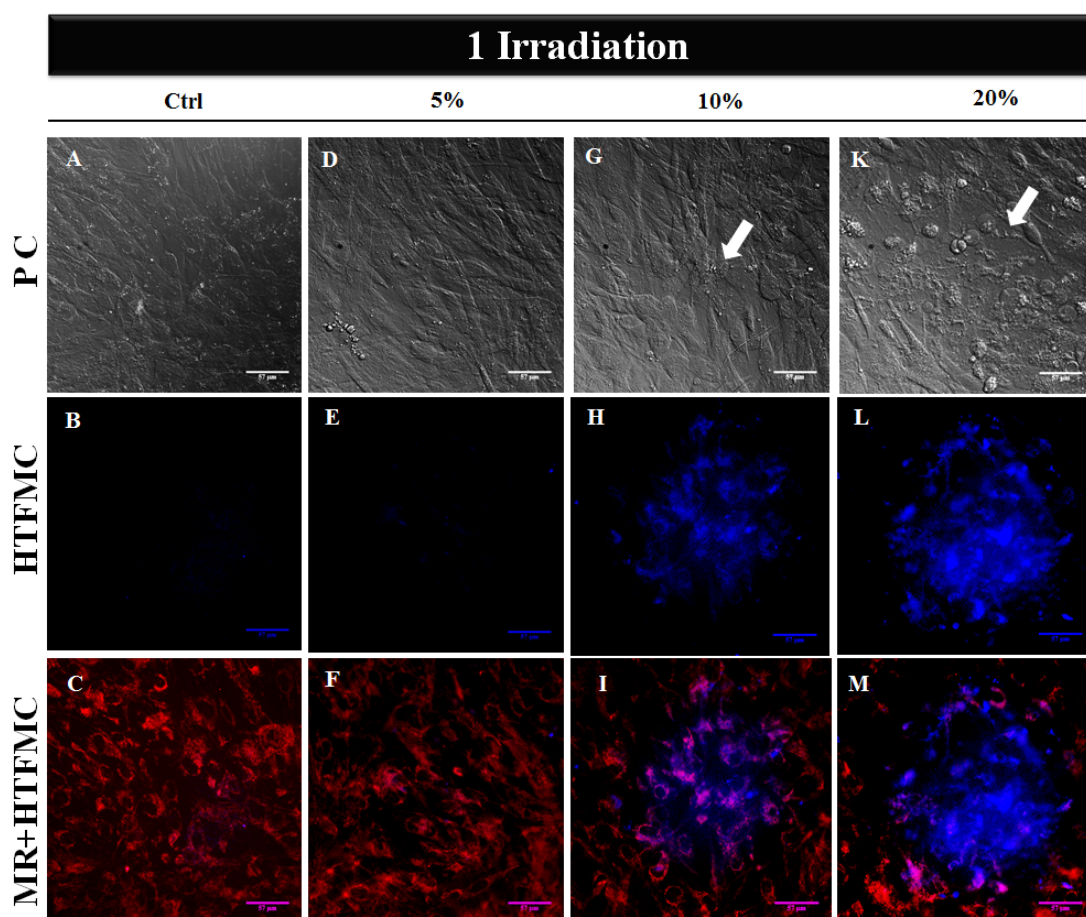


Figure 6.7: Effects of titrated porphyrin nanoplateforms in hMSCs upon single light dosage exposure. Cells were irradiated with LED light from a widefield Olympus delta vision elite deconvolution fluorescent microscope, Olympus U-plan S- Apo 60x/NA 1.42 and imaged with the same system and an Olympus U-plan S- Apo 20x/NA 0.85 . hMSCs were incubated with BPTFMC $\lambda_{exc}=390$ nm and $\lambda_{em}=435$ nm for its active form HTFMC stained with mitotracker red $\lambda_{exc}=575$ nm ; $\lambda_{em}=599$ nm to evaluate cellular viability dependent on mitochondrial membrane potential.

6.2.2.3 Effect of 5 % ZnPATNPC on cells when irradiated by light:

Controlled generation of ROS.

The latest results suggest that it is possible to attain a porphyrinic nanoplateform unresponsive to single light dosages by reducing the percentage of porphyrin conjugation to 5 %. Bearing this is mind, it was investigated how far hMSCs could be light stimulated and maintain cellular viability.

hMSCs treated with 5 % ZnPATNPC were submitted to cumulative light dosages

at 575 nm (512 μ W/2 sec each dosage) and analysed by time-lapse fluorescent microscopy. To evaluate ROS effects, it was important to follow variations in cellular viability, which was performed by mitochondrial staining with a MMP sensitive dye, mitotracker red CMXRos. It is important to note that, prior to mitochondrial staining, it was investigated whether any fluorescent signal of porphyrin was present when excited at 575 nm wavelength (data not shown) to avoid unspecific staining of mitochondria which would lead to misinterpretation of results.

Therefore, hMSCs incubated with porphyrinic nanoplateforms were stimulated by LED irradiation, 575 nm wavelength at 5 minutes each for a total period of 100 minutes. During this period the real time increase in oxidative stress was investigated.

The intention of the present study was to demonstrate that photosensitizing effects were a consequence of the photosensitizer activity of zinc porphyrins; in order to demonstrate this a control porphyrin (copper porphyrin) was used. As elucidated in Section 6.1.2, copper metallated porphyrins present a quenched fluorescence due to the interaction between the porphyrin π system and the unpaired electron from the orbital of the central metal ion [222–226]. Furthermore, the quenching of fluorescence also relates to inefficiency on the intersystem crossing of the singlet electronic state to originate the longer lived triplet excited state. Thus, copper porphyrin does not present photosensitizing activity upon light exposure. The use of a CuPATNPC allows the toxic effect to be specifically associated with the photosensitizing activity of ZnPATNPC.

The toxic activity of ZnPATNPC in stimulated hMSCs was then investigated in parallel with hMSCs treated with CuPATNPC. Figure 6.8 shows the effects of

cumulative live cell irradiation at 575 nm, 512 $\mu\text{W}/2$ sec. The left panel shows the response of hMSCs treated with CuPATNPC upon light stimulation. As expected, it is possible to observe that cellular morphology is maintained through all irradiation times. Likewise, cellular viability was established by the presence of mitochondrial staining of individual mitochondria (mitotracker red staining). Furthermore, as previously anticipated, hMSCs incubated with CuPTNPC did not show increase in ROS production through the period of irradiation, as shown by unresponsive HTFMC, which is indicative of the absence of H_2O_2 production. On the other hand, hMSCs incubated with ZnPTNPC showed unresponsive HTFMC in the first 30 minutes of light treatment, with a slight increase at 30 minutes of irradiation (cumulative administration of six light dosages); however, no changes were present in phase contrast imaging or mitochondrial staining. At 60 minutes of irradiation (cumulative administration of 12 light dosages), a visible increase in oxidative stress was noticed, due to H_2O_2 production (HTFMC activation).

The impact of increased oxidative stress was also visible in mitochondrial staining, where a decrease in mitotracker red intensity and alterations in the pattern of staining was observed, suggesting a decreased MMP. Also, oxidative stress signals were visible by alterations in cellular morphology (Figure 6.8, indicated by white arrows). Further increase in oxidative stress was present upon 100 minutes (cumulative administration of 20 light dosages) of light treatment, which verified an augmented fluorescence in HTFMC and, consequently, a decrease in MMP (MTR) and cellular viability (phase contrast white arrows). Taken together, the previous results indicate that it is possible to induce hMSCs to produce endogenously ROS in a controlled manner.

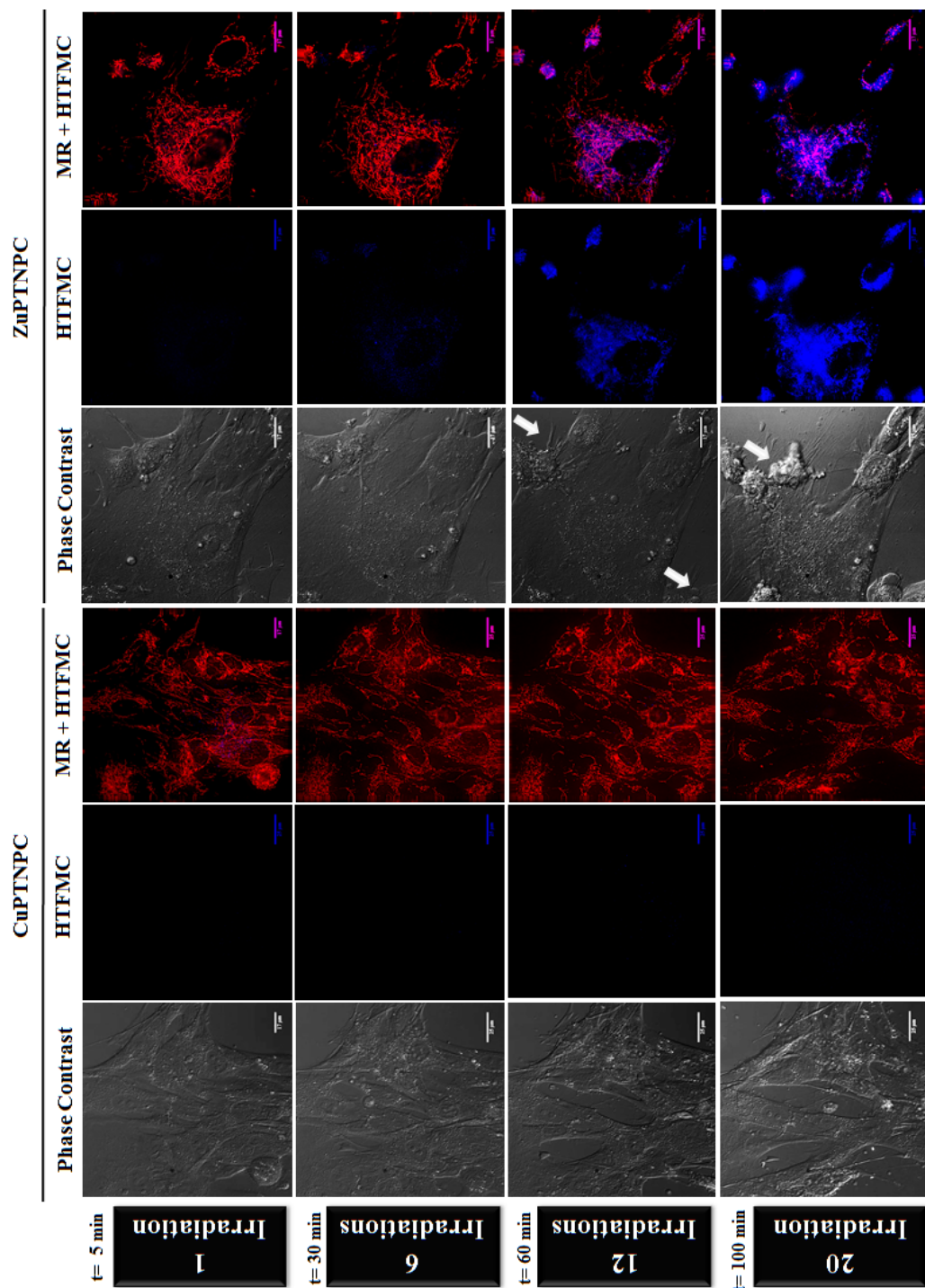


Figure 6.8: Live cell imaging of endogenous H_2O_2 production upon irradiation of hMSCs treated with either CuPATNPC or ZnPATNPC. LED irradiation of hMSCs at each 5 min for a total of 100 min. hMSCs were previously treated (overnight incubation) with CuPTNPC containing FITC-dextran entrapped (left panel) or ZnPATNPC containing FITC-dextran entrapped (right panel). It is possible to observe, by phase contrast imaging, spindle shaped fibroblastic-like MSCs (left and right panels, first and middle columns). The intracellular presence of CuPATNPC or ZnPATNPC can be visualized in green, due to FITC emission at $\lambda_{em} = 523$ nm (left and right panels, middle columns). Activation of HTFMC to BPTFMC was mediated by the presence of endogenous H_2O_2 , $\lambda_{em} = 435$ nm and can be observed only after 60 and 100 min of light treatment, exclusively in hMSCs treated with ZnPATNPC (left and right panels, third columns). Images obtained with a widefield Olympus delta vision deconvolution fluorescent microscope; Olympus U-plan S-Apo 60x/ NA 1.42. Scale = 12 μ m.

6.3 Conclusions

The research developed in the present chapter provides information on the photosensitizing effects of activated porphyrinic nanoplateforms in hMSCs. From the porphyrinic nanosystems in the study, ZnPATNPC and ZnPTNP, it was concluded that entrapment of porphyrins in the polyacrylamide matrix depresses the photosensitizing activity. Thus, conjugations of porphyrin at the surface of polyacrylamide nanoparticles have been shown produce a "blast" of ROS and induce oxidative stress at lethal levels in treated hMSCs upon light exposure. The conjugation of zinc porphyrins at the surface of nanoparticles produced efficaciously singlet oxygen.

In conclusion, nanoplateforms containing porphyrins entrapped were not a suitable methodology to control the photodynamic activity of porphyrins in cells. Further investigations of the photophysical properties of entrapped and free porphyrins are needed (e.g. spectroscopy, lifetime and quantum yields measurements) to bring better understanding of the interactions responsible for this event.

One of the main limitations of the present research was being unable to establish an association between porphyrin concentration and photosensitizer effect. The random nature of the free radical polymerization does not allow quantifying the number of functionalities introduced and, in consequence, the concentration of porphyrin.

ZnPATNPC produced a burst of ROS in hMSCs which, in part, was a promising result; however, the aim was to create a tool that would elicit, in situ, a progressive increase in ROS generation. Thus, the knowledge acquired from previous research (Chapters 3; 4; 5), allowed engineering porphyrinic nanoplateforms to confer

biological compatibility and controlled ROS production by modulating the coating of nanoplateforms with porphyrin.

The treatment of hMSCs with 5 % ZnPATNPC has been shown to successfully produce in situ small bursts of ROS by cumulative light dosages allowing to follow, in real time, an increase in oxidative stress culminating in cell death.

A means to prove production of ROS in a controlled manner following porphyrin activation by exposure to light dosages of specific wavelengths was achieved and included the use of a hydrogen peroxide sensitive dye which is accumulated in mitochondria. It was also necessary to evaluate cellular responses to an increase in oxidative stress, established by the use of a commercial dye (mitotracker red) that provides information on cellular viability. Mitotracker red dyes stain active mitochondria by exploiting their inner mitochondrial membrane potential, thus loss in cellular viability due to the deleterious effects of ROS produced (H_2O_2) was successfully followed.

By establishing that the viability of hMSCs treated with copper porphyrin nanoplateforms exposed to light of appropriate wavelength was unaltered, it was possible to conclude that the photosensitizing effect was restricted to the photo-activity of zinc porphyrin nanoplateforms.

In summary, the knowledge acquired from these nanosystems led to the successful development of a nanotool for the endogenous generation of ROS in a controlled manner. Such a system offers the possibility of investigating real time responses to ROS effects. Furthermore, it also provides the study of single cell and metabolic pathways in great detail by the use of a non-invasive system. Thus, it can greatly contribute to the development of basic science in the field of ROS and uncover

potential therapeutic targets in related diseases.

Chapter 7

Impact of ROS in the differentiation state of Mesenchymal Stem Cells

7.1 Mesenchymal Stem Cells

Stem cells are defined as biologically undeveloped cells with the capacity for proliferation, self-renewal and a high potential to generate one or more types of differentiated progeny [231–234]. According to their development potential, stem cells can be characterised as totipotent (differentiate into all embryonic and extraembryonic cell types), pluripotent (able to give rise to all embryonic cell types), multipotent (able to give rise to a great number of cellular lineages), oligopotential (originates a more limited number of cellular lineages) and unipotent (only able to originate one specific cellular lineage) [231, 234].

The notion of Stromal Cells, later called Mesenchymal Stem Cells (MSCs),

was first introduced by Alexander Friedenstein, *et al.* [88]. In 1970, they followed a culture of mouse bone marrow cells in plastic dishes, supplemented with foetal calf serum; Friedenstein observed the presence of a nonhematopoietic population (0.01% to 0.001%) of plastic adherent nucleated cells along with the non-adherent hematopoietic cells. A few years later, Friedenstein introduced a second breakthrough by exposing the idea of clonogenic stromal cells, showing that non-hematopoietic single adherent cells were capable of developing into fibroblast-like colonies, originating the term colony-forming unit fibroblasts (CFU-F) [235]. This same evidence was later reported in human bone marrow by Castro Malaspina, *et al.* [236]. Friedenstein's subsequent investigations provided evidence of osteogenic potential by the self-renewal capability of stem cells through regeneration of heterotopic bone tissue [235,237,238]. Further studies uncovered many other characteristics of this progeny; Schofield introduced the hypothesis of a stem cell niche within the bone marrow, suggesting that hematopoietic stem cells were regulated by an association with the bone marrow microenvironment [239–241].

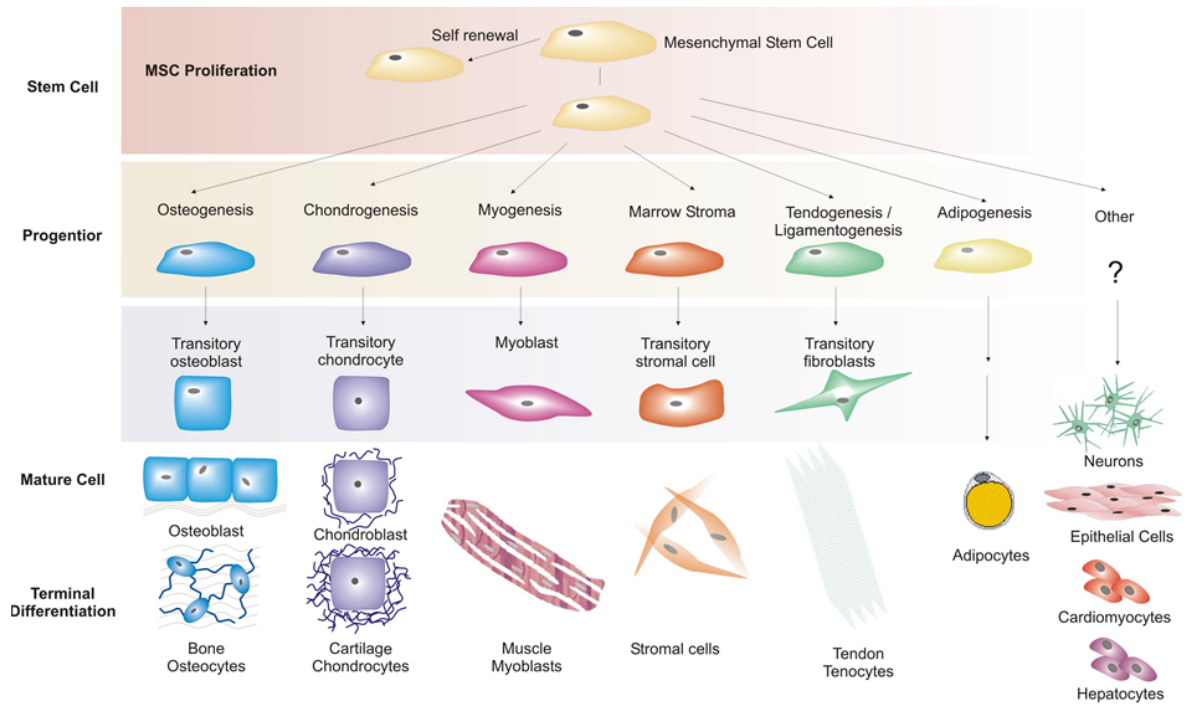


Figure 7.1: Representative multilineage differentiation potential of MSCs. MSCs self-renewal and differentiation into mesenchymal tissues, such as bone, cartilage, muscle, stroma and adipose. It also shows the plasticity of MSCs to differentiate into tissues such as heart, liver, skin and nervous tissue. Adapted from Caplan and Bruder, 2001 [242].

7.1.1 Immunophenotypic Characterisation of hMSCs

7.1.1.1 Cell Surface Molecules

The identification and characterisation of cell surface molecules follows a protocol designated as CD protocol, where CD stands for cluster of differentiation. The CD nomenclature was originally developed in 1984 by a group of immunologists at an International Workshop on Human Leukocyte Differentiation Antigens (HLDA) aiming to standardise and develop an understanding of surface molecules in leukocyte (white blood cells). These CD molecules are either membrane receptors or ligands responsible for transducing activation signals to the inside of the cell, and

therefore regulating activation mechanisms. Consequently, the presence of these molecules defines the function and specialisation of each cell. The potential of these antibodies to identify different types of cells at different stages was quickly understood and the CD nomenclature was subsequently extended to other types of cells, such as stem cells [243,244] .

As shown in Diagram 7.2, the different monoclonal antibodies are labelled with different fluorochromes, which allows for their individual identification. The interaction between the labelled paratope (part of the antibody that recognizes the epitope) and the epitopes (part of surface receptor that is recognized by the immune system) imparts a fluorescent signal to the cell. Specifically, for the monoclonal antibodies represented in Figure 7.2, single cells present fluorescent signals in the green (CD29) and yellow (CD105) regions of the visible spectra, due to paratope-epitope interaction. Absence of interactions between CD45 and CD 34 with the surface of MSCs leads to the absence of fluorescent emission in the orange and red, regions of the visible spectra, respectively, for single cell analysis.

7.1.1.2 Cell surface molecules characteristic of MSCs

As described above, MSCs were initially characterized by homogenous adherence to plastic (as a way to purify and isolate these non hematopoietic populations), spindle-shaped fibroblastic morphology and their tri-lineage differentiation potential into osteoblasts, chondroblasts and adipocytes. However, with increased knowledge about these cell types, allied to their presence in bone marrow (as well as many other tissues), it has led to difficulties in their identification. Firstly, a variation of differentiation potential and morphology arising from *in vivo* to *in vitro* conditions was observed. Additionally, alterations were identified according to the

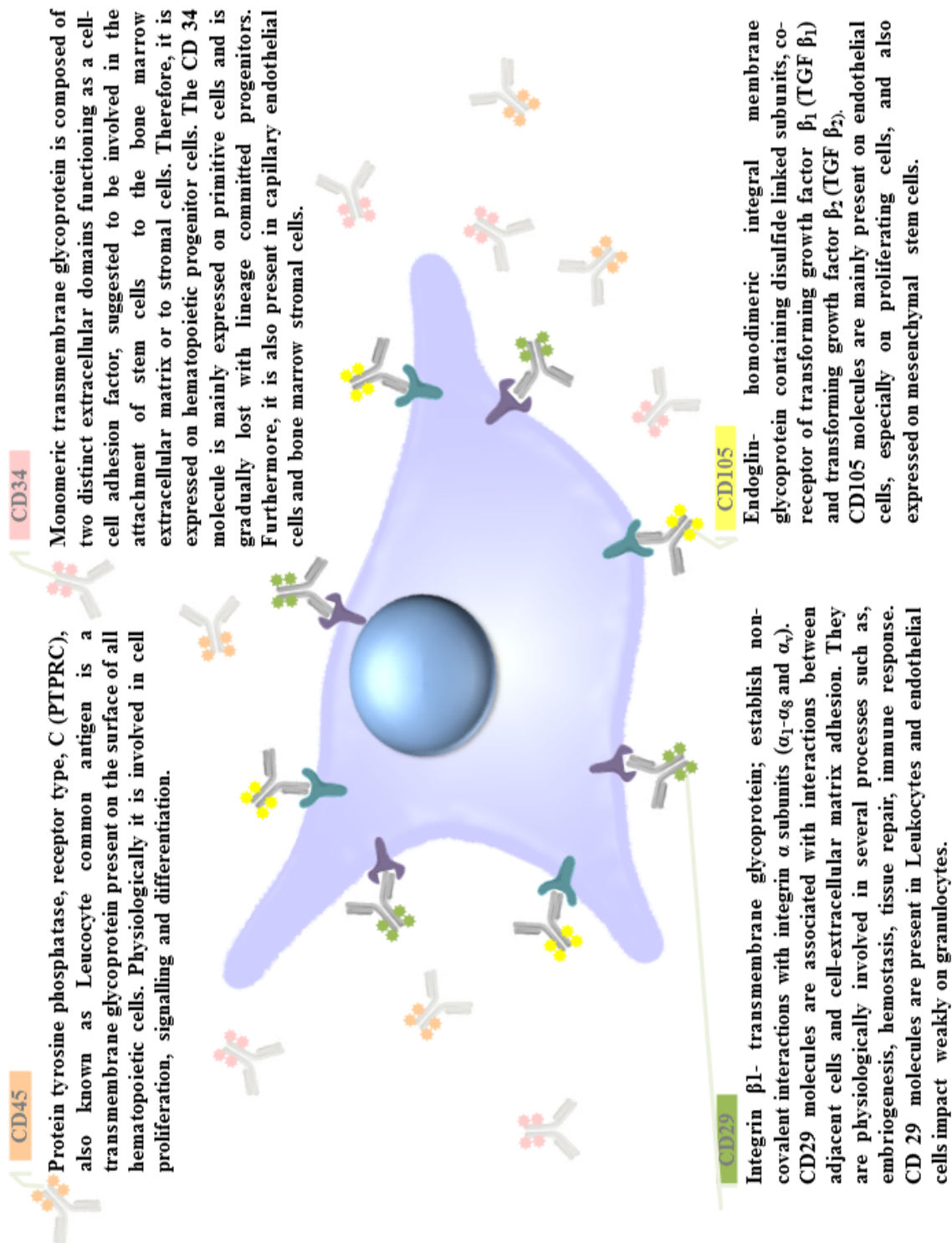


Figure 7.2: Schematic diagram of monoclonal antibody interaction with the surface receptors in Mesenchymal Stem Cells (MSCs). The antibodies represented, are specific for the multicolour analysis of the present work. Therefore, the interaction of CD29 and CD105 antibodies with the surface receptor in MSCs and the absence of interaction of CD 45 and CD 34, are represented. It also describes the main biological properties of [245-248].

tissue from where the cells were collected in an age dependent manner. These factors have led to enormous difficulty in developing a universal phenotypic characterisation of MSCs. Therefore, in 2006, The International Society for Cellular Therapy (ISCT), published a proposal for a minimum criteria panel of cell surface markers for the identification of MSCs. Thus, MSCs should be positive ($\geq 95\%$) for CD105, CD73, CD90 and negative ($\leq 2\%$) for CD45, CD34. CD14 or CD 11b, CD79 α or CD19 and HLA DR (Major Histocompatibility Complex class II cell surface receptor) [249]. Since then, it has been verified that hMSCs express a wide variety of other cell surface markers in addition to the ones defined by the ISCT. In 2011, Mafi, *et al.* presented a summary of the most common cell surface markers for MSCs isolated from different tissues. Thus, it was identified that CD105, CD29, CD90, CD44, CD73, CD13, CD146, CD106, CD54 and CD166 were the most frequently reported as positive and CD34, CD14, CD45, CD11b, Cd49d, CD106, CD10 and CD 31 as the most frequently absent [250].

The present study concerns itself with, a selection of the surface markers most commonly expressed by MSCs isolated from foetal liver, CD29 and CD105 as positive markers and CD34 and CD45, which are only expressed for the hematopoietic lineage (absent for MSCs).

7.1.1.3 Role of ROS on the undifferentiated state of hMSCs

Much attention has been given to MSCs, mainly because of their potential to contribute to tissue repair *in vivo* and thus, their applications in tissue engineering and regenerative medicine. To date, ROS have been primarily associated and investigated for their damaging effects. Chapter 1, noted the role of reactive oxygen species in stress and disease, however, the recent potential of these species to act

as intracellular signalling intermediates sheds new lights on uncovering the mechanisms involved in these processes. Therefore, in stem cell biology it has become important to investigate the role of ROS in stem cell renewal. It is well documented that stem cells normally reside in niches which are defined by a low level of ROS, which is important to maintain their self-renewal potential and stemness [251]. However, the levels at which ROS exert a homeostatic or a detrimental role on the balance between stem cell renewal and differentiation is still unknown. The aim of the present chapter is to contribute to recognising the impact of ROS on MSCs.

Aims

The aim of this chapter is the application of the previous nanotool (Chapter 6 and developed methodology to investigate the impact of ROS in the undifferentiated state of hMSCs. Initially, primary hMSCs isolated from a foetal liver microenvironment were investigated for the expression of characteristic surface markers of undifferentiated MSCs, as well as for hematopoietic markers. The effect of increasing doses of light on hMSCs treated with the photosensitizer-nanoplatfrom conjugated on the profile of antibodies surface markers was then investigated. The incidence of apoptosis and necrosis in stimulated hMSCs was also evaluated .

7.2 Results and Discussion

The goal of the present study was to investigate the impact of ROS on the undifferentiated state of hMSCs.

7.2.1 Morphology of hMSCs

hMSCs were used as a cellular model due to their therapeutic potential associated with regenerative medicine. The isolation of MSCs from foetal liver microenvironment was carried out according to the widely accepted methodology of plastic adherence [235]. Initially, the morphology of adherent cells was investigated and documented by widefield real time (RT) fluorescent and differential interference contrast (DIC) microscopy. As can be observed in Figure 7.3, expanded cells presented a fibroblast-like appearance with a homogeneous spindle shape. The same morphological features were consistently observed after all passages, 1-10. The results of this study were consistent with observations previously reported by many groups for expanded MSCs [232, 235, 252–254].

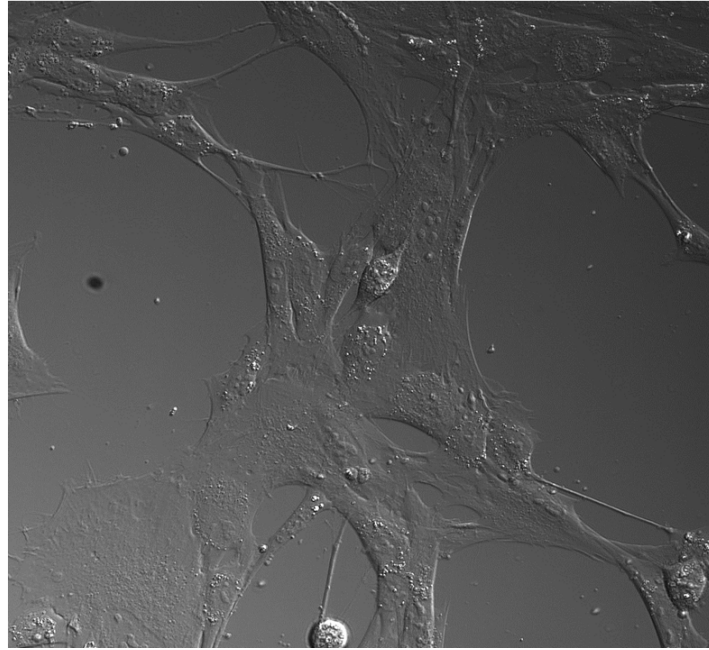


Figure 7.3: Representative phase contrast image of adherent cells isolated from fetal liver microenvironment, resembling spindle shaped fibroblastic-like MSCs. Olympus U-Plan S-Apo 20X/NA 0.85. Scale= 35 μm .

7.2.2 Characterisation of hMSCs:

The impact of ROS on undifferentiated hMSCs was assessed by flow cytometry (FCM). The characteristics of adherent cells, isolated from the foetal microenvironment, were analysed for specific surface antigen expression. The exact surface antigen expression for the characterisation of hMSCs is still a matter of debate, despite many reported profiles. Using the criteria published by ISCT based on the work reported by many groups [232, 249, 250, 252, 255, 256], profile for hMSCs characterisation has been postulated, which includes positive expression for CD29 and CD105, and the absence of hematopoietic markers CD34 and CD45 [232, 253, 257, 258]. This was the chosen criteria for this work.

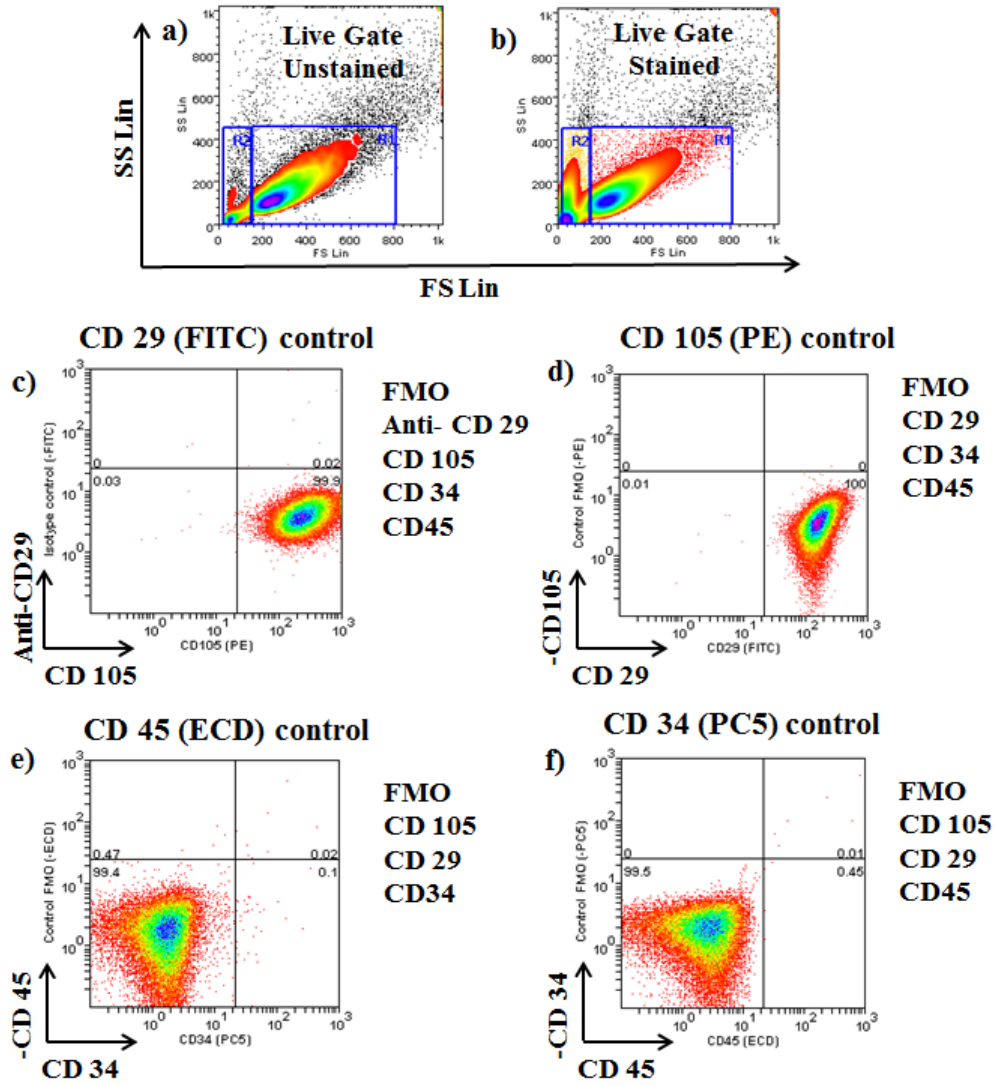


Figure 7.4: Characterisation of adherent cells isolated from foetal liver microenvironment (passage 3). a) Unstained live gate: elimination of sources of interference by exclusion of debris, sub-cellular particles and early apoptotic events(R2) and selection of viable events (R1); b) Live gate of stained hMSCs. R1 gated middle panels, controls of spectral overlap; c) CD105(PE) vs. isotype control CD29 (FITC); d) FMO (-CD105) CD29 (FITC) vs. CD105 (PE); e) FMO (-CD45) CD34 (PC5) vs. CD45 (ECD); f) FMO (-CD34) CD45 (ECD) vs. CDC (PC5). FITC- fluorescein isothiocyanate ($\lambda_{ex}=488$ nm; $\lambda_{em}=520$ nm). PE- phycoerythrin ($\lambda_{ex}=488$ nm; $\lambda_{em}=565$ nm). ECD- PhycoerythrinTexas Red-X ($\lambda_{ex}=488$ nm; $\lambda_{em}=620$ nm). PC5-phycoerythrin-cyanine5 ($\lambda_{ex}=488$ nm; $\lambda_{em}=665$ nm).

The evaluation of the phenotypic characteristics of hMSCs was performed on a minimum of 25000 cells. Cells were stained for the simultaneous detection of several markers; CD29 (FITC- fluorescein isothiocyanate); CD105 (PE- phycoerythrin); CD45 (ECD-PhycoerythrinTexas Red-X) and CD34 (PC5-phycoerythrin-

cyanine5).

Prior to characterisation by FCM, care was taken to avoid potential sources of artifacts. Thus, healthy populations were selected on the basis of contour plots, representing forward versus side scattered light measurements, through the creation of logical gates, as represented in Figure 7.4 a) and b) (R1, R2). Side and forward scattered light of cell debris and dying cells are low due to the smaller shape and lower amount of organelles present in these populations, a) and b) R2 Figure 7.4. It is important to note that the elimination of these populations is essential in phenotypic characterisation since they might present an altered marker expression or establish unspecific bonding with antibodies, either contributing for false positive or false negative readings.

Additionally, spectral overlap between the fluorochromes in use and background fluorescence was also considered. For these reasons, a compensation protocol was created. The term compensation is used in flow cytometry to refer to a process where the spectral overlap between different fluorochromes is mathematically removed. The creation of an appropriate compensation protocol avoids detection of false positive or false negative results and is thus essential for proper analysis. The principle chosen for compensation was based on the creation of hMSCs single staining controls for each antibody. Controls were also created where all the antibodies under study were present minus one, called fluorescence-minus-one (FMO), as represented in Figure 7.4. The application of this methodology was based on work previously developed by Coupland [195]. Figure 7.4 c) shows the FMO control for CD 29(FITC), which is an isotype control. An isotype control is an antibody that has no specific interaction with any component in the cell, therefore

it allows the elimination of non-specific binding. Controls of fluorescence overlap for CD105-PE, CD45-ECD and CD34-PC5 were based on FMO, the resultant bi-variate dot plots are presented in Figure 7.4 d), e) and f). It was not intended in this work to not detailed compensation principles; however, for further information regarding fluorescence compensation please refer to the work developed by Baumgarth and Roederer, Roederer Maecker and Trotter [84, 259, 260].

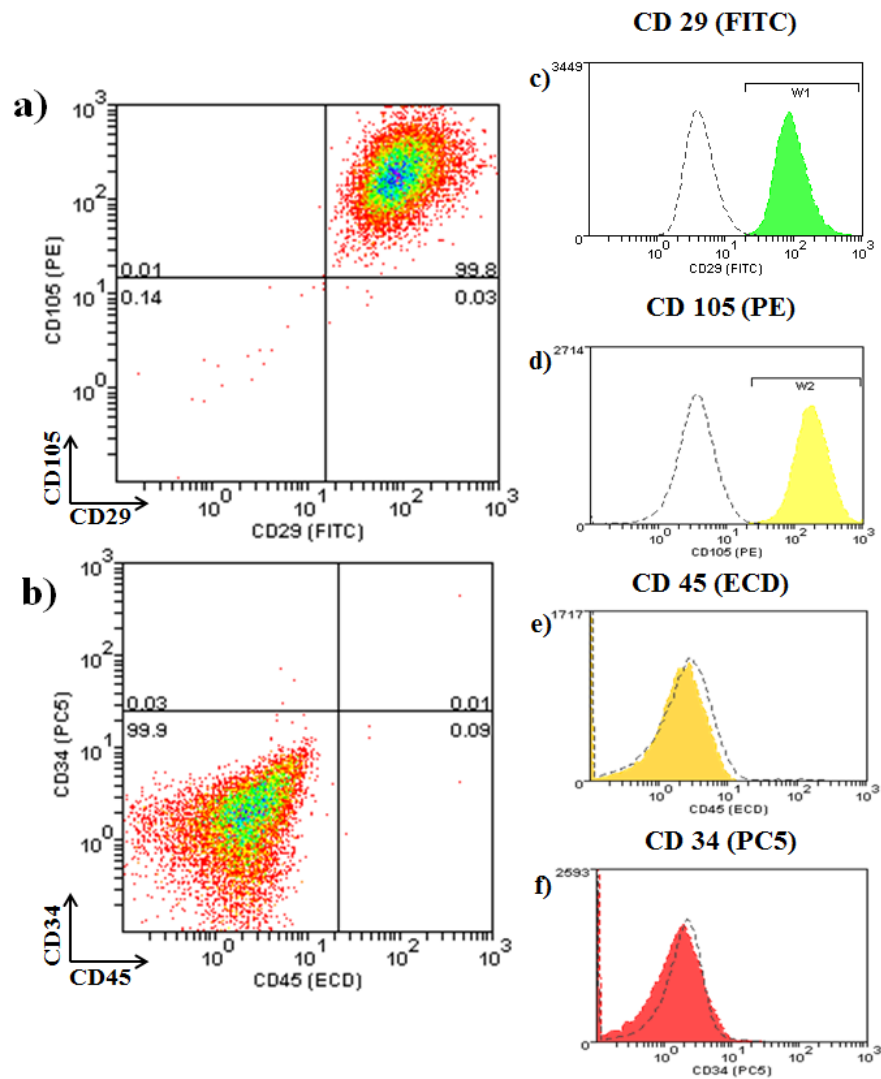


Figure 7.5: Representative immunophenotypic profile of hMSCs isolated from foetal liver microenvironment, P³ to P¹⁰. Flow cytometry bi-variate dot plots (R1 gated) show positive expression of a) CD29 and CD105 and absence b) for both CD45 and CD34. Histogram plots (R1 gated) showing the overlay between controls (dotted lines) and test samples (coloured lines) show that adherent cells stain positive for mesenchymal markers c) CD29 and d) CD105, and stain negative for hematopoietic markers, e) CD45 and f) CD34.

Finally, Figure 7.5 represents the characterisation of hMSCs in bi-variate dot plots of CD29 against CD105 and CD34 versus CD45. As shown on the right panel, hMSCs were strongly positive for both, CD29- FITC and CD105-PE antibody conjugates as previously reported human foetal liver MSCs by several authors [232,252]. On the other hand, as expected, the expression of hematopoietic progenitor markers CD34-PC5 and CD45-ECD antibody conjugates was not observed. The combined results of the controls (Figure 7.4), after compensation, and from the multiple colour staining (Figure 7.5), indicate the successful isolation of hMSCs from the foetal liver microenvironment.

7.2.3 Effect of nanoparticle delivery on the surface marker expression in hMSCs:

After successfully characterising adherent cells isolated from the foetal liver microenvironment as hMSCs, the effect of nanoparticle delivery on the surface profile of hMSCs was evaluated.

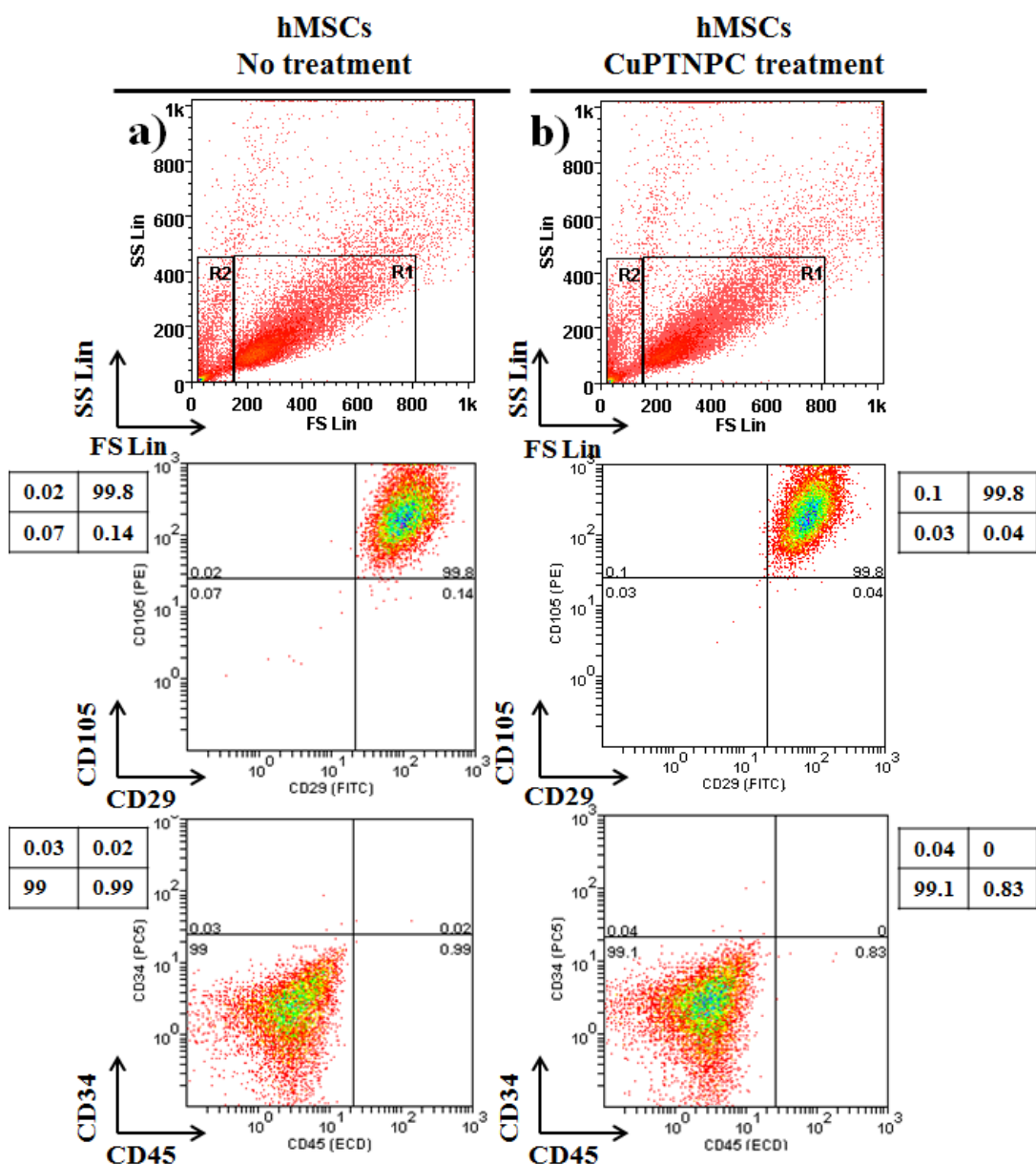


Figure 7.6: Effect of nanoparticle internalisation on the immunophenotypic profile of hMSCs, representative from P³ to P¹⁰. Flow cytometry bi-variate plots (R1 gated) FSS vs. SSC of MSCs incubated with nanoparticles do not show any alterations due to nanoparticle delivery, a) and, b). Analysis of the bi variate plots of surface markers, shows positive expression of CD29 and CD105 $\geq 99\%$ and very little expression for both CD45 and CD34 $\leq 1\%$ for cells without nanoparticle incubation (column a); the same pattern was verified for cells treated with CuPATNPC (column b).

Surface marker's characterisation in hMSCs was carried out by FMC analysis using four colour staining. To evaluate the impact of porphyrinic nanoplateforms on the surface profile of hMSCs, CuPATNPC were used. The rationale behind this experiment was to firstly investigate the impact of the nanoparticle itself

on the surface markers expression of hMSCs. In addition, knowing that copper porphyrins present a quenching of the triplet state when activated by light of appropriate wavelengths, alterations on the surface markers profile due to porphyrin photodynamic effects could then be excluded. CuPATNPC without FITC-dextran entrapped were incubated overnight with hMSCs. The impact of porphyrinic nanoplateforms in hMSCs is shown in Figure 7.6 and it can be ascertained that internalisation of nanoparticles does not affect the surface maker's expression in hMSCs. Comparison between control cells (absence of nanoparticles) and treated cells (CuPATNPC) showed very similar percentages of expression. Thus, expression of CD29 and CD105 were equally positive for 99.8% of the population, as opposed to CD45 and CD34 where expression was less than 1% of the population. The results presented were consistent with work previously reported by Coupland *et al.*, where it was shown that the delivery of polyacrylamide nanoparticles to hMSCs did not alter the expression of CD29 and CD105 while the absence of CD34 and CD45 expression was also observed [89].

7.2.4 Impact of ROS on surface marker expression in hMSCs:

Once it was verified that the internalisation of NPs did not affect the differentiation profile of hMSCs, a study was carried out to evaluate whether the generation of ROS would alter its phenotype. To investigate the effects of oxidative stress on hMSCs, the approach previously developed with light activated ZnPATNPC (Chapter 6; Section 6.2.2.3) for controlled generation of ROS was applied. In order to achieve this, it was necessary to first develop a light system for cell

irradiation that mimicked the one previously performed microscopically.

7.2.4.1 Light system for the irradiation of hMSCs

The development of a portable light system for porphyrin activation would then have to confer the same light intensity and wavelength when applied over the same exposure time. Thus, a system with a characteristic wavelength for porphyrin activation at 575 nm with an irradiation power of approximately 500 μW was constituted, as shown in Figure 7.7.

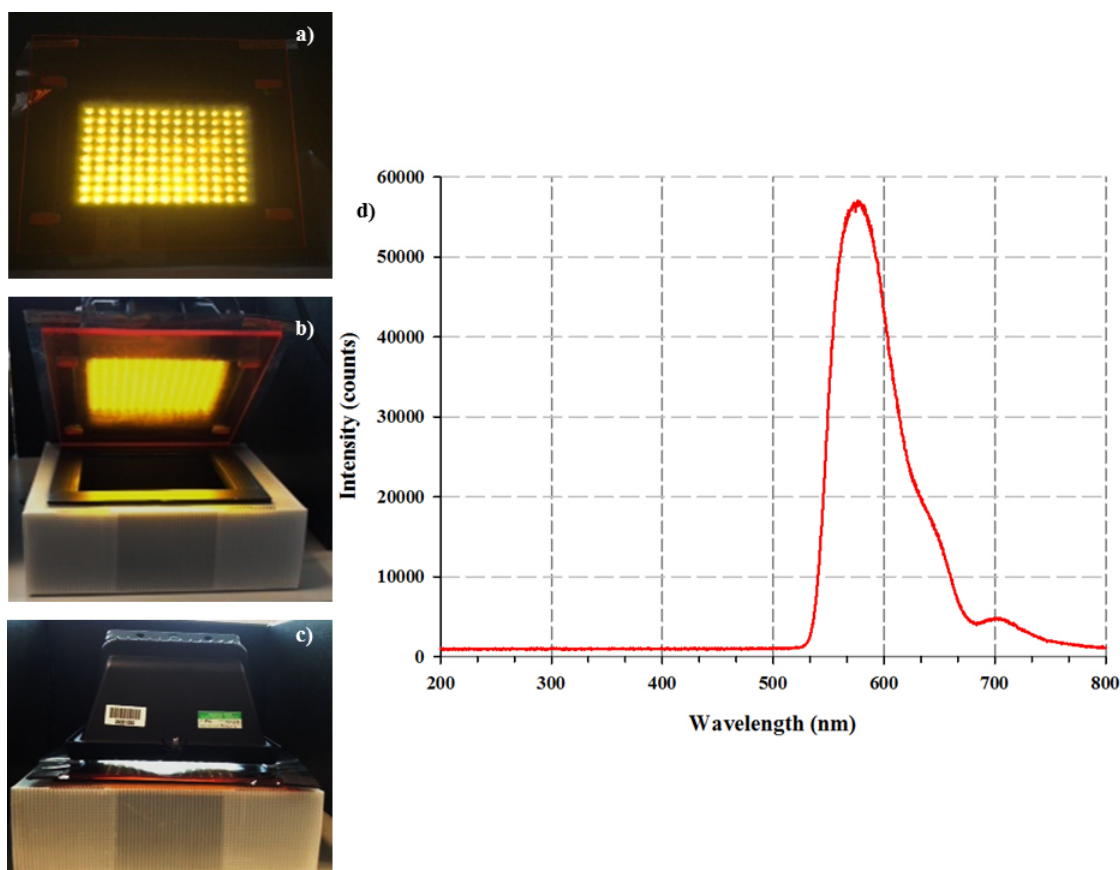


Figure 7.7: Portable light system for photosensitizer activation. a) Portable LED coated with 2 neutral density filters plus a fluorescent acrylic layer; b) Portable LED adapted to an opaque structure with black interior to restrict the area of irradiation; c) Last step of the system for cell irradiation; d) Graphical representation of the wavelength vs. intensity irradiation output, peak at 575 nm.

Confirmation of the effectiveness of the developed portable light system to

activate the porphyrinic nanoplateforms was investigated. In the same manner, microscopy was used to follow the effects in treated cells with ROS increase. Cells were firstly exposed to light by the use of the portable light system and then imaged by differential contrast imaging. The excitation wavelength of 488 nm (corresponding to FITC excitation) to confirm the presence of internalised nanoparticles was applied. Furthermore, wavelengths of 405 nm (corresponding to HTFMC excitation) were employed for the detection of HTFMC activation by intracellular production of H_2O_2 . In Figure 7.8, the effects of hMSCs irradiation using the portable light system are shown. Similar to the results previously obtained by microscopic irradiation (Chapter 6; Section 6.2.2.3), oxidative stress followed by H_2O_2 production was noticed with the use of the portable light system. As expected, cells treated with CuPATNPC were not affected by cumulative light irradiation during a 100 minutes period (20 irradiations), as can be observed by the unresponsive HTFMC (Figure 7.8, third column). However, cells treated with ZnPATNPC and irradiated with the portable light system showed evidence of ROS production after 30 minutes of irradiation (six light dosages), which became more pronounced with cumulative light dosages of 12 and 20 irradiations, respectively. These results indicate that hMSCs were capable of handling and scavenging the amount of ROS generated by the first six light dosages; however, further insults led to its accumulation and detrimental effects. Taken together, these results verified the effectiveness of portable light system irradiation to stimulate ROS production by ZnPATNPC internalized in hMSCs.

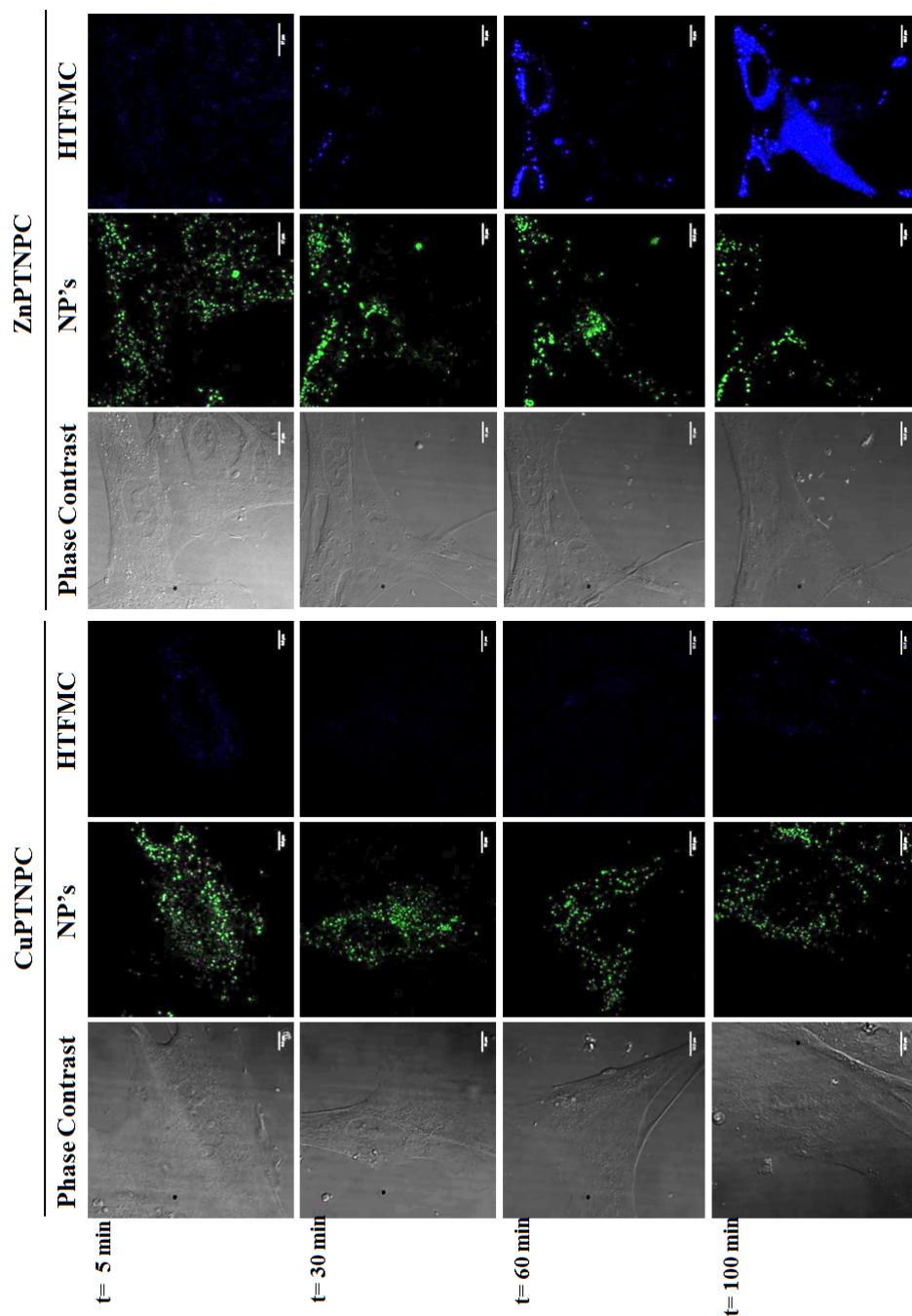


Figure 7.8: Live cell imaging of endogenous H_2O_2 production upon irradiation of hMSCs treated with either CuPATNPC or ZnPATNPC. PLS was used for the irradiation of hMSCs at 5 min intervals for a total of 100 min. hMSCs were previously treated (overnight incubation) with CuPATNPC containing FITC-dextran entrapped (left panel) or ZnPATNPC containing FITC-dextran entrapped (right panel). It is possible to observe, by phase contrast imaging, spindle shaped fibroblastic-like MSCs (left and right panels, first columns). The intracellular presence of CuPATNPC or ZnPATNPC can be visualised in green, due to FITC emission at $\lambda_{em} = 523$ nm (left and right panels, middle columns). Activation of HTFMC to BPTFMC was mediated by the presence of endogenous H_2O_2 , $\lambda_{em} = 435$ nm and can be observed only after 60 and 100 min of light treatment, exclusively in hMSCs treated with ZnPATNPC (left and right panels, third columns). Images obtained with a widefield Olympus delta vision deconvolution fluorescent microscope; Olympus U-plan S-Apo 60x/ NA 1.42. Scale= 12 μ m.

7.2.4.2 Surface profile of hMSCs upon light treatment

In order to study the impact of ROS on hMSCs identity, cells were exposed to numerous dosages of light (portable light system) and changes in expression of CD29- FITC, CD105- PE, CD45-ECD and CD34-PC5, antibody conjugates were monitored by flow cytometry.

To isolate any possible effects on the identity of hMSCs as a result of ROS stimulation, the experiment was performed in parallel with two controls. One control consisted of hMSCs free of nanoparticle treatment (negative control) and the other consisted of hMSCs treated with CuPATNPC (positive control). The bi-variate dot plots represented in Figure 7.9 show the surface molecule profiles for CD29- FITC versus CD105- PE and; CD45-ECD versus CD34-PC5 antibody conjugates following the administration of 5, 10, 15 and 20 light dosages. The results obtained suggested that 5 or 10 light irradiations did not impact on the expression of the selected surface markers. In addition, the dot plots of CD29 against CD105 showed a high level of expression of these two surface markers of approximately 99%. The expression of hematopoietic progenitor markers, CD45 and CD34, was completely absent. Upon 15 light dosages, a decrease of almost 4% in the expression of CD105 was detected. The same evidence was observed after the administration of 20 light dosages with a decrease of CD105 expression of approximately 6%. Variations of expression of CD 105 at 15 and 20 irradiations was isolated to hMSCs incubated with ZnPATNPC and was not observed in any of the controls.

The heterogeneity of CD 105 expression following the exposure of hMSCs oxidative stress (15-20 light dosages) could have been indicative of stem cell differentiation

stages. However, it is necessary to consider that hMSCs morphology was significantly impaired upon 15 and 20 light dosages exposure. Thus, variations in CD 105 expression could also be associated with an alteration in cellular membrane integrity leading to less affinity of the antibody to the membrane receptor.

Currently, there are not many investigations of the direct impact of ROS on the surface profile of hMSCs. However, a few reports indicate that augmented oxidative stress is related to signalling and initiation of cellular differentiation [196,261–263] while ROS have also been associated with *in vitro* senescence growth arrest of MSCs [39]. It is important to note that these studies involved the exogenous addition of hydrogen peroxide to mimic an oxidative environment. The subtle variations in hMSCs CD 105 marker expression have previously been associated with adipogenic differentiation by Tormos, *et al.* and also Kanda, *et al.* [261,264].

To further investigate the variation of CD105 expression in hMSCs, an evaluation of the incidence of apoptosis and necrosis upon 5, 10, 15 and 20 exposures to light was performed in parallel. This experiment aimed to investigate if an increase in apoptosis/necrosis was consistent with the decrease of CD105 expression. Specifically, during apoptosis the loss of phospholipidic membrane asymmetry occurs, which can result in decreased affinity of antibodies for the surface markers. Figure 7.10 shows two controls: a positive control, cells incubated with CuPATNPC, and a negative control, non-treated cells. For both controls an incidence of apoptosis of about 20 % was verified. This level of apoptosis was considered to result from experimental procedure as the hMSCs were submitted

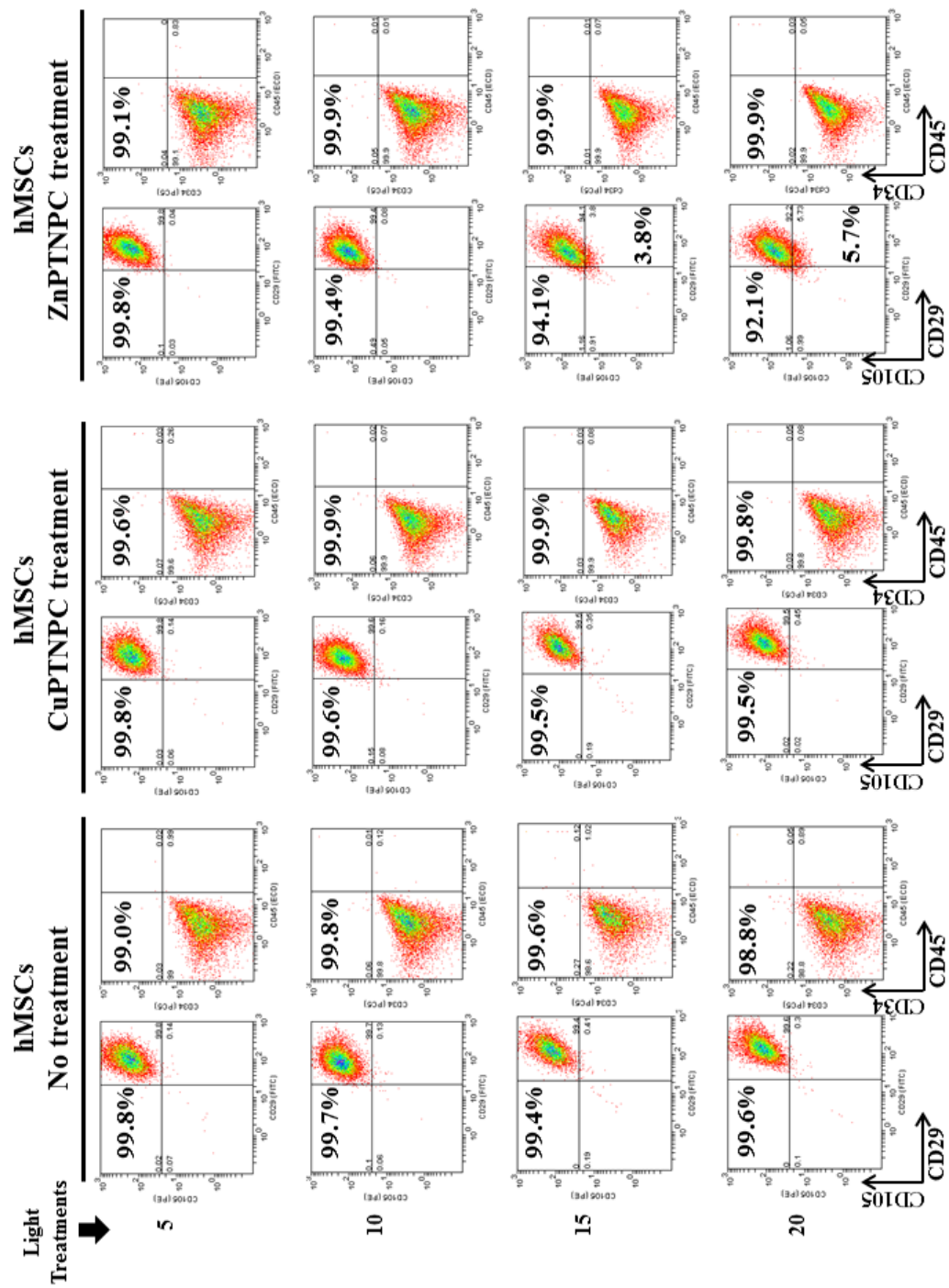


Figure 7.9: Immunophenotypic characterisation of hMSCs upon different light dosages. In the absence of nanoparticles cells were negative for hematopoietic markers CD34 and CD45 and positive for markers of undifferentiated MSCs CD29 and CD105 (left panel). The same pattern was observed for 5, 10, 15 and 20 light dosages. Similarly, hMSCs incubated with control CuPTNPC, at different light dosages, responded positively for CD29 and CD105 markers and negatively for CD34 and CD45 (middle panel). The analysis of hMSCs incubated with ZnPTNPC showed an undifferentiated profile after 5 and 10 light dosages; however, at 15 and 20 min a decrease in CD105 expression of 3.8 % and 5.7%, respectively (right panel) is observed.

to light exposure every 5 min with consequent variation of their environmental conditions, during a total period of 100 minutes. Furthermore, a subsequent staining with monoclonal antibodies presented a second disturbance to the cells, thereby representing another variation on its optimal growth conditions.

The analysis of hMSCs incubated with ZnPATNPC and consequently stimulated to produce ROS (upon light exposure) presented an augmented incidence of apoptosis with the increase of exposure to light. It was verified that, upon five irradiations, cells presented an incidence of apoptosis of approximately 29 %, which was similar to the results obtained after 10 irradiations (**30 %**). However, cells exposed to 15 and 20 irradiations presented higher values of 37 % and 44 %, respectively. Statistical analysis indicated that the variations observed on the incidence of apoptosis with exposure to light were statistically significant $P < 0.001$ (comparison between test samples at 5, 10, 15, and 20 irradiations).

When investigating the incidence of necrosis, no changes were observed (Figure 7.11). The percentage incidence of necrosis was inferior to 4%. These results do not preclude the existence of necrosis.

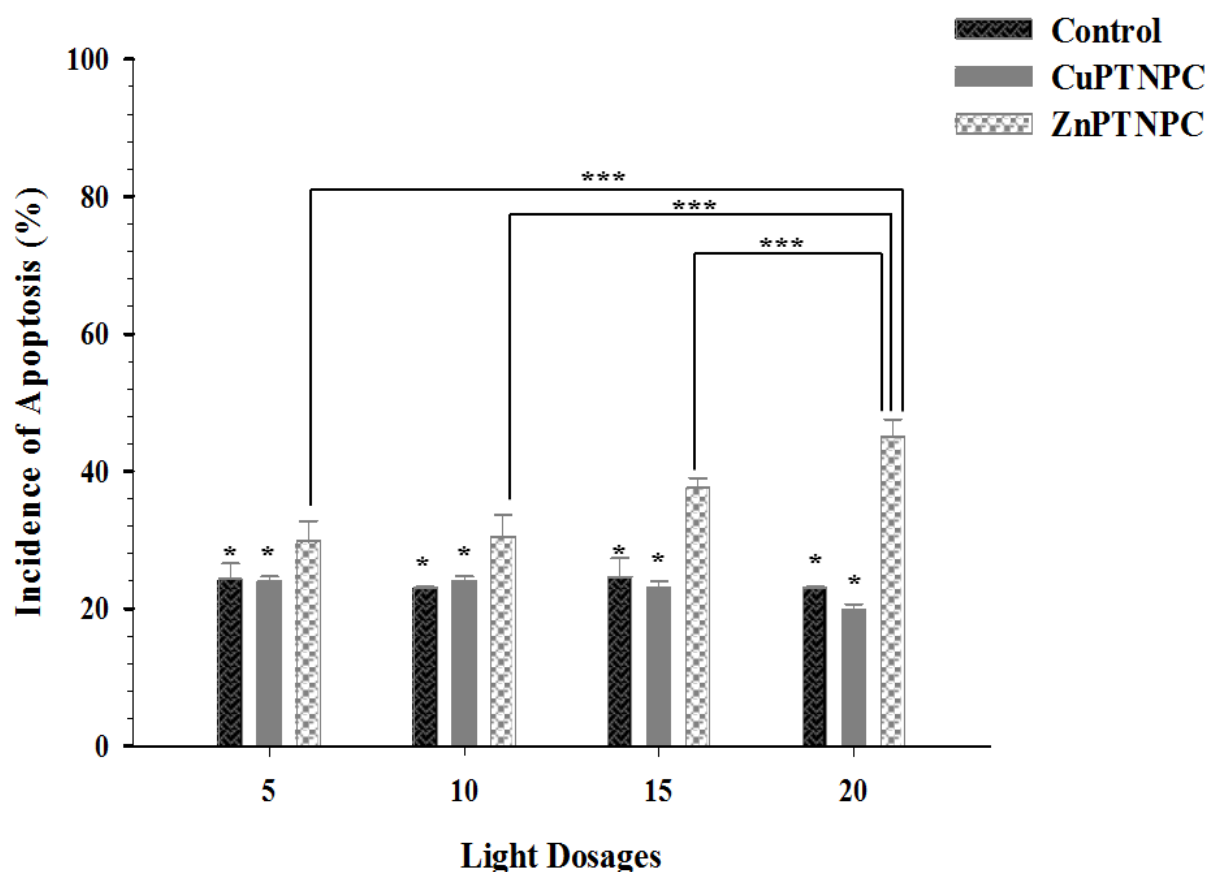


Figure 7.10: Flow cytometric analysis of the incidence of apoptosis in hMSCs stimulated to produce ROS upon light exposure. Live cells were stained with annexin V to determine the incidence of apoptosis; it is possible to observe an augmented incidence of apoptosis in cells incubated with ZnPATNPC. Means were calculated from two independent experiments conducted in triplicate. Error bars represent mean \pm SD (n=6). ZnPATNPC 20 dosages vs. ZnPATNPC 5,10,15: *** $p < 0.001$, One Way ANOVA; control vs. ZnPATNPC: * $p < 0.05$, One Way ANOVA; CuPATNPC vs. ZnPATNPC: * $p < 0.05$, One Way ANOVA. *textitP* values *textless* 0.05 were considered statistically different.

DNA labelling with propidium iodide (PI) requires the permeabilisation of the cellular membrane and interaction of the dye with DNA, which is only possible in late apoptotic/necrotic cells. At this stage, the integrity of the membrane is compromised allowing endogenous access of the dye. Furthermore, fragmentation of DNA is characteristic of necrotic/death cells with the subsequent loss of PI staining, which could justify such low percentage of necrosis.

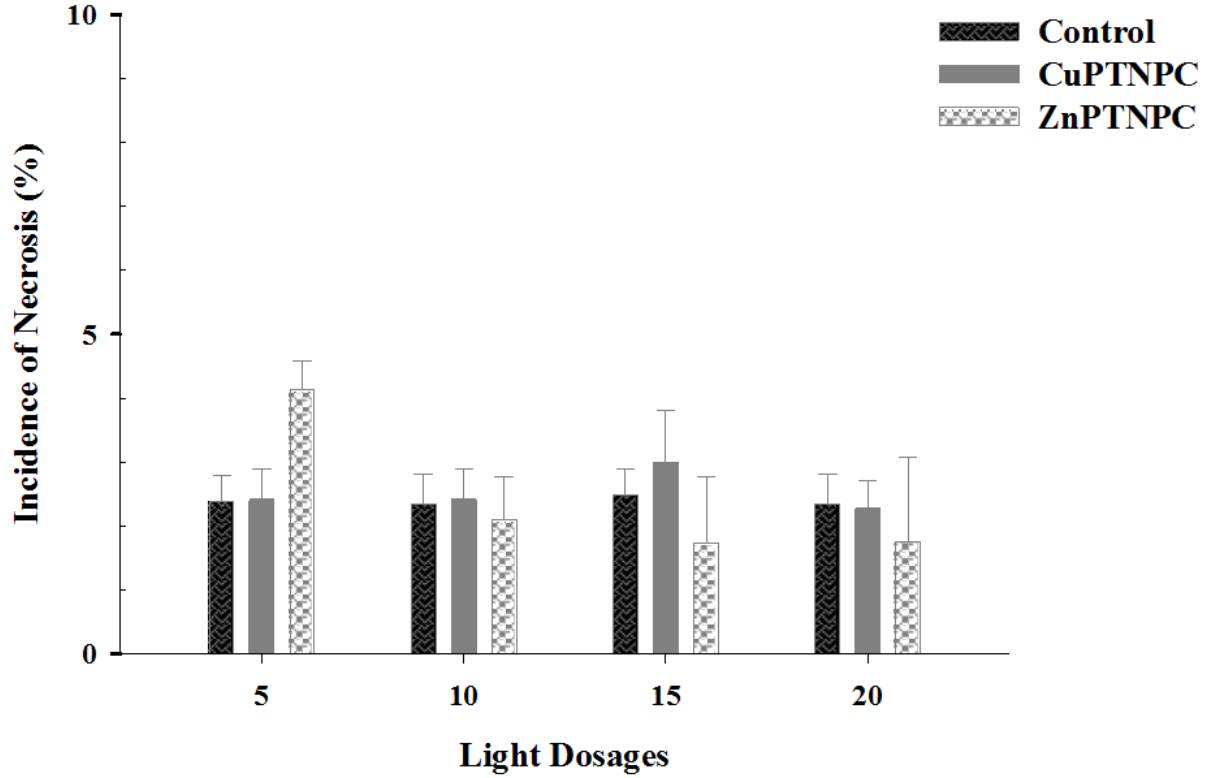


Figure 7.11: Flow cytometric analysis of the incidence of necrosis in hMSCs stimulated to produce ROS upon light exposure. Live cells were stained with PI to determine the incidence of necrosis; it is possible to observe there were no major variations of the levels of necrosis with values below to 5%. Results are representative two experiments conducted in triplicate (n=6).

The low level of propidium iodide fluorescence might also indicate that the levels of apoptosis refer to earlier apoptotic events. Apoptosis investigation by Annexin V staining happens because the phospholipidic membrane of the apoptotic cells remains asymmetric with the exposure of phosphatidyl serine, which binds to annexin V [79]. A late apoptotic stage would require the permeabilisation of membrane which would allow for propidium iodide to interact with DNA, and thus the observation of fluorescence at $\lambda_{em} = 608$ nm.

Overall, these results suggest that an increased light dosage leads to an aug-

mented level of incidence of apoptosis. Furthermore, the incidence of apoptosis might also explain the subtle decrease of the expression of CD105; alterations of the asymmetry of the phospholipidic membrane on apoptotic cells could lead to slightly lower affinity of the antibody with the endoglin surface receptor.

In order to closely investigate whether the increased amount of endogenous ROS induced changes in the profile of hMSCs, the surface marker expression was studied after two passages of light treated cells. To achieve this, hMSCs were firstly treated with 20 light dosages and then cultured under normal conditions. The morphology of hMSCs along the two subculture stages were investigated, no changes were observed . Cells were stained for CD29- FITC, CD105- PE, CD45-ECD and CD34-PC5 antibody conjugates after two subculture stages and studied by using FCM. Furthermore, there was also no indication of diminished proliferation.

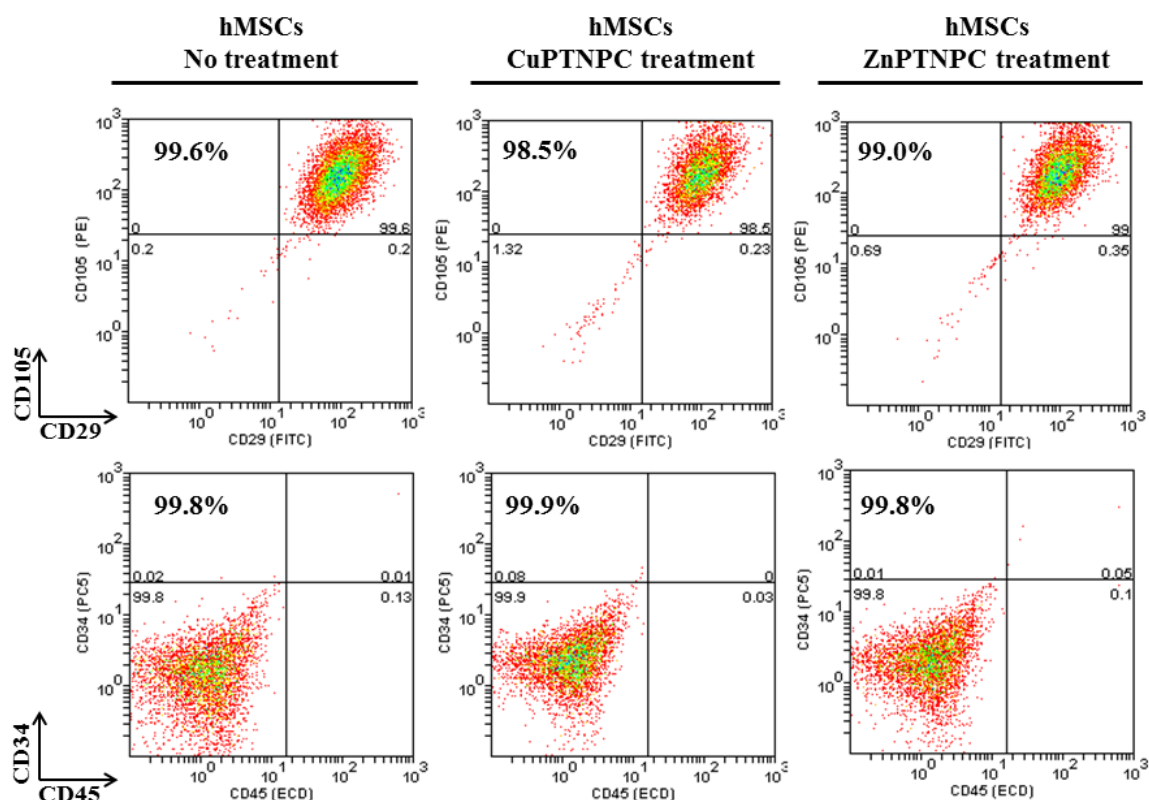


Figure 7.12: Immunophenotypic characterisation of hMSCs upon exposure to 20 light dosages followed by subculture (two passages). Left and middle panel show the expression profile for the negative and positive controls, respectively. It is observed that both controls present positive expression for CD29 and CD105 (top panels) and were equally negative for CD45 and CD34 (bottom panel). The test sample in the right panel shows a similar expression with both positive and negative control.

Bi-variate dot plots were analysed and are presented in Figure 7.12, showing the surface molecule profiles for CD29- FITC versus CD105- PE and CD45-ECD versus CD34-PC5 antibody conjugates. After two passages it was found that non-treated hMSCs and, hMSCs treated with CuPATNPC and ZnPATNPC presented the exact same profile. As initially observed in this chapter, hMSCs had shown positive expression of CD29 and CD105 ($\geq 99\%$) and reduced expression for both CD45 and CD34 ($\leq 1\%$). Therefore, the results suggested that a burst of ROS was not responsible for differentiation or senescence patterns in these MSCs. In

addition, the heterogeneity previously observed for CD 105 following 15 and 20 light dosages is suggested to be a consequence of the loss of membrane asymmetry and thus affinity for the antibody CD105, not an initiation of stem cell differentiation.

7.3 Conclusions

The present chapter enables the establishing of the effect of oxidative stress on the identity of hMSCs through the use of flow cytometry. This technique allows the performance of an in depth and overall analysis of the effects of ROS in treated hMSCs following several light dosages.

The porphyrinic nanoplateforms were successfully internalized in hMSCs and enabled to recreate an intracellular controlled oxidative environment, which produce very promising results. Lethal dosages of ROS in hMSCs maintained the characteristic surface marker expression, positive for CD29 and CD105 and negative for CD45 and CD34. Means of cellular viability by necrosis or apoptosis allowed the establishment of a response to the several ROS insults imposed on hMSCs upon activation of porphyrinic nanoplateforms by several light dosages. The major limitation of the present study was to estimate the amount of ROS produced upon each light dosage, information that would allow the establishment of cellular tolerance versus the deleterious effects of ROS.

A wide number of investigations have sought to establish the implications of ROS in stem cell differentiation and high levels of ROS are hypothesized to be associated with high metabolic demands and oxygen consumption for stem cell differentiation. The present study has shown that hMSCs have maintained identity even when exposed to high oxidative stress levels. Further investigation and reproduction of these results at different cellular passages and analysis of surface markers such as adiponectin/Acrp30 and Leptin/OB (adipogenesis differentiation) CD44 (chondrogenesis differentiation) and fibronectin (Osteogenesis differentiation) would bring greater knowledge about the role of ROS in stem cell differentiation and its thera-

peutics applications.

Chapter 8

Conclusions and Future Perspectives.

The main goal of the present research project was the development and characterization of a nanotool for monitoring the impact of ROS on the undifferentiated state of MSCs. In order to achieve this, firstly it was theorized that by exploiting the principle of photodynamic therapy using photosensitizers it would be possible to achieve the endogenous generation of ROS. In addition, its combination with a biocompatible polymeric matrix would allow it to control the photosensitiser activity at its intracellular location but also serve as a sensing platform.

Polyacrylamide nanoparticles have been widely accepted as resourceful and flexible tools to measure and investigate cellular signalling pathways. Thus, it was envisaged that would be possible the development of stable multifunctionalized nanoplatforms to act as carriers of photosensitizers (not interfering with its photophysical properties) based on previous approaches.

The synthesis of dually functionalised nanoparticles.

The development of mono and dually functionalised nanoparticles was successfully achieved by revisiting and combining previous approaches: (i) alkyne functionalities allowed the introduction of chemical reactivities exploiting the click chemistry principle for further conjugation; (ii) a trimethylammonium functionality would bring a facilitated cellular uptake and intracellular targeting. These approaches successfully generated stable multifunctionalized nanoplatforms. A limiting factor in this work was the characterising the number of functionalities introduced and its location. The aleatory nature of polyacrylamide polymerisation compromises the functionalization location, at the surface of nanoparticles or entrapped in the matrix.

The conjugation of porphyrinic moities with functionalised nanoplatforms

The major concerns in the development of conjugates are, how to maintain their final characteristics and stability, but also consider their interaction with biological microenvironment. The incorporation of photosensitizers was achieved based on approaches: (i) Porphyrins conjugated to alkyne/trimethylammonium functionalised NPs conferring to porphyrins surface conjugation; (ii) porphyrins monomers attached to the polymeric matrix and therefore entrapped, protecting the photosensitizer from the intracellular micro environment. Characterisation of these nanoplatforms suggested the successful development of porphyrinic nanoplatforms. The main obstacles found at this stage were in relation to the

photodynamic efficacy of photosensitizers conjugated and entrapped, but also regarding the concentration of photosensitisers combined with the polymeric nanoplatforms. A route for further investigation of these parameters could be by photophysical studies where the determination of quantum yields of fluorescence, singlet oxygen and fluorescence lifetimes could bring better knowledge of these nanoplatforms.

Delivery of nanoplatforms to hMSCs

A limiting factor in the use of nanoparticles as carriers, is an inadequate cellular delivery of these systems, which impacts on the development of new therapeutic agents and biomedical tools. In this study, it was envisaged that polymeric nanoparticles, due to their flexible matrix, could incorporate ligands that would promote internalization and intracellular targeting. The dual functionalisation of polyacrylamide nanoparticles with trimethyl ammonium and porphyrins accomplished a non-invasive nanoplatform capable of being internalized and preferentially accumulated at mitochondria.

The main aim of the project was to investigate the impact of and increased oxidative stress as consequence of ROS production. An increase in oxidative stress leads to alterations in cell homoeostasis and viability. Thus, to achieve an effective nanotool for ROS generation, dark toxic effects would not be acceptable. Flow cytometric analysis indicated the absence of dark toxicity was successfully accomplished for entrapped and conjugated porphyrins nanoplatforms.

The main limitations found for this approach were to clearly show the intracellular location of nanoparticles, this was a consequence of the diffraction limited

resolution-microscopy. The developments in super-resolution microscopy will provide new insights on nanoparticle co-localization, thus more studies would provide better information of the exact location of these nanosystems.

Porphyrinic nanoplateforms generating ROS in hMSCs.

The development of a non-invasive nanosystem to generate and evaluate the real time impact of ROS in cells, required the establishment of traceable levels of these species. Regardless of the short lifetimes of ROS, the development of fluorochromes responsive and specific for these species have greatly increased over the last couple of years. Therefore, it was anticipated that oxidative stress increase could be measured as a means of hydrogen peroxide production. A hydrogen peroxide specific switchable fluorochrome was allowed to identify the successful production of reactive oxygen species in hMSCs using porphyrin-nanoparticle conjugates. In addition, the presence of a “blast zone” also confirmed the efficient increase in oxidative stress with a major impact on cell viability. Unfortunately, porphyrinic entrapped nanoplateforms did not show the same evidence, as only a very small production of ROS was attained. The latest finding was most probably a consequence of photosensitizer entrapment and interaction with the polyacrylamide matrix. Porphyrinic nanoplateform conjugates were then found as excellent candidates for *in situ* ROS generation.

As the major aim of the project was to provide a controlled generation of ROS, it was anticipated that it would be necessary to control the level of toxicity of porphyrins. Therefore, the solution was to decrease the amount of porphyrin conjugated to nanoparticles until they reached non-toxic levels upon light exposure.

A small and controlled increase in oxidative stress would then be achieved by cumulative light exposure. This methodology allowed the successful development of a nanotool with the ability to generate oxidative stress in a controlled manner. Live cell fluorescence microscopy allowed the ability to successfully follow the controlled increase in oxidative stress by hydrogen peroxide production. This technology is a major advance for monitoring, diagnostics and therapeutics in ROS related diseases.

The main limitations of this study were to establish the non-toxic concentration of porphyrins at the surface of nanoparticles. This was a consequence of not yet being possible to determine the exact number of functionalisations on the nanoparticles and consequently the amount of porphyrin bonded. This problem was overcome by titrating porphyrin with functionalised nanoparticles and evaluating the phototoxic effects upon porphyrin activation. A second major limitation was to quantify/establish the efficiency of porphyrin to generate singlet oxygen, either for entrapped or conjugated porphyrin nanoparticles. Photophysical studies such as, quantum yields of fluorescence, singlet oxygen and fluorescence lifetimes could bring better knowledge of these nanoplatforms.

Impact of ROS in hMSCs surface identity

As a proof of the concept, the recently developed ROS generator nanotool was used to investigate the impact of this species on the surface marker expression of hMSCs. Flow cytometry analysis provides single cell analysis in a large population of cells. To investigate the impact of ROS, it was envisaged that treated hMSCs could be submitted to cumulative light dosages (low damage to lethal dosages)

and investigate the variations on its characteristic surface markers. This approach allowed successful verification that during ROS insults, hMSCs maintain their characteristic identity. The latest findings were supported by surface marker expression of two generations of hMSCs, submitted to nanoplateform treatment and oxidative stress insults. Cellular viability by necrosis or apoptosis allowed following with insults of ROS imposed to hMSCs upon activation of porphyrinic nanoplateforms by several light dosages. The impact of ROS in hMSCs was successfully investigated.

The major limitations of the present study were that to estimate the amount of ROS produced upon each light dosage, information would be needed that allow to establish cellular scavenge versus deleterious effects of ROS.

Further investigations and reproduction of these results at different cellular passages and analysis of surface markers, such as adiponectin/Acrp30 and Leptin/OB (adipogenesis differentiation); CD44 (chondrogenesis differentiation) and fibronectin (Osteogenesis differentiation), would bring higher knowledge about the role of ROS in stem cell differentiation and its therapeutics applications.

In summary, the knowledge acquired from these nanosystems led to the successful development of a nanotool for the endogenous generation of ROS in a controlled manner. Such a system offers the possibility to investigate real time responses to ROS effects. Furthermore, it also provides the study of single cell and metabolic pathways in great detail by the use of a non-invasive system. Thus, it can greatly contribute to the development of basic science in the field of ROS and to uncover potential therapeutic targets in related diseases.

Bibliography

- [1] M. DeRosa. Photosensitized singlet oxygen and its applications. *Coord. Chem. Rev.*, 233-234:351–371, 2002.
- [2] L. B. Josefsen. *Porphyrin- nanosensor conjugates: novel tools for the study of cellular response to oxidative stress*. PhD thesis, University of Hull, 2007.
- [3] V.J. Thannickal and B.L. Fanburg. Reactive oxygen species in cell signaling. *American Journal of Physiology-Lung Cellular and Molecular Physiology*, 279(6):L1005–L1028, 2000.
- [4] C. Chang, Y. T. Hu, C. F. Lo, and L. Luo. Photoactivation Studies of Zinc Porphyrin-Myoglobin System and Its Application for Light-Chemical Energy Conversion. *journal of biological*, 2011.
- [5] C. Nathan and A. Cunningham-Bussel. Beyond oxidative stress: an immunologist’s guide to reactive oxygen species. *Nature reviews. Immunology*, 13(5):349–61, 2013.
- [6] T. Finkel and N. J. Holbrook. Oxidants, oxidative stress and the biology of ageing. *Nature*, 408(6809):239–47, 2000.

- [7] B. C. Dickinson and C. J. Chang. Chemistry and biology of reactive oxygen species in signaling or stress responses. *Nat. Chem. Biol.*, 7(8):504–11, 2011.
- [8] B. D’Autréaux and M. B. Toledano. ROS as signalling molecules: mechanisms that generate specificity in ROS homeostasis. *Nat. Rev. Mol. Cell Biol.*, 8(10):813–24, 2007.
- [9] J. E. Klaunig, L. M. Kamendulis, and B. A. Hocevar. Oxidative stress and oxidative damage in carcinogenesis. *Toxicol. Pathol.*, 38(1):96–109, 2010.
- [10] P. T. Schumacker. Reactive oxygen species in cancer cells: live by the sword, die by the sword. *Cancer cell*, 10(3):175–6, 2006.
- [11] R. B. Hamanaka and N. S. Chandel. Mitochondrial reactive oxygen species regulate cellular signaling and dictate biological outcomes. *Trends Biochem. Sci.*, 35(9):505–13, 2010.
- [12] D. Hernández-García, C. D. Wood, S. Castro-Obregón, and L. Covarrubias. Reactive oxygen species: A radical role in development? *Free radical biology & medicine*, 49(2):130–43, 2010.
- [13] T. Nyokong and V. Ahsen, editors. *Photosensitizers in Medicine, Environment, and Security*. Springer Netherlands, 2012.
- [14] S. Wang, R. Gao, F. Zhou, and M. Selke. Nanomaterials and singlet oxygen photosensitizers: potential applications in photodynamic therapy. *Journal of Materials Chemistry*, 14(4):487, 2004.

- [15] A. S. Sobolev, D. A. Jans, and A. A. Rosenkranz. Targeted intracellular delivery of photosensitizers. *Progress in biophysics and molecular biology*, 73(1):51–90, 2000.
- [16] Mark Wainwright. *Photosensitisers in Biomedicine*. John Wiley & Sons Ltd, 1st ed. edition, 2009.
- [17] J. Zhao, W. Wu, J. Sun, and S. Guo. Triplet photosensitizers: from molecular design to applications. *Chemical Society reviews*, 42(12):5323–51, 2013.
- [18] I. J. Macdonald and T. J. Dougherty. Basic principles of photodynamic therapy. *Journal of Porphyrins and Phthalocyanines (JPP)*, 05(02):105–129, 2001.
- [19] T. A. Dix and J. Aikens. Mechanisms and biological relevance of lipid peroxidation initiation. *Chem. Res. Toxicol.*, 6(1):2–18, 1993.
- [20] A. Viola, N. W. Lutz, C. Maroc, C. Chabannon, M. Julliard, and P. J. Cozzzone. Metabolic effects of photodynamically induced apoptosis in an erythroleukemic cell line. A (31)P NMR spectroscopic study of Victoria-Blue-BO-sensitized TF-1 cells. *International journal of cancer. Journal internationale du cancer*, 85(5):733–9, 2000.
- [21] Q. Wang, T. R. Chan, R. Hilgraf, V. V. Fokin, K. B. Sharpless, and M. G. Finn. Bioconjugation by copper(I)-catalyzed azide-alkyne [3 + 2] cycloaddition. *Journal of the American Society*, 125(11):3192–3, 2003.
- [22] L. C. Penning and T. M. Dubbelman. Fundamentals of photodynamic therapy: cellular and biochemical aspects. *Anti-cancer drugs*, 5(2):139–46, 1994.

- [23] T. Grune, L. Klotz, J. Gieche, M. Rudeck, and H. Sies. Protein oxidation and proteolysis by the nonradical oxidants singlet oxygen or peroxynitrite. *Free Radic. Biol. Med.*, 30(11):1243–1253, 2001.
- [24] M. J. Davies. Singlet oxygen-mediated damage to proteins and its consequences. *Biochem. Biophys. Res. Commun.*, 305(3):761–770, 2003.
- [25] A. P. Castano, T. N. Demidova, and M. R. Hamblin. Mechanisms in photodynamic therapy: part one photosensitizers, photochemistry and cellular localization. *Photodiagnosis and Photodynamic Therapy*, 1(4):279–293, 2004.
- [26] S. Pervaiz. Pro-oxidant milieu blunts scissors: insight into tumor progression, drug resistance, and novel druggable targets. *Current pharmaceutical design*, 12(34):4469–77, 2006.
- [27] J. T. F. Lau. *Towards Dual and Targeted Cancer Therapy with Novel Phthalocyanine-based Photosensitizers*. Springer International Publishing, 2013.
- [28] L. B. Josefsen and R. W. Boyle. Unique diagnostic and therapeutic roles of porphyrins and phthalocyanines in photodynamic therapy, imaging and theranostics. *Theranostics*, 2(9):916–66, 2012.
- [29] L. R. Milgrom. *The colours of life: an introduction to the chemistry of porphyrins and related compounds*. Oxford University Press Inc., 1997.
- [30] I. Yoon, J. Z. Li, and Y. K. Shim. Advance in photosensitizers and light delivery for photodynamic therapy. *Clinical endoscopy*, 46(1):7–23, 2013.

- [31] S. Yano, S. Hirohara, M. Obata, Y. Hagiya, S. Ogura, A. Ikeda, H. Kataoka, M. Tanaka, and T. Joh. Current states and future views in photodynamic therapy. *Journal of Photochemistry and Photobiology C: Photochemistry Reviews*, 12(1):46–67, 2011.
- [32] S. J. Hurst, editor. *Biomedical Nanotechnology*, volume 726 of *Methods in Molecular Biology*. Humana Press, 2011.
- [33] M. Chakraborty, S. Jain, and V. Rani. Nanotechnology: emerging tool for diagnostics and therapeutics. *Appl. Biochem. Biotechnol.*, 165(5-6):1178–87, 2011.
- [34] T. L. Doane and C. Burda. The unique role of nanoparticles in nanomedicine: imaging, drug delivery and therapy. *Chem. Soc. Rev.*, 41(7):2885–911, 2012.
- [35] L. Y. T. Chou, K. Ming, and W. C. W. Chan. Strategies for the intracellular delivery of nanoparticles. *Chem. Soc. Rev.*, 40(1):233–45, 2011.
- [36] V. K. Varadan, L. Chen, and J. Xie, editors. *Nanomedicine Design and Applications of Magnetic Nanomaterials, Nanosensors and Nanosystems*. John Wiley & Sons, Ltd, 1st ed. edition, 2008.
- [37] J. W. Aylott. Optical nanosensors- an enabling technology for intracellular measurements. *The Analyst*, 128(4):309–312, 2003.
- [38] Y.-E. K. Lee, R. Smith, and R. Kopelman. Nanoparticle PEBBLE sensors in live cells and in vivo. *Annual review of analytical chemistry (Palo Alto, Calif.)*, 2:57–76, 2009.

- [39] J. S. Lee, M.-O. Lee, B. H. Moon, S. H. Shim, A. J. Fornace, and H. J. Cha. Senescent growth arrest in mesenchymal stem cells is bypassed by Wip1-mediated downregulation of intrinsic stress signaling pathways. *Stem cells (Dayton, Ohio)*, 27(8):1963–75, 2009.
- [40] M. N. Velasco-Garcia. Optical biosensors for probing at the cellular level: a review of recent progress and future prospects. *Seminars in cell & developmental biology*, 20(1):27–33, 2009.
- [41] A. Webster, P. Coupland, F. D. Houghton, H. J. Leese, and J. W. Aylott. The delivery of PEBBLE nanosensors to measure the intracellular environment. *Biochemical Society transactions*, 35(3):538–43, 2007.
- [42] M. Brasuel, R. Kopelman, M. Philbert, and J.W. Aylott. PEBBLE nanosensors for real time intracellular chemical imaging. In *Opt. Biosens*, pages 497–518. 2002.
- [43] H. Clark, M. Hoyer, M. Philbert, and R. Kopelman. Optical nanosensors for chemical analysis inside single living cells. 1. Fabrication, characterization, and methods for intracellular delivery of PEBBLE sensors. *Anal. Chem.*, 71(21):4831–6, 1999.
- [44] H. Clark, R. Kopelman, R. Tjalkens, and M. Philbert. Optical nanosensors for chemical analysis inside single living cells. 2. Sensors for pH and calcium and the intracellular application of PEBBLE sensors. *Analytical chemistry*, 71(21):4837–43, 1999.
- [45] M. Elsayahy and K.L. Wooley. Design of polymeric nanoparticles for biomedical delivery applications. *Chem. Soc. Rev.*, 41:2545–2561, 2012.

- [46] A. H. Faraji and P. Wipf. Nanoparticles in cellular drug delivery. *Bioorganic & medicinal chemistry*, 17(8):2950–62, 2009.
- [47] Nguyen T.K. Thanh and Luke a.W. Green. Functionalisation of nanoparticles for biomedical applications. *Nano Today*, 5(3):213–230, 2010.
- [48] R. A. Petros and J. M. DeSimone. Strategies in the design of nanoparticles for therapeutic applications. *Nature reviews. Drug discovery*, 9(8):615–27, 2010.
- [49] J. Wang, J. D. Byrne, M. E. Napier, and J. M. DeSimone. More effective nanomedicines through particle design. *Small (Weinheim an der Bergstrasse, Germany)*, 7(14):1919–31, 2011.
- [50] A. Chaudhuri, G. Battaglia, and R. Golestanian. The effect of interactions on the cellular uptake of nanoparticles. *Phys. Biol.*, 8(4):9, 2011.
- [51] E. Fröhlich. The role of surface charge in cellular uptake and cytotoxicity of medical nanoparticles. *International journal of nanomedicine*, 7:5577–91, 2012.
- [52] S. E. McNeil, editor. *Characterization of Nanoparticles Intended for Drug Delivery*, volume 697 of *Methods in Molecular Biology*. Humana Press, 2011.
- [53] J. P. Sumner, N. M. Westerberg, A. K. Stoddard, T. K. Hurst, M. Cramer, R. B. Thompson, C. Fierke, and R. Kopelman. DsRed as a highly sensitive, selective, and reversible fluorescence-based biosensor for both Cu(+) and Cu(2+) ions. *Biosensors & bioelectronics*, 21(7):1302–8, 2006.

- [54] J. P. Sumner, N. M. Westerberg, A. K. Stoddard, C. A. Fierke, and R. Kopelman. Cu⁺ and Cu²⁺ sensitive PEBBLE fluorescent nanosensors using DsRed as the recognition element. *Sensors And Actuators*, 113:760–767, 2006.
- [55] J.P. Sumner, J.W. Aylott, E. Monson, and R. Kopelman. A fluorescent PEBBLE nanosensor for intracellular free zinc. *Analyst*, 127(1):11–16, 2001.
- [56] H. Xu, J. W. Aylott, and R. Kopelman. Fluorescent nano-pebble sensors designed for intracellular glucose imaging. *Analyst*, 127:1471–1477, 2002.
- [57] H. Sun, K. Almdal, and T. L. Andresen. Expanding the dynamic measurement range for polymeric nanoparticle pH sensors. *Chemical communications (Cambridge, England)*, 47(18):5268–70, 2011.
- [58] V. M. Chauhan, G. R. Burnett, and J. W. Aylott. Dual-fluorophore ratiometric pH nanosensor with tuneable pKa and extended dynamic range. *The Analyst*, 136(9):1799–801, 2011.
- [59] H. Sun, T. L. Andresen, R. V. Benjaminsen, and K. Almdal. Polymeric Nanosensors for Measuring the Full Dynamic pH Range of Endosomes and Lysosomes in Mammalian Cells. *Journal of Biomedical Nanotechnology*, 5(6):676–682, 2009.
- [60] Y.-E. K. Lee, E. E. Ulbrich, G. Kim, H. Hah, C. Strollo, W. Fan, R. Gurjar, S. Koo, and R. Kopelman. Near infrared luminescent oxygen nanosensors with nanoparticle matrix tailored sensitivity. *Analytical chemistry*, 82(20):8446–55, 2010.

- [61] Y.-E. L. Koo, Y. Cao, R. Kopelman, S. M. Koo, M. Brasuel, and M. Philbert. Real-time measurements of dissolved oxygen inside live cells by organically modified silicate fluorescent nanosensors. *Analytical chemistry*, 76(9):2498–505, 2004.
- [62] R. Kopelman, Y. Lee Koo, M. Philbert, B. A. Moffat, G. Ramachandra Reddy, P. McConville, D. E. Hall, T. L. Chenevert, M. S. Bhojani, S. M. Buck, A. Rehemtulla, and B. D. Ross. Multifunctional nanoparticle platforms for in vivo MRI enhancement and photodynamic therapy of a rat brain cancer. *J. Magn. Mater.*, 293(1):404–410, 2005.
- [63] S. Wang, W. Fan, G. Kim, H. J. Hah, Y. E. Lee, R. Kopelman, M. Ethirajan, A. Gupta, L. N. Goswami, P. Pera, J. Morgan, and R. K. Pandey. Novel methods to incorporate photosensitizers into nanocarriers for cancer treatment by photodynamic therapy. *Lasers in surgery and medicine*, 43(7):686–95, 2011.
- [64] W. Tang, H. Xu, R. Kopelman, and M. A. Philbert. Photodynamic characterization and in vitro application of methylene blue-containing nanoparticle platforms. *Photochemistry and photobiology*, 81(2):242–9, 2005.
- [65] M. E. Wieder, D. C. Hone, M. J. Cook, M. M. Handsley, J. Gavrilovic, and D. A. Russell. Intracellular photodynamic therapy with photosensitizer-nanoparticle conjugates: cancer therapy using a 'Trojan horse'. 5(8):727–34, 2006.
- [66] H. J. Hah, G. Kim, Y.-E. K. Lee, D. A. Orringer, O. Sagher, M. A. Philbert, and R. Kopelman. Methylene blue-conjugated hydrogel nanoparticles

- and tumor-cell targeted photodynamic therapy. *Macromolecular bioscience*, 11(1):90–9, 2011.
- [67] A. Gupta, S. Wang, P. Pera, K. V. R. Rao, N. Patel, T. Y. Ohulchanskyy, J. Missert, J. Morgan, Y.-E. Koo-Lee, R. Kopelman, and R. K. Pandey. Multifunctional nanoplatforms for fluorescence imaging and photodynamic therapy developed by post-loading photosensitizer and fluorophore to polyacrylamide nanoparticles. *Nanomedicine : nanotechnology, biology, and medicine*, 8(6):941–50, 2012.
- [68] M. Kuruppuarachchi, H. Savoie, A. Lowry, C. Alonso, and R. W. Boyle. Polyacrylamide nanoparticles as a delivery system in photodynamic therapy. *Molecular pharmaceutics*, 8(3):920–31, 2011.
- [69] D. Gao, R. R. Agayan, H. Xu, M. A. Philbert, and R. Kopelman. Nanoparticles for two-photon photodynamic therapy in living cells. *Nano Lett.*, 6(11):2383–6, 2006.
- [70] L. B. Josefsen, J. W. Aylott, A. Beeby, P. Warburton, J. P. Boyle, C. Peers, and R. W. Boyle. Porphyrin-nanosensor conjugates. New tools for the measurement of intracellular response to reactive oxygen species. *Photochemical & photobiological sciences*, 9(6):801–11, 2010.
- [71] K. Y. Win and S. S. Feng. Effects of particle size and surface coating on cellular uptake of polymeric nanoparticles for oral delivery of anticancer drugs. *Biomaterials*, 26(15):2713–22, 2005.

- [72] K. T. Thurn, E. M. B. Brown, A. Wu, S. Vogt, B. Lai, J. Maser, T. Paunesku, and G. E. Woloschak. Nanoparticles for Applications in Cellular Imaging. *Nanoscale Research Letters*, 2(9):430–441, 2007.
- [73] J. Jiang, G. Oberdörster, and P. Biswas. Characterization of size, surface charge, and agglomeration state of nanoparticle dispersions for toxicological studies. *Journal of Nanoparticle Research*, 11(1):77–89, 2008.
- [74] S. E. Gratton, P. Ropp, P. D. Pohlhaus, J. C. Luft, V. J. Madden, M. E. Napier, and J. M. DeSimone. The effect of particle design on cellular internalization pathways. *Proc. Natl. Acad. Sci. U. S. A.*, 105(33):11613–8, 2008.
- [75] H. Hillaireau and P. Couvreur. Nanocarriers entry into the cell: relevance to drug delivery. *Cellular and molecular life sciences : CMLS*, 66(17):2873–96, 2009.
- [76] S. Podzimek. *Light scattering, size exclusion chromatography and asymmetric flow field flow fractionation : powerful tools for the characterization of polymers, proteins and nanoparticles*. John Wiley & Sons, Inc., 2011.
- [77] R. G. Driggers, C. Hoffman, and R. Driggers. *Encyclopedia of Optical Engineering*. CRC Press, Taylor & Francis Group, 2003.
- [78] T. S. Hawley and R. G. Hawley, editors. *Flow Cytometry Protocols*, volume 699 of *Methods in Molecular Biology*. Humana Press, 2011.
- [79] M. G. Macey. *Flow Cytometry Principles and Applications*. Humana Press Inc., 2007.

- [80] M. J. Jaroszeski and G. Radcliff. Fundamentals of flow cytometry. *Mol. Biotechnol.*, 11(1):37–53, 1999.
- [81] M. Brown and C. Wittwer. Flow cytometry: principles and clinical applications in hematology. *Clin. Chem.*, 46(8):1221–9, 2000.
- [82] Life Technologies. Introduction to flow cytometry.
- [83] T. S. Hawley and R. G. Hawley. *Flow Cytometry Protocols*, volume 699 of *Methods in Molecular Biology*. Humana Press, 2011.
- [84] N. Baumgarth and M. Roederer. A practical approach to multicolor flow cytometry for immunophenotyping. *J. Immunol. Methods*, 243(1-2):77–97, 2000.
- [85] K. Sivakumar, F. Xie, B. M. Cash, S. Long, H. N. Barnhill, and Q. Wang. A fluorogenic 1,3-dipolar cycloaddition reaction of 3-azidocoumarins and acetylenes. *Organic letters*, 6(24):4603–6, 2004.
- [86] E. P. Magennis. *Bacterial Auto-nemesis-Templating polymers for cell sequestration*. Phd thesis, University of Nottingham, 2013.
- [87] K. Welser, M. A. Perera, J. W. Aylott, and W. C. Chan. A facile method to clickable sensing polymeric nanoparticles. *Chemical communications (Cambridge, England)*, (43):6601–3, 2009.
- [88] A. J. Friedenstein, R. K. Chailakhyan, N. V. Latsinik, A. F. Panasyuk, and I. V. Keiliss-Borok. Stromal cells responsible for transferring the microenvironment of the hemopoietic tissues. Cloning in vitro and retransplantation in vivo. *Transplantation*, 17(4):331–40, 1974.

- [89] P. G. Coupland, K. A. Fisher, D. R. E. Jones, and J. W. Aylott. Internalisation of polymeric nanosensors in mesenchymal stem cells: analysis by flow cytometry and confocal microscopy. *Journal of controlled release*, 130(2):115–20, 2008.
- [90] J. F. Morgan, M. E. Campbell, and H. J. Morton. The nutrition of animal tissues cultivated in vitro. I. A survey of natural materials as supplements to synthetic medium 199. *Journal of the National Cancer Institute*, 16(2):557–67, 1955.
- [91] A. Aldahmash, M. Haack-Sørensen, M. Al-Nbaheen, L. Harkness, B. M. Abdallah, and M. Kassem. Human serum is as efficient as fetal bovine serum in supporting proliferation and differentiation of human multipotent stroma 1 (mesenchymal) stem cells in vitro and in vivo. *Stem cell reviews*, 7(4):860–8, 2011.
- [92] F. Candau, Y.S. Leong, G. Pouyet, and S. Candau. Inverse microemulsion polymerization of acrylamide: characterization of the water-in-oil microemulsions and the final microlatexes. *J. Colloid Interface Sci.*, 101(1):167–183, 1984.
- [93] C. Daubresse, Ch. Grandfils, R. Jérôme, and Ph. Teyssié. Enzyme immobilization in reactive nanoparticles produced by inverse microemulsion polymerization. *Colloid & Polymer Science*, 274(5):482–489, 1996.
- [94] F. Di Benedetto, A. Biasco, D. Pisignano, and R. Cingolani. Patterning polyacrylamide hydrogels by soft lithography. *Nanotechnology*, 16:S165, 2005.

- [95] C. P. Yong and L. M. Gan. *Polymer Particles*, volume 175. Springer Berlin Heidelberg, 2005.
- [96] T. Tadros, editor. *Self-organized surfactant structures*. Wiley-VCH Verlag & Co. KGaA, 2011.
- [97] T. P. Hoar and J. H. Schulman. Transparent Water-in-Oil Dispersions: the Oleopathic Hydro-Micelle. *Nature*, 152(3847):102–103, 1943.
- [98] C. Stubenrauch. *Microemulsions Background, New concepts, Applications, Perspectives*. Blackwell Publishing Ltd., 2009.
- [99] D. Langevin. Micelles and Microemulsions. *Annual Review of Physical Chemistry*, 43(1):341–369, 1992.
- [100] T. Cosgrove. *Colloid Science, Principles, Methods and Applications*. Wiley-Blackwell, 2nd edition, 2010.
- [101] J. Koetz and S. Kosmella. *Polyelectrolytes and Nanoparticles*. Springer Laboratory. Springer Berlin Heidelberg, 2007.
- [102] J. Barton. Free-radical polymerization in inverse microemulsions. *Prog. Polym. Sci.*, 21(3):399–438, 1996.
- [103] F. M. Pavel. Microemulsion Polymerization. *Journal of Dispersion Science and Technology*, 25(1):1–16, 2004.
- [104] J. R. Herrera, R. D. Peralta, R. G. Lopez, L. C. Cesteros, E. Mendizábal, and J. E. Puig. Cosurfactant effects on the polymerization of vinyl acetate in anionic microemulsion media. *Polymer*, 44(6):1795–1802, 2003.

- [105] A. K. Poulsen, L. Arleth, K. Almdal, and A. M. Scharff-Poulsen. Unusually large acrylamide induced effect on the droplet size in AOT/Brij30 water-in-oil microemulsions. *Journal of colloid and interface science*, 306(1):143–53, 2007.
- [106] M. K. Mishra and Y. Yagci, editors. *Handbook of Vinyl Polymers Radical Polymerization, Process and Technology*. CRC Press, Taylor & Francis Group, 2nd ed. edition, 2009.
- [107] N. Orakdogan and O. Okay. Influence of the initiator system on the spatial inhomogeneity in acrylamide-based hydrogels. *Journal of applied polymer science*, 103(5):3228–3237, 2007.
- [108] George Odian. *Principles of Polymerization*. John Wiley & Sons, Inc., fourth edi edition, 2004.
- [109] B. M. Moore. *Development of Energy-transfer-based nanoconstructs for the detection of proteases*. PhD thesis, Uniiversity of Nottingham, 2008.
- [110] S. Myhra and J. C. Reviere. *Characterisation of Nanostructures*. CRC Press, Taylor & Francis Group, 2013.
- [111] Clive Washington. *Particle size analysis in pharmaceuticals and other industries*. Ellis Horwood Limited, 1992.
- [112] T. Provder, editor. *Particle size distribution Assessment and characterization*. Acs Symposium Series: Amer Chemical Society, 1987.
- [113] M. Malkoch, R. J. Thibault, E. Drockenmuller, M. Messerschmidt, B. Voit, T. P. Russell, and C. J. Hawker. Orthogonal approaches to the simultan-

- eous and cascade functionalization of macromolecules using click chemistry. *Journal of the American Chemical Society*, 127(42):14942–9, 2005.
- [114] K. Welser. *Development of protease responsive nanoprobos with tethered coumarin substances*. PhD thesis, University of Nottingham, 2009.
- [115] Malvern. Dynamic Light Scattering : Common terms defined., 2011.
- [116] E. J. Park, M. Brasuel, C. Behrend, M. a Philbert, and R. Kopelman. Ratiometric optical PEBBLE nanosensors for real-time magnesium ion concentrations inside viable cells. *Analytical chemistry*, 75(15):3784–91, 2003.
- [117] M.G. Brasuel, T.J. Miller, R. Kopelman, and M.A. Philbert. Liquid polymer nano-PEBBLEs for Cl⁻ analysis and biological applications. *Analyst*, 128(10):1262–1267, 2003.
- [118] E. Monson, M. Brasuel, and M. Philbert. PEBBLE nanosensors for in vitro bioanalysis. *photonics handbook*. Boca, 2003.
- [119] H. Sun, A. M. Scharff-poulsen, H. Gu, I. Jakobsen, J. M. Kossmann, W. B. Frommer, and K. Almdal. Phosphate Sensing by Fluorescent Polyacrylamide Nanoparticles. 2(1):19–24, 2008.
- [120] K. Almdal, H. Sun, A.K. Poulsen, L. Arleth, I. Jakobsen, H. Gu, and A.M. Scharff-Poulsen. Fluorescent gel particles in the nanometer range for detection of metabolites in living cells. *Polym. Adv. Technol.*, 17(9-10):790–793, 2006.

- [121] A. Lapresta-Fernández, P.J. Cywinski, A.J. Moro, and G.J. Mohr. Fluorescent polyacrylamide nanoparticles for naproxen recognition. *Analytical and Bioanalytical Chemistry*, 395(6):1821–1830, 2009.
- [122] G. Reddy, M. S. Bhojani, P. McConville, J. Moody, B. A. Moffat, D. E. Hall, G. Kim, Y. E. L. Koo, M. J. Woolliscroft, J. V. Sugai, T. D. Johnson, M. A. Philbert, R. Kopelman, A. Rehemtulla, and B. D. Ross. Vascular targeted nanoparticles for imaging and treatment of brain tumors. *Clinical cancer research : an official journal of the American Association for Cancer Research*, 12(22):6677–86, 2006.
- [123] W. R. Algar, D. E. Prasuhn, M. H. Stewart, T. L. Jennings, J. B. Blanco-Canosa, P. E. Dawson, and I. L. Medintz. The controlled display of biomolecules on nanoparticles: a challenge suited to bioorthogonal chemistry. *Bioconjugate chemistry*, 22(5):825–58, 2011.
- [124] M. Rubinstein, R. H. Colby, A. V. Dobrynin, and J. F. Joanny. Elastic Modulus and Equilibrium Swelling of Polyelectrolyte Gels. *Macromolecules*, 29(1):398–406, 1996.
- [125] M. Lundqvist, J. Stigler, G. Elia, I. Lynch, T. Cedervall, and K. A. Dawson. Nanoparticle size and surface properties determine the protein corona with possible implications for biological impacts. *Proceedings of the National Academy of Sciences of the United States of America*, 105(38):14265–70, 2008.
- [126] O. Elizalde, G. P. Leal, and J. R. Leiza. Particle Size Distribution Measurements of Polymeric Dispersions: A Comparative Study. *Particle & Particle*

- Systems Characterization*, 17(5-6):236–243, 2000.
- [127] H. Nolte, C. Schilde, and A. Kwade. Determination of particle size distributions and the degree of dispersion in nanocomposites. *Composites Science and Technology*, 72(9):948–958, 2012.
- [128] R. Sperling and W. J. Parak. Surface modification, functionalization and bioconjugation of colloidal inorganic nanoparticles. *Philosophical transactions. Series A, Mathematical, physical, and engineering sciences*, 368(1915):1333–83, 2010.
- [129] G. T. Hermanson, editor. *Bioconjugate Techniques*. Elsevier Inc., 2nd ed. edition, 2008.
- [130] M. Meldal and C. W. Tornø e. Cu-catalyzed azide-alkyne cycloaddition. *Chemical reviews*, 108(8):2952–3015, 2008.
- [131] W. H. Binder and R. Sachsenhofer. Click Chemistry in Polymer and Material Science: An Update. *Macromol. Rapid Commun.*, 29(12-13):952–981, 2008.
- [132] Joerg L., editor. *Click Chemistry for Biotechnology and Materials Science*. John Wiley & Sons Ltd, 1st ed. edition, 2009.
- [133] C.D. Hein, X.M. Liu, and D. Wang. Click chemistry, a powerful tool for pharmaceutical sciences. *Pharm. Res.*, 25(10):2216–2230, 2008.
- [134] H. C. Kolb, M. G. Finn, and K. B. Sharpless. Click Chemistry: Diverse Chemical Function from a Few Good Reactions. *Angewandte Chemie (International ed. in English)*, 40(11):2004–2021, 2001.

- [135] G. C. Tron, T. Pirali, R. A. Billington, P. L.i Canonico, G. Sorba, and A. A. Genazzani. Click Chemistry Reactions in Medicinal Chemistry : Applications of the 1 , 3-dipolar Cycloaddition Between Azides and Alkynes. *Medicinal Research Reviews*, 28(2):278–308, 2007.
- [136] J. E. Moses, A. D. Moorhouse, and K. B. Sharpless. The growing applications of click chemistry. *Chemical Society reviews*, 36(8):1249–62, 2007.
- [137] R. Chinchilla and C. Najera. The Sonogashira reaction: a booming methodology in synthetic organic chemistry. *Chem. Rev.*, 107(3):874–922, 2007.
- [138] T. R. Chan, R. Hilgraf, K. B. Sharpless, and V. Fokin. Polytriazoles as copper(I)-stabilizing ligands in catalysis. *Org. Lett.*, 6(17):2853–5, 2004.
- [139] H. A. Orgueira, D. Fokas, Y. Isome, P. C. M. Chan, and C. M. Baldino. Regioselective synthesis of [1,2,3]-triazoles catalyzed by Cu(I) generated in situ from Cu(0) nanosize activated powder and amine hydrochloride salts. *Tetrahedron Letters*, 46(16):2911–2914, 2005.
- [140] S. Gupta, J. Kuzelka, P. Singh, W. G. Lewis, M. Manchester, and M. G. Finn. Accelerated bioorthogonal conjugation: a practical method for the ligation of diverse functional molecules to a polyvalent virus scaffold. *Bioconjugate chemistry*, 16(6):1572–9, 2005.
- [141] M. Makarska, S. Radzki, and J. Legendziewicz. Spectroscopic characterization of the water-soluble cationic porphyrins and their complexes with Cu(II) in various solvents. *Journal of Alloys and Compounds*, 341(1-2):233–238, 2002.

- [142] R. Wiglusz, J. Legendziewicz, A. Graczyk, S. Radzki, P. Gawryszewska, and J. Sokolnicki. Spectroscopic properties of porphyrins and effect of lanthanide ions on their luminescence efficiency. *Journal of Alloys and Compounds*, 380(1-2):396–404, 2004.
- [143] W. Zheng, N. Shan, L. Yu, and X. Wang. UV-visible, fluorescence and EPR properties of porphyrins and metalloporphyrins. *Dyes and Pigments*, 77(1):153–157, 2008.
- [144] J. Rodriguez, C. Kirmaier, and D. Holten. Optical properties of metalloporphyrin excited states. *Journal of the American Chemical Society*, 111(17):6500–6506, 1989.
- [145] S. Udenfriend, S. Stein, P. Böhlen, W. Dairman, W. Leimgruber, and M. Weigle. Fluorescamine: a reagent for assay of amino acids, peptides, proteins, and primary amines in the picomole range. *Science (New York, N.Y.)*, 178(4063):871–2, 1972.
- [146] M. Weigle, S. De Bernardo, and W. Leimgruber. Fluorescent labeling of proteins. A new methodology. *Biochemical and biophysical research communications*, 54(3):899–906, 1973.
- [147] R. Hakanson, L. I. Larsson, and F. Sundler. Fluorescamine: A novel reagent for the histochemical detection of amino groups. *Histochemistry*, 39(1):15–23, 1974.
- [148] R. A. Sperling and W. J. Parak. Surface modification, functionalization and bioconjugation of colloidal inorganic nanoparticles. 368(1915):1333–1383, 2010.

- [149] K. McAllister, P. Sazani, M. Adam, M. J. Cho, M. Rubinstein, R. J. Samulski, and J. M. DeSimone. Polymeric Nanogels Produced via Inverse Microemulsion Polymerization as Potential Gene and Antisense Delivery Agents. *Journal of the American Chemical Society*, 124(51):15198–15207, 2002.
- [150] A. Albanese, P. S. Tang, and W. C. W. Chan. The effect of nanoparticle size, shape, and surface chemistry on biological systems. *Annual review of biomedical engineering*, 14:1–16, 2012.
- [151] R. E. Serda, J. Gu, Rohan C. B., X. Liu, C. Chiappini, P. Decuzzi, and M. Ferrari. The association of silicon microparticles with endothelial cells in drug delivery to the vasculature. *Biomaterials*, 30(13):2440–8, 2009.
- [152] A. Prokop, editor. *Intracellular Delivery*, volume 5 of *Fundamental Biomedical Technologies*. Springer Netherlands, 2011.
- [153] J. G. Huang, T. Leshuk, and F. X. Gu. Emerging nanomaterials for targeting subcellular organelles. *Nano Today*, 6(5):478–492, 2011.
- [154] I. Canton and G. Battaglia. Endocytosis at the nanoscale. *Chem. Soc. Rev.*, 41(7):2718–39, 2012.
- [155] H. T. McMahon and E. Boucrot. Molecular mechanism and physiological functions of clathrin-mediated endocytosis. *Nature reviews. Molecular cell biology*, 12(8):517–33, 2011.
- [156] D. A. Brown and E. London. Functions of lipid rafts in biological membranes. *Annu. Rev. Cell Dev. Biol.*, 14:111–36, 1998.

- [157] L. Pelkmans and A. Helenius. Endocytosis Via Caveolae. *Traffic*, 3(5):311–320, 2002.
- [158] A. Hayer, M. Stoeber, D. Ritz, S. Engel, H. H. Meyer, and A. Helenius. Caveolin-1 is ubiquitinated and targeted to intralumenal vesicles in endolysosomes for degradation. *The Journal of cell biology*, 191(3):615–29, 2010.
- [159] J. Couet, M. M. Belanger, E. Roussel, and M. C. Drolet. Cell biology of caveolae and caveolin. *Adv. Drug Delivery Rev.*, 49(3):223–35, 2001.
- [160] F. Zhao, Y. Y. Zhao, Y. Liu, X. Chang, and C. Chen. Cellular uptake, intracellular trafficking, and cytotoxicity of nanomaterials. *Small (Weinheim an der Bergstrasse, Germany)*, 7(10):1322–37, 2011.
- [161] O. Harush-Frenkel, E. Rozentur, S. Benita, and Y. Altschuler. Surface charge of nanoparticles determines their endocytic and transcytotic pathway in polarized MDCK cells. *Biomacromolecules*, 9(2):435–43, 2008.
- [162] G. Su, H. Zhou, Q. Mu, Y. Zhang, L. Li, P. Jiao, G. Jiang, and B. Yan. Effective Surface Charge Density Determines the Electrostatic Attraction between Nanoparticles and Cells. *The Journal of Physical Chemistry C*, 116(8):4993–4998, 2012.
- [163] A. El-Sayed, S. Futaki, and H. Harashima. Delivery of macromolecules using arginine-rich cell-penetrating peptides: ways to overcome endosomal entrapment. *The AAPS journal*, 11(1):13–22, 2009.
- [164] Sean Marrache and Shanta Dhar. Engineering of blended nanoparticle platform for delivery of mitochondria-acting therapeutics. *Proceedings of the Na-*

- tional Academy of Sciences of the United States of America*, 109(40):16288–93, 2012.
- [165] I. Behrens, A. I. V. Pena, M. J. Alonso, and T. Kissel. Comparative uptake studies of bioadhesive and non-bioadhesive nanoparticles in human intestinal cell lines and rats: the effect of mucus on particle adsorption and transport. *Pharm. Res.*, 19(8):1185–93, 2002.
- [166] J. Panyam and V. Labhasetwar. Biodegradable nanoparticles for drug and gene delivery to cells and tissue. *Advanced Drug Delivery Reviews*, 55(3):329–347, 2003.
- [167] A. K. Varkouhi, M. Scholte, G. Storm, and Haisma H. J. Endosomal escape pathways for delivery of biologicals. *Journal of Controlled Release*, 151(3):220 – 228, 2011.
- [168] H. W. Huang, F.-Y. Chen, and M.-T. Lee. Molecular mechanism of peptide-induced pores in membranes. *Phys. Rev. Lett.*, 92, 2004.
- [169] T. Lazaridis, Y. He, and L. Prieto. Membrane interactions and pore formation by the antimicrobial peptide protegrin. *Biophysical journal*, 104(3):633–42, 2013.
- [170] M-T. Lee, W-C. Hung, F-Y. Chen, and H. W. Huang. Mechanism and kinetics of pore formation in membranes by water-soluble amphipathic peptides. *Proceedings of the National Academy of Sciences of the United States of America*, 105(13):5087–92, 2008.

- [171] A. V. Ulasov, Y. V. Khramtsov, G. A. Trusov, A. A. Rosenkranz, E. D. Sverdlov, and A. S. Sobolev. Properties of PEI-based polyplex nanoparticles that correlate with their transfection efficacy. *19*(1):103–12, 2011.
- [172] M. Thomas and A. M. Klibanov. Conjugation to gold nanoparticles enhances polyethylenimine’s transfer of plasmid DNA into mammalian cells. *Proceedings of the National Academy of Sciences of the United States of America*, 100(16):9138–43, 2003.
- [173] M. S. Huh, S.-Y. Lee, S. Park, S. Lee, H. Chung, S. Lee, Y. Choi, Y.-K. Oh, J. H. Park, S. Y. Jeong, K. Choi, K. Kim, and I. C. Kwon. Tumor-homing glycol chitosan/polyethylenimine nanoparticles for the systemic delivery of siRNA in tumor-bearing mice. *Journal of controlled release : official journal of the Controlled Release Society*, 144(2):134–43, 2010.
- [174] R. V. Benjaminsen, M. A. Matthebjerg, J. R. Henriksen, S. M. Moghimi, and T. L. Andresen. The possible ”proton sponge ” effect of polyethylenimine (PEI) does not include change in lysosomal pH. *Molecular therapy : the journal of the American Society of Gene Therapy*, 21(1):149–57, 2013.
- [175] K. Berg, P. K. Selbo, L. Prasmickaite, T. E. Tjelle, K. Sandvig, J. Moan, G. Gaudernack, O. Fodstad, S. Kjølset, H. Anholt, G. H. Rodal, S. K. Rodal, and A. Høget. Photochemical internalization: a novel technology for delivery of macromolecules into cytosol. *Cancer Res.*, 59(6):1180–3, 1999.
- [176] E. Paszko, C. Ehrhardt, M. O. Senge, D. P. Kelleher, and J. V. Reynolds. Nanodrug applications in photodynamic therapy. *Photodiagnosis and photodynamic therapy*, 8(1):14–29, 2011.

- [177] P. Juzenas, W. Chen, Y. Sun, M. A. Coelho, R. Generalov, N. Generalova, and I. L. Christensen. Quantum dots and nanoparticles for photodynamic and radiation therapies of cancer. *Adv. Drug Delivery Rev.*, 60(15):1600–14, 2008.
- [178] I. Moserova and J. Kralova. Role of ER stress response in photodynamic therapy: ROS generated in different subcellular compartments trigger diverse cell death pathways. *PloS one*, 7(3):329–372, 2012.
- [179] A. Gupta, P. Avci, M. Sadasivam, R. Chandran, N. Parizotto, D. Vecchio, W. C. de Melo, T. Dai, L. Y. Chiang, and M. R. Hamblin. Shining light on nanotechnology to help repair and regeneration. *Biotechnology advances*, 31(5):607–31, 2013.
- [180] T. Iversen, T. Skotland, and K. Sandvig. Endocytosis and intracellular transport of nanoparticles: Present knowledge and need for future studies. *Nano Today*, 6(2):176–185, 2011.
- [181] M. Morille, C. Passiran, A. Vonarbourg, A. Clavreul, and J.-P. Benoit. Progress in developing cationic vectors for non-viral systemic gene therapy against cancer. *Biomaterials*, 29(2425):3477 – 3496, 2008.
- [182] P. S. Brookes, Y. Yoon, J. L. Robotham, M. W. Anders, and S. Sheu. Calcium, ATP, and ROS: a mitochondrial love-hate triangle. *American journal of physiology. Cell physiology*, 287(4):C817–33, 2004.
- [183] A. Daiber. Redox signaling (cross-talk) from and to mitochondria involves mitochondrial pores and reactive oxygen species. *Biochimica et Biophysica Acta (BBA)-Bioenergetics*, 1797(6-7):897–906, 2010.

- [184] Y. Andreyev, Y. E. Kushnareva, and A. Starkov. Mitochondrial metabolism of reactive oxygen species. *Biochemistry.*, 70(2):200–14, 2005.
- [185] M. P. Murphy. How mitochondria produce reactive oxygen species. *The Biochemical journal*, 417(1):1–13, 2009.
- [186] S. Trapp and R. W. Horobin. A predictive model for the selective accumulation of chemicals in tumor cells. *European biophysics journal : EBJ*, 34(7):959–66, 2005.
- [187] C. Pavani, A. F. Uchoa, C. S. Oliveira, Y. Iamamoto, and M. S. Baptista. Effect of zinc insertion and hydrophobicity on the membrane interactions and PDT activity of porphyrin photosensitizers. *Photochemical & photobiological sciences*, 8(2):233–40, 2009.
- [188] V. Mailänder, K. Landfester, and Volker Maila. Interaction of nanoparticles with cells. *Biomacromolecules*, 10(9):2379–2400, 2009.
- [189] R. Adsley. *Visualization of the cellular uptake of nanoparticles*. Phd, University of Nottingham, 2013.
- [190] D.K. Adigbli and A.J. MacRobert. Photochemical internalisation: the journey from basic scientific concept to the threshold of clinical application. *Current Opinion in Pharmacology*, 12(4):434 – 438, 2012.
- [191] P. Selbo, A. Weyergang, A. Hgset, Norum O-J., M. B. Berstad, M. Vikdal, and K. Berg. Photochemical internalization provides time- and space-controlled endolysosomal escape of therapeutic molecules. *Journal of Controlled Release*, 148(1):2 – 12, 2010.

- [192] O.-J. Norum, P. K. Selbo, g A. Weyergan, K-E. Giercksky, and K. Berg. Photochemical internalization (pci) in cancer therapy: From bench towards bedside medicine. *Journal of Photochemistry and Photobiology B: Biology*, 96(2):83 – 92, 2009.
- [193] J. Moan and K. Berg. The photodegradation of porphyrins in cells can be used to estimate the lifetime of singlet oxygen. *Photochemistry and Photobiology*, 53(4):549–553, 1991.
- [194] M. J. Niedre, M. S. Patterson, A. Giles, and B. C. Wilson. Imaging of photo-dynamically generated singlet oxygen luminescence in vivo. *Photochemistry and Photobiology*, 81(4):941–943, 2005.
- [195] P. G. Coupland, S. J. Briddon, and J. W. Aylott. Using fluorescent pH-sensitive nanosensors to report their intracellular location after Tat-mediated delivery. *Integrative biology : quantitative biosciences from nano to macro*, 1(4):318–23, 2009.
- [196] X. Jiang, J. Dausend, M. Hafner, A. Musyanovych, C. Röcker, K. Landfester, V. Mailänder, and G. U. Nienhaus. Specific effects of surface amines on polystyrene nanoparticles in their interactions with mesenchymal stem cells. *Biomacromolecules*, 11(3):748–53, 2010.
- [197] K. Gilmore and M. Wilson. The use of chloromethyl-X-rosamine (Mito-tracker red) to measure loss of mitochondrial membrane potential in apoptotic cells is incompatible with cell fixation. *Cytometry*, 36(4):355–8, 1999.
- [198] W. Pendergrass, N. Wolf, and M. Poot. Efficacy of MitoTracker Green and CMXrosamine to measure changes in mitochondrial membrane potentials in

- living cells and tissues. *Cytometry. Part A : the journal of the International Society for Analytical Cytology*, 61(2):162–9, 2004.
- [199] H. Suzuki, T. Toyooka, and Y. Ibuki. Simple and Easy Method to Evaluate Uptake Potential of Nanoparticles in Mammalian Cells Using a Flow Cytometric Light Scatter Analysis. *Environmental Science & Technology*, 41(8):3018–3024, 2007.
- [200] R. M. Zucker, E. J. Massaro, K. M. Sanders, L. L. Degn, and W. K. Boyes. Detection of TiO₂ nanoparticles in cells by flow cytometry. *Cytometry. Part A : the journal of the International Society for Analytical Cytology*, 77(7):677–85, 2010.
- [201] A. Kumar, A. K. Pandey, S. S. Singh, R. Shanker, and A. Dhawan. A flow cytometric method to assess nanoparticle uptake in bacteria. *Cytometry. Part A : the journal of the International Society for Analytical Cytology*, 79(9):707–12, 2011.
- [202] T. Dos Santos, J. Varela, I. Lynch, A. Salvati, and K. A. Dawson. Quantitative assessment of the comparative nanoparticle-uptake efficiency of a range of cell lines. *Small (Weinheim an der Bergstrasse, Germany)*, 7(23):3341–9, 2011.
- [203] P. Coupland. *Targeted fluorescent optical nanosensors for imaging and measuring function in intracellular microdomains*. PhD thesis, University of Nottingham, 2008.
- [204] M. C. Garnett. Gene-delivery systems using cationic polymers. *Crit. Rev. Ther. Drug Carrier Syst.*, 16(2):147–207, 1999.

- [205] E. Wagner, M. Ogris, and W. Zauner. Polylysine-based transfection systems utilizing receptor-mediated delivery. *Advanced drug delivery reviews*, 30(1-3):97–113, 1998.
- [206] M. Henriksen, B. Miller, J. Newmark, Y. Al-Kofahi, and E. Holden. Laser scanning cytometry and its applications: a pioneering technology in the field of quantitative imaging cytometry. *Methods Cell Biol.*, 102:161–205, 2011.
- [207] E. J. Ngen, P. Rajaputra, and Y. You. Evaluation of delocalized lipophilic cationic dyes as delivery vehicles for photosensitizers to mitochondria. *Bioorganic & medicinal chemistry*, 17(18):6631–40, 2009.
- [208] N. Dias and C. Bailly. Drugs targeting mitochondrial functions to control tumor cell growth. *Biochemical pharmacology*, 70(1):1–12, 2005.
- [209] J. Morgan and A. R. Oseroff. Mitochondria-based photodynamic anti-cancer therapy. *Advanced drug delivery reviews*, 49(1-2):71–86, 2001.
- [210] S. Hirohara, M. Obata, S. Ogura, I. Okura, S. Higashida, C. Ohtsuki, S. Ogata, Y. Nishikawa, M. Takenaka, H. Ono, Y. Mikata, and S. Yano. Hydrophobicity parameters (Log P) of glycoconjugated porphyrins for photodynamic therapy evaluated by reversed phase HPLC. *J. Porphyrins Phthalocyanines*, 08(11):1289–1292, 2004.
- [211] C. L. Peng, P. S. Lai, C. C. Chang, P. J. Lou, and M. J. Shieh. The synthesis and photodynamic properties of meso-substituted, cationic porphyrin derivatives in HeLa cells. *Dyes and Pigments*, 84(1):140–147, 2010.

- [212] R. W. Boyle and D. Dolphin. Structure and biodistribution relationships of photodynamic sensitizers. *Photochem. Photobiol.*, 64(3):469–85, 1996.
- [213] E. D. Sternberg, D. Dolphin, and C. Brickner. Porphyrin-based Photosensitizers for Use in Photodynamic Therapy. 54(447):4151–4202, 1998.
- [214] F. Anquez, I. El Yazidi-Belkoura, S. Randoux, P. Suret, and E. Courtade. Cancerous cell death from sensitizer free photoactivation of singlet oxygen. *Photochem. Photobiol.*, 88(1):167–74, 2012.
- [215] Y. E. K. Lee and R. Kopelman. Polymeric nanoparticles for photodynamic therapy. *Methods in molecular biology (Clifton, N.J.)*, 726:151–78, 2011.
- [216] D. E. Dolmans, D. Fukumura, and R. K. Jain. Photodynamic therapy for cancer. *Nat. Rev. Cancer*, 3(5):380–7, 2003.
- [217] D. A. Al-Mutairi, J. D. Craik, I. Batinic-Haberle, and L. T. Benov. Induction of oxidative cell damage by photo-treatment with zinc meta N-methylpyridylporphyrin. *Free Radic. Res.*, 41(1):89–96, 2007.
- [218] W. H. Chan, J. S. Yu, and S. D. Yang. Apoptotic signalling cascade in photosensitized human epidermal carcinoma A431 cells: involvement of singlet oxygen, c-Jun N-terminal kinase, caspase-3 and p21-activated kinase 2. *The Biochemical journal*, 351(1):221–32, 2000.
- [219] N. L. Oleinick, R. L. Morris, and I. Belichenko. The role of apoptosis in response to photodynamic therapy : what , where , why , and how. pages 1–21, 2002.

- [220] C. S. Oliveira, R. Turchiello, A. J. Kowaltowski, G. L. Indig, and M. S. Baptista. Major determinants of photoinduced cell death: Subcellular localization versus photosensitization efficiency. *Free radical biology & medicine*, 51(4):824–33, 2011.
- [221] M. E. Milanesio, M. G. Alvarez, S. G. Bertolotti, and E. N. Durantini. Photophysical characterization and photodynamic activity of metallo 5-(4-(trimethylammonium)phenyl)-10,15,20-tris(2,4,6-trimethoxyphenyl)porphyrin in homogeneous and biomimetic media. *Photochem. Photobiol. Sci*, 7:963–972, 2008.
- [222] M. Biesaga, K. Pyrzyska, and M. Trojanowicz. Porphyrins in analytical chemistry. A review. *Talanta*, 51(2):209–24, 2000.
- [223] G. Szintay and A. Horváth. Five-coordinate complex formation and luminescence quenching study of copper(II) porphyrins. *Inorganica Chimica Acta*, 324(1-2):278–285, 2001.
- [224] K. Stavrev and M. C. Zerner. A theoretical treatment of the absorption and emission properties of Cu(II) porphyrin. *Chemical Physics Letters*, 233(1-2):179–184, 1995.
- [225] F. Liu, K. L. Cunningham, W. Uphues, G. W. Fink, J. Schmolt, and D. R. McMillin. Luminescence Quenching of Copper(II) Porphyrins with Lewis Bases. *Inorganic Chemistry*, 34(8):2015–2018, 1995.
- [226] A Harriman. Luminescence of porphyrins and metalloporphyrins. Part 2. Copper(II), chromium(III), manganese(III), iron(II) and iron(III) por-

- phyrins. *Journal of the Chemical Society, Faraday Transactions 1*, 77(2):369, 1981.
- [227] X. Chen, X. Tian, I. Shin, and J. Yoon. Fluorescent and luminescent probes for detection of reactive oxygen and nitrogen species. *Chem. Soc. Rev.*, 40(9):4783–804, 2011.
- [228] C. C. Winterbourn. The Challenges of using Fluorescent Probes to Detect and Quantify Specific Reactive Oxygen Species in Living Cells. *Biochimica et biophysica acta*, 2013.
- [229] T. Patrice, editor. *Photodynamic Therapy*. Royal Society of Chemistry, 2003.
- [230] D. Gao, H. Xu, M. A. Philbert, and R. Kopelman. Ultrafine hydrogel nanoparticles: synthetic approach and therapeutic application in living cells. *Angewandte Chemie (International ed. in English)*, 46(13):2224–7, 2007.
- [231] A. J. Wagers and I. L. Weissman. Plasticity of adult stem cells. *Cell*, 116(5):639–48, 2004.
- [232] L. Da Silva Meirelles, P. C. Chagastelles, and N. B. Nardi. Mesenchymal stem cells reside in virtually all post-natal organs and tissues. *J. Cell Sci.*, 119(11):2204–13, 2006.
- [233] P. C. Aveline, J. I. Bourseguin, and G.Y. Rochefort. Mesenchymal stem cells and acquisition of a bone phenotype: An ion channel overview. *Journal of Developmental Biology and Tissue Engineering*, 3(9), 2011.
- [234] V. B. Fernández Vallone, M. A. Romaniuk, H. Choi, V. Labovsky, J. Otaegui, and N. A. Chasseing. Mesenchymal stem cells and their use in therapy:

What has been achieved? *Differentiation; research in biological diversity*, 85(1-2):1–10, 2013.

- [235] A. J. Friedenstein, R. K. Chailakhjan, and K. S. Lalykina. The development of fibroblast colonies in monolayer cultures of guinea-pig bone marrow and spleen cells. *Cell Tissue Kinet.*, 3(4):393–403, 1970.
- [236] H. Castro-Malaspina, R. E. Gay, G. Resnick, N. Kapoor, P. Meyers, D. Chiarieri, S. McKenzie, H. E. Broxmeyer, and M. A. Moore. Characterization of human bone marrow fibroblast colony-forming cells (CFU-F) and their progeny. *Blood*, 56(2):289–301, 1980.
- [237] A. J. Friedenstein, K. V. Petrakova, A. I. Kurolesova, and G. P. Frolova. Heterotopic of bone marrow. Analysis of precursor cells for osteogenic and hematopoietic tissues. *Transplantation*, 6(2):230–47, 1968.
- [238] P. Bianco, P. G. Robey, and P. J. Simmons. Mesenchymal stem cells: revisiting history, concepts, and assays. *Cell stem cell*, 2(4):313–9, 2008.
- [239] R. Schofield. The relationship between the spleen colony-forming cell and the haemopoietic stem cell. *Blood cells*, 4(1-2):7–25, 1978.
- [240] T. M. Dexter and N. G. Testa. Differentiation and proliferation of hemopoietic cells in culture. *Methods Cell Biol.*, 14:387–405, 1976.
- [241] T. M. Dexter, T. D. Allen, and L. G. Lajtha. Conditions controlling the proliferation of haemopoietic stem cells in vitro. *J. Cell. Physiol.*, 91(3):335–44, 1977.

- [242] A. I. Caplan and S. P. Bruder. Mesenchymal stem cells: building blocks for molecular medicine in the 21st century. *Trends Mol. Med.*, 7(6):259–64, 2001.
- [243] H. Zola. Medical applications of leukocyte surface molecules—the CD molecules. *Molecular medicine (Cambridge, Mass.)*, 12(11-12):312–6, 2006.
- [244] M. C. Cohen. Leukocyte and Stomal Cell Molecules. *Shock*, 28(4):498, 2007.
- [245] N. L. Kovach, T. M. Carlos, E. Yee, and J. M. Harlan. A monoclonal antibody to beta 1 integrin (CD29) stimulates VLA-dependent adherence of leukocytes to human umbilical vein endothelial cells and matrix components. *The Journal of cell biology*, 116(2):499–509, 1992.
- [246] N. A. Dallas, S. Samuel, L. Xia, F. Fan, M. J. Gray, S. J. Lim, and L. M. Ellis. Endoglin (CD105): a marker of tumor vasculature and potential target for therapy. *Clinical cancer research*, 14(7):1931–7, 2008.
- [247] A. M. Dang, J. A. Phillips, T. Lin, and E. S. Raveche. Altered CD45 expression in malignant B-1 cells. *Cell. Immunol.*, 169(2):196–207, 1996.
- [248] A. B. Satterthwaite, T. C. Burn, M. M. Le Beau, and D. G. Tenen. Structure of the gene encoding CD34, a human hematopoietic stem cell antigen. *Genomics*, 12(4):788–794, 1992.
- [249] M. Dominici, K. Le Blanc, I. Mueller, I. Slaper-Cortenbach, F. Marini, D. Krause, R. Deans, A. Keating, D. Prockop, and E. Horwitz. Minimal criteria for defining multipotent mesenchymal stromal cells. The International

- Society for Cellular Therapy position statement. *Cytotherapy*, 8(4):315–7, 2006.
- [250] P. Mafi, S. Hindocha, R. Mafi, M. Griffin, and Khan. W. Adult mesenchymal stem cells and cell surface characterization - a systematic review of the literature. *The open orthopaedics journal*, 5(Suppl 2):253–60, 2011.
- [251] K. Wang, T. Zhang, Q. Dong, E. C. Nice, C. Huang, and Y. Wei. Redox homeostasis: the linchpin in stem cell self-renewal and differentiation. *Cell death & disease*, 4:e537, 2013.
- [252] C. Götherström, O. Ringdén, M. Westgren, C. Tammik, and K. Le Blanc. Immunomodulatory effects of human foetal liver-derived mesenchymal stem cells. *Bone Marrow Transplant.*, 32(3):265–72, 2003.
- [253] C. Campagnoli. Identification of mesenchymal stem/progenitor cells in human first-trimester fetal blood, liver, and bone marrow. *Blood*, 98(8):2396–2402, 2001.
- [254] E. A. Jones, S. E. Kinsey, A. English, R. A. Jones, L. Straszynski, D. M. Meredith, A. F. Markham, A. Jack, P. Emery, and D. McGonagle. Isolation and characterization of bone marrow multipotential mesenchymal progenitor cells. *Arthritis Rheum.*, 46(12):3349–60, 2002.
- [255] C. L. Cetrulo and K. J. Cetrulo, editors. *Perinatal Stem Cells*. John Wiley & Sons, Inc., 2009.
- [256] A. A. Nery, I. C. Nascimento, T. Glaser, V. Bassaneze, J. E. Krieger, and H. Ulrich. Human mesenchymal stem cells: from immunophenotyping by

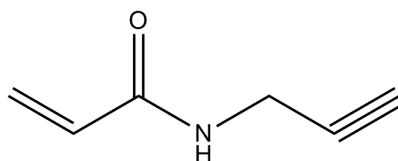
- flow cytometry to clinical applications. *Cytometry. Part A : the journal of the International Society for Analytical Cytology*, 83(1):48–61, 2013.
- [257] M. F. Pittenger. Multilineage Potential of Adult Human Mesenchymal Stem Cells. *Science*, 284(5411):143–147, 1999.
- [258] R. Gaebel, D. Furlani, H. Sorg, B. Polchow, J. Frank, K. Bieback, W. Wang, C. Klopsch, L. Ong, W. Li, N. Ma, and G. Steinhoff. Cell origin of human mesenchymal stem cells determines a different healing performance in cardiac regeneration. *PloS one*, 6(2):e15652, 2011.
- [259] M. Roederer. Spectral compensation for flow cytometry: visualization artifacts, limitations, and caveats. *Cytometry*, 45(3):194–205, 2001.
- [260] H. T. Maecker and J. Trotter. Flow cytometry controls, instrument setup, and the determination of positivity. *Cytometry. Part A : the journal of the International Society for Analytical Cytology*, 69(9):1037–42, 2006.
- [261] K. V. Tormos, E. Anso, R. B. Hamanaka, J. Eisenbart, J. Joseph, B. Kalyanaraman, and N. S. Chandel. Mitochondrial complex III ROS regulate adipocyte differentiation. *Cell metabolism*, 14(4):537–44, 2011.
- [262] P. Anderson, A. Carrillo-Gálvez, A. García-Pérez, M. Cobo, and F. Martín. CD105 (endoglin)-negative murine mesenchymal stromal cells define a new multipotent subpopulation with distinct differentiation and immunomodulatory capacities. *PloS one*, 8(10):769–79, 2013.
- [263] M. Leyva-Leyva, L. Barrera, C. López-Camarillo, L. Arriaga-Pizano, G. Orozco-Hoyuela, E. M. Carrillo-Casas, J. Calderón-Pérez, A. López-Díaz,

- F. Hernandez-Aguilar, R. González-Ramírez, S. Kawa, J. Chimal-Monroy, and L. Fuentes-Mera. Characterization of mesenchymal stem cell subpopulations from human amniotic membrane with dissimilar osteoblastic potential. *Stem cells and development*, 22(8):1275–87, 2013.
- [264] Y. Kanda, T. Hinata, S. W. Kang, and Y. Watanabe. Reactive oxygen species mediate adipocyte differentiation in mesenchymal stem cells. *Life Sci.*, 89(7-8):250–8, 2011.

Appendix A

Analytical data Monomers

(B)- *N*-Propargyl acrylamide



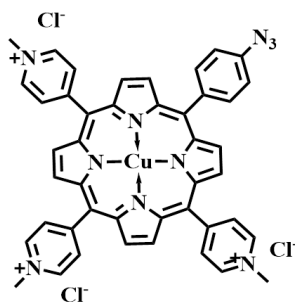
***N*-propargylacrylamide**

White solid; ¹H NMR (δ , 400MHz, CDCl₃): 6.32(dd, J =17.2 and 1.6 Hz, 1H, CH_{2,trans}=CH); 6.10 (dd, J =17.2 and 10.4 Hz, 1H, CH=CH₂), 5.79 (Bs, 1H, NH), 5.69 (dd, J =10.4 and 1.2 Hz, 1H, CH_{2,cis}=CH, 4.14(dd, J =5.2 and 2.4 Hz, 1H, CH₂—NH), 2.25 (t, J = 2.4 Hz, 1H, CH—C); ¹³C NMR (δ , 100MHz, CDCl₃): 165.1 (C), 130.1 (CH), 127.3 (CH₂), 79.3 (C), 71.8 (CH), 29.3 (CH₂); m/z found 110.1333 (MH⁺) calc. 110.1327

Appendix B

Analytical data Porphyrins

(10)- 5-4-[2-(azidoethoxy)ethyl]phenyl-10,15,20-tris-[(4-methylpyridinium)yl] porphyrinato copper(II)trichloride

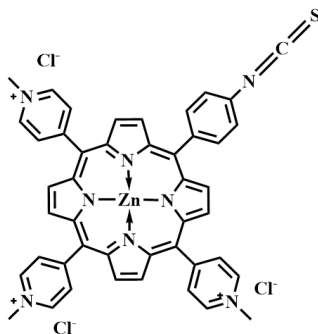


Red solid; ^1H NMR (δ , 400MHz, $\text{DMSO}-d_6$): 9.55-9.52(6H, 10+15+20-m-Ar); 9.16 (br, 4H, β -H); 9.07-9.00 (m, 10H, β -H and 10+15+20-o-Ar); 8.38 (2H, d, $J=9.2$), 8.32 (2H, d, $J=9.2$), 4.75-4.74 (9H, m, s, CH_3); 3.75-3.73 (4H, m, $\text{CONHCH}_2\text{CH}_2\text{OCH}_2$); 3.65-3.62 (2H, m, $\text{CONHCH}_2\text{CH}_2\text{COCH}_2$); 3.49 (2H, t, $J=4.7$ $\text{COCH}_2\text{CH}_2\text{NH}_3$); -3.02 (2H, s, pyrrole NH)

^{13}C NMR (δ , 100MHz, $\text{DMSO}-d_6$): 166.1; 156.5; 156.4; 144.2; 143.0; 134.2; 134.1; 132.1; 126.1; 121.9; 115.4; 114.7; 69.0; 68.8; 50.1; 47.8. m/z : $\text{C}_{49}\text{H}_{45}\text{N}_{11}\text{O}_2\text{Cu}$ found 819.4056 $[\text{M}-3\text{Cl}+\text{H}]^+$ calc. 819.3741 UV/vis (H_2O): $\lambda(\%)$:425 (100); 549(6.9); 590(1.4); $\log\epsilon_{425}$: 5.16; $R_t(\text{min})$: 10.45 ; M.p: $>300^\circ\text{C}$

(11)- 5-(4-isothiocyanatophenyl)-10,15,20-tris-[(4-N-methylpyridinium)yl]

porphyrinato zinc(II)trichloride



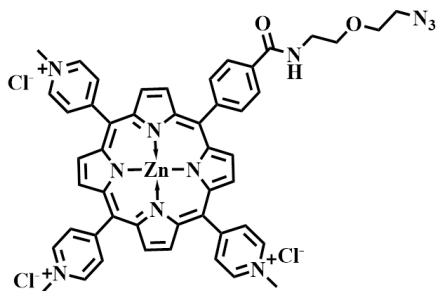
Green solid; ^1H NMR (δ , 400MHz, $\text{DMSO-}d_6$): 9.33-9.31 (6H, 10+15+20-m-Ar); 9.13-9.11 (4H, m, β -H); 9.03-8.99 (4H, β -H) 8.91-8.89 (6H, 10+15+20-o-Ar); 8.54 (2H, d, $J=8.3$, 5-o-Ar), 8.40 (2H, d, $J=8.3$, 5-m-Ar), 4.8 (9H, s, CH_3)

^{13}C NMR (δ , 100MHz, $\text{DMSO-}d_6$): 172.2; 161.3; 151.8; 150.3; 149.9; 144.8; 136.2; 134.7; 134.1; 133.6; 133.3; 132.8; 129.7; 116.8

m/z : $\text{C}_{45}\text{H}_{33}\text{N}_8\text{SZn}$ found 781.2476 $[\text{M}-3\text{Cl}+\text{H}]^+$ calc. 781.1824

UV/vis (H_2O): $\lambda(\%)$: 435 (100); 565(8.6); 607(5.5); $\log\epsilon_{435}$: 5.09; $R_t(\text{min})$: 6.50

(13)- 5-4-[2-(azidoethoxy)ethyl]phenyl-10,15,20-tris-[(4-methylpyridinium)yl]
 porphyrinato zinc(II)trichloride



Green solid; ^1H NMR (δ , 400MHz, $\text{DMSO}-d_6$): 9.35-9.31 (6H, m, 10+15+20-m-Ar); 9.12 (4H, s, β -H); 9.01-8.97 (4H, s, β -H) 8.92-8.88 (6H, m, 10+15+20-o-Ar); 8.27-8.21 (4H, m, 5-o-Ar and 5-m-Ar), 4.79 (9H, s, CH_3), 3.78-3.72 (6H, m, $\text{CONHCH}_2\text{CH}_2\text{OCH}_2$); 3.42 (2H, t, $J=9.2$ $\text{ROCH}_2\text{CH}_2\text{N}_3$)

^{13}C NMR (δ , 100MHz, $\text{DMSO}-d_6$): 167.3; 158.5; 149.3; 147.4; 146.9; 143.9; 142.0; 141.9; 132.7; 131.8; 131.2; 130.6; 130.4; 129.6; 123.9; 121.5; 113.9; 113.1; 68.1; 67.6; 49.1; 38.2

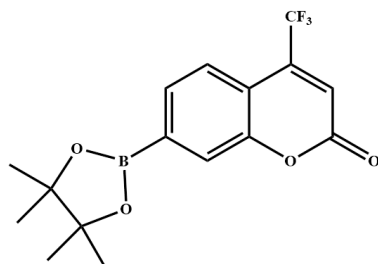
m/z : $\text{C}_{49}\text{H}_{42}\text{N}_{11}\text{N}_2\text{Zn}$ found 880.3026 $[\text{M}-3\text{Cl}]^+$ calc. 880.2800

UV/vis (H_2O): $\lambda(\%)$: 434 (100); 564(7.2); 606(3.2); $\log\epsilon_{435}$: 5.26; $R_t(\text{min})$: 6.15

Appendix C

Analytical data probe for ROS detection

(B)- 4-trifluoromethyl coumarin pinacol boronate



Yellow solid; ^1H NMR (δ , 400MHz, $\text{DMSO-}d_6$): 7.73 (dd, $J=8$ Hz, $J=1.7$ Hz, 1H, C6—H); 7.70 (dd, $J=8$ Hz, $J=0.8$ Hz, 1H, C5—H); 7.66 (s, 1H, C8—H); 7.13 s, 1H, C3—H); 1.32 (s, 12H)

^{13}C NMR (δ , 100MHz, $\text{DMSO-}d_6$): 158.56; 153.54; 139.33; 124.67; 123.36; 122.74; 120.63; 119.09; 119.03; 115.73; 84.89; 25.01

m/z : found 382.1761 [$\text{MH}^+ + 42$] calc. 382.1432; $R_t(\text{min})$: 5.28